

# **Laser-to-RF Phase Detection with Femtosecond Precision for Remote Reference Phase Stabilization in Particle Accelerators**

Vom Promotionsausschuss der  
Technischen Universität Hamburg-Harburg  
zur Erlangung des akademischen Grades  
Doktor-Ingenieur (Dr.-Ing.)  
genehmigte Dissertation

von  
Thorsten Lamb

aus  
Bad Kreuznach

2016

1. Gutachter: Prof. Dr. Ernst Brinkmeyer
2. Gutachter: Prof. Dr.-Ing. Arne Jacob
3. Gutachter: Dr. Holger Schlarb

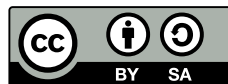
Datum der mündlichen Prüfung: 24.06.2016

**Laser-to-RF Phase Detection with Femtosecond Precision  
for Remote Reference Phase Stabilization  
in Particle Accelerators**

LAMB, Thorsten: *Laser-to-RF Phase Detection with Femtosecond Precision for Remote Reference Phase Stabilization in Particle Accelerators – DESY-THESIS-2017-016*. Verlag Deutsches Elektronen Synchrotron: Hamburg, 2017. ISSN: 1435-8085. doi: [10.3204/PUBDB-2017-02117](https://doi.org/10.3204/PUBDB-2017-02117)  
Zugleich: Hamburg, Technische Universität Hamburg-Harburg, Dissertation, 2016

ORCID: [0000-0001-6682-9450](https://orcid.org/0000-0001-6682-9450)

© 2017 by Thorsten Lamb  
This dissertation is licensed under a  
Creative Commons Attribution-ShareAlike 4.0 International License.



To view a copy of this license, visit  
<https://creativecommons.org/licenses/by-sa/4.0/>

**keywords (HEP)** free electron laser ; interferometer ; laser: erbium ; laser: pulsed ; microwaves: phase ; microwaves: stability ; optics: design ; optics: laser ; optics: time delay ; stability: phase ; time: stability

**Schlagwörter (SWD)** Empfindlichkeit ; Faseroptik ; Femtosekundenbereich ; Femtosekundenlaser ; Freie-Elektronen-Laser ; Hochfrequenz ; Hochfrequenztechnik ; Impulslaser ; Integrierte Optoelektronik ; Interferometer ; Mikrowellenoszillator ; Mikrowellenspektrum ; Optisches Verfahren ; Optoelektronische Schaltung ; Phasenmessung ; Phasenrauschen ; Phasenregelkreis ; Phasensynchronisierung ; Rauschspektrum ; Röntgenlaser ; Ultrakurzer Lichtimpuls ; VCO

**keywords (LCSH)** Electrooptical devices ; Femtosecond lasers ; Fiber optics ; Free electron lasers ; Laser pulses, ultrashort ; Mode-locked lasers ; Optical detectors ; Phase-locked loops ; Radio frequency ; Synchronization

**keywords (free)** Balanced Optical-Microwave Phase Detector ; BOM-PD ; FEL ; Fiber-Loop Optical-Microwave Phase Detector ; FLOM-PD ; Laser-to-RF Phase Detector ; L2RF ; Mach-Zehnder Interferometer ; MZI ; Mach-Zehnder Modulator ; MZM ; Microwave Generation ; Microwave Oscillators ; Microwave Synthesis ; Optische Synchronisation ; Phase Measurement ; Phase Noise ; Pulsed Optical Synchronization System ; Sagnac-Loop ; Timing Jitter ; Ultrafast Optics ; Ultrafast Technology

*für Malte, meinen Sonnenschein*

*Reality is frequently inaccurate.*

— DOUGLAS ADAMS, *The Restaurant at the End of the Universe* (1980)



## Abstract

The operation of modern [free-electron lasers \(FELs\)](#) requires the synchronization of different accelerator subsystems with femtosecond precision. A pulsed optical synchronization system is for this reason operated at the [Free-Electron Laser in Hamburg \(FLASH\)](#) and it is under construction for the upcoming European [X-ray Free-Electron Laser \(XFEL\)](#). Laser pulses from the optical master oscillator are transmitted by timing stabilized optical fiberlinks to dedicated end stations along the accelerator.

Devices which cannot operate with optical synchronization signals are instead conventionally synchronized with [radio frequency \(RF\)](#) reference signals. These signals are distributed in the accelerator by coaxial cables. Especially the [low-level radio frequency \(LLRF\)](#) system requires [RF](#) reference signals with femtosecond stability in order to meet nowadays femtosecond demands. Due to cable drifts and the length of the accelerators, this level of stability cannot be provided by conventional [RF](#) transport.

A [laser-to-RF \(L2RF\)](#) phase detector has been invented, which allows to measure with femtosecond precision the relative phase between a phase stable optical pulse train from an optical fiberlink and an [RF](#) signal. The [L2RF](#) phase detector is based on an integrated [MACH-ZEHNDER modulator \(MZM\)](#) in which the phase error between both signals is encoded in an amplitude modulation of the optical pulse train. Different configurations, based on single output and dual output [MZMs](#) have been evaluated for different operation scenarios. A full mathematical representation of the chosen configuration has been derived. The impact of multiple error sources has been investigated. It has been proven that most error sources have only second or higher order influence on the detection principle which is a significant advantage over existing schemes. The invented [L2RF](#) phase detector is for example balanced and in its working point insensitive to power variations of the optical reference pulse train.

The femtosecond performance has been verified with two different prototypes. Error sources of the measurement setup have been identified and eliminated. The achieved stability of 3.6 fs over 12 h for a [L2RF](#) phase detector is currently unmatched.

The optical setup of the [L2RF](#) phase detector has been engineered and the detector electronics have been integrated into a custom unit. All components were finally combined to a prototype of the [optical reference module \(REFM-OPT\)](#) which makes use of the [L2RF](#) phase detector in order to provide [RF](#) reference signals in the accelerator tunnel with femtosecond precision.

## Kurzdarstellung

Der Betrieb moderner Freie-Elektronen-Laser (FELs) setzt die femtosekundengenaue Synchronisation verschiedener Teilsysteme des Beschleunigers voraus. Bei FLASH wird aus diesem Grund ein gepulstes optisches Synchronisationssystem betrieben. Für den im Bau befindlichen European XFEL wird ebenfalls ein solches System implementiert. Im optischen Synchronisationssystem werden Laserpulse eines zentralen Referenzlasers mit Hilfe von längenstabilisierten Glasfasern zu dedizierten Komponenten des Beschleunigers transportiert.

Geräte, die nicht mit Hilfe von Laserpulsen synchronisiert werden können, werden stattdessen mit Hochfrequenzsignalen versorgt. Insbesondere das LLRF System benötigt femtosekundengenaue Hochfrequenz Referenzsignale, um die heutigen Stabilitätsanforderungen im Femtosekundenbereich erfüllen zu können. Wegen Kabeldriften und durch die Länge der Beschleuniger kann diese Stabilität mit herkömmlicher Hochfrequenztechnik allerdings nicht bereitgestellt werden.

Mit Hilfe des neu entwickelten L2RF-Phasendetektors kann die relative Phase zwischen einem phasenstabilen optischen Referenzpulszug und einem Hochfrequenzsignal femtosekundengenau bestimmt werden. Der L2RF-Phasendetektor basiert auf einem integrierten MACH-ZEHNDER-Modulator (MZM), in dem der gemessene Phasenfehler dem optischen Pulszug in Form einer Amplitudenmodulation aufgeprägt wird. Verschiedene Konfigurationen des L2RF Phasendetektors, basierend auf einem MZM mit einem oder zwei Ausgängen wurden für unterschiedliche Betriebsbedingungen ausgearbeitet. Die vollständige Übertragungsfunktion des Phasendetektors in der gewählten Ausführung wurde anschließend unter dem Einfluss verschiedener Störgrößen mathematisch analysiert. Es konnte gezeigt werden, dass die meisten Störgrößen zweiter oder höherer Ordnung sind, was einen signifikanten Vorteil des L2RF Phasendetektors gegenüber alternativen Verfahren darstellt. Das Detektionsschema ist im Arbeitspunkt zum Beispiel insensitive gegenüber Variationen der optischen Leistung des Referenzpulszuges.

Die Genauigkeit im Bereich weniger Femtosekunden wurde in Labormessungen bestätigt, nachdem Phasendriften des Messaufbaus beseitigt wurden. Die gezeigte Stabilität von 3,6 fs in 12 h ist für einen L2RF Phasendetektor unübertroffen.

Der optische Teil des Phasendetektors wurde durchkonstruiert und der elektronische Teil des Detektors zu einem kompakten Gerät integriert. Unter Verwendung dieser Komponenten wurde schließlich der Prototyp des optischen Referenzmoduls (REFM-OPT) gebaut, das mit Hilfe eines L2RF Phasendetektors die femtosekundengenaue Bereitstellung von Hochfrequenz-Referenzsignalen unmittelbar im Beschleuniger ermöglicht.



## Acknowledgements

The present thesis has been prepared and written during my research in the MSK group at [DESY](#) in Hamburg. I highly appreciate the international atmosphere, the support and the inspiration I experience there.

I would like to express my sincere thanks to Prof. Dr. Brinkmeyer from the Hamburg University of Technology (TUHH), who accepted the proposal for this thesis, gave advice and supported me during the whole time, and also to Prof. Dr.-Ing. Jacob who kindly agreed to review my thesis.

I am furthermore deeply grateful to the head of the MSK group and mastermind behind our pulsed optical synchronization systems Dr. Holger Schlarb. He welcomed me with open arms back in 2010 when I started my diploma thesis in his group. Ever since he was a great source of inspiration and ideas to me and especially to my dissertation. Thank you for this opportunity.

All present and former colleagues and fellow PhD students from the laser-based synchronization team provided invaluable support to my work in countless ways. Thank you for all the fruitful discussions, for your help and your motivation. I very much enjoy working with all of you.

I want to especially thank our team leader Dr.-Ing. Cezary Sydlo and my office mate Matthias Felber who both never hesitated to share their knowledge with me and who finally proofread my thesis. Likewise many thanks to Ewa Janas who made a large contribution to the electrical engineering by first implementing the readout electronics during her master's thesis and by later engineering the [RF](#) electronics. In this context, I also want to express special thanks to Martin Schäfer who helped to construct and fabricated most mechanical parts which I used.

Grateful thanks to all further colleagues from the MSK and the FLA groups, to the members of our collaborations and especially to the technicians of both groups. You were always around and helped to assemble the next prototype or to prepare the next component. I'm indebted to all of you.

Many thanks go to my family, especially to my parents, my brother and to Deborah my beloved partner. You always backed me up and found the right words for me whenever I was lost in details. Thank you for your patience and your support.



---

# Contents

<b>Preface</b>	<b>XIII</b>
List of Figures . . . . .	XIII
List of Tables . . . . .	XIV
<b>Glossaries</b>	<b>XV</b>
Acronyms . . . . .	XV
Symbols . . . . .	XVII
<b>1 Introduction</b>	<b>1</b>
1.1 Introduction to Free-Electron Lasers . . . . .	2
1.2 An Optical Synchronization System for Free-Electron Lasers . . . . .	6
1.3 Thesis Outline . . . . .	11
<b>2 The Laser-to-RF Phase Detection Principle</b>	<b>13</b>
2.1 A Basic MZM Based Laser-to-RF Phase Detection Scheme . . . . .	14
2.2 An Advanced Laser-to-RF Phase Detection Scheme . . . . .	16
2.3 Improved Bias Voltage Control Using Dual Output MZMs . . . . .	19
2.4 The Origin of the Spectral Amplitude Modulation . . . . .	22
2.5 Extended Repetition Rate and RF Frequency Ratios . . . . .	23
2.6 Extended Working Scheme with Single Output MZMs . . . . .	24
2.6.1 Determination of the Length of the First Delay in Front of the MZM	26
2.6.2 Calculation of the Modulation Frequency and First Delay Length	29
2.6.3 Summary for the Operation with Single Output MZMs . . . . .	31
2.7 Extended Working Scheme with Dual Output MZMs . . . . .	32
2.7.1 Calculation of the Modulation Frequency and Second Delay Length	33
2.7.2 Summary for the Operation with Dual Output MZMs . . . . .	35
<b>3 Mathematical Analysis of the Laser-to-RF Principle</b>	<b>37</b>
3.1 Situation at FLASH and the European XFEL . . . . .	38
3.2 Splitting Ratio at the First Delay Line and Incoupling Efficiency . . . . .	39
3.3 The MZM Transfer Function . . . . .	41
3.4 Detection with an InGaAs PIN Photodiode . . . . .	43

## Contents

3.5	Derivation of the Power Spectral Density and Its Envelope . . . . .	45
3.6	Analysis of the Power Spectral Density and Its Envelope . . . . .	48
3.7	Fourier Transform of the Photodiode Signals . . . . .	54
3.8	Extraction of a Single Frequency Component from the Spectrum . . . . .	55
3.9	Phase Sensitive Amplitude Detection Principle . . . . .	57
3.10	Definition of the Measurement Channels . . . . .	60
3.11	Analysis of the General Laser-to-RF Output Equations . . . . .	64
3.11.1	Examination of the Phase Error Channel . . . . .	65
3.11.2	Sensitivity and Noise of the L2RF Phase Detector . . . . .	68
3.11.3	Evaluation of the Bias Voltage Error Channel . . . . .	70
3.11.4	Analysis of the Splitting Ratio Error Channel . . . . .	72
3.11.5	First Order Error Contributions to the Output Signals . . . . .	72
3.12	Summary of the Theoretical Analysis . . . . .	75
<b>4</b>	<b>Prototypes and Implementation</b>	<b>77</b>
4.1	The First Laboratory Prototype . . . . .	78
4.1.1	Construction of the First Delay Line . . . . .	79
4.1.2	Construction of the Second Delay Line . . . . .	81
4.1.3	Readout Setup of the First Laboratory Prototype . . . . .	82
4.1.4	Assembly of the First Laboratory Prototype . . . . .	84
4.2	Operation and Adjustment of the L2RF Phase Detector . . . . .	86
4.3	Practical Considerations on Possible Error Sources . . . . .	89
4.4	RF Cable Characterization . . . . .	90
4.5	The Second Laboratory Prototype . . . . .	93
4.5.1	Integrated Optics for the L2RF Phase Detector . . . . .	93
4.5.2	Integrated Readout Electronics . . . . .	100
4.6	The Accelerator Prototype of the REFM-OPT . . . . .	101
4.6.1	The REFM-OPT 1.3 GHz Actuator Electronics . . . . .	102
4.6.2	Integration and Assembly of the REFM-OPT Prototype . . . . .	104
4.7	Measurement Results from the L2RF Prototypes . . . . .	105
4.7.1	Measurement Results from the First Prototype . . . . .	105
4.7.2	Measurement Results from the Second Prototype . . . . .	108
<b>5</b>	<b>RF Distribution Techniques</b>	<b>115</b>
5.1	Conventional RF Transport . . . . .	115
5.2	RF Transport Based on Continuous Wave Lasers . . . . .	116
5.3	RF Transport Based on Pulsed Lasers . . . . .	117
<b>6</b>	<b>Outlook</b>	<b>119</b>
<b>7</b>	<b>Summary</b>	<b>121</b>

**Appendix**

<b>A</b>	<b>Integrated MZI Based Optical Amplitude Modulators</b>	<b>125</b>
<b>B</b>	<b>Synchronous Detection Using Double-Balanced RF Mixers</b>	<b>129</b>
<b>C</b>	<b>Pulse Trains and Their Fourier Transform</b>	<b>133</b>
C.1	Important Properties of FOURIER Transforms . . . . .	134
C.2	The DIRAC Delta Pulse and the DIRAC Pulse Train . . . . .	134
C.3	FOURIER Series and FOURIER Transform of DIRAC Pulse Trains . . . . .	136
C.4	Spectral Representations of Signals . . . . .	138
C.5	The Power Spectral Density of General FOURIER Series . . . . .	140
C.6	The Power Spectral Density of DIRAC Pulse Trains . . . . .	143
<b>D</b>	<b>Photographs</b>	<b>145</b>
	<b>Bibliography</b>	<b>159</b>
	Data Sheets . . . . .	165
	<b>Publications</b>	<b>169</b>
	Patents . . . . .	169
	Conference Proceedings . . . . .	169



---

# Preface

## List of Figures

1.1	General (X)FEL Layout . . . . .	2
1.2	Electron Bunch Passing Through an Undulator . . . . .	3
1.3	Comparison of the Peak Brilliance of Different Light Sources . . . . .	4
1.4	Block Diagram of the Pulsed Optical Synchronization System . . . . .	8
1.5	Schematic Overview of FLASH and Its Optical Synchronization System . . . . .	11
2.1	Example of the Pulse Pattern Generation with a Single Output MZM . . . . .	14
2.2	Pulse Pattern and Spectra for an Integer Frequency Ratio . . . . .	16
2.3	Pulse Pattern and Spectra for an Half Integer Frequency Ratio . . . . .	17
2.4	Example of the Pulse Pattern Generation with a Dual Output MZM . . . . .	19
2.5	Pulse Pattern and Spectra for a Half Integer Frequency Ratio Using a Dual Output MZM in a Basic L2RF Scheme . . . . .	21
2.6	Extended Pulse Pattern Generation with a Single Output MZM . . . . .	24
2.7	Pulse Patterns and Spectra Using a Single Output MZM at a Full Integer Frequency Ratio in an Extended L2RF Scheme . . . . .	25
2.8	Modulated Frequency Combs for Different Delays . . . . .	28
2.9	Extended Pulse Pattern Generation with a Dual Output MZM . . . . .	33
2.10	Pulse Patterns and Spectra Using a Dual Output MZM at a Full Integer Frequency Ratio in an Extended L2RF Scheme . . . . .	36
3.1	Block Diagram of a Basic L2RF Readout Scheme . . . . .	38
3.2	L2RF Output Power Spectral Density Under Different Error Conditions . . . . .	51
3.3	L2RF Output Phase for Operation on Different Sides of the Working Point . . . . .	57
3.4	Phasor Representation of the Signal Superposition at the First Harmonic . . . . .	62
3.5	Phasor Representation of the Signal Superposition at the Second Harmonic . . . . .	63
3.6	Normalized Output Voltage of the L2RF Phase Error Measurement Channel . . . . .	67
4.1	Block Diagram of the First Part of the Optical Setup . . . . .	79
4.2	Block Diagram of the Second Part of the Optical Setup . . . . .	81

## List of Tables

4.3	Block Diagram of a Single Channel Detector for the L2RF Phase Detector	82
4.4	Complete Block Diagram of the First Laboratory Prototype . . . . .	85
4.5	Typical Sources for Phase Drifts of the Measurement Setup . . . . .	89
4.6	Experimentally Determined RF Cable Temperature Coefficients . . . . .	92
4.7	Humidity Stability in Housings for the L2RF Phase Detector . . . . .	97
4.8	Schematic Block Diagram of the Integrated Readout Electronics . . . . .	101
4.9	Long-term Drift Measurement of the First Laboratory Prototype . . . . .	106
4.10	Detector Noise Measurement of the First Laboratory Prototype . . . . .	108
4.11	Long-term Drift Measurement of the Second Laboratory Prototype . . . . .	110
4.12	Detector Noise Floor Measured at the Second Laboratory Prototype . . . . .	111
4.13	Long-term Drift Measurement of the Second Laboratory Prototype . . . . .	113
A.1	Schematic Sketch of an MZM . . . . .	125
B.1	Schematic Circuit of a Double-Balanced Diode Ring Mixer . . . . .	130
D.1	The First Delay Line of the First Laboratory Prototype . . . . .	145
D.2	The Second Delay Line of the First Laboratory Prototype . . . . .	146
D.3	The Readout Electronics of the First Laboratory Prototype . . . . .	147
D.4	Rapid Prototyping of the Integrated L2RF Optics . . . . .	148
D.5	Thermal Control of the Integrated L2RF Optics Using Peltier Elements . . . . .	149
D.6	Side View on the Integrated L2RF Optics Showing the Humidity Buffer . . . . .	149
D.7	RF Feed-Through Sealing with Ruber O-Ring Gaskets . . . . .	150
D.8	RF Feed-Through Sealing Assembled . . . . .	150
D.9	Temperature and Humidity Characterization in a Climate Chamber . . . . .	151
D.10	Final Integrated Optics for the L2RF Phase Detector . . . . .	152
D.11	Out-of-Loop Measurement of the Second L2RF Prototype (Optics) . . . . .	153
D.12	Out-of-Loop Measurement of the Second L2RF Prototype (Readout) . . . . .	154
D.13	Internals of the Integrated Readout Electronics . . . . .	155
D.14	Vibration Damping for the Integrated Optics inside the REFM-OPT . . . . .	155
D.15	REFM-OPT Prototype Internals . . . . .	156
D.16	REFM-OPT Prototype Front View . . . . .	157
D.17	REFM-OPT Prototype Rear View . . . . .	157

## List of Tables

2.1	Modulation Factors for Selected Sub-Harmonics . . . . .	30
4.1	Experimentally Determined Humidity Coefficients of RF Cables . . . . .	91



---

# Glossaries

## Acronyms

<b>ACC</b>	acceleration module
<b>ADC</b>	analog-to-digital converter
<b>AM/PM</b>	amplitude modulation/phase modulation
<b>BAM</b>	bunch arrival-time monitor
<b>BC</b>	bunch compressor
<b>BOM-PD</b>	balanced optical-microwave phase detector
<b>CCR</b>	corner-cube retroreflector
<b>CW</b>	continuous wave
<b>DAC</b>	digital-to-analog converter
<b>DC</b>	direct current
<b>DCF</b>	dispersion compensating fiber
<b>DCM</b>	drift calibration module
<b>DESY</b>	Deutsches Elektronen-Synchrotron
<b>DIN</b>	Deutsches Institut für Normung e.V.
<b>DRO</b>	dielectric resonator oscillator
<b>EDFA</b>	erbium-doped fiber amplifier
<b>EDFL</b>	erbium-doped fiber laser
<b>EMI</b>	electro-magnetic interference
<b>EO</b>	electro-optic
<b>EOM</b>	electro-optic modulator
<b>EOSD</b>	electro-optic spectral decoding
<b>ESD</b>	energy spectral density
<b>FE</b>	finite element
<b>FEL</b>	free-electron laser
<b>FLASH</b>	Free-Electron Laser in Hamburg
<b>FLOM-PD</b>	fiber-loop optical-microwave phase detector

## Acronyms

<b>FPGA</b>	field-programmable gate array
<b>FRED</b>	fuse and relay board
<b>FRM</b>	FARADAY rotating mirror
<b>FSD</b>	free-space signal distribution
<b>FWHM</b>	full width at half maximum
<b>HD-PE</b>	high density polyethylene
<b>I/Q</b>	in-phase and quadrature phase
<b>IF</b>	intermediate frequency
<b>InGaAs</b>	indium gallium arsenide
<b>ITU</b>	International Telecommunication Union
<b>L2L</b>	laser-to-laser
<b>L2RF</b>	laser-to-RF
<b>LBNL</b>	Lawrence Berkeley National Laboratory
<b>LED</b>	light-emitting diode
<b>linac</b>	linear accelerator
<b>LiNbO<sub>3</sub></b>	Lithium-Niobate
<b>LLRF</b>	low-level radio frequency
<b>LNA</b>	low-noise amplifier
<b>LO</b>	local oscillator
<b>LOGM</b>	LO generation module
<b>LSU</b>	link stabilization unit
<b>MEMS</b>	micro-electro-mechanical system
<b>MLO</b>	master laser oscillator
<b>MZI</b>	MACH-ZEHNDER interferometer
<b>MZM</b>	MACH-ZEHNDER modulator
<b>NTC</b>	negative temperature coefficient of resistance
<b>OXC</b>	optical cross-correlator
<b>PBC</b>	polarizing beam cube
<b>PCB</b>	printed circuit board
<b>PDL</b>	polarization-dependent loss
<b>PI</b>	proportional-integral
<b>PLL</b>	phase-locked loop
<b>PM</b>	polarization maintaining
<b>PP</b>	pump-probe
<b>PRDS</b>	phase reference distribution system
<b>PSD</b>	power spectral density
<b>PSM</b>	power supply module

<b>REACT</b>	<b>REFM-OPT</b> actuator
<b>REFM-OPT</b>	optical reference module
<b>RF</b>	radio frequency
<b>RF-MO</b>	radio frequency master oscillator
<b>rms</b>	root mean square
<b>SASE</b>	self-amplified spontaneous emission
<b>SESAM</b>	semiconductor saturable absorber mirror
<b>SM</b>	single mode
<b>SMA</b>	SubMiniature version A
<b>SMF</b>	single mode fiber
<b>SNR</b>	signal-to-noise ratio
<b>SPI</b>	serial parallel interface
<b>SSB</b>	single sideband
<b>TESLA</b>	TeV-Energy Superconducting Linear Accelerator
<b>TMCB</b>	temperature monitoring and control board
<b>TTF</b>	<b>TESLA</b> Test Facility
<b>TTF-FEL</b>	<b>TESLA</b> Test Facility Free-Electron Laser
<b>U</b>	rack unit
<b>VSD</b>	voltage spectral density
<b>VUV</b>	vacuum ultraviolet
<b>XFEL</b>	X-ray Free-Electron Laser

## Symbols

$a_{\{.\}}$	scaling factors used on various occasions
$a_{bp}$	pass-band insertion loss factor of an <b>RF</b> band-pass filter
$a_{el}$	electrical gains of the detector chain
$a_{LNA}$	voltage gain factor of a low-noise amplifier
$a_{mix}$	conversion gain factor of an <b>RF</b> mixer
$a_{MZM}$	insertion loss factor of the regular output of an <b>MZM</b> at full transmission
$a'_{MZM}$	insertion loss factor of the inverted output of an <b>MZM</b> at full transmission
$a_{RF}$	gain factor of an <b>RF</b> amplifier
$c_b, c_d$	FOURIER coefficients of a general FOURIER series
$c_{III}$	FOURIER coefficient of the FOURIER representation of the Sha function . . . 1/s

## Symbols

$\delta(t)$	DIRAC delta pulse at the point $t$ of time . . . . .	1/s
$d$	distance between the electrodes of an integrated MZM . . . . .	m
$\Delta n_r$	change of the index of refraction caused by the Pockels effect	
$\Delta\phi$	externally induced phase difference between the arms of an MZM . . . . .	rad
$\Delta\varphi_{LO}$	error of the LO phase . . . . .	rad
$\Delta\varphi_{RF}$	error of the RF phase relative to the laser pulse train at the MZM . . . . .	rad
$\Delta r_s$	error of the splitting ratio at the first delay line	
$\Delta T_{\{.,.\}}$	error of the time delay 1 and 2 of the first and second delay line . . . . .	s
$\Delta t_{RF}$	timing error of an RF signal . . . . .	s
$\Delta V_b$	error of the bias voltage applied to an MZM . . . . .	V
$\eta$	incoupling efficiency of a laser pulse train into a fiber collimator	
$\eta_{\{.,.\}}$	incoupling efficiency of the pulse trains 1 and 2 from the first delay line	
$\eta_d$	efficiency of the polarization adjustment after the first delay line	
$\eta_m$	average incoupling efficiency of the pulse trains from the first delay line	
$e$	elementary charge, $1.602\,176\,53 \times 10^{-19}$ . . . . .	C
$E_{eff}$	effective electrical field . . . . .	V/m
$E_p$	optical pulse energy . . . . .	J
$f$	frequency or repetition rate of a periodic signal . . . . .	Hz
$f_c$	center frequency of an RF band-pass filter . . . . .	Hz
$f_{LO}$	frequency of the LO signal at an RF mixer . . . . .	Hz
$f_{mod}$	modulation frequency – the lowest comb line in the spectrum which is extinct by combining two laser pulse trains with a fixed delay . . . . .	Hz
$f_{mod}^\pi$	$\pi$ modulation frequency – the lowest frequency which is canceled by destructive interference of two laser pulse trains combined at a fixed delay . . . . .	Hz
$f_{rep}$	repetition rate of a laser pulse train . . . . .	Hz
$f_{RF}$	frequency of an RF signal . . . . .	Hz
$\gamma$	optical confinement factor, part of an optical mode confined in the active layer of an optical waveguide	
$\Gamma$	transmission of an MZM	
$g_{bp}$	pass-band insertion loss of an RF band-pass filter . . . . .	dB
$g_c$	conversion gain of an RF mixer . . . . .	dB
$g_{RF}$	gain of an RF amplifier . . . . .	dB

$h$	integer, denoting the harmonics of a laser pulse train	
$h_{\{.\}}$	harmonic, at which the error measurement channels denoted in the subscript can be detected, the channels are $\varphi_{\text{RF}}$ , $V_{\text{b}}$ and $r_{\text{s}}$	
$\mathcal{H}(h)$	normalized envelope function of the <a href="#">L2RF PSD</a>	
$\mathcal{H}_{\text{abs}}(f)$	absolute envelope function of the <a href="#">PSD</a> of the <a href="#">L2RF</a> photodiode signal	W/Hz
$\mathcal{H}_{\text{dB}}(h)$	normalized envelope function of the <a href="#">L2RF PSD</a> in decibel	dB
$\mathcal{H}_{\{.\}}(h)$	normalized envelope of the <a href="#">L2RF PSD</a> , all errors are assumed to be zero except the error denoted in the subscript, e.g. $\varphi_{\text{RF}}$ , $V_{\text{b}}$ , $r_{\text{s}}$ , $T_1$ and $T_2$	
$i_{\text{PD}}(t)$	time varying photocurrent of a photodiode	A
$I$	optical intensity	W/m <sup>2</sup>
$I_{\text{n,shot}}$	shot noise from a photodiode	A
$k$	integer modulation factor – highest power of two which is still an aliquot divisor of the $n$ th sub-harmonic of an <a href="#">RF</a> signal	
$K$	BOLTZMANN's constant, $1.380\,650\,5 \times 10^{-23}$	J/K
$K_{\varphi}$	voltage to phase calibration constant of a phase detector	V/s
$K_{\varphi,\text{rad}}$	voltage to phase calibration constant of a phase detector	V/rad
$\lambda$	wavelength	m
$L$	modulation length in an <a href="#">EO</a> modulator	m
$n$	integer ratio of the laser repetition rate $f_{\text{rep}}$ and the <a href="#">RF</a> frequency $f_{\text{RF}}$	
$n_{\text{r,eff}}$	effective index of refraction without externally applied electrical field	
$\mathbb{N}^*$	natural numbers without zero, according to <a href="#">DIN 5473</a>	
$\omega_{\text{in}}$	angular frequency of a signal connected to the <a href="#">RF</a> input of an <a href="#">RF</a> mixer	rad/s
$\omega_{\text{LO}}$	angular frequency equivalent to the frequency $f_{\text{LO}}$ of an <a href="#">LO</a> signal	rad/s
$\omega_{\text{rep}}$	angular frequency equivalent to the laser repetition rate $f_{\text{rep}}$	rad/s
$\omega_{\text{RF}}$	angular frequency equivalent to the frequency $f_{\text{RF}}$ of an <a href="#">RF</a> signal	rad/s
$\phi_0$	phase shift between two <a href="#">MZM</a> arms due to an intrinsic length difference	rad
$\varphi_{h,\{.\}}$	<a href="#">RF</a> mixer input phases 1 to 4 of band-pass filtered signals	rad
$\varphi_{\text{in}}$	phase of a signal connected to the <a href="#">RF</a> input of an <a href="#">RF</a> mixer	rad
$\varphi_{\text{LO}}$	<a href="#">LO</a> phase at an <a href="#">RF</a> mixer	rad
$\varphi_{\text{LO},\{.\}}$	<a href="#">LO</a> phase, at which the error measurement channels denoted in the subscript can be detected, the channels are $\varphi_{\text{RF}}$ , $V_{\text{b}}$ and $r_{\text{s}}$	rad

## Symbols

$\varphi_{\text{mix}}$	relative phase between LO and RF signals at an RF mixer . . . . .	rad
$\varphi_{\text{RF}}$	phase of an RF signal . . . . .	rad
$\Phi_{\text{RF}}$	relative phase between the RF and optical signal at the MZM . . . . .	rad
$\Phi_{\text{RF},\{\cdot\}}$	relative phase at the MZM between the RF signal and the two laser pulse trains 1 and 2 from the first delay line . . . . .	rad
$p_{\{\cdot\}}(t)$	time varying optical power of the laser pulse trains 1 to 4 leaving the MZM . . .	W
$p_{\{\cdot\}}^*(t)$	time varying optical power of the delayed and undelayed laser pulse trains 1 and 2 from the first delay line before passing through an MZM . . . . .	W
$p_{\text{in}}^*(t)$	time varying optical input power of the L2RF phase detector . . . . .	W
$p_{\text{MZM}}(t)$	time varying output power at the regular output of an MZM . . . . .	W
$p'_{\text{MZM}}(t)$	time varying output power at the inverted output of an MZM . . . . .	W
$p_{\text{opt}}(t)$	time varying optical power . . . . .	W
$P_{\text{dBm}}$	average RF power in decibel relative to 1 mW . . . . .	dBm
$P_{\text{IF}}$	average power at the IF output of an RF mixer . . . . .	W
$P_{\text{in}}$	average input power of an RF mixer . . . . .	W
$P_{\text{in}}^*$	average optical input power of the L2RF phase detector . . . . .	W
$P_{\text{opt}}$	average optical power . . . . .	W
$P_{\text{PD}}$	optical power at the photodiode of the L2RF phase detector . . . . .	W
$P_{\text{PD,eq}}$	optical power at a photodiode where shot- and thermal noise are equal . . .	W
$P_{\text{PD,Hz}}$	normalization factor, average signal power per hertz from a photodiode . . .	W/Hz
$P_{\text{RF}}$	average RF power in watt . . . . .	W
$P_x$	average power of a signal $x(t)$ . . . . .	W
$r_{\{\cdot\}}$	nondimensional scaling terms for the laser pulse trains 1 to 4, defined by the associated splitting ratio and the MZM modulation factor	
$r_{\text{eff}}$	effective EO coefficient . . . . .	m/V
$r_{\text{MZM}}$	modulation factor of an MZM	
$r_{\text{MZM},\{\cdot\}}$	modulation factor of an MZM for two laser pulse trains 1 and 2 from the first delay line	
$r_s$	ideal splitting ratio at the first delay line	
$r_{s,r}$	real splitting ratio at the first delay line	
$R_{\mathcal{FF}}(t)$	autocorrelation function of a general FOURIER series	
$R_{\mathcal{FF}_+}(t)$	autocorrelation function of the sum of two general FOURIER series	
$R_{\mathcal{FF}_+}^\dagger(t)$	autocorrelation function of the sum of two FOURIER series with real coefficients	

$R_{PD}$	responsivity of a photodiode	A/W
$R_{IIII}(t)$	autocorrelation function of two identical sha functions	
$R_{xx}(t)$	autocorrelation function of a signal $x(t)$	
$s_{beat}$	slope of a phase detector beat-note at its zero crossing	V/s
$S_{\mathcal{F}\mathcal{F}_+}^{\dagger}(f)$	PSD of the sum of two FOURIER series with real coefficients	
$S_{\mathcal{F}\mathcal{F}_\Sigma}^{\dagger}(f)$	PSD of the sum of four FOURIER series with real coefficients	
$S_{IIII}(f)$	PSD of two pulse trains simulated by Sha functions	
$S_{IIII_\Sigma}(f)$	PSD of the sum of four pulse trains simulated by Sha functions	
$S_{vv_\Sigma}(f)$	PSD of the sum of four voltage signals, created by photodetecting modulated and time shifted laser pulse trains	W/Hz
$S_{xx}(f)$	PSD of two signals $x(t)$	
$\Theta_\pi$	normalization factor for the $\pi$ modulation voltage	rad/V
$t$	time	s
$T$	period or repetition period of a periodic signal	s
$T_{\{.,.\}}$	time delay 1 and 2 introduced by the first and second delay line	s
$T_0$	time delay used on various occasions	s
$T_{abs}$	absolute temperature	K
$T_{beat}$	period of a phase detector beat-note	s
$T_{rep}$	repetition period of a laser pulse train – inverse of the repetition rate $f_{rep}$	s
$v_{bp,\{.,.\}}(t)$	time varying voltage signals 1 to 4 created by band-pass filtering a signal	V
$v_{Hz,\{.,.\}}(f)$	FOURIER transformed photodiode signals 1 to 4 in the frequency domain	V/Hz
$v_{IF}(t)$	time varying voltage signal originating from the IF output of an RF mixer	V
$v_{in}(t)$	time varying voltage signal connected to the RF input of an RF mixer	V
$v_{LO}(t)$	time varying voltage signal connected to the LO port of an RF mixer	V
$v_{PD}(t)$	time varying voltage signal created by a photodiode	V
$v_{PD,\{.,.\}}(t)$	time varying voltage signal created from the laser pulse trains 1 to 4 after detection by a photodiode	V
$V$	average signal voltage	V
$\hat{V}$	peak output voltage of a L2RF phase detector	V
$\hat{V}_{\{.,.\}}$	peak output voltage of the signals 1 to 4 of a L2RF phase detector	V
$\mathcal{V}^{\dagger}$	L2RF output signal disregarding delay errors of both delay lines	V
$\tilde{\mathcal{V}}$	linearized output signal of a L2RF phase detector	V

## Symbols

$\mathcal{V}_{\{.\}}$	full <b>L2RF</b> output signal, the error measurement channels $\varphi_{\text{RF}}$ and $V_{\text{b}}$ are denoted in the subscript . . . . .	V
$\mathcal{V}_{\{.\}}^{\dagger}$	<b>L2RF</b> output signal disregarding delay errors of both delay lines, the error measurement channels $\varphi_{\text{RF}}$ , $V_{\text{b}}$ and $r_{\text{s}}$ are denoted in the subscript . . . . .	V
$\tilde{\mathcal{V}}_{\{.\}}$	full and linearized <b>L2RF</b> output signal, the error measurement channels $\varphi_{\text{RF}}$ and $V_{\text{b}}$ are denoted in the subscript . . . . .	V
$\tilde{\mathcal{V}}_{\{.\}}^{\dagger}$	linearized <b>L2RF</b> output signal disregarding delay errors of both delay lines, the error measurement channels $\varphi_{\text{RF}}$ and $V_{\text{b}}$ are denoted in the subscript . . . . .	V
$V_{\text{b}}$	bias voltage applied to an <b>MZM</b> . . . . .	V
$V_{\text{b},0}$	bias voltage needed to tune an <b>MZM</b> into its working point . . . . .	V
$\mathcal{V}_h$	output signal of a <b>L2RF</b> phase detector at a specific harmonic . . . . .	V
$\hat{V}_{\text{in}}$	peak voltage of a signal connected to the <b>RF</b> input of an <b>RF</b> mixer . . . . .	V
$\hat{V}_{\text{LO}}$	peak voltage of the <b>LO</b> signal of an <b>RF</b> mixer . . . . .	V
$V_{\text{mix}}$	voltage output signal of an <b>RF</b> mixer when mixing two signals with identical frequency and picking the difference frequency signal at <b>DC</b> . . . . .	V
$V_{\text{n,shot}}$	shot noise from a photodiode converted to voltage . . . . .	V
$V_{\text{n,thermal}}$	thermal noise of a resistor . . . . .	V
$V_{\pi}$	voltage needed to switch an <b>MZM</b> from full to zero transmission . . . . .	V
$V_{\pi,\text{DC}}$	<b>DC</b> voltage needed to switch an <b>MZM</b> from full to zero transmission . . . . .	V
$V_{\pi,\text{RF}}$	<b>RF</b> voltage needed to switch an <b>MZM</b> from full to zero transmission . . . . .	V
$V_{\text{PD}}$	average voltage of a signal created by a photodiode . . . . .	V
$\hat{V}_{\text{RF}}$	peak voltage of an <b>RF</b> signal . . . . .	V
$Z$	impedance . . . . .	$\Omega$
$Z_{50}$	impedance of 50 $\Omega$ . . . . .	$\Omega$



## Introduction

In the mid 1990's the TeV-Energy Superconducting Linear Accelerator (TESLA) Test Facility (TTF) has been built at DESY (Deutsches Elektronen-Synchrotron) in Hamburg in the effort to develop and test new technology for a future linear collider. The project included the implementation of a vacuum ultraviolet (VUV) free-electron laser (FEL) pilot facility called the TTF-FEL. In February 2000, the first lasing at a wavelength of 109 nm has been observed at the TTF-FEL and thereby the feasibility of the self-amplified spontaneous emission (SASE) principle in the VUV wavelength range has been practically demonstrated [And<sup>+</sup>00].

The first description of the SASE process dates back to the year 1971 [Mad71]. The feasibility for the VUV and X-ray wavelength range however depends on the achievable electron beam quality and therefore on the available accelerator technology. The TTF-FEL was the first accelerator to provide the required technology to actually reach the VUV and soft X-ray wavelength range in a SASE FEL.

After a major upgrade in 2003, the TTF-FEL has been regularly operated since 2005 as the world's first VUV FEL user facility. In 2006, the TTF-FEL has been renamed to Free-Electron Laser in Hamburg (FLASH)<sup>1</sup>. Only one year later, the facility was already three times overbooked by scientists who wanted to explore the new scientific opportunities offered by the unique radiation produced at FLASH [Fle11].

The worldwide first lasing of an FEL in the soft X-ray range has been observed in 2007 with a wavelength of 6.7 nm at FLASH at its design electron beam energy of 1 GeV [Hon<sup>+</sup>14]. During the next years, further milestones have been accomplished. The so-called water window was reached in 2011 with a wavelength of 4.1 nm [Sch11a] after the accelerator had been upgraded to an electron beam energy of 1.25 GeV. In the water window, the FEL radiation is absorbed by carbon while water becomes transparent, such that for example water based biologic specimens can finally be investigated. The user capacity of FLASH has just recently been extended by a second beamline, called FLASH II [Hon<sup>+</sup>14].

---

<sup>1</sup>see <http://flash.desy.de> for further information about FLASH

During the past years, further FELs have been built or are under construction around the globe<sup>1</sup>. The worlds largest and brightest FEL, the European X-ray Free-Electron Laser (XFEL)<sup>2</sup> is currently under construction at DESY in Hamburg. Although FELs are subject to continuous improvement, they meanwhile are routinely used in several fields of research, for instance bio-chemistry, materials science and nanotechnology. FELs have frequently become an indispensable tool to conduct for example pump-probe or scattering experiments in order to investigate ultra-fast processes and small structures. They are the only devices which can satisfy todays demand in science for X-ray and short wavelength laser pulses with the required brilliance.

The following introduction to FELs will briefly cover the working principle of FELs and thereby specifically point out technical challenges in their operation, which result actually from requirements of the user experiments that are conducted at FELs. These requirements will subsequently lead to the optical synchronization system implemented at FLASH. The laser-to-RF (L2RF) phase detector developed in this thesis is an essential component of this optical synchronization system and it is required to further increase the FEL performance in order to allow new experiments. A thesis outline will be finally given to conclude the introduction.

## 1.1 Introduction to Free-Electron Lasers

FELs consist of a particle accelerator where relativistic electron bunches are first produced in an electron source. These electron bunches are accelerated further and guided through a magnetic undulator section as presented in figure 1.1. The accelerated electron bunches are stimulated to coherently radiate intense and short pulses of X-ray laser light by the alternating magnetic field along the undulator.



**Figure 1.1: General (X)FEL Layout** | Electron bunches are created in an electron source, accelerated and coherently radiate in an undulator. Finally, the electrons are dumped while the radiation can be used in multiple applications. Figure adapted from [SDR08].

<sup>1</sup>For example:

LCLS in Menlo Park, CA, USA, see <http://lcls.slac.stanford.edu>

FERMI@Elettra in Trieste, Italy, see <http://www.elettra.eu/lightsources/fermi.html>

SACLA in Sayo-gun, Hyogo, Japan, see <http://xfel.riken.jp/eng/index.html>

but also in South Korea (PAL XFEL), the People's Republic of China (SXFEL) and Switzerland (SwissFEL)

<sup>2</sup>see <http://www.xfel.eu> for further information about the European XFEL

The electron source of **SASE FELs** is usually a laser-driven photo injector which can provide the required high brightness (high beam current and low beam emittance) electron beams. While the electron beam passes the undulator, the intensity of the generated **FEL** light pulses grows exponentially up to saturation in the so-called **self-amplified spontaneous emission (SASE)** process. The coherent radiation during the **SASE** process is enabled by microbunching, which is a self-induced spatial density modulation of the electron bunch. The microbunching develops when the electron bunch is forced on a sinusoidal trajectory by passing the undulator while it simultaneously interacts with its emitted radiation (see figure 1.2). The beam parameter requirements for successful **SASE** operation with respect to high charge density and low energy spread are usually so demanding, that they can only be met by **linear accelerators (linacs)** [SDR08]. The **FEL** pulse duration is mainly influenced by the bunch charge and compression, while with fixed-gap undulators like at **FLASH**<sup>1</sup>, the **FEL** wavelength is tuned by the electron beam energy.

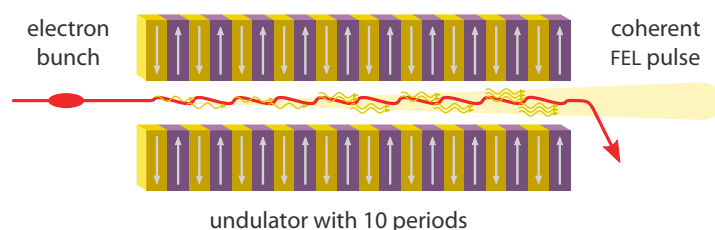


**Figure 1.2: Electron Bunch Passing Through an Undulator** | The periodic magnetic poling of the undulator forces the electron bunches on a transverse sinusoidal trajectory. The high gain and efficiency are enabled by the **SASE** process which allows the electron bunches to radiate coherently. Figure adapted from [SDR08].

The stimulated emission of electromagnetic radiation by the accelerated electron bunches in the undulator has led to the name **free-electron laser (FEL)**. The **FEL** pulses are monochromatic and coherent if only one **SASE** mode is actually excited. **FELs** can be characterized by different properties of the accelerator and the generated laser pulses like the achievable wavelength range, the maximum electron energy, the peak brilliance<sup>2</sup> and sometimes also the timing jitter of the **FEL** pulses.

Besides the coherence and the short pulse durations achieved by the **SASE FEL**, the high brilliance is the main difference from synchrotron based light sources and the cause for

<sup>1</sup>The newly commissioned second undulator beamline **FLASH II** however is equipped with variable gap undulators which allow to tune the **FEL** wavelength independently of the electron beam energy.

<sup>2</sup>The brilliance in this context is defined as the number of photons per second within a spectral bandwidth of 0.1 % divided by the **root mean square (rms)** transverse beam size and the divergence of the photon beam.

the high demand. In Figure 1.3 the achievable peak brilliance of selected light sources around the globe are presented where this circumstance is clearly visible.

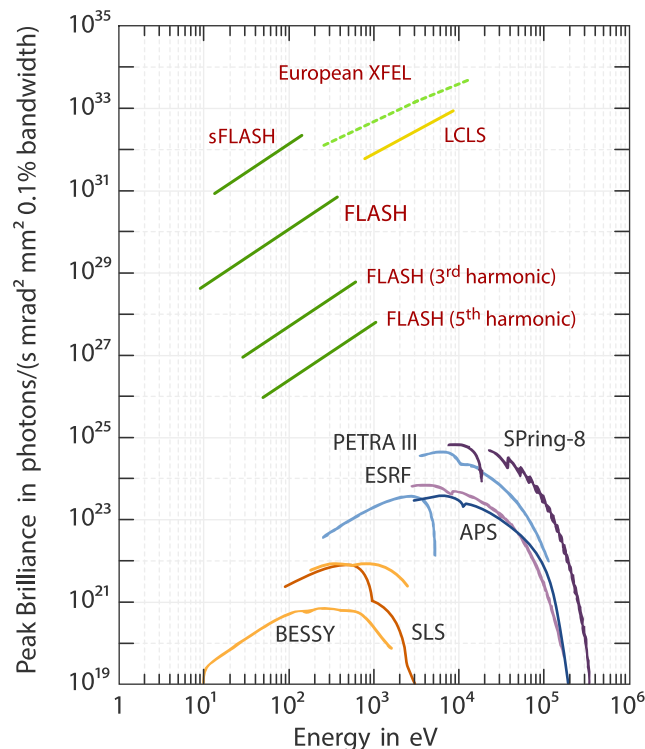


**Figure 1.3: Comparison of the Peak Brilliance of Different Light Sources** | Free-electron lasers are labeled in red while synchrotron based light sources are labeled in gray. Figure adapted from [Sch11b] initially published by [Sch10].

Since FELs are driven by linacs, very short electron bunches down to the femtosecond level can be produced. The femtosecond short FEL pulses generated from them allow for example to take snapshots of molecules before they are destroyed by the intense radiation. At X-ray wavelengths, atomic structures can be resolved while the short pulses allow to achieve the level of time resolution which is required to observe many atomic processes. The coherence of the produced light allows to extract three-dimensional information from scattering experiments (*coherent scattering imaging*). Another kind of experiments conducted at FELs are so-called pump-probe experiments. This kind of time-resolved measurement makes use of two signals. One is the FEL pulse, while the second signal is frequently provided by an external laser system. The external laser is used for example to excite a specimen or to trigger a chemical reaction (*pump*) while the FEL pulse is used to sample (*probe*) the specimen. If the synchronization between both signals is precisely known – or if it is even controllable – the measurement can be repeated to capture different, time-resolved stages

of the observed process. Therefore the precise synchronization of the pump-probe laser on a 10 femtosecond scale is required.

The demands towards general FEL properties have been and still are increasing continuously towards shorter FEL pulses, higher pulse energies and the best achievable control of the FEL arrival-time at the place of the experiment. The arrival-time of the electron bunches and therefore also the arrival-time of the FEL pulses depends on the energy stability of the electron beam which depends on the amplitude and phase stability of the accelerating radio frequency (RF) fields within the acceleration modules. The energy stability influences the arrival-time via the magnetic bunch compressors (BCs) which are needed to compress the beam in order to create short electron and FEL pulses. The BCs however also translate energy fluctuations from upstream acceleration modules into timing fluctuations.

In order to obtain a sub 10 femtosecond arrival-time stability, the required levels of amplitude and phase stability of the low-level radio frequency (LLRF) system which controls the acceleration modules have been demonstrated in [Sch<sup>+</sup>05]. Meanwhile a pulse to pulse amplitude stability of the accelerating field of the first accelerating structure at FLASH of  $1.7 \times 10^{-5}$  has been achieved [Sch<sup>+</sup>14]. This value corresponds almost to the demanded amplitude stability of the accelerating field of  $1 \times 10^{-5}$  [Sch<sup>+</sup>05]. A phase stability of the accelerating RF field of  $0.005^\circ$  is required at the same time to fulfill the synchronization requirements on the 10 femtosecond level. This phase stability actually corresponds to about 10 fs at a frequency of 1.3 GHz.

Moreover, in order to produce ultra short FEL pulses it is indispensable to precisely control the superconducting accelerating structures on a comparable scale. Recent developments aim towards short FEL pulse lengths of 10 fs [Rön<sup>+</sup>14]. As the electrons are accelerated by the superconducting accelerating structures, the precise control of the acceleration process is also crucial for high performance FEL operation with short pulses. Consequently, the task to deliver RF synchronization signals within FEL facilities with femtosecond precision has become crucial for the operation of FELs under the mentioned requirements. The key to achieve high performance FEL operation is the implementation of a synchronization system which provides the quoted level of accuracy.

RF based synchronization setups have not reached femtosecond accuracy in large scale accelerators. Due to the huge dimensions of FELs (several hundred meters to a few kilometers length), the transport of RF signals via cables is limited by cable losses and phase drifts. Even RF cables with low temperature coefficients or interferometric stabilization do still heavily suffer from cable losses for the required distances in an accelerator environment. The transport of phase stable signals to dedicated locations in the accelerator has however been achieved by the pulsed optical synchronization system. This synchronization system benefits from the low losses of optical fibers, which are used to transport the laser pulses through the accelerator.

This synchronization system is not only supposed to provide RF synchronization signals in the accelerator. It already allows to precisely phase-lock lasers which are needed to operate the FEL – like the injector laser which drives the photo injector or the pump-probe laser which is required for experiments. Additionally, this synchronization system provides a method to measure the bunch arrival-time within the accelerator on a femtosecond level in order to actively stabilize it.

A sub 10 femtosecond synchronization of essential components throughout the accelerator is envisioned and it especially includes the currently missing stabilization of the RF reference signals provided to the LLRF system for control of the accelerating structures. This thesis will present means to achieve this goal particularly for RF signals at 1.3 GHz at specific points within the accelerator facility. The fundamental concept behind the presented method for phase stabilization of RF signals however is not limited to this frequency and can be as well adopted for different scenarios. The implementation of the presented scheme requires a pulsed optical synchronization system like it is implemented at FLASH and currently being constructed for the European XFEL.

## 1.2 An Optical Synchronization System for Free-Electron Lasers

In order to fulfill the tight synchronization requirements presented in the last section, a pulsed optical synchronization system has been implemented at FLASH during the past years and will be implemented for the European XFEL which is currently under construction. The overall concept for such a pulsed optical synchronization system has first been presented in [Kim<sup>+</sup>04]. The system works by the use of a short pulse laser as timing source and the distribution of the laser pulses by timing stabilized optical fiberlinks. The paper focuses on potential ideas for the generation of phase stable RF signals which at that time was the main application foreseen for a synchronization system.

Subsequently, the presently used optical cross-correlator (OXC) based fiberlinks have been investigated in detail together with first options for the synchronization of RF signals. These investigations are summarized in [Kim07]. Around the same time the concept for the so-called bunch arrival-time monitor (BAM) has been worked out. The precise measurement of the bunch arrival-time turned out to be an important part of the overall synchronization system. In [Löh09], proof-of-principle experiments at FLASH were conducted with a first prototype of an optical synchronization system. This prototype actually consisted of two BAMs, which were synchronized by two optical fiberlinks. The measured arrival-time was used in a feedback loop to stabilize the electron bunch arrival-time by controlling the LLRF system. At DESY, the results of these successful proof-of-principle experiments led to follow-up projects during which a constantly operated, pulsed optical synchronization

system has been implemented for FLASH. The OXC based fiberlinks have been thoroughly engineered while the BAM has been developed to a routinely operated device at FLASH [Boc12]. At the same time, different lasers have been investigated as a possible central synchronization reference which is called the master laser oscillator (MLO) in the optical synchronization system. Additionally, reliable OXC based laser-to-laser (L2L) synchronization techniques have been developed [Sch11b] while the optical synchronization system matured. At that time, the availability of arrival-time data already allowed to conduct pump-probe experiments, where the arrival-time data is used to perform a time-resolved analysis of the obtained measurement data. The routine availability of arrival-time data concluded in the implementation of beam-based feedbacks which operate on the arrival-time information collected by the BAMs [Pfe14]. The developed L2L techniques additionally allow to synchronize different laser systems at the accelerator, which includes the important pump-probe laser system and finally allows in conjunction with the beam-based arrival-time stabilization precise time-resolved pump-probe measurements on the scale of 30 fs rms [Sch<sup>+</sup>15]. Especially for the implementation of this pulsed optical synchronization system at the newly constructed European XFEL but also to improve the performance at FLASH, constant research and developments are performed in order to increase the performance of the system [Syd<sup>+</sup>14; Fel<sup>+</sup>14; Zum<sup>+</sup>13; Czw<sup>+</sup>14].

Figure 1.4 shows a schematic block diagram of the pulsed optical synchronization system. The MLO is a commercial Origami-15 semiconductor saturable absorber mirror (SESAM) based pulsed laser [Orig15] which operates at a wavelength of 1553 nm and at a repetition rate of 216.6 MHz. In order to ensure long-term frequency stability of the MLO, it is phase-locked to the accelerator radio frequency master oscillator (RF-MO). While the frequency of the RF-MO is defined by the resonance frequency of the accelerating cavities in the accelerator, the laser repetition rate has been chosen to be a full integer sub-harmonic of the RF frequency, in order to be frequency compatible to the RF-MO and to all kinds of subsystems within the accelerator. A second MLO is installed in the synchronization system for redundancy.

The laser pulse train from the MLO is subsequently guided through the free-space signal distribution (FSD) where it is distributed to the individual link stabilization units (LSUs). At FLASH the FSD is a free-space setup on a custom fabricated plate made from Invar<sup>1</sup> in order to minimize phase drifts between the MLO and the LSUs as well as relative drifts between individual LSUs. The actual splitting process is performed by polarizing beam cubes (PBCs) and waveplates. Individual power levels are therefore adjustable. Detailed information on both the MLO and the FSD can be found in [Sch11b].

<sup>1</sup>Invar is used as a generic term for alloys of usually 65 % iron and 35 % nickel which has a low thermal coefficient of expansion. The mechanical properties of the alloy can be altered by adding additional alloying elements. SuperInvar, which is enhanced by about 5 % of cobalt for example has a thermal coefficient of expansion which crosses zero at room temperature.

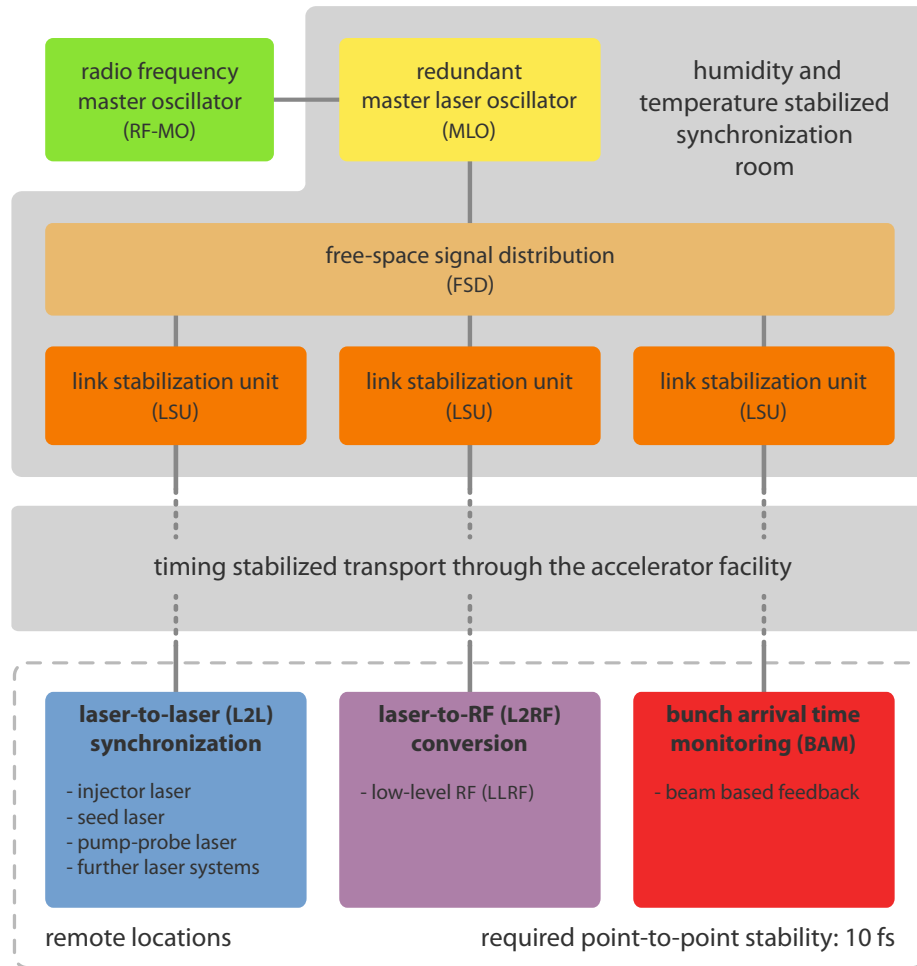


**Figure 1.4: Block Diagram of the Pulsed Optical Synchronization System** | The most critical components are housed in the environmentally controlled synchronization room close to the RF-MO. Actively stabilized optical fibers ensure the ultra-low drift transport of the synchronization signals to multiple remote locations. The star topology is clearly visible. Different types of end stations are tailored to specific subsystems of the accelerator. This kind of synchronization system is implemented at FLASH and will be implemented for the European XFEL. Figure adapted from [Sch11b].



The **LSU** stabilizes the actual transport of laser pulses from the **MLO** through fibers to specific devices in the accelerator in a point-to-point scheme. The fiberlinks are terminated by a partly reflecting **FARADAY rotating mirror (FRM)**. A fraction of the light is reflected back from the **FRM** to the **LSU** while the transmitted light is foreseen for the actual end station. The fiberlink is stabilized exactly up to the **FRM** such that all subsequent and unstabilized components need to be kept as short as possible in order to avoid additional timing drifts. The **LSU** detects the relative delay changes between a reference pulse train from the **MLO** and the pulse train returning from the fiberlink with a balanced **OXC**. A mechanical delay line and a piezoelectric actuated fiber stretcher are used to actively compensate the detected timing changes. The **LSU** also contains **dispersion compensating fiber (DCF)**. One of the main reasons to choose a wavelength in the C-band<sup>1</sup> is the commercial availability of **DCF**, which is suited to compensate the dispersive pulse broadening which occurs during the transport in the fiberlink to the individual end stations. Depending on the power budget of the **MLO** and the number of **LSUs** which need to be operated, **erbium-doped fiber amplifiers (EDFAs)** are operated in each **LSU** to create the required optical power levels. A detailed description of the **LSU** is available from [Boc12].

Because both the **FSD** and the **LSU** contain unstabilized components which can introduce drifts to the synchronization system, all components are housed in an environment where temperature and humidity are actively stabilized. A special synchronization room is used or foreseen for this purpose at **FLASH** and the European **XFEL**.

Following figure 1.4, three different kinds of end stations are operated behind the stabilized fiberlinks. The **BAM** is the first device which has been implemented at **FLASH**. The electrical field of the electron bunch is detected by pick-up electrodes in the beam pipe. The transient signal is used to modulate the amplitude of single pulses from the timing stabilized fiberlink. The modulation depth depends on the timing between the electron bunch and the laser pulse. The method is non-destructive to the electron beam and can be operated with the full repetition rate of the accelerator. The **BAM** uniquely relies on a pulsed optical synchronization system and currently no alternative device is available which can measure the electron bunch arrival-time with long-term femtosecond accuracy. Measurement data and a detailed description of the working principle is provided in [Boc12].

The second kind of end station allows the **L2L** synchronization and thereby the connection of lasers, which are operated at an **FEL**. The **L2L** synchronization is performed by optical cross-correlation. In contrast to the fiberlink, where an optical cross-correlator is used to stabilize pulse trains of the same wavelength, the **L2L** synchronization usually has to be performed between different wavelengths. A so-called two-color **OXC** has been developed for this purpose, which can be used to synchronize for example a Ti:sapphire oscillator, operating at a wavelength of 800 nm to an optical fiberlink. The phase detection in an **OXC**

<sup>1</sup>International Telecommunication Union (ITU) definition: The C-band corresponds to a wavelength range of 1530 nm to 1565 nm, see [MM09]

is performed directly in the optical domain and therefore mostly independent of any kind of environmental influence. The two-color [OXC](#) and [L2L](#) synchronization in general are in detail covered by [\[Sch11b\]](#).

The techniques described in this section – namely the [LSU](#), the [BAM](#) and the direct [L2L](#) synchronization – provide femtosecond accuracy and they are uniquely possible in a pulsed optical synchronization system. The missing component has been a way to provide phase stable [RF](#) signals in the accelerator to devices, which cannot operate with optical pulses. At [FLASH](#), these devices are currently supplied by unstabilized [RF](#) cables. A femtosecond stable [L2RF](#) phase detector has been invented in order to phase stabilize [RF](#) signals at dedicated locations in the accelerator. Possible phase drifts of the utilized [RF](#) signal can be measured with femtosecond accuracy and corrected with respect to a phase stable optical pulse train supplied by the optical synchronization system. The problem to provide phase stable [RF](#) signals within the accelerator has thus been narrowed down to the development of a femtosecond accurate [L2RF](#) phase detector which is presented in this thesis.

Figure 1.5 shows a schematic layout of [FLASH](#) and gives an overview of synchronization critical components. The accelerator starts with a normal conduction photo injector on the left hand side. The pulsed injector laser shoots onto the cathode inside the electron gun and creates the electron bunches which are immediately accelerated. Downstream of the first acceleration module ([ACC](#)), a bunch compressor ([BC](#)) is installed and subsequently the bunch arrival-time is measured by a [BAM](#). It is used to operate a feedback to the [LLRF](#) system which itself is controlling the first acceleration module. After two further acceleration modules, the second bunch compressor is again followed by a [BAM](#) which is used to operate another feedback loop around the second [LLRF](#) station. [FLASH](#) contains seven acceleration modules and each of them consists of eight superconducting 9-cell Niobium cavities. Further [BAMs](#) are installed or planned to be installed before and within the undulator section. All [BAMs](#) are supplied with phase stable optical reference signals.

Besides the photo injector laser, additional laser systems are located along the accelerator. The [electro-optic spectral decoding \(EOSD\)](#) setup is used to characterize the electron beam. At the seeding experiment, the seeding laser is used to seed the [FEL](#) radiation in the undulators such that properties like for example the [FEL](#) wavelength are determined by the seed laser pulse instead of the [SASE](#) process. The [pump-probe \(PP\)](#) laser is finally used for user experiments. All lasers are supposed to be precisely synchronized in order to allow reliable operation of the [FEL](#).

Not yet implemented, but still shown are the [L2RF](#) setups which will provide phase stable [RF](#) signals to the [LLRF](#) system and which will also be supplied by the pulsed optical synchronization system. The novel [L2RF](#) phase detector even has a second important application in the optical synchronization system. According to [\[Sch11b\]](#) the phase-lock between the [RF-MO](#) and [MLO](#) (see figure 1.4), which is currently accomplished by a direct conversion

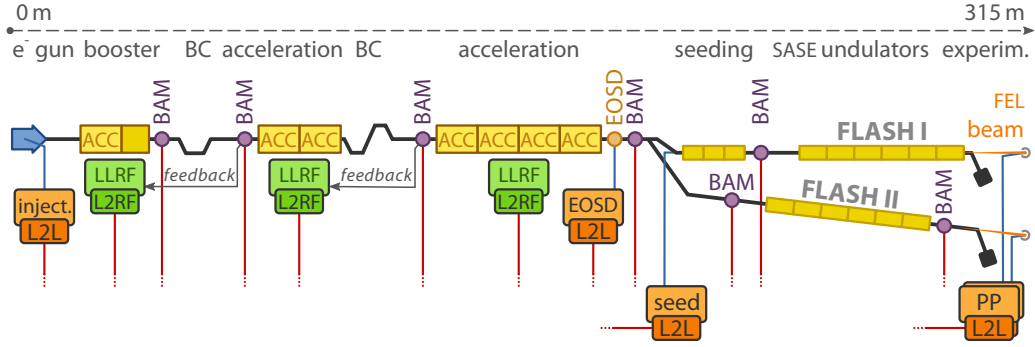


**Figure 1.5: Schematic Overview of FLASH and Its Optical Synchronization System** | The L2RF phase detectors are not yet installed. The optical synchronization system delivers phase stable laser pulse trains to important devices throughout the accelerator via individually timing stabilized fiberlinks which are indicated by red line segments. FLASH II is currently being commissioned. Figure adapted from [Sch<sup>+</sup>13].

setup, has the largest contribution to phase jitter and phase drifts of the MLO and thereby the whole optical synchronization system. The L2RF phase detector is therefore additionally foreseen to establish a long-term stable phase-lock of the MLO with respect to the RF-MO.

## 1.3 Thesis Outline

An introduction to FELs and the pulsed optical synchronization system at FLASH and the European XFEL has already been presented at this point. The special requirements of FELs towards femtosecond level synchronization have been introduced and the existing infrastructure at FLASH has been presented as an example of a state of the art FEL.

Chapter 2 introduces the L2RF phase detector from a functional point of view. Details of the working principle are worked out in a bottom-up approach which allows to transfer the presented scheme also to different operating conditions and adapt it for example to different frequency ratios.

A mathematical analysis of the L2RF phase detector is presented in chapter 3. Spectral properties of the amplitude modulated reference laser pulse train are derived and a full mathematical representation of the detector chain is composed. The sensitivity of the detector and possible error sources are investigated and the theoretical detector limit in terms of noise floor is briefly quoted. Necessary prerequisites which are mainly needed during the mathematical analysis of the presented L2RF phase detector are discussed in the appendix. This includes a presentation of MACH-ZEHNDER modulators (MZMs) as central component of the L2RF phase detector (appendix A) and RF mixers, which are extensively

used to read out the error signals created by the [L2RF](#) phase detector (appendix [B](#)). Theoretical considerations on [DIRAC](#) combs are presented in appendix [C](#) which include the derivation of a general mathematical model for signals composed by ideal pulse trains.

Two laboratory prototypes and one integrated device for operation in an accelerator environment have been implemented during the course of this thesis. They are presented in chapter [4](#). The required development steps are presented and details on the actual implementation and operation are provided. Measurement results prove the required stability of the device. In appendix [D](#), photographs of prototype setups, implementation details and development stages are presented together with short descriptions. The photographs are also referenced from the corresponding sections of the thesis.

Finally, alternative methods to phase stabilize [RF](#) signals in an accelerator environment are evaluated in chapter [5](#). By providing this overview at the end of the thesis, it is possible to make use of previously established terms and findings while different solutions are briefly compared.

An outlook on future developments and extensions of the [L2RF](#) phase detector is provided in chapter [6](#) followed by a summary of this thesis in chapter [7](#).

## The Laser-to-RF Phase Detection Principle

The **laser-to-RF (L2RF)** phase detector allows to accurately and reliably detect the phase relation between a laser pulse train and a **radio frequency (RF)** signal. The most common application for this setup is to operate a **phase-locked loop (PLL)**, in order to lock the phase of one signal to the second one.

The full featured **L2RF** phase detector is not only delivering a signal indicating phase errors ( $\Delta\phi_{\text{RF}}$ ) – which is its fundamental purpose, but it can also generate additional error signals for internal parameters. Monitoring and controlling these internal parameters improves the reliability of the setup, as will be explained in the course of this chapter. The availability and need for these internal feedback loops depends on the actual implementation of the **L2RF** phase detector. They are therefore discussed together with the presentation of different options for constructing **L2RF** phase detectors for different frequency ratios and available components.

The key component of the **L2RF** phase detector is a voltage controlled **MACH-ZEHNDER modulator (MZM)** (see appendix A for further details on **MZMs** or their mathematical representation), in which the laser pulse train and the **RF** signal interact. Integrated, fiber-coupled modulators are used in the present implementation, which have the advantage of small size and simple handling. Changes of the **RF** voltage while the pulse passes through the modulator are negligible, since the typical optical pulse duration is short compared to the period of usual **RF** frequencies in the lower GHz regime. The laser pulses are attenuated proportionally to the momentary **RF** and bias voltages while traveling through the **MZM**. The process in the **L2RF** phase detector can be referred to as synchronous sampling of the instantaneous **RF** voltage with a laser pulse train. For detection, this pulse train is guided on a photodiode and the generated electrical signal is evaluated.

The nomenclature during this chapter will make use of common indices. The description of different possible constructions of **L2RF** phase detectors will be defined by the use of a few physical quantities. Different cases will be discussed which mainly depend on the ratio between **RF** frequency and laser repetition rate. Different ratios lead to different solutions for the ideal length of the involved internal delays and for the detection frequencies. The most general definitions are quite theoretical and this chapter will therefore start with some

practical considerations and actual examples after which the fully qualified L2RF detection scheme is developed. The involved quantities will nevertheless be fully specified, although some formal conditions might not be explained immediately. The involved superscripts will show gray letters indicating the frequency ratio between RF frequency and laser repetition rate which can be a (h)alf or a (f)ull integer ratio, where the (f)ull integer ratio will be subdivided in (e)ven and (o)dd sub-harmonics. Additionally, some quantities have to be defined for either the first or the second of the involved delay lines. This will be indicated by the numbers 1 and 2 appended to the subscript of the according quantity. Starting from one single pulse train for a basic L2RF setup, there can be up to four individual pulse trains involved which are indexed by numbers from 1 to 4.

## 2.1 A Basic MZM Based Laser-to-RF Phase Detection Scheme

A single output MZM can be imagined as working like a voltage controlled optical attenuator with sinusoidal characteristic. An ideal MZM can be tuned continuously and repeatedly between isolation and full transmission<sup>1</sup>. The output pulse train  $p_1(t)$  is created by applying the modulation factor  $r_{\text{MZM}}$  to the input pulse train  $p_1^*(t)$ . The asterisk is in general used to refer to pulse trains in front of the MZM, while signals behind the MZM will be named without asterisk. For proper operation the MZM needs to be biased into the working point with the steepest voltage response – which is the 50 % transmission point. On top of the bias voltage  $V_b$ , the transmission is controlled by the instantaneous voltage of the RF signal  $V_{\text{RF}}(t)$ , which is also connected to the MZM. The overall and still simplistic setup is presented in figure 2.1.

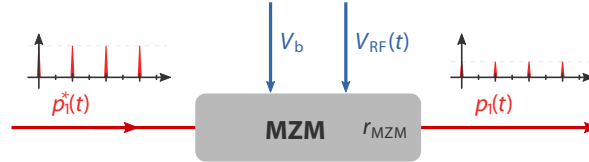


**Figure 2.1: Example of the Pulse Pattern Generation with a Single Output MZM |**  
The input pulse train is modulated inside the MZM in order to measure the phase difference between the laser pulse train and the RF signal.

In addition to the correct bias voltage, the sensitivity of the setup depends on the steepness of the RF signal at the point where the RF interacts with the laser pulses. The highest sensitivity of a L2RF phase detector can therefore be achieved by overlapping the laser pulses with the zero crossings of the RF wave where this sinusoidal signal can cause the strongest amplitude modulation of the laser pulses per phase change between both signals.

<sup>1</sup> A real MZM however suffers from insertion loss and a limited extinction ratio due to leakage.

The intended working point of the L2RF phase detector implies therefore a special frequency and phase relation between the laser repetition rate and the RF frequency.

If every laser pulse of a laser pulse train hits zero crossings of the same slope – which happens in case the laser repetition rate and the RF frequency are for example identical – each laser pulse exhibits the same attenuation as long as the relative phase between laser pulse train and RF frequency is constant. These conditions are met for every laser repetition rate  $f_{\text{rep}}^f$  which is a full integer<sup>1</sup> sub-harmonic of the frequency  $f_{\text{RF}}$  of the involved RF signal as defined in equation (2.1).

$$f_{\text{rep}}^f = \frac{1}{n} f_{\text{RF}} \quad \{n \in \mathbb{N}^*\} \quad (2.1)$$

Phase changes between both signals change in this case the amplitude of the complete laser pulse train. An actual measurement of the relative phase change by observing the amplitude of the laser pulse train under these conditions is error prone because it relies on the knowledge of the absolute power level of the input laser pulse train and perfectly constant gains and losses of the complete detection chain.

Additionally, the working point – once adjusted by the bias voltage applied to the MZM – is not static and needs to be actively stabilized with a bias voltage feedback. The internal effects leading to this circumstance are discussed in appendix A. An active feedback of the bias voltage however requires a measure for the bias voltage error. It is theoretically possible to use the average optical output power of the MZM for this purpose.

This procedure however does not work for the just outlined implementation of a L2RF phase detector because phase drifts between the laser pulse train and the RF signal as well as drifts of the working point both affect the average output power and both errors are therefore indistinguishable from one another. This situation is depicted in figure 2.2. The laser repetition rate and the RF frequency are identical and thus fulfill equation (2.1). The output pulse train  $p_1(t)$  is aligned to zero crossing of the RF wave with identical slopes. Subfigure (a) shows the working point condition and the initial RF spectrum.

In case a regular spaced train of laser pulses impinges on a photodiode, the generated electrical signal is also a regular spaced pulse train. The RF spectrum of such a pulse train is a frequency comb, with spectral lines at the repetition rate  $f_{\text{rep}}$  and all subsequent harmonics, limited practically by the bandwidth of the photodiode. A single pulse train together with its associated spectrum is sketched in subfigure (a) of figure 2.2.

Phase changes of the RF signal as presented in subfigure (b) and deviations from the ideal bias voltage presented in subfigure (c) both influence the overall amplitude of the laser

<sup>1</sup>The natural numbers used to denote the harmonics and sub-harmonics are defined according to the German Institute for Standardization (DIN, Deutsches Institut für Normung e.V.) as described in DIN 5473, such that  $\mathbb{N}^* = \{1, 2, 3, 4, \dots\}$ .

pulse train in the same way. This influence is reflected by the amplitude of the harmonics in the RF spectrum while the shape of the RF spectrum is not affected by these changes.

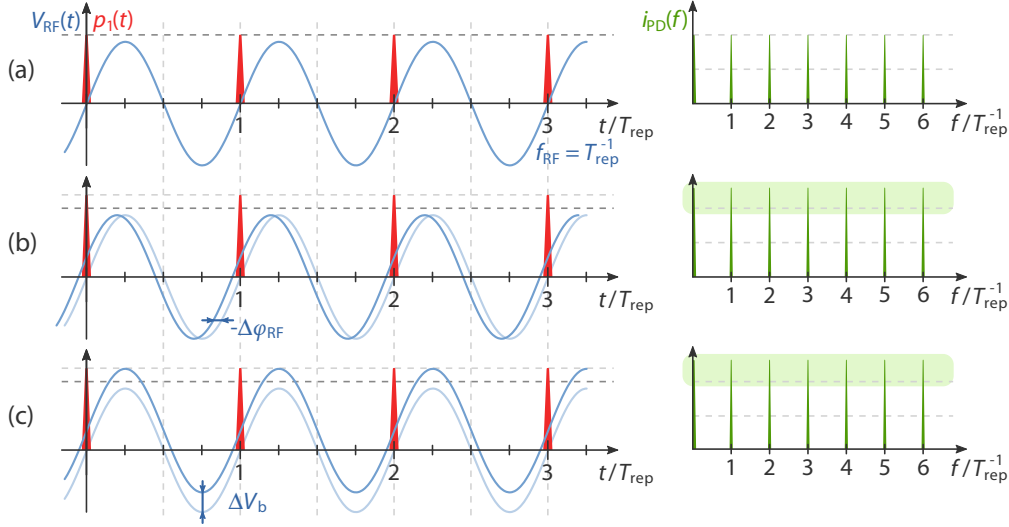


**Figure 2.2: Pulse Pattern and Spectra for an Integer Frequency Ratio** | (a) All laser pulses are aligned to the identical zero crossing of the RF wave. The pulse train is unmodulated. (b and c) Phase or bias voltage errors both change the amplitudes of the laser pulse train and the spectra. The shape of the spectra is not altered.

There is however a more promising approach available by which the bias voltage error can be measured independently of actual phase errors and the detection of phase changes between the laser pulse train and the RF signal is mostly unaffected by environmental conditions like the stability of optical input power or the working point of the MZM.

## 2.2 An Advanced Laser-to-RF Phase Detection Scheme

This alternative operation scheme of a L2RF phase detector works by aligning the laser pulses to zero crossing with alternating slopes of the RF wave. An input laser pulse train  $p_1^*(t)$  with the repetition rate of twice the RF frequency is guided through an MZM and interacts with this RF signal. The general layout of the setup still corresponds to figure 2.1 but the pulse patterns and spectra from figure 2.2 are no longer valid. The frequency ratio leading to the repetition rate  $f_{\text{rep}}^h$  can be described as half integer ratio and it is defined in equation (2.2). In this configuration, phase errors imprint an amplitude modulation on the laser pulse train which completely changes the shape of its RF spectrum. The lowest



modulated spectral component, as defined in equation (2.3), is recommended to detect the phase relation of the laser pulse train and the RF signal.

$$f_{\text{rep}}^h = \frac{2}{2m-1} f_{\text{RF}} \quad \{m \in \mathbb{N}^*\} \quad (2.2)$$

$$f_{\text{mod}}^h = \frac{1}{2} f_{\text{rep}}^h \quad (2.3)$$

The alignment to zero crossings with alternating slopes in combination with a phase offset leads to the situation, where subsequent laser pulses are modulated by voltages which deviate in opposite directions from the nominal working point. The overall power of the modulated laser pulse train does not change in this case. The spectrum of the modulated laser pulse train however does change such that one can measure the actual phase drift by observing the spectrum. This configuration is illustrated in figure 2.3.

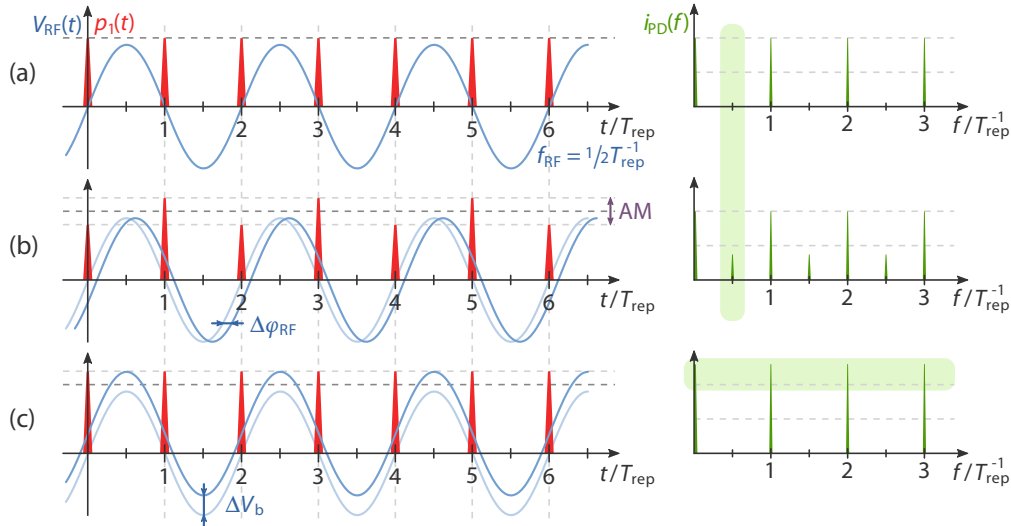


**Figure 2.3: Pulse Pattern and Spectra for an Half Integer Frequency Ratio | (a)**

The laser pulses are aligned to the zero crossings of the RF wave. **(b)** The laser pulse train is periodically modulated due to a phase error of the RF signal. In this case new frequency components appear in the spectrum. **(c)** The amplitude of the complete pulse train is increased by a bias voltage error but the shape of the spectrum is not influenced. The overall optical power however is increased and therefore also the amplitude of the harmonics in the spectrum.

The output laser pulse train  $p_1(t)$  in subfigure (a) is aligned to alternating zero crossings of the RF wave. The RF induced voltage is zero such that effectively only the bias voltage

is present at the **MZM**. In this state, the laser pulses pass through the modulator and the amplitude of all laser pulses at the output of the **MZM** is equally adjusted to 50 % of the maximum transmission value. The pulse train is not amplitude modulated in this case. The photodetected **RF** spectrum of the pulse train is presented on the right hand side of the figure.

The phase shift  $\Delta\phi_{\text{RF}}$  introduced in subfigure (b) imprints the discussed amplitude pattern on the depicted pulse train  $p_1(t)$ . An additional frequency component at half of the fundamental repetition rate – which did not exist originally – and at the odd harmonics of this new frequency component are visible in the spectrum in subfigure (b).

The lowest of these new frequency components will be called the modulation frequency  $f_{\text{mod}}^h$  for half integer frequency ratios. This frequency has already been introduced in equation (2.3). The modulation frequency is the preferred frequency for the detection of the associated error signal. Around the working point where the **RF** wave and the laser pulses are perfectly aligned, the amplitude of the new spectral components behaves proportional to the phase between the **RF** wave and the laser pulse train. The amplitude of the new spectral components is in the working point independent of optical input power changes and – as illustrated in figure 2.3 (c) – not affected by bias voltage errors.

It is still recommended to set up a reliable bias controller for a **L2RF** setup. The sensitivity of the **L2RF** setup is reduced, in case the **MZM** is not biased properly. The bias voltage  $V_b$  has to be continuously fed back, because the 50 % transmission point, which is the most sensitive point of the **MZM** response curve, is drifting due to environmental changes or internal charge relaxation in the **MZM** (again, see appendix A for further information). Because phase errors no longer influence the average output power of the **MZM** in this case, the previously proposed but rejected option to use the average optical output power as a measure for the bias voltage has to be reevaluated.

The measure for the bias voltage depends in this configuration on the optical input power. The bias controller, stabilizing the output power to the 50 % transmission level, needs to take the input power level into account because no independent measure for the working point is available using a single output **MZM**<sup>1</sup>. A superior bias voltage control which is independent from the optical input power can be implemented in case the single output **MZM** considered up to now can be replaced by a dual output **MZM**.

<sup>1</sup>The term single output **MZM** refers here to the fiber-coupled optical output. As introduced in appendix A, integrated **MZMs** can be built with two inverse outputs if the recombination of the two arms of the internal **MACH-ZEHNDER interferometer (MZI)** is performed by a directional coupler.

## 2.3 Improved Bias Voltage Control Using Dual Output MZMs

There are certain laser wavelengths or RF frequencies for which single output MZMs are the only option, because no dual output MZMs are commercially available. However, a new and robust approach for the bias control can be implemented if a dual output modulator is available at the desired operating parameters.

While a single output MZM works like a voltage controlled attenuator with nonlinear characteristic, a dual output MZM can be described as a voltage adjustable splitter. Each output of the ideal dual output MZM can be tuned in the ideal case continuously and repeatedly between isolation and full transmission and the outputs behave inversely to each other.

As the working point with the steepest voltage response, 50 % transmission have to be adjusted. Both outputs are balanced in this point by the applied bias voltage  $V_b$ . In the case of the L2RF setup, the dual output MZM allows to detect a possible bias voltage error by monitoring the balancing of the two outputs. This bias voltage error measurement is independent of input power fluctuations because compared to the absolute power level measured at the single output MZM, the relative imbalance between the outputs is the figure of merit. This balanced detection principle is a significant advantage for the operation of the L2RF setup in terms of reliability.

In order to detect the bias induced output imbalance and the RF induced amplitude modulation of the pulse train, both outputs are combined and guided to a common photodiode. A block diagram of the modified setup is presented in figure 2.4. The new pulse train from the inverted output of the MZM is called  $p_3(t)$  and this output is delayed by a fixed delay of  $T_2$  with respect to the pulse train  $p_1(t)$  from the regular output.

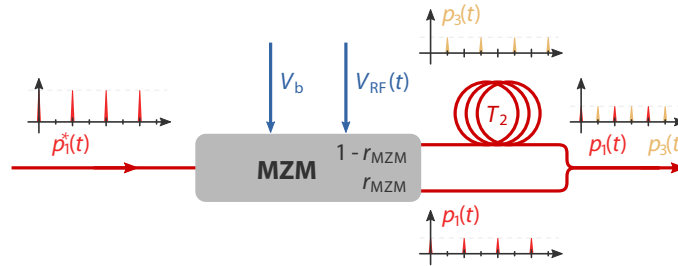


**Figure 2.4: Example of the Pulse Pattern Generation with a Dual Output MZM |**

The two outputs of the MZM are recombined at a fixed delay. This method allows to operate a reliable bias voltage feedback independent of the phase error detection.

It is self-evident that both output signals should be delayed with respect to each other before recombination, such that the pulses cannot directly interfere. An imbalance between

the outputs, caused by the slightest discrepancy from the ideal bias voltage, imprints an amplitude modulation on the combined signal in a similar way as it was described before for the detection of phase errors.

In contrast to the phase error detection, there are no new frequency components created in the spectrum by this technique. The detection thus has to be performed at one of the genuine frequency components of the initial laser pulse train. In order to achieve the steepest possible response from the phase detector, only delays leading to harmonics of the original repetition rate as modulation frequency are considered. The modulation frequency  $f_{\text{mod},2}$  at which this output imbalance and thereby bias voltage errors are supposed to be detected depends on the delay  $T_2$ .

The following definitions only apply for the application of a laser repetition rate  $f_{\text{rep}}^{\text{h}}$  having a half integer relation to the frequency of the involved RF signal. This relation serves as a first example used to illustrate the properties of a dual output MZM with the delayed output recombination in a L2RF setup. The example will be extended throughout this chapter to more generic working conditions.

For practical reasons it is convenient to choose a low frequency  $f_{\text{mod},2}^{\text{h}}$  from the spectrum for the detection of bias voltage errors, which implies to select a long delay  $T_2^{\text{h}}$ . The proposed solution is therefore to pick the lowest frequency from the initial comb as modulation frequency  $f_{\text{mod},2}^{\text{h}}$  which is the spectral component exactly at the repetition rate  $f_{\text{rep}}^{\text{h}}$  as presented in equation (2.4). The delay  $T_2^{\text{h}}$  leading to this modulation frequency as defined in equation (2.5). The choice of higher frequencies is possible although it is advised to utilize the smallest possible frequency which requires to implement a delay of at most the length of half the repetition period. General delay selection guidelines will be provided for the final configuration in section 2.6.1.

$$f_{\text{mod},2}^{\text{h}} = f_{\text{rep}}^{\text{h}} \quad (2.4)$$

$$T_2^{\text{h}} = \frac{1}{2} T_{\text{rep}}^{\text{h}} \quad (2.5)$$

The phase error detection is not disturbed by the recombination of the two MZM outputs. Quite the contrary effect can be observed for the proposed delay  $T_2^{\text{h}}$  which defines the relative phase between the combined signals, as the sensitivity of the phase error detection is even increased by the constructive combination of the signals from both outputs. Following the above mentioned proposal about the choice of the lowest modulation frequency, the best parameters for the implementation of a L2RF phase detector under the given conditions have already been presented in equations (2.4) and (2.5).

Bias voltage errors and phase drifts of the RF signal cause amplitude modulations of the pulse trains guided through the MZM. The pulse trains and the associated RF spectra under different operation conditions are presented in figure 2.5.

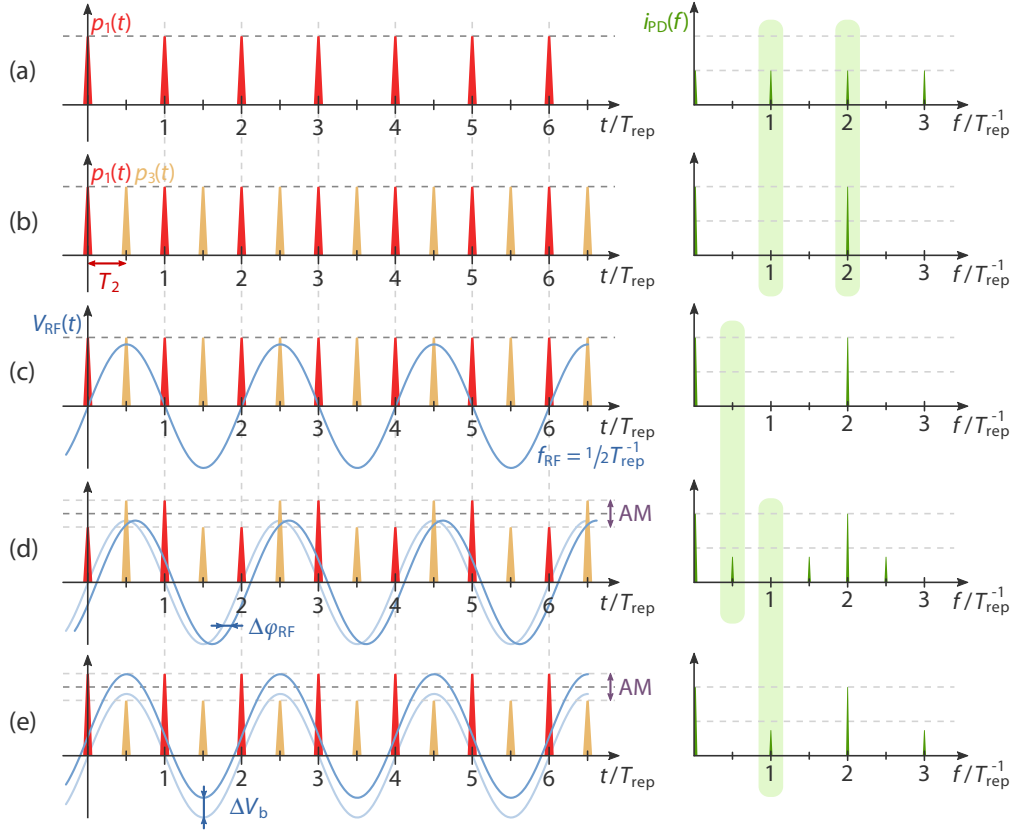


**Figure 2.5: Pulse Pattern and Spectra for a Half Integer Frequency Ratio Using a Dual Output MZM in a Basic L2RF Scheme** | (a and b) The delayed combination of the regular and inverted output signals significantly influences the RF spectrum after photodetection. Every second harmonic vanishes and the remaining ones grow in amplitude. (c) All pulses are aligned to the zero crossing of the RF wave. The spectrum is not altered in the working point. (d) Phase errors introduce a new frequency component at half the repetition rate into the spectrum. (e) Bias voltage errors cause a different amplitude modulation of the laser pulses which causes a previously vanished harmonic in the spectrum to reappear.

Subfigure (a) shows the pulse train from the regular output together with its original RF spectrum. The combination of both output signals of the MZM with the delay  $T_2^h$  is presented in subfigure (b). The delay  $T_2^h$  amounts to half the repetition period  $T_{\text{rep}}^h$  of the laser pulse train, which causes all odd frequency components in the spectrum to disappear because these RF frequency components interfere destructively. The remaining harmonics are affected by constructive RF interference from the two pulse trains, therefore their amplitude is increased. The RF voltage in subfigure (c) is aligned to the laser pulses, such

that no additional voltage is present when the laser pulses travel through the MZM and the spectrum remains unchanged. In subfigure (d) a phase error between the RF signal and the laser pulse trains is present. The amplitude modulation of the combined pulse train shows up at half of the original repetition rate in the spectrum. Bias voltage errors cause a different amplitude modulation as presented in subfigure (e). This modulation originates from the imbalance between the two MZM outputs. The odd frequency components which previously disappeared by combining the two outputs are again present in the spectrum and can be taken as a measure for the bias voltage error.

## 2.4 The Origin of the Spectral Amplitude Modulation

If two laser pulse trains impinge on the same photodiode, the amplitude of the generated frequency comb is modulated. The process can be easier understood by assuming that each pulse train generates a discrete frequency comb in the photodiode. The amplitude of each frequency comb depends on the amplitude of the respective optical pulse train, and the phase relation of the frequency components is defined by the delay  $T_0$  between the involved pulse trains. If both pulse trains have exactly the same repetition rate such that identical frequency components show up in their corresponding RF spectra, each frequency component interferes with its counterpart from the other frequency comb, depending on the phase and amplitude relation between the two pulse trains.

A simple example for this process are two combined pulse trains with equal amplitude and a delay  $T_0$  between each other that corresponds to exactly half their repetition period. This example is equivalent to the situation presented in figure 2.5 (b). In the time domain, the repetition rate of the combined pulse trains has doubled. In the frequency domain, the first and every following odd frequency component (for all of which  $T_0$  corresponds to a phase of  $\pi$  or any odd integer multiple of  $\pi$  at that particular frequency) is – compared to the spectrum caused by one single pulse train – extinct. The RF spectrum is now identical to a spectrum originating from a laser pulse train with doubled repetition rate. The missing frequency components are canceled out by interference between the RF spectra of the individual pulse trains.

There exists always a frequency, for which a particular delay translates to a  $\pi$  phase shift. This frequency will be called the  $\pi$  modulation frequency  $f_{\text{mod}}^\pi$ , which is defined as

$$f_{\text{mod}}^\pi = \frac{1}{2} \frac{1}{T_0} . \quad (2.6)$$

All frequencies with a  $\pi$  (or any other odd integer multiple of  $\pi$ ) phase shift destructively interfere with their counterpart from the second pulse train and vanish completely from the

RF spectrum if the amplitude of the two involved pulse trains is equal. For different delays  $T_0$ , different frequencies are extinct in this way from the spectrum. The  $\pi$  modulation frequency does not necessarily coincide with one of the frequency components of the frequency comb. The modulation frequency  $f_{\text{mod}}$  is defined for a certain delay  $T_0$  as the lowest possible frequency vanishing completely from the frequency comb of the combined laser pulse trains, if both pulse trains have the same amplitude. In other words it is the lowest multiple of the  $\pi$  modulation frequency  $f_{\text{mod}}^{\pi}$  which coincides with one of the spectral lines from the frequency comb. In order to read out an error signal, encoded by a L2RF setup in an amplitude modulation of a pulse train, this is also the frequency, one should use to detect this error.

If the delay is fixed at a certain value, one can monitor such an extinct frequency component (for example at the modulation frequency  $f_{\text{mod}}$ ) in order to detect relative amplitude fluctuations between the two pulse trains. If the amplitudes of both signals are not exactly the same, the combined pulse train exhibits an amplitude modulation in the time domain. Even if the delay is still set up accurately, the destructive interference cannot fully take place because the amplitudes are no longer equal. A residual signal – proportional to the amplitude mismatch – can now be found at the monitored frequency in the RF spectrum. This frequency can be used in a detector and the RF power at this frequency can be taken as a measure for the amplitude ratio between the two pulse trains. This scheme is used as detection principle in the L2RF phase detector. The mathematical background to the detection principle will be provided in chapter 3.

## 2.5 Extended Repetition Rate and RF Frequency Ratios

The previously presented schemes for L2RF phase detectors for half integer ratios between the laser repetition rate and the RF frequency are insensitive to input power changes in their working point. They additionally allow to detect bias voltage errors and phase drifts separately. A new delay line prior to the MZM can be introduced in order to achieve a similar operating scheme with the same advantages for integer frequency ratios. The input pulse train is split equally in front of the MZM, one pulse train is delayed and both pulse trains are recombined before entering the MZM. The delay is chosen such, that both parts of the pulse train are aligned to opposite slope zero crossings of the RF signal.

The pulse train which allows to sample positive and negative slopes of the RF signal is thereby created artificially. In this way, the advantageous solution for half integer frequency ratios from sections 2.2 and 2.3 can as well be utilized for integer frequency ratios. This requirement is still mandatory, because the pulse trains can otherwise not be aligned to zero crossings of the RF signal. The relation between the repetition rate and the RF frequency therefore has to follow equation (2.1) where the laser repetition rate  $f_{\text{rep}}^f$  is defined as a full

integer sub-harmonic of the RF frequency. The new procedure introduces a new parameter within the L2RF setup which needs to be monitored or if possible actively controlled which is the splitting ratio  $r_s$  in front of the newly introduced delay line.

Following this scheme, one can subdivide the possible solutions into cases where the laser repetition rate is an even or an odd sub-harmonic of the RF frequency where different simplifications can be applied during the selection of the delays and the determination of the modulation frequencies. A second subdivision has to be performed by the availability of dual output MZMs. The bias voltage control without a dual output MZM is still troublesome under this novel method and the application of a second delay line will therefore be discussed as a possible solution.

## 2.6 Extended Working Scheme with Single Output MZMs

A delay line in front of the MZM is used in the extended working scheme to create a pulse pattern which can be aligned to different slopes of the RF signal. After entering the setup, the input pulse train with the average optical power  $P_{in}^*$  is split up into two identical parts  $p_1^*(t)$  and  $p_2^*(t)$  with a splitting ratio of  $r_s$ . The pulse train  $p_2^*(t)$  is delayed by  $T_1^f$  in a delay line. Both parts are recombined before entering the MZM. A schematic sketch illustrating this process can be found in figure 2.6. The delay line in front of the MZM will subsequently be called the first delay while the delay employed in the previous setup behind the MZM is called the second delay. Nevertheless this first example for the extended working scheme will be explained using a single output MZM.

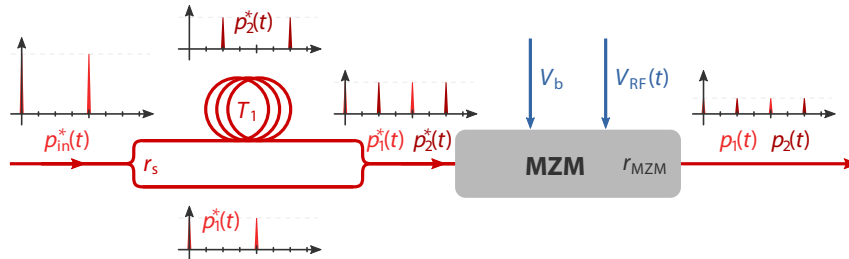


**Figure 2.6: Extended Pulse Pattern Generation with a Single Output MZM** | The input pulse train is split, delayed and recombined in front of the MZM in order to create the desired pulse pattern.

The associated pulse patterns are presented in figure 2.7. The repetition rate and the RF frequency are chosen to be identical in this example which actually corresponds to an odd frequency ratio. Subfigure (a) shows how every second line from the RF spectrum



of a single laser pulse train  $p_1(t)$  vanishes, if a second pulse train  $p_2(t)$  with the same repetition rate is superimposed with the first one at the first delay

$$T_1^o = \frac{1}{2} T_{\text{rep}}^o \quad (2.7)$$

of for example half the laser repetition period  $T_{\text{rep}}^o$ . No RF is yet applied to the MZM. This delay represents one specific of many theoretically possible solutions. The general solution will be discussed in the next section after the description of the sketched example.

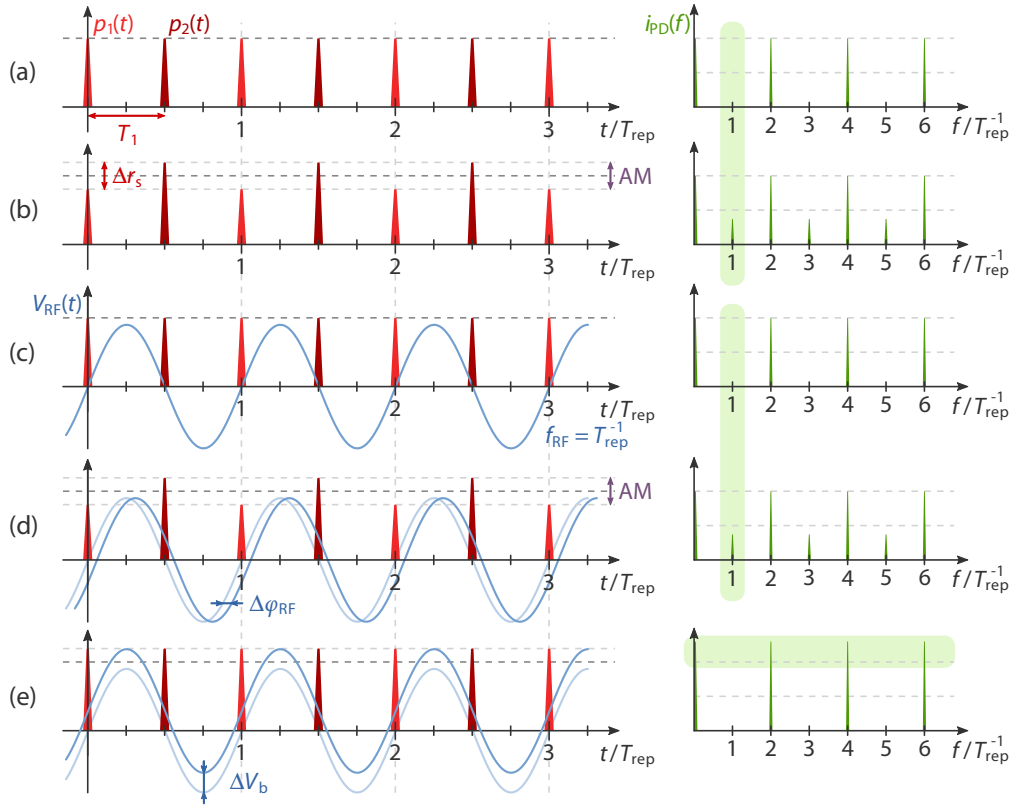


**Figure 2.7: Pulse Patterns and Spectra Using a Single Output MZM at a Full Integer Frequency Ratio in an Extended L2RF Scheme** | (a) Two pulse trains are combined with a fixed delay in front of the MZM. (b) Splitting ratio errors can be detected in this configuration at the first harmonic of the spectrum. (c) If the laser pulses are aligned to the zero crossings of the RF the spectrum remains unchanged. (d) Phase changes of the RF cause identical spectral changes as splitting ratio errors. (e) Bias voltage errors influence the overall amplitude of the laser pulse train and spectrum.

In subfigure (b) the influence of errors of the splitting ratio  $\Delta r_s$  at the first delay line is presented which causes the previously vanished signal component at the fundamental repetition rate and its odd multiples to reappear. Subfigure (c) shows that the original RF spectrum is not altered if an RF with the same frequency as the repetition rate is applied to the MZM with the correct phase, such that the laser pulses are aligned to the zero crossings of the RF wave. Next, subfigure (d) illustrates that if a phase error of  $\Delta\varphi_{\text{RF}}$  is introduced between the two signals, the amplitude of the combined laser pulse train is modulated in the time domain. In the RF spectrum several previously vanished lines in the frequency comb reappear. The lowest reappearing frequency in the spectrum is regarded as the modulation frequency and if this frequency is monitored in a detector, the power at this frequency could be used as measure for the phase error  $\Delta\varphi_{\text{RF}}$ . However, the amplitude modulation and spectral changes induced by phase errors is identical to the influence of splitting ratio errors depicted in subfigure (b). These two errors cannot be separated and a splitting ratio error can be misinterpreted as phase change.

A wrongly adjusted bias voltage is presented in subfigure (e). The resulting spectrum is characteristic for the usage of single output MZMs where bias voltage errors have no influence on the shape of the spectra but only on the overall output power. This situation also implies the same difficulties presented at the beginning of this chapter concerning the implementation of a bias voltage feedback with single output MZMs.

In summary, the presented configuration includes two weak points, which are the missing separation between the splitting ratio and phase error channels and the difficult construction of a bias voltage feedback without a dual output MZM due to the non differential bias voltage error detection. These weak points will be addressed in the next iteration of the L2RF phase detector which will be presented in section 2.7.

### 2.6.1 Determination of the Length of the First Delay in Front of the MZM

The number of full RF periods fitting between two laser pulses increases, while the selected laser repetition rate is shifted towards lower, integer sub-harmonics of the RF frequency as defined in equation (2.8). At the same time the number of feasible lengths of the first delay line also increases, because each new RF period, fitted between two subsequent laser pulses, contains one potentially usable opposite slope zero crossing to which the delayed pulse train can be aligned. Each of these zero crossings provides therefore a possible solution for the first delay  $T_1^f$  as presented in equation (2.9).

The  $\pi$  modulation frequency  $f_{\text{mod},1}^\pi$  is, as defined in equation (2.10), the frequency for which the length of the first delay line corresponds exactly to a phase shift of  $\pi$ . This frequency cancels out if the amplitude of both pulse trains is equal. The general relations between the

mentioned variables need to follow equations (2.8) to (2.10).

$$f_{\text{rep}}^f = \frac{1}{n} f_{\text{RF}} \quad \{n \in \mathbb{N}^*\} \quad (2.8)$$

$$T_1^f \Big|_{\text{general}} = \frac{2m-1}{2n} \frac{1}{f_{\text{rep}}^f} \quad \{m \in \mathbb{N}^* \mid m \leq n\} \quad (2.9)$$

$$f_{\text{mod},1}^\pi = \frac{1}{2} \frac{1}{T_1^f} \quad (2.10)$$

The  $\pi$  modulation frequency  $f_{\text{mod},1}^\pi$  may not coincide with a line of the frequency comb for many delays  $T_1^f$ . In this case one has to find the lowest common multiple between the repetition rate and odd multiples of the  $\pi$  modulation frequency in order to determine, which is the lowest, fully extinct frequency in the spectrum. This frequency is finally called the modulation frequency  $f_{\text{mod},1}^f$ . The modulation frequency is only defined for one specific delay and one specific repetition rate while the corresponding line in the spectrum only vanishes for a balanced amplitude ratio between the involved pulse trains.

Figure 2.8 shows modulated RF spectra of two overlapped pulse trains for the case that the laser repetition rate is the sixth sub-harmonic of the RF frequency, which is the actual frequency ratio present at [Free-Electron Laser in Hamburg \(FLASH\)](#) and the [European X-ray Free-Electron Laser \(XFEL\)](#). Six delays  $T_1^f$  can be calculated for this frequency ratio following equation (2.9) because six opposite slope zero crossings of the RF signal are available between two subsequent laser pulses of the original pulse train. Three of them are unique, because they are shorter or equal than half the laser repetition period  $T_{\text{rep}}^f$ . These three delays are therefore depicted. The amplitude of both pulse trains is assumed to be equal.

The shape of the combined frequency comb and the extinct or attenuated frequencies depend on the  $\pi$  modulation frequency  $f_{\text{mod},1}^\pi$  and thus also on the delay  $T_1^f$ . To illustrate the modulation one can print an envelope on top of the RF spectrum of the combined laser pulse trains which is indicating the modulated amplitude of each line. This envelope qualitatively follows the absolute value of a cosine function with a frequency equal to four times the modulation frequency  $f_{\text{mod},1}^\pi$ .

Figure 2.8 (a) shows the case of the shortest possible delay for the given frequency ratio. The  $\pi$  modulation frequency  $f_{\text{mod},1}^\pi$  is aligned to the spectrum and the modulation frequency  $f_{\text{mod},1}^f$  is therefore identical to the  $\pi$  modulation frequency.

Figure 2.8 (b) illustrates the next option for  $T_1^f$ . Again, the modulation frequency  $f_{\text{mod},1}^f$  is identical to the  $\pi$  modulation frequency  $f_{\text{mod},1}^\pi$  because the  $\pi$  modulation frequency is aligned to the spectrum. The frequency this time is three times lower compared to subfigure (a) which is why this solution is preferred over the first one.

Figure 2.8 (c) presents the third possible delay. Although the  $\pi$  modulation frequency  $f_{\text{mod},1}^\pi$  is even lower than in the previous cases, it is this time not aligned to the spectrum. For this reason the fully extinct modulation frequency  $f_{\text{mod},1}^f$  is higher compared to subfigure (b) and identical to the one depicted in subfigure (a).

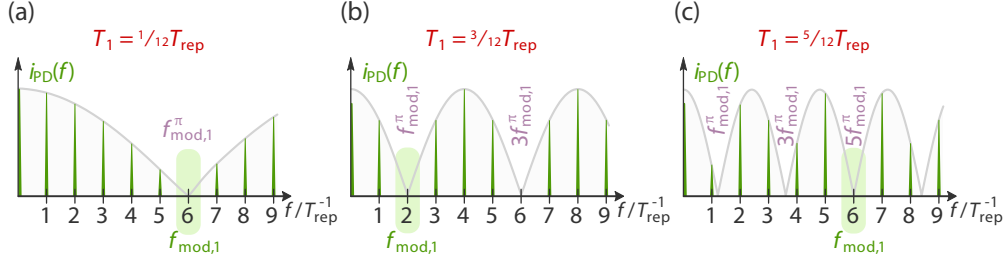


**Figure 2.8: Modulated Frequency Combs for Different Delays** | Two pulse trains with identical repetition rate overlap with different delays. For each case the RF spectrum is depicted together with the according modulation frequency.

As presented in subfigure (b), the lowest modulation frequency  $f_{\text{mod},1}^f$  in figure 2.8 can be achieved for the given ratio between repetition rate and RF frequency by applying a delay of

$$T_1^f \Big|_{\substack{n=6 \\ m=2}} = \frac{1}{4} T_{\text{rep}}^f. \quad (2.11)$$

For low sub-harmonics of the RF frequency it can be difficult to decide, which delay  $T_1^f$  is best suited for the second pulse train because many zero crossings of the RF signal come into question. There are however two general guidelines, which can be taken into account to narrow down the options for the delay  $T_1^f$ .

**Delay Selection Guidelines:** Delays longer than half the repetition period are redundant and therefore neglected immediately.

It will become obvious during the mathematical evaluation in chapter 3 that low modulation frequencies render the detection scheme more tolerant to length changes of the delay lines. The delays which lead to the lowest modulation frequency are therefore preferred.

In case multiple delays lead to the lowest possible modulation frequency, it is beneficial to favor short delays over longer ones in order to minimize the physical size of the delay line and thus ease the implementation. The delayed pulse train shows a different spot size in a longer delay line due to beam divergence and exhibits a worse pointing stability due to environmental influences which accumulate over the longer beam transport.

In summary, it is proposed to evaluate the potentially feasible delays – or in other words feasible opposite slope zero crossings of the RF wave – starting at half of the repetition period and moving on with the evaluation to shorter delays while looking for the lowest achievable modulation frequency. This incremental procedure arises from the fact that the longest reasonable delay does not necessarily facilitate the lowest possible modulation frequency for detection.

In order to find the lowest existing modulation frequency for a given sub-harmonic of the RF frequency, one has to effectively test all possible delays for the lowest achievable modulation frequency. It is comprehensible and might seem obvious to approach the problem by individually evaluating all possible delays and looking for the lowest modulation frequency. Nevertheless, this procedure can easily become tedious for lower sub-harmonics of the RF frequency. An algorithmic approach to the problem will therefore be presented next.

### 2.6.2 Calculation of the Modulation Frequency and First Delay Length

A generic procedure where all relations are calculated can be established by first choosing the modulation frequency and later picking the corresponding delay instead of testing all possible delays.

**Modulation Frequency Calculation:** If the repetition rate  $f_{\text{rep}}^f$  is the  $n$ th sub-harmonic of the RF frequency  $f_{\text{RF}}$ , one first has to determine the modulation factor  $k$ , such that  $k$  is the highest power of two which is still an aliquot divisor of  $n$ . The  $k$ th harmonic of the repetition rate  $f_{\text{rep}}^f$  represents the lowest achievable modulation frequency  $f_{\text{mod},1}^f$  for the given sub-harmonic (see table 2.1 for some examples).

Furthermore one can find  $k$  different delays  $T_1^f$  leading to this very modulation frequency, while again only those smaller or equal than the repetition period are unique with respect to the combined pulse trains. Expressed in a more formal way

$$f_{\text{rep}}^f = \frac{1}{n} f_{\text{RF}} \quad \{n \in \mathbb{N}^*\}, \quad (2.12)$$

$$f_{\text{mod},1}^f = k f_{\text{rep}}^f \quad \text{and} \quad (2.13)$$

$$T_1^f \Big|_{\substack{\text{general} \\ n=k}} = \frac{2m-1}{2k} T_{\text{rep}}^f \quad \{m \in \mathbb{N}^* \mid m \leq k\}. \quad (2.14)$$

According to equation (2.14),  $k$  different delays can be calculated for each sub-harmonic, each leading to the very same modulation frequency. Following the delay selection guidelines, the smallest delay is the one to favorably select. This is exactly the ideal first delay,

## 2 The Laser-to-RF Phase Detection Principle

satisfying equation (2.15).

$$T_1^f = \frac{1}{2k} T_{\text{rep}}^f \quad (2.15)$$

Modulation factors  $k$  for a couple of selected sub-harmonics are shown in table 2.1. Odd sub-harmonics are always associated with a modulation factor of one, therefore only the first three of them are listed. Furthermore, all sub-harmonics at powers of two show up as themselves, because they obviously directly comply with the rule for the modulation factor  $k$ . One can see that many modulation factors show up multiple times and thus a wide range of sub-harmonics can be covered with a small number of delay and modulation frequency combinations.

**Table 2.1: Modulation Factors for Selected Sub-Harmonics**

sub-harmonic $n$	1	2	3	4	5	6	8	10	12	14	16	18	20	22
modulation factor $k$	1	2	1	4	1	2	8	2	4	2	16	2	4	2

If the repetition rate is an even sub-harmonic of the RF frequency, the modulation factor  $k^e$  can take different values depending on the ratio of laser repetition rate to RF frequency. If however the repetition rate is an odd sub-harmonic of the RF frequency,  $n$  is not divisible by two and the modulation factor  $k^o$  can only become one. This allows to provide a general solution for all odd sub-harmonics of the laser RF frequency.

$$f_{\text{rep}}^o = \frac{1}{2m-1} f_{\text{RF}} \quad \{m \in \mathbb{N}^*\} \quad (2.16)$$

$$k^o = 1 \quad (2.17)$$

The equations revealing in this case the only suitable value for the first delay and satisfying all previously mentioned guidelines are unique, as shown in equations (2.18) and (2.19) and they represent special cases of equations (2.13) and (2.15).

$$f_{\text{mod},1}^o = f_{\text{rep}}^o \quad (2.18)$$

$$T_1^o = \frac{1}{2} T_{\text{rep}}^o \quad (2.19)$$

Regarding odd sub-harmonics, the delayed pulse train is always delayed by half the repetition period. The repetition rate is doubled and odd harmonics of the original repetition rate vanish from the spectrum. This is the case for all odd sub-harmonics, for which one example has been illustrated in figure 2.7. The  $\pi$  modulation frequency is in this case equal to the repetition rate  $f_{\text{rep}}^o$  and thus leads directly to the modulation frequency  $f_{\text{mod},1}^o$ . This

is the lowest frequency in the comb and therefore also the lowest frequency at all, which can be used to detect amplitude imbalances between the two involved pulse trains.

Figure 2.8 can be taken as an example for an even sub-harmonic where the general rules for full integer sub-harmonics apply. The figure depicts modulated spectra created by pulse trains at the sixth sub-harmonic of the RF frequency. The selected modulation frequency  $f_{\text{mod},1}^f$  and the delay  $T_1^f$  correspond to table 2.1 and equation (2.15) and they confirm the statements from this section.

### 2.6.3 Summary for the Operation with Single Output MZMs

A generic solution, needed to determine a working delay and to find the proper modulation frequency has been laid out in equations (2.12) to (2.15). Some general problems of single output MZM based setups however remain unsolved.

An artificially created pulse train is needed for all integer ratios between laser repetition rate and RF frequency as described in the previous sections. This artificial pulse train is generated by splitting the input pulse train, delaying one of the created parts and recombining both pulse trains before sending them to the MZM. Both pulse trains are supposed to have the same amplitude, because inside the MZM, the phase error between pulse train and RF signal is imprinted in the form of an amplitude modulation on the pulse trains. If the pulse trains are not balanced at the input of the MZM, this mismatch looks at the output exactly like a phase error. If the splitting ratio  $r_s$  drifts and a splitting ratio error  $\Delta r_s$  builds up over time, this is falsely detected as a phase drift.

There is no way to avoid this crosstalk when working with single output MZMs, except by actively controlling the splitting ration or by avoiding the splitting process at all, which can be performed by choosing an half integer ratio between the laser repetition rate and the RF frequency where pulses can immediately sample positive and negative slopes of the RF. The input pulse train can be directly fed to the MZM in this last case.

The active stabilization of the splitting ratio is therefore crucial in cases where only single output MZMs can be employed and no half integer frequency ratio between RF and laser pulse train is available which could be operated without a delay line in front of the MZM. Further details on a possible implementation of an active splitting ratio stabilization can be found in chapter 6 because this newly invented idea has not yet been tested and it thus relates more to future implementations.

The troublesome bias voltage control of single output MZMs due to a missing differential measure for bias voltage errors is another general problem.

Many of the just mentioned problems can be solved by employing a dual output MZM in the extended working scheme.

## 2.7 Extended Working Scheme with Dual Output MZMs

In the previous sections, two techniques to improve the L2RF phase detector have been presented. The newly introduced delay line implemented in front of the MZM allows to build L2RF phase detectors for an extended range of frequency ratios where the phase error detection can be performed differentially at a harmonic of the laser repetition rate. The usage of dual output MZMs and the recombination of both outputs allows on the other hand to implement a differential bias control. These techniques can be combined in one setup.

This final setup allows to measure phase errors  $\Delta\phi_{\text{RF}}$  but it can also generate up to two additional error signals used to drive internal feedback loops. One signal is proportional to the bias voltage error  $\Delta V_b$  and used to set up a bias feedback loop for the MZM, while the other one is proportional to the internal splitting ratio error  $\Delta r_s$  of the first delay line and can as well be used to set up a feedback. All three error signals are imprinted in form of different amplitude modulation patterns on the involved laser pulse train.

The splitting and recombination in front of the MZM is employed in order to sample different slopes of the RF wave and to thereby detect phase shifts between the laser pulses and the RF – such that the setup generally works as a L2RF phase detector. The guidelines for the selection of the first delay  $T_1$  have not changed, and can be inherited from the section about the single output MZM.

After recombining the two outputs of the dual output MZM four pulse trains are involved in the generation of the amplitude modulation. The pulse trains will be named  $p_1(t)$  to  $p_4(t)$ , where  $p_1(t)$  and  $p_2(t)$  name the pulse trains  $p_1^*(t)$  and  $p_2^*(t)$  from the first delay line after traveling to the regular output of the modulator, while  $p_3(t)$  and  $p_4(t)$  name the pulse trains  $p_1^*(t)$  and  $p_2^*(t)$  after traveling to the second output of the modulator and experiencing the inverse modulation compared to  $p_1(t)$  and  $p_2(t)$  in the MZM. The general arrangement of delays around a dual output MZM can be found in figure 2.9.

Changes of the pulse train  $p_1^*(t)$  influence  $p_1(t)$  and  $p_3(t)$  equally, while changes of the modulator voltage affect them inversely.

Furthermore, changes of the pulse train  $p_2^*(t)$  influence  $p_2(t)$  and  $p_4(t)$  equally, while changes of the modulator voltage affect them also inversely.

The input pulse trains  $p_1^*(t)$  and  $p_2^*(t)$  are aligned to different slopes of the RF signal and are therefore inversely modulated in the case of RF phase drifts between the laser pulse train and the RF wave, while bias voltage drifts have the same influence on these two input pulse trains although the two outputs are now modulated inversely

The calculation of the modulation frequencies and delays at this scheme will be pursued in the next section.



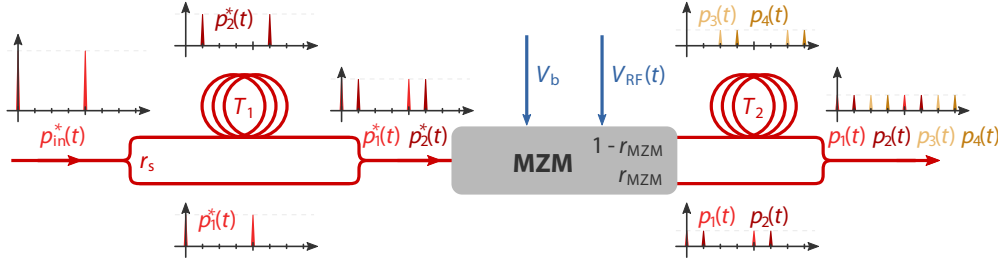


**Figure 2.9: Extended Pulse Pattern Generation with a Dual Output MZM** | The input pulse train is split, delayed and recombined two times – once in front of the MZM and once behind – in order to create the desired pulse pattern and to detect all error signals simultaneously.

### 2.7.1 Calculation of the Modulation Frequency and Second Delay Length

The pulse train modulations in this arrangement occur at different frequencies which depend on the first and second delay. The established delay selection guidelines for the selection of the first delay also apply for the selection of the second delay. In order to keep both modulation frequencies low a careful choice has to be made for both of them. The first delay has already been determined according to section 2.6.1. There are two general solutions for the second delay which are either half or two times the first delay. Odd and Even frequency ratios have to be regarded separately.

#### Parameters for Odd Frequency Ratios

If the laser repetition rate is an odd sub-harmonic of the RF frequency only one suitable solution for the first delay exists according to equation (2.19). Likewise only one solution for the second delay, presented in equation (2.20), exists then. The first delay  $T_1^o$  therefore has to be cut in half to obtain the second delay  $T_2^o$ .

$$T_2^o = \frac{1}{2} T_1^o = \frac{1}{4} T_{\text{rep}}^o \quad (2.20)$$

At the same time the three investigated errors emerge at two specific modulation frequencies according to equations (2.21). Potential splitting ratio errors  $\Delta r_s$  in the first delay line and phase errors  $\Delta \varphi_{\text{RF}}$  show up at the modulation frequency  $f_{\text{mod},1}^o$ , while bias voltage errors  $\Delta V_b$  show up at the modulation frequency  $f_{\text{mod},2}^o$ . The two error signals which simultaneously manifest at the modulation frequency  $f_{\text{mod},1}^o$  have a phase difference of  $\pi/2$  and can thus be told apart in a phase sensitive detector. More details on this topic can be found in section 4.1.3.

$$f_{\text{mod},1}^o = f_{\text{rep}}^o \quad f_{\text{mod},2}^o = 2f_{\text{rep}}^o \quad (2.21)$$

### Parameters for Even Frequency Ratios

In the second case the laser repetition rate is an even sub-harmonic of the RF frequency.

$$f_{\text{rep}}^e = \frac{1}{2m} f_{\text{RF}} \quad \{m \in \mathbb{N}^*\} \quad (2.22)$$

It is still desired to detect the error signals at the lowest possible modulation frequency. For this reason, doubling the first delay in order to obtain the second delay as shown in equation (2.23) is the favored solution. The definition of the first delay  $T_1^e$  still follows the general definition from equation (2.15) and leads to the definition of the second delay, where both equations include the modulation factor  $k^e$ . Some examples for calculated modulation factors are provided in table 2.1.

$$T_1^e = \frac{1}{2k^e} T_{\text{rep}}^e \quad T_2^e = 2T_1^e = \frac{1}{k^e} T_{\text{rep}}^e \quad (2.23)$$

The two modulation frequencies are again defined by the respective lengths of the delays  $T_1^e$  and  $T_2^e$ . In this case splitting ratio errors  $\Delta r_s$  at the first delay line emerge at the modulation frequency  $f_{\text{mod},1}^e$  while bias voltage errors  $\Delta V_b$  and phase errors  $\Delta \phi_{\text{RF}}$  show up at the modulation frequency  $f_{\text{mod},2}^e$ . Two error signals are encoded at the same frequency. They can be separated during detection by their phase shift of  $\pi/2$  like in the previous case.

$$f_{\text{mod},1}^e = k^e f_{\text{rep}}^e \quad f_{\text{mod},2}^e = \frac{k^e}{2} f_{\text{rep}}^e \quad (2.24)$$

Figures 2.10 (a) to 2.10 (e) depict different pulse patterns and the associated RF spectra for typical error conditions in a dual output MZM based extended L2RF phase detector. The presented setup works with an RF frequency of twice the laser repetition rate. The modulation factor  $k^e$  is in this case two. The delays can be calculated according to equations (2.23) to be

$$T_1 = \frac{1}{4} T_{\text{rep}} \quad \text{and} \quad T_2 = \frac{1}{2} T_{\text{rep}}. \quad (2.25)$$

Figure 2.10 (a) shows the initial condition when no RF is yet applied to the MZM. The pulse trains are delayed according to equations (2.25). The amplitude of both pulse trains is perfectly balanced and no splitting, bias or phase error is present. The repetition rate is quadrupled and the first three harmonics have disappeared in the RF spectrum.

In subfigure (b) the combined pulse train is amplitude modulated by a splitting ratio error  $\Delta r_s$ . In this case the modulation frequency  $f_{\text{mod},1}^e$  according to equation (2.24) appears in the spectrum at twice the original repetition rate.

Figure 2.10 (c) looks identical to subfigure (a), except that now the RF is connected. The pulse train and RF spectra however are unmodulated because the pulse trains are aligned perfectly to the zero crossings of the RF.

The amplitude modulation caused by a phase error  $\Delta\phi_{\text{RF}}$  is depicted in figure 2.10 (d). The modulation occurs now at the modulation frequency  $f_{\text{mod},2}^c$  according to equation (2.24).

The bias voltage error present in figure 2.10 (e) causes also an amplitude modulation at the modulation frequency  $f_{\text{mod},2}^c$ . By comparing the pulse patterns in subfigures (d) and (e), one can clearly see that the generated RF signals are phase shifted with respect to each other by exactly the delay  $T_1$ , which corresponds at the present frequency ratio precisely to the predicted phase shift of  $\pi/2$ .

The depicted situation can be regarded as representative for all even sub-harmonics of an RF signal with the same modulation factor  $k^c$  of two. The sixth sub-harmonic has for example the same modulation factor assigned. If one would exchange the RF in figure 2.10 with a three times higher RF frequency the pulses would still be aligned to the correct zero crossings and slopes of the RF signal and the amplitude modulations would be identical.

In fact, for any modulation factor  $k$  only one perfect solution with respect to delays and modulation frequencies exists and thus identical pulse patterns can be used for various frequency ratios between laser repetition rate and RF frequency as long as the modulation factor  $k$  is the same.

### 2.7.2 Summary for the Operation with Dual Output MZMs

In the previous section the numerous advantages of using a dual output MZM within the extended working scheme have been explained. Mainly the option to individually detect the three signals for phase ( $\Delta\phi_{\text{RF}}$ ), bias voltage ( $\Delta V_b$ ) and splitting ratio errors ( $\Delta r_s$ ) is an improvement compared to the single output modulator. Beyond that, the increased power efficiency, achieved by the recombination of both MZM outputs before the photodiode is an important advantage.

Restrictions for a quick choice of the second delay and the identification of the according modulation frequencies have been formulated in equations (2.20) to (2.24). The rules for the calculation of the first delay which were specified in the previous section for L2RF implementations with single output MZMs still apply when using dual output MZMs.

The dual output MZM based setup will also benefit from the later proposed all-fiber solution (see chapter 6). The natural ability to measure the splitting ratio error  $\Delta r_s$  is already an attribute of dual output MZM based setups, but the all-fiber setup will easily allow to control the splitting ratio  $r_s$  at the first delay and thus to further stabilize the overall setup.

A deeper insight into the working principle of the L2RF phase detector can be gathered by creating a model for the setup and deriving equations for the output signals which depend on various parameters. The next chapter therefore assembles this representation by moving through the setup and covering all essential components.

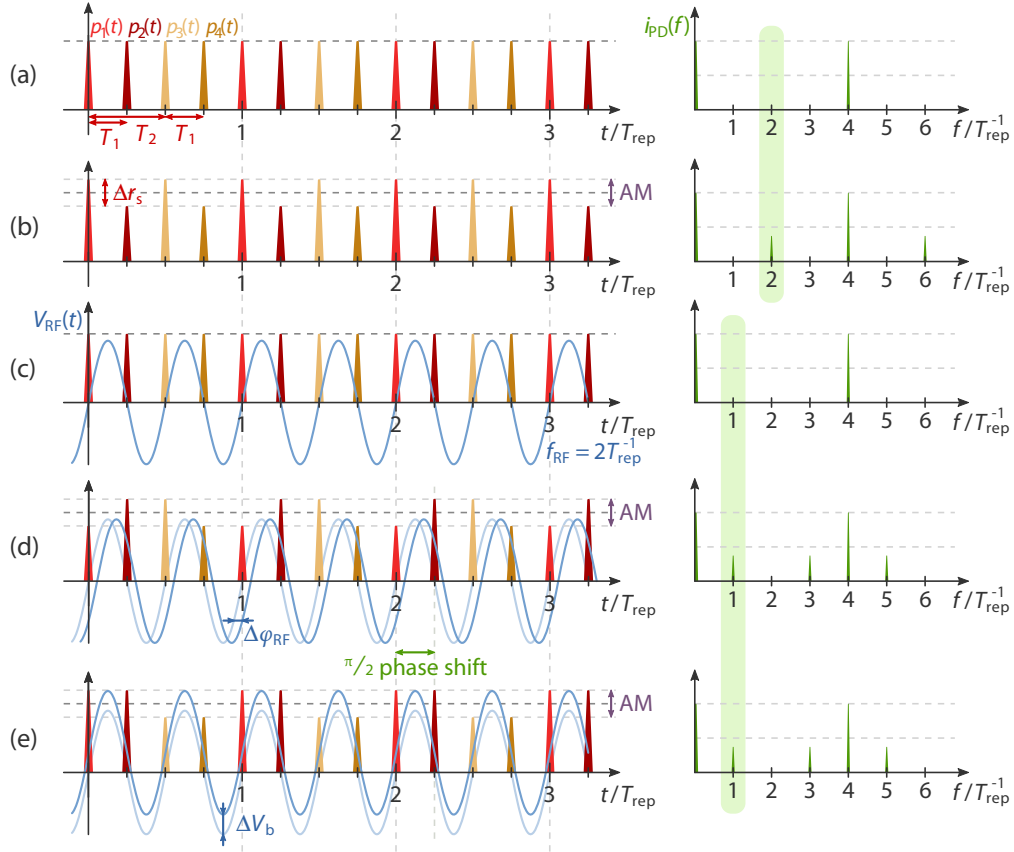


**Figure 2.10: Pulse Patterns and Spectra Using a Dual Output MZM at a Full Integer Frequency Ratio in an Extended L2RF Scheme** | (a) The setup uses two split and delay procedures by which four pulse trains are generated and overlapped. The repetition rate is practically quadrupled. (b) Errors of the splitting ratio at the first delay line cause an amplitude modulation which manifests in the frequency domain at the second harmonic. (c) The laser pulse trains are perfectly aligned to the RF signal. The pulse trains are not amplitude modulated. (d) Phase errors of the RF signal cause an amplitude modulation at the repetition rate. (e) Bias voltage errors cause an amplitude modulation at the same frequency as phase errors. Nevertheless, both signals are phase shifted by  $\pi/2$  and can therefore be separately detected using a phase sensitive amplitude detector.

## Mathematical Analysis of the Laser-to-RF Principle

The illustrative development of the working principle of the [laser-to-RF \(L2RF\)](#) phase detector from the previous chapter will now be supported by a formal, mathematical approach taking into account the frequency ratio present at the [Free-Electron Laser in Hamburg \(FLASH\)](#) and at the European [X-ray Free-Electron Laser \(XFEL\)](#) and leading to an analysis of potential error sources. Only the full featured [L2RF](#) phase detector implemented with a dual output [MACH-ZEHNDER modulator \(MZM\)](#) will be covered here, but the simpler situation for single output modulators can be derived fully analogously.

Starting from the incoming reference pulse train, the splitting, delay and recombination will be described. Then the modulation in the [MZM](#) together with the second delay and the subsequent recombination are formally explained. Furthermore, the detection of the combined pulse train with a photodiode is expressed mathematically. The [power spectral density \(PSD\)](#) of the generated electrical pulse train is derived next, in order to investigate the spectral properties of the modulated frequency comb associated with the signal.

The [FOURIER](#) transform of the photodiode signal is used to simulate the [radio frequency \(RF\)](#) band-pass filter and to extract the frequency component at the modulation frequency  $f_{\text{mod}}$ . After the inverse transform back to the time domain, the phase sensitive amplitude detection is performed using an [RF](#) mixer after amplifying the signal with [RF](#) amplifiers. The baseband signal at the difference frequency is selected from the [RF](#) mixer output with a low-pass filter and finally amplified in an [low-noise amplifier \(LNA\)](#). The analytically obtained output equations will be analyzed subsequently for possible error sources and the robustness of the [L2RF](#) phase detector will be discussed.

The creation of the different pulse trains in the [L2RF](#) phase detector has been introduced already in the previous chapter. A block diagram of the optical part of the setup which shows the creation of the four pulse trains with a dual output [MZM](#) has been presented in [figure 2.9](#). The electrical readout chain starting from the photodiode is shown in [figure 3.1](#) together with device specific parameters. The figure is meant to provide an overview on the components which will be covered subsequently. The depicted parameters will be introduced together with the according components during the course of this chapter.

### 3 Mathematical Analysis of the Laser-to-RF Principle

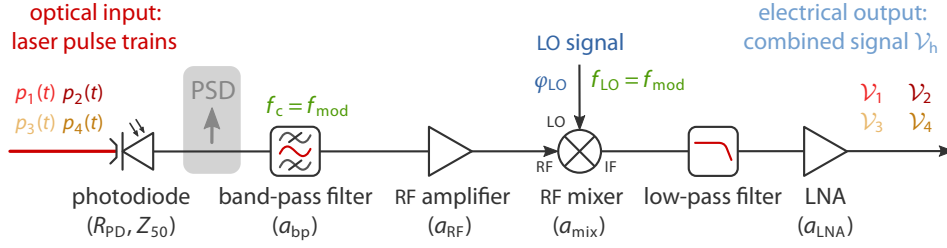


**Figure 3.1: Block Diagram of a Basic L2RF Readout Scheme** | The signals from the four overlapped pulse trains are treated independently up to the end of the detection chain, where they are superposed. The **local oscillator (LO)** signal can also be extracted with a photodiode and a band-pass filter from a laser pulse train where all frequencies from the comb are naturally available. The **PSD** is calculated for signals directly behind the photodiode as indicated.

The readout scheme presented in figure 3.1 has to be duplicated for each measurement channel. The measurement channel is defined by adjusting the correct **LO** phase  $\phi_{LO}$ , by choosing the correct center frequency of the band-pass filter  $f_c$  and by choosing the according **LO** frequency  $f_{LO}$ . The term measurement channel refers to the independent detection of phase ( $\Delta\phi_{RF}$ ), bias voltage ( $\Delta V_b$ ) and splitting ratio errors ( $\Delta r_s$ ).

#### 3.1 Situation at FLASH and the European XFEL

At **FLASH** and the European **XFEL** optical synchronization signals will be used in the future to stabilize the phase of **RF** signals in the accelerator tunnel [Czu<sup>+</sup>13; Bra<sup>+</sup>12]. The **master laser oscillator (MLO)** operates at both facilities [Sch11b; Syd<sup>+</sup>14] in the C-band. Integrated dual output **MZMs** are commercially available at this wavelength, such that full featured **L2RF** phase detectors can be implemented.

The **RF** frequency and laser repetition rate of the **MLO** at both accelerators are identical. The accelerator is operated at an **RF** frequency  $f_{RF}$  and the **MLO** at a laser repetition  $f_{rep}$  rate of

$$f_{RF} = 1.3 \text{ GHz} \quad \text{and} \quad f_{rep} = \frac{1}{6} f_{RF} = 216.\bar{6} \text{ MHz}. \quad (3.1)$$

The laser repetition rate is the sixth sub-harmonic of the **RF** frequency and the modulation factor  $k$  according to table 2.1 in the previous chapter amounts to two.

According to equations (2.15) and (2.23) the involved delays  $T_1$  and  $T_2$  need to be

$$T_1 = \frac{1}{4} \frac{1}{f_{\text{rep}}} \quad \text{and} \quad T_2 = \frac{1}{2} \frac{1}{f_{\text{rep}}}, \quad (3.2)$$

while the error signals according to equations (2.24) can be detected at the modulation frequencies

$$f_{\text{mod},1} = 2f_{\text{rep}} \quad \text{and} \quad f_{\text{mod},2} = f_{\text{rep}}. \quad (3.3)$$

The laser repetition rate is quadrupled by the superposition of four pulse trains with the above specified delays. The generated pulse train is depicted in figure 2.10 on page 36 while the RF frequency is three times higher compared to the RF signal used in this figure. In the working point only every fourth spectral line is present in the frequency comb, while the detector has to monitor the first and second harmonic of the repetition rate. These harmonics show up in the output signal if the setup is not in its working point and indicate certain error conditions. The implementation of the optical setup and the readout electronics for the L2RF phase detector are explained in detail in chapter 4.

In general, the RF frequency  $f_{\text{RF}}$  and the repetition rate  $f_{\text{rep}}$  can be transferred to the angular frequency domain following:

$$\omega = 2\pi f, \quad (3.4)$$

which leads to  $\omega_{\text{RF}}$  and  $\omega_{\text{rep}}$  respectively. After the explanation of the delays and the modulation frequencies it is possible to follow the laser pulse trains through the setup starting with the first delay line.

### 3.2 Splitting Ratio at the First Delay Line and Incoupling Efficiency

In the current implementation of the L2RF phase detector for FLASH and the European XFEL the first delay is realized as a free-space delay (see figure 4.1 for a block diagram). The input pulse train  $P_{\text{in}}^*(t)$  is split into two pulse trains  $p_1^*(t)$  and  $p_2^*(t)$ . The delayed pulse train  $p_2^*(t)$  covers a longer free-space distance and passes more optical components than pulse train  $p_1^*(t)$ . After recombination both pulse trains have to be launched into the same fiber collimator. The optical properties of both pulse trains and thus the incoupling efficiency  $\eta$  are different due to differences in the beam sizes, while dispersion can be neglected because the pulses are detected with a photodiode where the pulse duration plays no significant role.

As both pulse trains are supposed to have exactly the same average power when entering the **MZM**, the incoupling induced mismatch has to be precompensated by the real splitting ratio  $r_{s,r}$ , overcoming the different incoupling efficiencies. This condition is defined in equation (3.5) with one pulse train on each side of the equation. The real splitting ratio  $r_{s,r}$  leading to balanced pulse trains at the **MZM** can be described as a function of the individual incoupling efficiencies  $\eta_1$  and  $\eta_2$  of the respective pulse trains  $p_1^*(t)$  and  $p_2^*(t)$  as shown in equation (3.6).

$$r_{s,r}\eta_1 = (1 - r_{s,r})\eta_2 \quad (3.5)$$

$$r_{s,r} = \frac{\eta_2}{\eta_1 + \eta_2} \quad (3.6)$$

The mean incoupling efficiency  $\eta_m$  of both pulse trains amounts to

$$\eta_m = 2 \frac{\eta_1 \eta_2}{\eta_1 + \eta_2} . \quad (3.7)$$

The utilization of the mean incoupling efficiency allows to rewrite equation (3.5) with the ideal splitting ratio  $r_s$ .

$$r_s \eta_m = (1 - r_s) \eta_m \quad (3.8)$$

The real splitting ratio  $r_s$  amounts by definition to  $1/2$ . It is extended by the error term  $\Delta r_s$  in order to investigate small deviations from this value.

$$r_s = \frac{1}{2} + \Delta r_s \quad (3.9)$$

If beam properties drift over time and one or both of the incoupling efficiencies changes, the pulse trains at the input of the **MZM** become unbalanced. Under ideal circumstances the unbalance is compensated via a modified real splitting ratio  $r_{s,r}$  and controlled in a feedback loop. The controller keeps the pulse trains balanced at the cost of changing the overall power sent to the **MZM**. At the **MZM** one would observe no pulse train imbalance, but an overall power change. This behavior is represented in equations (3.7) to (3.9).

The integrated **MZM** used in the **L2RF** setup is equipped with a **polarization maintaining (PM)** input fiber and an internal clean-up polarizer [**EOMz**]. It only accepts linearly polarized light coupled to the slow axis of the input fiber (see appendix A for more details). The delay in front of the **MZM** however is realized with **polarizing beam cubes (PBCs)** used to split and to recombine the pulse trains. After the recombination the two parts  $p_1^*(t)$  and  $p_2^*(t)$  are of orthogonal polarization. The additional delay efficiency  $\eta_d$  covers the fact,



that half of the optical power of each pulse train is lost in the polarizer because the pulse trains need to be balanced.

$$\eta_d = \frac{1}{2} \quad (3.10)$$

After passing the first optical delay line and coupling the pulses into a fiber they arrive at the MZM.

### 3.3 The MZM Transfer Function

The working principle of integrated MZMs is presented in appendix A. The optical output power at the regular output  $p_{\text{MZM}}(t)$  and the optical output power at the inverted output  $p'_{\text{MZM}}(t)$  are stated in equations (3.11) and (3.12). They have been derived in equations (A.7) and (A.8). The factors  $a_{\text{MZM}}$  and  $a'_{\text{MZM}}$  represent the persistent insertion loss during full transmission of each output. The optical input power  $p_{\text{opt}}(t)$  is altered by the modulation factor  $r_{\text{MZM}}$ . The modulation factor is not time-dependent because the laser repetition rate was required to be a sub-harmonic of the RF frequency. Therefore all laser pulses hit the RF with a fixed relative phase and they are always modulated to the same extend.

$$p_{\text{MZM}}(t) = a_{\text{MZM}} \left( \frac{1}{2} + r_{\text{MZM}} \right) p_{\text{opt}}(t) \quad (3.11)$$

$$p'_{\text{MZM}}(t) = a'_{\text{MZM}} \left( \frac{1}{2} - r_{\text{MZM}} \right) p_{\text{opt}}(t) \quad (3.12)$$

The equation for the modulation factor  $r_{\text{MZM}}$  has been derived in equation (A.9). It is defined as

$$r_{\text{MZM}} = \frac{1}{2} \sin \left( \frac{\pi}{V_{\pi, \text{DC}}} (V_b - V_{b,0}) + \frac{\pi}{V_{\pi, \text{RF}}} (\hat{V}_{\text{RF}} \sin(-\Phi_{\text{RF}})) \right). \quad (3.13)$$

The  $\pi$  modulation voltages  $V_{\pi, \text{DC}}$  and  $V_{\pi, \text{RF}}$  are characteristic for each individual MZM and denote how much direct current (DC) bias or RF voltage has to be applied to the MZM in order to switch from minimum to maximum transmission. The internal interferometer arms of an MZM are usually not perfectly balanced. The voltage  $V_{b,0}$  has to be applied to the MZM in order to balance the interferometer arms and to tune the MZM into its working point. This is actually a parameter of each individual MZM. Finally  $V_b$  and  $\hat{V}_{\text{RF}}$  are the bias and RF voltages actually applied to the MZM and  $\Phi_{\text{RF}}$  is the relative phase between the laser pulse train and the RF signal.

Only small variations around the working point are of interest. Therefore, the bias voltage  $V_b$  is replaced according to equation (3.14) by the ideal bias voltage  $V_{b,0}$  and the bias voltage error  $\Delta V_b$ .

$$V_b = V_{b,0} + \Delta V_b \quad (3.14)$$

The  $\pi$  modulation voltages  $V_{\pi,DC}$  and  $V_{\pi,RF}$  are replaced by the generalized  $\pi$  modulation voltage  $V_\pi$  as presented in equation (3.15). The same applies to the insertion loss per output. Only the unified insertion loss  $a_{MZM}$  as defined in equation (3.16) is taken into account for the following derivations.

$$V_{\pi,DC} = V_{\pi,RF} = V_\pi \quad (3.15)$$

$$a_{MZM} = a'_{MZM} \quad (3.16)$$

In the working point the first laser pulse train ideally passes the MZM aligned to the zero crossings of the RF wave and thus with a relative RF phase of zero while a phase error term is retained in equation (3.17) which will be used to investigate small deviations from this working point. The second pulse train is shifted with respect to the first one by a phase difference corresponding to the delay  $T_1$ . Small variations around the working point are again of interest and the RF phase error term  $\Delta\phi_{RF}$  is therefore also introduced in equation (3.18).

$$\Phi_{RF,1} = \Delta\phi_{RF} \quad (3.17)$$

$$\Phi_{RF,2} = \Delta\phi_{RF} + 2\pi f_{RF} T_1 \quad (3.18)$$

The argument of the sine in equation (3.13) is additionally simplified by replacing  $\pi$  and  $V_\pi$  with the normalized  $\pi$  modulation factor  $\Theta_\pi$ .

$$\Theta_\pi = \frac{\pi}{V_\pi} \quad (3.19)$$

The proposed substitutions finally lead to equation (3.20) for the modulation factor  $r_{MZM,1}$  of the initial pulse train and equation (3.21) for the modulation factor  $r_{MZM,2}$  of the pulse train delayed by  $T_1$ .

$$r_{MZM,1} = \frac{1}{2} \sin(\Theta_\pi (\Delta V_b + \hat{V}_{RF} \sin(-\Delta\phi_{RF}))) \quad (3.20)$$

$$r_{MZM,2} = \frac{1}{2} \sin(\Theta_\pi (\Delta V_b + \hat{V}_{RF} \sin(-(\Delta\phi_{RF} + 2\pi f_{RF} T_1)))) \quad (3.21)$$

Equations (3.20) and (3.21) both contain the RF peak voltage  $\hat{V}_{RF}$ . RF signals are frequently quantified by their RF power in dBm, which means relative to 1 mW. The power  $P_{dBm}$  in

dBm can be converted to  $P_{\text{RF}}$  in W according to equation (3.22) while the relation of the RF peak voltage  $\hat{V}_{\text{RF}}$  to the power  $P_{\text{RF}}$  is defined by the system impedance  $Z$  and given in equation (3.23).

$$P_{\text{RF}} = (1 \text{ W}) \cdot 10^{\frac{P_{\text{dBm}} - 30}{10}} \quad (3.22)$$

$$\hat{V}_{\text{RF}} = \sqrt{2P_{\text{RF}}Z} \quad (3.23)$$

The two output signals from the MZM are in the L2RF phase detector recombined after the signals from the inverted output have been delayed by the second delay  $T_2$ . A block diagram of the second delay line is depicted in figure 4.2. There are in-fiber combiners available for the recombination, but using free-space optics like for example PBCs is also possible.

The combined signal is subsequently sent to the photodiode for detection. The combination of both output signals behind the MZM does not facilitate additional losses like in the first delay line, because the photodiode can detect orthogonally polarized light and there is no need to isolate one plane of polarization from the combined pulse trains.

### 3.4 Detection with an InGaAs PIN Photodiode

Photodiodes can suffer from polarization-dependent loss (PDL) and for the best achievable performance, photodiodes with low PDL have to be selected for the L2RF phase detector readout in order to work well with the orthogonally polarized signals. The combined signals however arrive with a stable polarization at the photodiode which reduces the PDL influence to a constant attenuation for each of the combined pulse trains. The balancing between the pulse trains does not influence the phase error measurement but only the bias error measurement, which still allows to achieve a high phase error measurement accuracy despite of the PDL influence.

In order to simulate the photodetection process it is first necessary to establish a mathematical representation of an optical pulse train. The laser pulses in the optical synchronization system at FLASH and the European XFEL are with  $\sim 210$  fs full width at half maximum (FWHM) pulse duration<sup>1</sup> [Sch11b] much shorter than the pulse distance<sup>2</sup> of  $\sim 4.6$  ns.

<sup>1</sup>The pulse duration has been measured with an autocorrelator and a sech<sup>2</sup> pulse has been fitted to the measurement data in order to obtain the FWHM pulse duration. The measurement was performed at a commercial Origami-15 [Orig15] semiconductor saturable absorber mirror (SESAM) based laser (serial number 072), which is the type also used as MLO in the optical synchronization system.

<sup>2</sup>The pulse distance corresponds to  $T_{\text{rep}}$  which in this case is  $6 f_{\text{RF}}^{-1}$ , where  $f_{\text{RF}} = 1.3$  GHz.

The optical pulse train can for this reason be approximated by an unlimited sum of time shifted DIRAC delta pulses called the Sha function (III). The Sha function is introduced in appendix C, equation (C.13) and defined as

$$\text{III}_T(t) = \sum_{b=-\infty}^{\infty} \delta(t - bT). \quad (3.24)$$

The DIRAC delta pulses have to be scaled with the total energy of a single laser pulse  $E_p$ . This approach is evident after recalling that the DIRAC delta pulse is not a regular function although it has a well defined integral – which is now scaled with the pulse energy or in other words the integral of the optical power over time. The pulse energy  $E_p$  of a single optical pulse can actually be calculated by dividing the average optical power of the pulse train  $P_{\text{opt}}$  by the repetition rate  $f_{\text{rep}}$  or multiplying it with the repetition period  $T_{\text{rep}}$  as presented in equation (3.25).

$$E_p = \frac{P_{\text{opt}}}{f_{\text{rep}}} = P_{\text{opt}} T_{\text{rep}} \quad (3.25)$$

This procedure is valid for the optical synchronization systems at FLASH and the European XFEL because the distributed pulse trains are regular, such that one can determine a repetition rate and have a negligible continuous wave (CW) background. The complete optical power in other words is contained in the actual pulses in order to allow this simplified approach. The scaled Sha function simulating the optical pulse train by its instantaneous power  $p_{\text{opt}}(t)$  can finally be found in equation (3.26).

$$p_{\text{opt}}(t) = E_p \text{III}_{T_{\text{rep}}}(t - T_0) \quad (3.26)$$

The time shift  $T_0$  in equation (3.26) denotes a possible delay of the whole pulse train, while the repetition period  $T_{\text{rep}}$  is defined as the inverse of the repetition rate  $f_{\text{rep}}$ . It was already pointed out that a DIRAC delta pulse has the inverse physical unit of its argument (see equation (C.9) on page 135). The same is true for the Sha function which is composed of DIRAC delta pulses. The presented approximation of the laser pulse train is therefore indeed equal to the instantaneous power delivered by the pulse train.

The optical synchronization systems of both FLASH and the European XFEL operate at a wavelength of 1553 nm [Syd<sup>+</sup>14]. Indium gallium arsenide (InGaAs) based photodiodes are well suited for this wavelength, because InGaAs can offer a high responsivity  $R_{\text{pD}}$  – which for example amounts to  $\sim 0.95 \text{ A W}^{-1}$  in case of the implemented photodiode [ET3.5k]. The photodiode is reverse biased and operated in the so-called photoconductive mode [Mai13]. The generated photocurrent  $i_{\text{pD}}(t)$  can be transferred to a voltage  $v_{\text{pD}}(t)$  by sending it

through a load resistor. In order to match the photodiode to successive RF components, it is necessary to use a load resistor  $Z_{50}$  of  $50 \Omega$ .

$$i_{PD}(t) = R_{PD} p_{opt}(t) \quad (3.27)$$

$$v_{PD}(t) = Z_{50} i_{PD}(t) \quad (3.28)$$

The previously derived equations still present an idealization of the real optical pulse train because they do not take the finite pulse width of the laser pulses into account. According to [Zha<sup>+</sup>12], the time response of a laser pulse being much shorter than 1 ps impinging on a photodiode with GHz RF bandwidth does not directly relate to the optical pulse width or shape because the photodiode bandwidth is in this case the determining factor. The optical power influences the electrical pulse amplitude (up to saturation). The electrical pulse shape and duration is defined by the photodiode response and the optical power but it does not depend on the optical pulse duration. The necessity of actually modeling realistic pulses will be discussed together with the properties of the FOURIER transform in the next section.

The actual photodiode signal can finally be assembled by connecting equations (3.25) to (3.28). The result in equation (3.29) defines the voltage signal created by photodetecting an optical pulse train.

$$v_{PD}(t) = P_{opt} T_{rep} R_{PD} Z_{50} \text{III}_{T_{rep}}(t - T_0) \quad (3.29)$$

In the next section, the spectral properties of the actually photodetected signal from the L2RF setup will be analyzed. The use of pulses with a finite duration in the simulation will be also evaluated in this section.

### 3.5 Derivation of the Power Spectral Density and Its Envelope

Specifically the power spectral density (PSD) of the time domain signal generated by the photodiode will now be derived in order to analyze the spectrum and to prove the statements about the spectral modulation from the previous chapter. The question whether a simulation with realistic pulses in favor of the ideal DIRAC pulse train does significantly change the result of the simulation however has to be discussed first.

It was already pointed out before that the photodiode response and not the shape of the laser pulses dominates the pulse shape of the electrical signal. In order to simulate realistic

pulses, the Sha function therefore has to be convoluted with the function describing the photodiode response in the time domain before performing any further analysis.

The time domain pulse train however is in any case a periodic signal, no matter how the individual pulses are shaped. The spectrum of a periodically spaced pulse train is furthermore always a regular spaced DIRAC comb. The difference between the spectrum obtained from a realistic pulse train with finite pulse duration and the spectrum obtained from an ideal DIRAC delta pulse train is the fact that in the first case the amplitude of the frequency lines in the spectrum decreases for higher frequencies. Realistic pulses have – practically speaking – just a lower or in other words finite bandwidth while the ideal DIRAC pulse has unlimited bandwidth. The rate of the spectral decay depends on the time domain pulse shape and width. While the frequency domain representation of pulse trains with finite width is closer to reality, the FOURIER transform and also the additional calculations needed to compute the PSD become much more complex if the usually nonlinear photodiode response function is taken into account.

The L2RF scheme aims towards analyzing the lower harmonics in the spectrum – often even the lowest. As the use of real time domain pulses only considerably influences the high frequency parts of the spectrum, it is not necessary to use such a complicated model during this analysis. The following steps will thus be carried out with a simple DIRAC delta pulse train providing adequate accuracy.

Four individual pulse trains with a repetition period  $T_{\text{rep}}$  arrive at the photodiode of the L2RF phase detector based on a dual output MZM for detection. The input pulse train  $p_{\text{in}}^*(t)$  with the average power  $P_{\text{in}}^*$  is split in the first delay line and both generated pulse trains are split again within the MZM such that a fraction of the two pulse trains from the first delay exits each output fiber of the MZM. The splitting at the first delay was derived already in equation (3.9) with the ideal splitting ration  $r_s$  of  $1/2$  and the splitting ratio error  $\Delta r_s$  while the optical losses  $\eta_m$  and  $\eta_d$  are introduced in equations (3.7) and (3.10). The MZM response of both outputs can be found in equations (3.11) and (3.12). The MZM transmission coefficients  $r_{\text{MZM},1}$  and  $r_{\text{MZM},2}$  are defined in equations (3.20) and (3.21) and it is important to note that the value of the latter depends not only on MZM specific parameters but also on the length of the first delay line.

Three of the four pulse trains are individually delayed with respect to the first one by a delay of either  $T_1$ ,  $T_2$  or the sum of  $T_1$  and  $T_2$ . All pulse trains are finally converted to a voltage signal according to equation (3.29). The optical power in this equation is individually replaced for each of the four pulse trains by the actual optical power of this particular pulse train, which results from scaling the overall optical input power by the before mentioned parameters.

The laser pulse trains – or more specifically their instantaneous voltage  $v_{PD}(t)$  – is simulated by individually scaled DIRAC pulse trains. Each of the following equations contains one scaling term representing the splitting ratio error  $\Delta r_s$  at the first delay line and another term representing the second splitting ratio  $r_{MZM}$ , applied by the MZM. Both terms scale in each equation the overall mean photodiode voltage  $V_{PD}$ , which is defined according to equation (3.29) by the mean optical input power  $P_{in}^*$  converted via the photodiode responsivity  $R_{PD}$  and the RF impedance  $Z_{50}$ , while already taking the efficiency factors  $\eta$  and the MZM insertion loss  $a_{MZM}$  into account.

$$\begin{aligned} v_{PD,1}(t) &= V_{PD} (1/2 + \Delta r_s) (1/2 + r_{MZM,1}) T_{rep} \text{III}_{T_{rep}}(t) \\ v_{PD,2}(t) &= V_{PD} (1/2 - \Delta r_s) (1/2 + r_{MZM,2}) T_{rep} \text{III}_{T_{rep}}(t - T_1) \\ v_{PD,3}(t) &= V_{PD} (1/2 + \Delta r_s) (1/2 - r_{MZM,1}) T_{rep} \text{III}_{T_{rep}}(t - T_2) \\ v_{PD,4}(t) &= V_{PD} (1/2 - \Delta r_s) (1/2 - r_{MZM,2}) T_{rep} \text{III}_{T_{rep}}(t - T_1 - T_2) \end{aligned} \quad (3.30)$$

$$V_{PD} = Z_{50} R_{PD} P_{in}^* a_{MZM} \eta_m \eta_d \quad (3.31)$$

The combined signal generated by the photodiode consists of the superposition of the four signals from equation (3.30). The PSD of the sum of these signals  $S_{vv_\Sigma}(f)$  is calculated by deriving the autocorrelation of this sum and FOURIER transforming the result. This procedure is carried out in appendix C with four DIRAC pulse trains. The result is a single DIRAC comb, scaled with the squared norm of the superposition of the complex scaling factors. The general result can be found in equation (C.54) on page 144. Tailored to the application of the L2RF setup output signal, this equation has to be modified considering the signals from equations (3.30) and (3.31). The result is presented below.

$$S_{vv_\Sigma}(f) = \left| \frac{V_{PD}}{\sqrt{Z_{50}}} \left( r_1 + r_2 e^{-j2\pi f T_1} + r_3 e^{-j2\pi f T_2} + r_4 e^{-j2\pi f (T_1 + T_2)} \right) \right|^2 \text{III}_{f_{rep}}(f) \quad (3.32)$$

$$\begin{aligned} r_1 &= (1/2 + \Delta r_s) (1/2 + r_{MZM,1}) & r_2 &= (1/2 - \Delta r_s) (1/2 + r_{MZM,2}) \\ r_3 &= (1/2 + \Delta r_s) (1/2 - r_{MZM,1}) & r_4 &= (1/2 - \Delta r_s) (1/2 - r_{MZM,2}) \end{aligned} \quad (3.33)$$

In equation (3.32) the parameters  $T_1$  and  $T_2$  represent the according delays of the L2RF setup and  $T_{rep}$  the repetition period of the laser pulse train. The repetition rate  $f_{rep}$  is the reciprocal of the repetition period  $T_{rep}$  and the coefficients  $r_1$  to  $r_4$  have to be replaced by their definitions from equation (3.33). The mean photodiode voltage  $V_{PD}$  has been defined in equation (3.31). The final equation for the PSD is already scaled with the RF impedance

$Z_{50}$  in order to not only provide the PSD in equation (3.32) in the sense of signal theory but also in a physical sense and in the correct dimension.

Three of the four signals in equation (3.32) actually have a phase factor in the form of a complex exponential function attached to them because the pulse train associated with these signals is shifted in the time domain with respect to the first pulse train. During superposition of the four signals the phase terms may not be dropped, although for the spectrum only the magnitude of the combined signal is finally of interest.

By omitting the Sha function in equation (3.32) and thus ignoring the comb nature of the PSD, one can investigate the magnitude of the L2RF output signal in the frequency domain continuously. The remaining part can be regarded as the absolute spectral envelope  $\mathcal{H}_{\text{abs}}(f)$  of the PSD. The equation for the absolute envelope of the PSD can finally be found in equation (3.34). A factor of  $(1 \text{ Hz})^{-1}$  has been kept from the omitted Sha function, such that the physical dimension of the equation is not altered. It should be mentioned that there are still various undetermined variables within the equation, for which reasonable values have to be assumed in order to be able to plot and analyze it.

$$\mathcal{H}_{\text{abs}}(f) = \left| \frac{V_{\text{PD}}}{\sqrt{Z_{50}}} \left( r_1 + r_2 e^{-j2\pi f T_1} + r_3 e^{-j2\pi f T_2} + r_4 e^{-j2\pi f (T_1 + T_2)} \right) \right|^2 \frac{1}{1 \text{ Hz}} \quad (3.34)$$

### 3.6 Analysis of the Power Spectral Density and Its Envelope

The absolute envelope  $\mathcal{H}_{\text{abs}}(f)$  will now be normalized for the further analysis with respect to the average electrical power per hertz  $P_{\text{PD,Hz}}$  emitted by the photodiode. The PSD is meant to provide an impression of the different shapes of the spectral envelope while absolute levels are of no importance during this examination. The normalization removes additionally all constant loss and efficiency terms contained in the average input power, which are virtually neglected for now. The shape of the PSD is anyway not influenced by these parameters and a quantitative analysis can still be immediately conducted.

$$P_{\text{PD,Hz}} = \frac{V_{\text{PD}}^2}{Z_{50} \cdot 1 \text{ Hz}} \quad (3.35)$$

The frequency  $f$  which is the parameter of the envelope function  $\mathcal{H}_{\text{abs}}(f)$  will be – especially for the plots – normalized to the laser repetition rate according to equation (3.36) such that  $h$  represents the according harmonics of the repetition rate.

$$h = \frac{f}{f_{\text{rep}}} \quad (3.36)$$



Substituting the frequency  $f$  and normalizing the absolute envelope  $\mathcal{H}_{\text{abs}}(f)$  of the PSD with the average electrical power per hertz  $P_{\text{PD,HZ}}$  reveals the normalized envelope  $\mathcal{H}(h)$ .

$$\mathcal{H}(h) = \left| r_1 + r_2 e^{-j2\pi h f_{\text{rep}} T_1} + r_3 e^{-j2\pi h f_{\text{rep}} T_2} + r_4 e^{-j2\pi h f_{\text{rep}} (T_1 + T_2)} \right|^2 \quad (3.37)$$

The analysis can now be started and one has to choose values for all undefined variables in the normalized envelope equation  $\mathcal{H}(h)$ . The delays  $T_1$  and  $T_2$  in the phase terms are replaced with their nominal values determined according to the RF frequency and laser repetition rate in equation (3.2). An additional offset term is added in equation (3.38), which can be used later to simulate small deviations from the *nominal working point*. For the first analysis the offset terms  $\Delta T_1$  and  $\Delta T_2$  in

$$T_1 = \frac{1}{4} \frac{1}{f_{\text{rep}}} + \Delta T_1 \quad \text{and} \quad T_2 = \frac{1}{2} \frac{1}{f_{\text{rep}}} + \Delta T_2 \quad (3.38)$$

are assumed to be zero, leaving only the nominal delay.

Following the conditions at FLASH and the European XFEL the RF frequency  $f_{\text{RF}}$  corresponds to six times the laser repetition rate  $f_{\text{rep}}$ . The phase error  $\Delta\varphi_{\text{RF}}$  has to be specified in radians and it is also initially assumed to be zero. The MZM transmission coefficients  $r_{\text{MZM},1}$  and  $r_{\text{MZM},2}$  contain according to equations (3.20) and (3.21) several undefined variables themselves. The bias voltage error  $\Delta V_b$  is initially assumed to be zero and will later be specified as a fraction of the  $\pi$  modulation voltage  $V_\pi$ , such that  $V_\pi$  always cancels out. A similar procedure has to be applied to the RF peak voltage  $\hat{V}_{\text{RF}}$  which is for the investigation of the envelope set to a value of  $1/2 V_\pi$  such that  $V_\pi$  cancels here out as well. This value allows full modulation of the MZM transmission by the RF signal. Finally, the last unspecified parameter is the splitting ratio error  $\Delta r_s$ , which is also initially assumed to be zero. The parameters previously described represent together the *nominal working point*.

The normalized envelope function  $\mathcal{H}(h)$  in the *nominal working point* can now be immediately calculated. If all  $\Delta$  terms are set to zero, all scaling terms evaluate to one quarter.

$$r_1 = r_2 = r_3 = r_4 = 1/4 \quad (3.39)$$

Using these scaling factors and the delays  $T_1$  and  $T_2$  from equation (3.38) one obtains the *nominal working point* in equation (3.40). The squared norm is calculated by multiplying the argument with its complex conjugate leading to equation (3.41). After some rearrangements

using different trigonometric identities the simplified equation representing the normalized envelope in the *nominal working point* is presented in equation (3.46).

$$\mathcal{H}(h) \Big|_{\text{working point}} = \left| \frac{1}{4} + \frac{1}{4}e^{-j\frac{h\pi}{2}} + \frac{1}{4}e^{-jh\pi} + \frac{1}{4}e^{-j\frac{3h\pi}{2}} \right|^2 \quad (3.40)$$

$$= \frac{1}{16} \left[ 1 + e^{-j\frac{h\pi}{2}} + e^{-jh\pi} + e^{-j\frac{3h\pi}{2}} \right] \left[ 1 + e^{j\frac{h\pi}{2}} + e^{jh\pi} + e^{j\frac{3h\pi}{2}} \right] \quad (3.41)$$

$$= \frac{1}{16} \left[ 4 + 3 \left( e^{j\frac{h\pi}{2}} + e^{-j\frac{h\pi}{2}} \right) + 2 \left( e^{jh\pi} + e^{-jh\pi} \right) + \left( e^{j\frac{3h\pi}{2}} + e^{-j\frac{3h\pi}{2}} \right) \right] \quad (3.42)$$

$$= \frac{1}{4} \left[ 1 + \frac{3}{2} \cos\left(\frac{h\pi}{2}\right) + \cos(h\pi) + \frac{1}{2} \cos\left(\frac{3h\pi}{2}\right) \right] \quad (3.43)$$

$$= \frac{1}{4} \left[ \frac{1}{2} + \frac{1}{2} \cos\left(\frac{h\pi}{2}\right) + 2 \frac{1}{2} \left( \cos(h\pi) + \cos\left(\frac{h\pi}{2}\right) \right) + \frac{1}{2} + \frac{1}{2} \cos\left(\frac{3h\pi}{2}\right) \right] \quad (3.44)$$

$$= \frac{1}{4} \left[ \cos\left(\frac{h\pi}{4}\right)^2 + 2 \cos\left(\frac{h\pi}{4}\right) \cos\left(\frac{3h\pi}{4}\right) + \cos\left(\frac{3h\pi}{4}\right)^2 \right] \quad (3.45)$$

$$= \frac{1}{4} \left[ \cos\left(\frac{h\pi}{4}\right) + \cos\left(\frac{3h\pi}{4}\right) \right]^2 \quad (3.46)$$

The PSD however undergoes characteristic changes if individual error terms do not vanish as previously assumed. Therefore these error terms are now individually investigated and plotted in figure 3.2. The actual graphical analysis is performed in decibels by plotting ten times the logarithm to base ten of the normalized PSD. This procedure requires the normalization to a reference value and the average input power per hertz is supposed to be taken as this reference by using the already normalized envelope  $\mathcal{H}(h)$  for the conversion to dB, leading to  $\mathcal{H}_{\text{dB}}(h)$ .

$$\mathcal{H}_{\text{dB}}(h) = 10 \log_{10}(\mathcal{H}(h)) \quad (3.47)$$

The normalized PSD and the normalized envelope, both in the *nominal working point* (see equation (3.46)), are plotted in figure 3.2 (a). Although the PSD is only defined for integer harmonics of the repetition rate due to the discrete nature of the DIRAC comb in the equation of the PSD, the idea behind the envelope is to investigate it for a continuous  $h$  in order to achieve a better visualization.

All quantities specified as  $\Delta$  values can possibly deviate from zero in a real setup. Some of the values represent measurands, while others are error sources and thereby disturb the operation of the L2RF phase detector. The quantities can be used to simulate in which way small offsets influence the output signal of the whole L2RF setup. This influence is therefore successively analyzed.

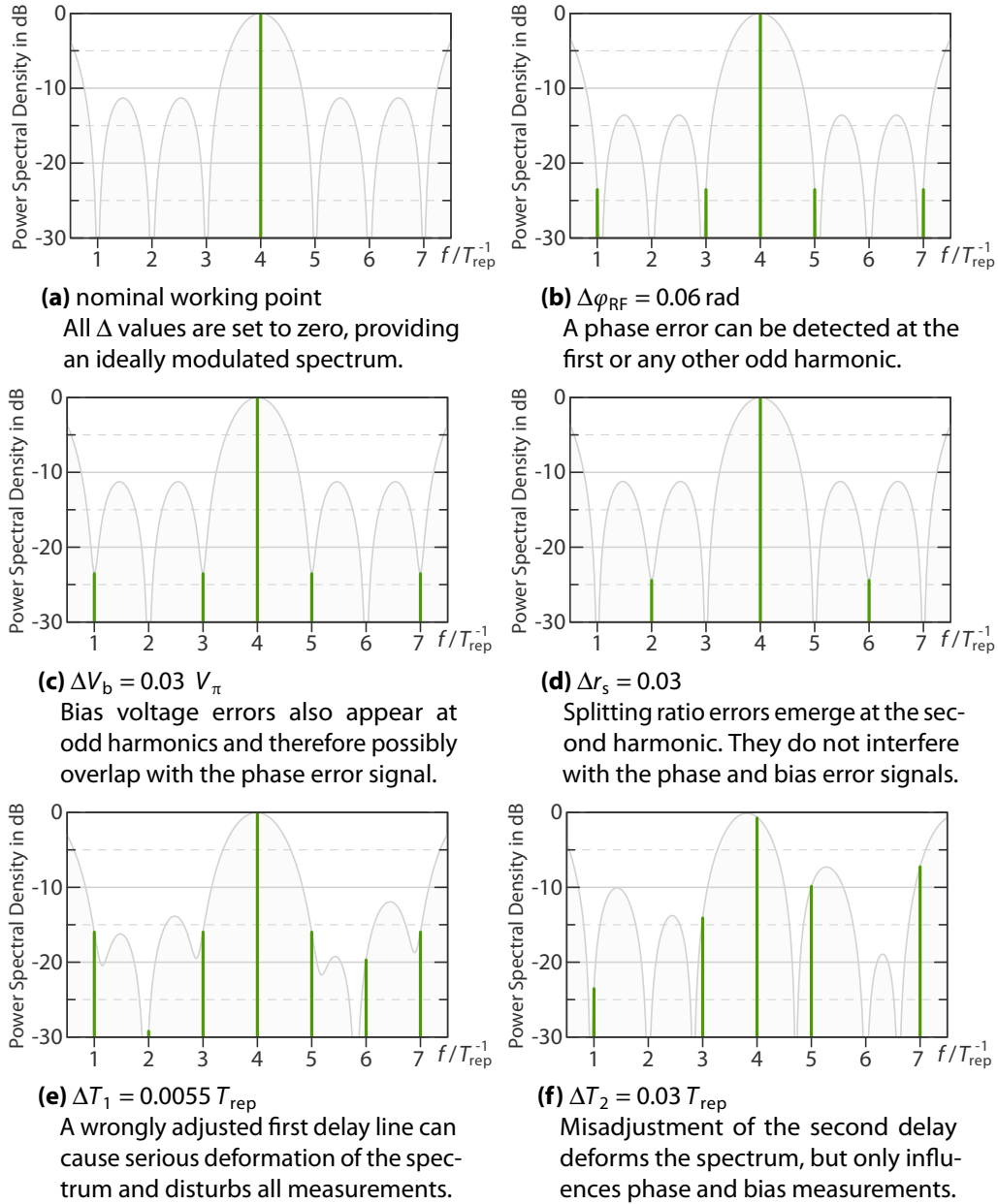


**Figure 3.2: L2RF Output Power Spectral Density Under Different Error Conditions** | The output power spectral density (PSD) of the L2RF phase detector changes significantly under different error conditions. The most common error conditions are depicted together with a spectrum in the nominal working point. The envelope curves (gray) are for visualization only. Practically only the harmonics of the laser repetition rate (green) are available at the setup.

The phase error  $\Delta\varphi_{\text{RF}}$  is the most important parameter because it is the designated output signal of the phase detector. The spectrum is supposed to change in response to phase errors, in order to be able to measure the extent of the phase offset. In the spectrum this error signal shows up at the first harmonic combined with the bias voltage mismatch signal. Both signals have to be told apart in a phase sensitive amplitude measurement as demanded in the previous chapter. The mathematical derivation, describing the PSD under this condition can be found in equation (3.48) and is visualized in figure 3.2 (b). The phase error causes the minima at the odd harmonics to change in frequency. The minima loose their alignment with the comb lines and the reemerging line at the first harmonic is clearly visible. The second harmonic, where the splitting ratio error measurement takes place is not affected. Effectively, the associated envelope has fixed points for specific harmonics which in this case originate from the first cosine term in the equation.

$$\mathcal{H}_{\varphi_{\text{RF}}}(h) = \cos\left(\frac{h\pi}{4}\right)^2 \left[ \left(1 - \cos\left(\frac{h\pi}{2}\right)\right) \left(1 - \sin\left(\frac{\pi}{2} \sin(\Delta\varphi_{\text{RF}})\right)\right) - 1 \right]^2 \quad (3.48)$$

In equation (3.49) the influence of a bias voltage mismatch  $\Delta V_b$  is presented. The same cosine term in the equation leads to the same fixed points like in the previous case. The bias voltage mismatch is also supposed to be detected at the first harmonic of the repetition rate in the spectrum. The same minima as in the previous figure are affected by this error condition, while this time these minima are not frequency shifted but show a lower modulation depth caused by the now unbalanced MZM outputs. This case is depicted in figure 3.2 (c). As predicted no influence on the second harmonic is visible. One can conclude that the phase error and bias voltage error channels are well separated from the splitting ratio error detection, if no additional errors are present in each case.

$$\mathcal{H}_{V_b}(h) = \frac{1}{8} \cos\left(\frac{h\pi}{4}\right)^2 \left[ (2 \cos(h\pi) - 2) \left(1 + \cos\left(2\pi \frac{\Delta V_b}{V_\pi}\right)\right) + 8 \right] \quad (3.49)$$

The influence of the splitting ratio mismatch  $\Delta r_s$  can be found in equation (3.50) and figure 3.2 (d). This quantity is actually meant to be measured at the second harmonic in the spectrum and should possibly not interfere with the first harmonic, where the other measurements take place. The plot confirms both assumptions. This time the minima at the second and sixth harmonic are clearly elevated while the other properties of the spectrum are not altered. Specifically, all odd harmonics are not affected by splitting ratio errors because – again – the leading cosine term assures that the whole function evaluates to zero for these harmonics.

$$\mathcal{H}_{r_s}(h) = \frac{1}{2} \cos\left(\frac{h\pi}{2}\right)^2 \left[ \left(\cos\left(\frac{h\pi}{2}\right) - 1\right) (1 - 4\Delta r_s^2) + 2 \right] \quad (3.50)$$

The delay  $T_1$  is no quantity to be measured but a pure error source. Compared to the previous derivations, equation (3.51) is complex because the delay error  $\Delta T_1$  not only shows up in the phase terms of the complex scaling factors, but also inside of the MZM response. The corresponding envelope curve and spectrum are plotted in figure 3.2 (e). All spectral lines depicted are modulated up to different magnitudes including the second harmonic which is barely visible but also elevated. The delay  $T_1$  has a combined effect on the spectrum. In the present case the minima at odd harmonics are elevated again, but additionally all minima of the envelope are shifted in frequency, causing the irregular modulation pattern presented. There is no global cosine term present in the equation, such that no fixed point can be found.

$$\begin{aligned} \mathcal{H}_{T_1}(h) = & \frac{1}{2} + \frac{1}{2} \cos\left(\frac{h\pi}{2}\right)^2 \cos\left(h\left(\frac{\pi}{2} + \omega_{\text{rep}} \Delta T_1\right)\right) \\ & + \frac{1}{16} (\cos(h\pi) - 1) (\cos(\pi \sin(\omega_{\text{RF}} \Delta T_1)) + 3) \\ & + \frac{1}{4} \sin(h\pi) \sin\left(h\left(\frac{\pi}{2} + \omega_{\text{rep}} \Delta T_1\right)\right) \sin\left(\frac{\pi}{2} \sin(\omega_{\text{RF}} \Delta T_1)\right) \end{aligned} \quad (3.51)$$

The influence of the second delay error  $\Delta T_2$  condenses in a shorter formula, but still presents a pure error source and not a valuable measurement to the setup. The envelope is defined in equation (3.52), while the effect of this potential error source is depicted in figure 3.2 (f). Again the modulation pattern is highly irregular and affects all graphed harmonics except for the second and sixth, of which the modulation is only caused by  $\Delta T_1$  and therefore stable with respect to  $\Delta T_2$ . The fixed points are confirmed by the equation.

$$\mathcal{H}_{T_2}(h) = \cos\left(\frac{h\pi}{4}\right)^2 \cos\left(\frac{h}{2} (\pi + \omega_{\text{rep}} \Delta T_2)\right)^2 \quad (3.52)$$

The previous analysis demonstrated that all three measurement channels are well separated with respect to the harmonic they show up. The phase separation between the bias and phase measurement was not discussed yet, because this property is not covered by the PSD. The error term  $\Delta T_1$  has an influence on both measurement signals and the whole frequency comb changed while this parameter was modified. The second delay error  $\Delta T_2$  however has no influence on the splitting ratio error measurement at the second harmonic, although the first harmonic is affected by this quantity. The analysis does not cover potential crosstalk between the channels caused by possible delay errors or errors of the later introduced LO phase. A different approach is needed to see the influence of these error terms on the measurement channels. The individual output equations for the three measurement channels will therefore be derived in the next section.

### 3.7 Fourier Transform of the Photodiode Signals

The analysis of the PSD of the photodiode signals  $v_{PD}(t)$  does not reveal all required signal properties although it provides important information on the general behavior of the L2RF phase detector. The phase of the created signals is for instance not covered by this analysis even though the signal phase is finally needed to particularly distinguish between the bias and phase error signals which emerge at the same frequency in the L2RF output spectrum. The next step is therefore to go back to equation (3.30) where the photodiode signals have been defined and to FOURIER transform them directly to the frequency domain.

When the L2RF phase detector is read out, effectively the desired frequencies are picked from the spectrum for analysis with the help of appropriate RF band-pass filters. Mathematically this process can be described by convolving the photodiode response with the complex transfer function of the RF band-pass filter. This procedure is carried out much easier in frequency domain so again the FOURIER transform of the signals is helpful.

In fact, the four optical pulse trains in the L2RF setup are already overlapped at the photodiode. The *principle of linearity* as a basic property of the FOURIER transform (see equation (C.5)) and the concept of superposition however permit to analyze each of these pulse trains independently and to combine the individual signals at the very end of the analysis. This includes the filtering and the subsequently performed RF mixing explained in the next two sections.

Meanwhile, the frequency domain representation  $v_{Hz}(f)$  of the photodiode signals from equation (3.30) is presented in equations (3.53). The parameters are already well known from the previous equations. Equations (3.53) contain the splitting ratio error  $\Delta r_s$ , the delays  $T_1$  and  $T_2$  and the repetition rate  $f_{rep}$ . The mean photodiode voltage  $V_{PD}$  has been defined in equation (3.31), while the modulation factors  $r_{MZM,1}$  and  $r_{MZM,2}$  have been introduced in equations (3.20) and (3.21). The scaling factors  $r_1$  to  $r_4$  have been presented in equation (3.33). The FOURIER transform was found by applying its *time shifting property* (see equation (C.4)).

$$\begin{aligned} v_{Hz,1}(f) &= r_1 V_{PD} \text{III}_{f_{rep}}(f) \\ v_{Hz,2}(f) &= r_2 V_{PD} e^{-j2\pi f T_1} \text{III}_{f_{rep}}(f) \\ v_{Hz,3}(f) &= r_3 V_{PD} e^{-j2\pi f T_2} \text{III}_{f_{rep}}(f) \\ v_{Hz,4}(f) &= r_4 V_{PD} e^{-j2\pi f (T_1+T_2)} \text{III}_{f_{rep}}(f) \end{aligned} \quad (3.53)$$

$$V_{PD} = Z_{50} R_{PD} P_{in}^* a_{MZM} \eta_m \eta_d \quad (3.54)$$

The next step after having successfully transformed the output signals to the frequency domain is the simulation of the RF filtering process and thus the extraction of the frequency components which are carrying the desired output signals of the L2RF phase detector.

### 3.8 Extraction of a Single Frequency Component from the Spectrum

The electrical signals emitted by the photodiode have already been described in equation (3.30) and transferred to the frequency domain spectrum in equation (3.53). Within the final L2RF setup it is indeed not the complete spectrum which is monitored, but only specific frequencies from the spectrum represented by lines from the frequency comb. The signal amplitude of this frequency component, which is modulated proportionally to the measured quantity, is actually detected.

If the bandwidth of the band-pass filter is sufficiently narrow and the center frequency  $f_c$  corresponds to the frequency of interest, effectively just one line from the spectrum is picked. The neighboring comb lines in the spectrum are in this case in the stop-band of the filter and ideally they are suppressed completely while the single comb line picked out by the filter is only attenuated by the pass band insertion loss of the filter.

The process of band-pass filtering the photodiode signal is simulated by selecting the desired comb line from the spectrum before applying the inverse FOURIER transform and additionally introducing a scaling factor  $g_{bp}$  representing the pass band insertion loss.

The FOURIER transformed signals represent a double-sided spectrum. To be consistent with the inverse FOURIER transform it is mandatory to select a symmetric pair of frequencies ( $\pm f$ ) from the spectrum. The selection is performed by restricting the infinite sum of DIRAC delta pulses to the harmonic  $h$  and its negative counterpart  $-h$  of the repetition rate  $f_{rep}$ .

The inverse FOURIER transform back to the time domain can be subsequently performed according to equation (C.3). The process of inverse FOURIER transforming a frequency pair from a general DIRAC comb instead of the complete comb is identical for all four photodiode signals. The transform will therefore be presented here on the example of a sample DIRAC comb, such that the resulting equation can later be applied to the actual signals from equation (3.53). The obtained time domain signal  $v_{bp}(t)$  can be regarded as the band-pass filtered representation of the input signal. The insertion loss  $g_{bp}$  of the band-pass filter is usually known in dB and thus has to be converted to a scaling factor  $a_{bp}$  following equation (3.55).

$$a_{bp} = 10^{\frac{g_{bp}}{20}} \quad [g_{bp}] = \text{dB} \quad (3.55)$$

The real scaling factor  $a_{bp}$  and the photodiode voltage  $V_{PD}$  can be pulled out of the FOURIER transform from equation (3.56), because they are constant with respect to the frequency  $f$ . Due to the *sifting property* of the DIRAC delta function, the natural exponential term in equation (3.57) is picked at exactly  $bf_{rep}$ . After evaluating the sum in equation (3.58), the equation is expanded by the harmonics  $\pm h$ . The sum of two natural exponentials

in equation (3.59) represents two complex phasors, rotating in opposite directions and forming together in equation (3.60) a real oscillation of the frequency  $hf_{\text{rep}}$ , shifted by the delay  $T_0$  and scaled by the factor of  $2a_{\text{bp}}V_{\text{PD}}$  in the time domain.

$$v_{\text{bp}}(t) = \mathcal{F} \left\{ a_{\text{bp}} V_{\text{PD}} e^{-j2\pi f T_0} \sum_{b=\pm h} \delta(f - bf_{\text{rep}}) \right\} (t) \quad (3.56)$$

$$= a_{\text{bp}} V_{\text{PD}} \sum_{b=\pm h} \int_{-\infty}^{\infty} \delta(f - bf_{\text{rep}}) e^{j2\pi f(t-T_0)} df \quad (3.57)$$

$$= a_{\text{bp}} V_{\text{PD}} \sum_{b=\pm h} e^{j2\pi b f_{\text{rep}}(t-T_0)} \quad (3.58)$$

$$= a_{\text{bp}} V_{\text{PD}} \left[ e^{j2\pi h f_{\text{rep}}(t-T_0)} + e^{-j2\pi h f_{\text{rep}}(t-T_0)} \right] \quad (3.59)$$

$$= 2a_{\text{bp}} V_{\text{PD}} \cos(2\pi h f_{\text{rep}}(t - T_0)) \quad (3.60)$$

By selecting in this way a single harmonic from the DIRAC comb the band-pass filter is limited to a single DIRAC delta function at the center frequency  $f_c$  of the band-pass filter, implying that the bandwidth of this filter is narrow enough to do so. The inverse FOURIER transform returns the amplitude of the selected frequency component. This signal turns naturally out to have the form of a harmonic oscillation in the time domain. The idealized band-pass filtering as described above can be performed independently on the four pulse trains emitted by the photodiode using the *principle of linearity* (see equation (C.5)). The resulting equations finally lead to the time domain band-pass filtered voltage signals  $v_{\text{bp}}(t)$  created by each of the modulated pulse trains at a certain harmonic  $h$  of the laser repetition rate.

$$\begin{aligned} v_{\text{bp},1}(t) &= r_1 a_{\text{bp}} 2 V_{\text{PD}} \cos(2\pi h f_{\text{rep}} t) \\ v_{\text{bp},2}(t) &= r_2 a_{\text{bp}} 2 V_{\text{PD}} \cos(2\pi h f_{\text{rep}} (t - T_1)) \\ v_{\text{bp},3}(t) &= r_3 a_{\text{bp}} 2 V_{\text{PD}} \cos(2\pi h f_{\text{rep}} (t - T_2)) \\ v_{\text{bp},4}(t) &= r_4 a_{\text{bp}} 2 V_{\text{PD}} \cos(2\pi h f_{\text{rep}} (t - T_1 - T_2)) \end{aligned} \quad (3.61)$$

The sum of these signals represents the band-pass filtered photodiode output. The observed harmonic is denoted with the parameter  $h$ . All previously discussed  $\Delta$  parameters are contained within the above equations, but the kind of their influence on individual output signals is not obviously visible.

It was already discussed that a simple amplitude or power measurement of the output signal of the band-pass filter is not sufficient in order to unambiguously detect the desired error signals. Instead a phase sensitive amplitude measurement with RF mixers is used, where



the signals are mixed down to baseband for analysis. There are further options to perform this detection which are discussed in chapter 6. The mixing is the last step before the signals are superposed in the mathematical model and the final combined output signals are assembled for analysis. The following section focuses on the mixing process and the derivation of the output signals.

### 3.9 Phase Sensitive Amplitude Detection Principle

In the working point of the L2RF phase detector – and if no error signal is present – no signal is visible at the modulation frequencies. The corresponding lines in the spectrum are not present. Observing for example the bias voltage error signal, a perfectly adjusted bias voltage causes no amplitude modulation at the associated modulation frequency. A wrongly adjusted bias voltage however leads to an increased amplitude of the signal measured at the modulation frequency. Unfortunately, a simple amplitude or power measurement is not sufficient to unambiguously detect this signal, because the amplitude at the measured frequency rises for both, the under biased and the over biased case. The phase of the bias error signal however flips by  $\pi$  when the bias is tuned through the working point. The same is the case for the phase error signal and the splitting ratio error signal.

An example for this principle is depicted in figure 3.3, where the RF phase is shifted by  $\Delta\varphi_{\text{RF}}$  in subfigure (a) and by  $-\Delta\varphi_{\text{RF}}$  in subfigure (b). No difference is visible in the spectrum, although the phase of the amplitude modulation obviously differs by  $\pi$ . Therefore, only a

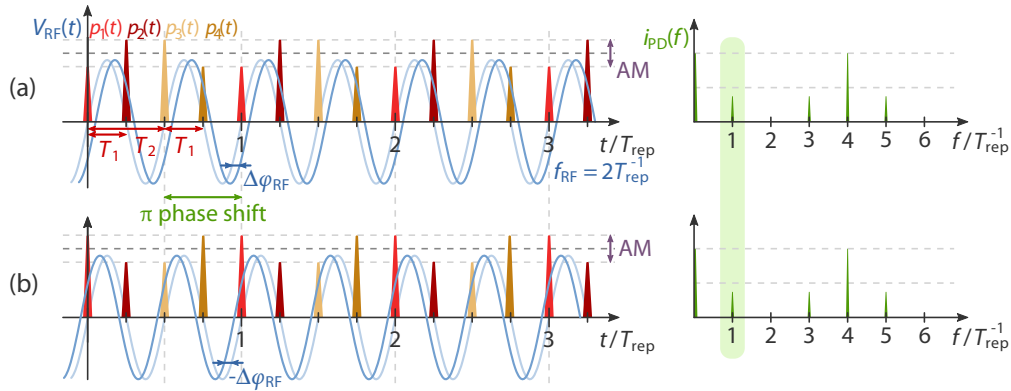


**Figure 3.3: L2RF Output Phase for Operation on Different Sides of the Working Point** | Positive and negative drifts of the RF phase away from the working point cause an amplitude modulation at the same frequency but with a  $\pi$  phase shift. The phase of the error signal flips when the error is tuned through the working point. The illustration applies to all three measured error signals.

phase sensitive detector can unambiguously detect the signal in question. RF mixers are perfectly suited for this task. Practically, the error signal at the modulation frequency  $f_{\text{mod}}$  has to be mixed with a LO signal of the same frequency while the relative phase between the two signals at the mixer  $\varphi_{\text{mix}}$  needs to be adjusted to zero or any multiple of  $\pi$ . Under these conditions the mixer works exactly as a phase sensitive amplitude detector. In the working point the cosine in the mixer term is insensitive to small variations of the LO phase while a phase flip of the error signal flips the sign of the cosine as expected.

The RF mixer ideally delivers two output signals, one at the sum of the input frequencies and one at the difference of these frequencies. The difference frequency shows up as a DC voltage because the input and the LO frequency are required to be equal. The sum frequency is filtered from the output signal with a low-pass filter. The insertion loss of the low-pass filter is neglected because it is close to zero for DC signals. A detailed explanation of the working principle of RF mixers can be found in appendix B. Transferred from there the mixer output voltage in the above defined operating mode follows the simplified formula stated in equation (3.62). In this equation,  $a_{\text{mix}}$  stands for the conversion gain  $g_c$  of the mixer, converted to a voltage gain as shown in equation (3.63).  $\hat{V}_{\text{in}}$  names the peak voltage of the input signal at the mixer which is the band-pass filtered error signal detected by the photodiode in the L2RF phase detector. The phase  $\varphi_{\text{in}}$  denotes the phase of the error signal and  $\varphi_{\text{LO}}$  the phase of the LO signal. The equation takes the newly introduced LO phase error  $\Delta\varphi_{\text{LO}}$  into account.

$$V_{\text{mix}} = a_{\text{mix}} \hat{V}_{\text{in}} \cos(\varphi_{\text{in}} - (\varphi_{\text{LO}} + \Delta\varphi_{\text{LO}})) \quad (3.62)$$

$$a_{\text{mix}} = 10^{\frac{g_c}{20}} \quad [g_c] = \text{dB} \quad (3.63)$$

All error signals – including the phase error signal – are imprinted solely on the amplitude of the pulse train. The phase of the error signals depends only on the timing of the laser pulse trains and not on the actually measured phase error. Therefore it is easily possible to provide an LO signal that is phase stable with respect to the error signal in order to allow a reliable operation of the mixer. This overall detection principle is frequently referred to as synchronous detection scheme.

It should be recalled that two error signals are encoded at the same modulation frequency just with a phase shift of  $\pi/2$  when a dual output MZM is used in the L2RF setup. Keeping the above proposal for a detector in mind it becomes immediately evident that the detection principle is not disturbed by this circumstance. In this case the additional error signal has a  $\pi/2$  phase relation to the LO signal at the first RF mixer and can thus not contribute to the first output signal. Hence, to detect the second error signal, it is simply possible to build a second detector at the same frequency, but operated with a LO signal, shifted by  $\pi/2$  with respect to the LO signal at the first mixer. Each detector senses one error signal, while being insensitive to the second one and the mixers are operated orthogonal.

The LO signal can be extracted from an unmodulated laser pulse train originating from the L2RF setup by RF filtering. This procedure has the huge advantage that the modulation frequency and the LO frequency are intrinsically identical because they are generated from the same pulse trains. Additionally, phase drifts of the LO signal are limited, because the signals are generated locally and the transmission within the L2RF setup to the RF mixer can be kept short.

In order to improve the signal gain and to boost the filtered photodiode signal, an additional RF amplifier can be used to amplify the signal between the band-pass filter and the RF mixer. The gain  $g_{\text{RF}}$  of this RF amplifier has to be accounted for in the calculations. The L2RF setup is meant to be operated around its working point, in which the monitored frequency components are vanished or at least very small. This fact allows to use high gain amplifiers without risking to drive them into saturation. The overall sensitivity from the setup can thus be increased without leaving the linear regime of the amplifier. The amplifier gain has to be converted to a voltage gain  $a_{\text{RF}}$  in order to fit into the equations, following

$$a_{\text{RF}} = 10^{\frac{g_{\text{RF}}}{20}}, \quad [g_{\text{RF}}] = \text{dB}. \quad (3.64)$$

The output signal from the mixer is finally amplified in a DC low-noise amplifier with a gain of  $a_{\text{LNA}}$ .

As the combined equation of all four signals would lead to a very complicated combined mixer term, the signals generated by the four individual pulse trains are treated independently and the superposition is finally performed after the mixing process. Combining all the statements outlined above, one can formulate the general L2RF output signal  $\mathcal{V}_h$ . The individual components  $\hat{\mathcal{V}}_1$  to  $\hat{\mathcal{V}}_4$  and  $\varphi_{h,1}$  to  $\varphi_{h,4}$  defined in equations (3.65) and (3.66) are formulated, using the band-pass filtered voltage signals from equation (3.61). The scaling parameters  $r_1$  to  $r_4$  of the individual pulse trains have been defined in equation (3.33).

$$\hat{\mathcal{V}}_w = r_w \hat{\mathcal{V}} \quad \{w \in \mathbb{N}^* \mid w \leq 4\} \quad (3.65)$$

$$\begin{aligned} \varphi_{h,1} &= 0 & \varphi_{h,2} &= 2\pi h f_{\text{rep}} T_1 \\ \varphi_{h,3} &= 2\pi h f_{\text{rep}} T_2 & \varphi_{h,4} &= 2\pi h f_{\text{rep}} (T_1 + T_2) \end{aligned} \quad (3.66)$$

The peak output voltage  $\hat{\mathcal{V}}$  in equation (3.67) is common for all four signals and can be regarded as an extension of the photodiode voltage  $V_{\text{PD}}$ , taking into account the newly introduced scaling parameters  $a_{\text{mix}}$ ,  $a_{\text{bp}}$ ,  $a_{\text{RF}}$  and  $a_{\text{LNA}}$  and the factor of two from the inverse FOURIER transform of a frequency pair during the modeling of the RF filtering process.

$$\hat{\mathcal{V}} = 2Z_{50} R_{\text{PD}} P_{\text{in}}^* a_{\text{MZM}} a_{\text{mix}} a_{\text{RF}} a_{\text{bp}} a_{\text{LNA}} \eta_{\text{m}} \eta_{\text{d}} \quad (3.67)$$

The harmonic  $h$  has to be selected according to the frequency of interest in order to investigate the desired output channel. Furthermore, the LO phase  $\varphi_{\text{LO}}$  has to be correctly adjusted in order to finally detect the signal of interest. Equation (3.68) shows the output equation  $\mathcal{V}_h$  for a signal detected by the L2RF phase detector obtained by the final superposition of the individual output signals with the parameters from equations (3.65) to (3.67).

$$\mathcal{V}_h = \sum_{w=1}^4 \hat{\mathcal{V}}_w \cos(\varphi_{h,w} - (\varphi_{\text{LO}} + \Delta\varphi_{\text{LO}})) \quad (3.68)$$

There is no time dependency in the final output signal in equation (3.68) because the input signals of the mixer are mixed down to baseband. This is only true for the static case, where all frequencies are constant and fulfill the ratios, proclaimed throughout this chapter. The output signal is especially not constant over time, if RF frequency and laser repetition rate are not synchronized. In this case a beat-note of the frequency difference is visible at the output of the phase detector although this case is not covered by the simplified mixer equation and therefore not reproduced here.

Finally, the phase term in the mixer equation has to be regarded. In order to detect one of the output signals the relative LO phase is supposed to be zero or  $\pi$  with respect to the combined signal, such that the mixer works as amplitude detector with the largest possible sensitivity. Additionally, in this state the mixer is insensitive to LO phase drifts up to a certain extent because it is operated in the minimum or maximum of its cosine shaped characteristic. The LO phase error  $\Delta\varphi_{\text{LO}}$  can be used to analyze small drifts of the LO phase from the nominal value.

### 3.10 Definition of the Measurement Channels

The phase of the first output pulse train  $p_1(t)$  has been the phase reference for the remaining – time shifted – laser pulse trains up to now. This pulse train now also serves as phase reference for the LO signal. For the frequency ratios present at FLASH and the European XFEL and the implementation of the L2RF phase detector there, the bias voltage error  $\Delta V_b$  and the phase error  $\Delta\varphi_{\text{RF}}$  both cause a modulation of the first harmonic of the laser repetition rate in the spectrum. While for the detection of the phase error a LO phase  $\varphi_{\text{LO}}$  of  $-\pi/4$  is needed, the bias voltage error has to be detected at the same frequency with a LO phase of  $\pi/4$ . Both signals are separated by a phase shift of  $\pi/2$  as previously proclaimed.

The parameters for the three measurement channels under the FLASH and European XFEL conditions are summarized in equations (3.69) to (3.71) where  $h$  denotes the harmonic

at which the measurement has to be performed and  $\varphi$  represents the LO angle needed to detect the signal.

$$h_{\varphi_{\text{RF}}} = 1 \quad \varphi_{\text{LO}, \varphi_{\text{RF}}} = -\pi/4 \quad (3.69)$$

$$h_{V_b} = 1 \quad \varphi_{\text{LO}, V_b} = \pi/4 \quad (3.70)$$

$$h_{r_s} = 2 \quad \varphi_{\text{LO}, r_s} = 0 \quad (3.71)$$

The error detection phases can be derived from equation (3.66) by considering in which way the signals for different error conditions are created. The careful observation of figures 2.10 and 3.3 also gave a first lead on the actual phase relations of the signals. There is however a far more comprehensive presentation of the signals possible by plotting the four phasors associated with the four individual pulse trains. The amplitudes  $\hat{V}_1$  to  $\hat{V}_4$  and the signal phases  $\varphi_{h,1}$  to  $\varphi_{h,4}$  needed for this kind of representation can be found in equations (3.65) to (3.67). The LO phase relations for the signal detection become obvious while investigating the phasor diagram at both the first and second harmonic, where together all three error signals can be detected.

The phasor diagrams for the first harmonic of the laser repetition rate are presented in figure 3.4. Subfigure (a) shows – for reference – the case when no error signal is present. Due to the specific phase shifts  $T_1$  and  $T_2$  introduced previously to the pulse trains, it turns out that the phasors depicted for the first harmonic of the repetition rate align with the two axes of the coordinate system while always two of them point into opposite directions. All signals have the same magnitude  $\hat{V}$ , such that their sum – due to their special phase relation – vanishes completely.

The phasor diagram for the measurement of potential phase errors  $\Delta\varphi_{\text{RF}}$  is depicted in subfigure (b). The amplitude modulation in the time domain shows up in this presentation as an unbalance of the phasors leading to a non vanishing sum of the four signals. The phase angle of this resulting signal is evidently  $-\pi/4$  with respect to the first pulse train. The LO phase  $\varphi_{\text{LO}}$  needed to detect this signal has to be identical to the phase of the combined signal.

Figure 3.4(c) depicts the case of bias voltage errors  $\Delta V_b$ . Different pulse trains are now attenuated or amplified such that the sum of all four phasors emerges at a new angle of  $\pi/4$ . As previously predicted, the new error signal is phase shifted with respect to the first one by  $\pi/2$ . The LO phase to detect this signal has to be again identical to the signal phase. A phase sensitive measurement of this error signal is not disturbed by the previously described phase error signal because these signals are orthogonal to each other.

In the case of a splitting ratio error  $\Delta r_s$  at the first delay line, the phasors cancel out at the first harmonic, as depicted in subfigure (d). A detection of this error signal at the first harmonic of the repetition rate is therefore not possible.

The situation at the second harmonic is presented in figure 3.5. As the frequency at which this measurement takes place is doubled, the phase angles resulting from the time domain delays  $T_1$  and  $T_2$  are doubled as well from  $\pi/2$  to  $\pi$ . The phasors for  $\hat{V}_1$  and  $\hat{V}_3$  align therefore both to the positive side of the x-axis, while the signals  $\hat{V}_2$  and  $\hat{V}_4$  show up on the negative side of the x-axis in the phasor diagram. The LO frequency has to be doubled as well in order to be identical with the detected error signal at the second harmonic which also has to be mixed down to baseband.

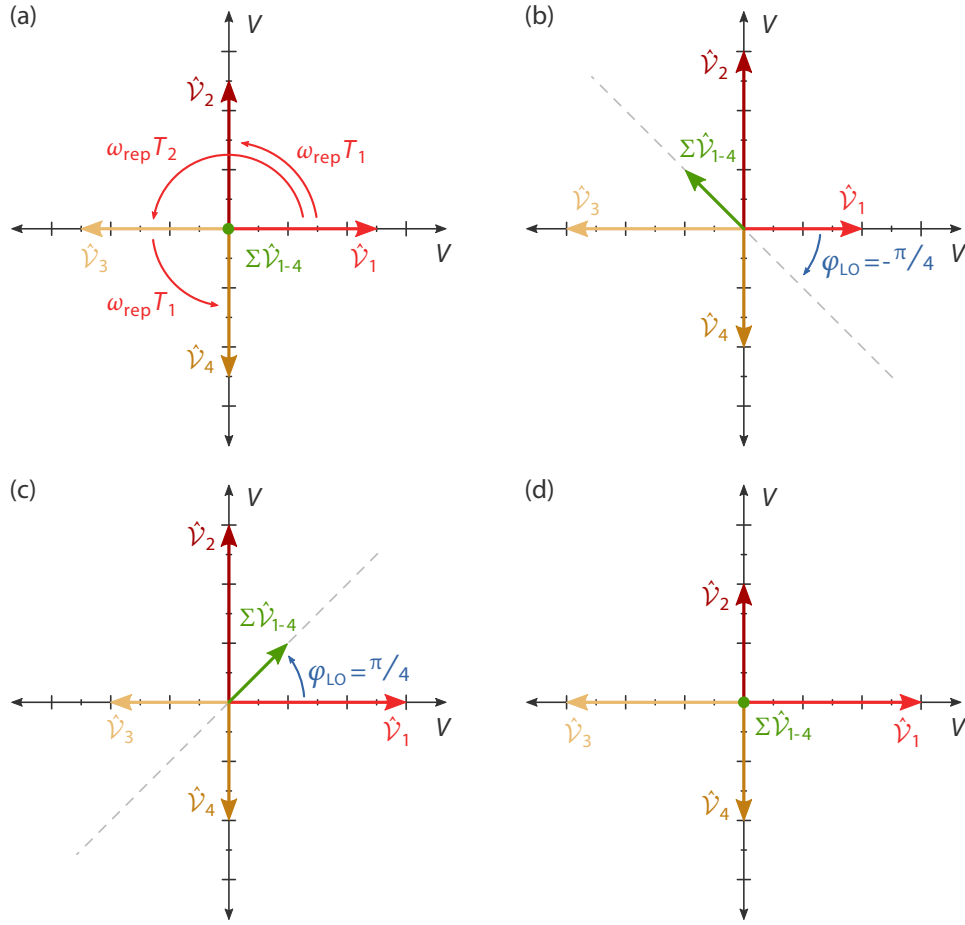


**Figure 3.4: Phasor Representation of the Signal Superposition at the First Harmonic** | The four pulse trains created in the L2RF setup are plotted at their correct phase angle while the dimensions are scaled according to the depicted error condition such that the phase of the created error signal becomes obvious.

(a) nominal working point

(b) phase error  $\Delta\varphi_{\text{RF}}$

(c) bias voltage error  $\Delta V_b$

(d) splitting ratio error  $\Delta r_s$

The unmodulated case is again depicted in subfigure (a), where all phasors have the same amplitude and therefore cancel each other out. For phase and bias voltage error signals depicted in subfigures (b) and (c) the generated phasors also cancel out, which means these error signals have no influence on the second harmonic. The splitting ratio error signal depicted in (d) however creates actually a signal at the second harmonic which has to be detected at an LO phase  $\varphi_{LO}$  of zero.

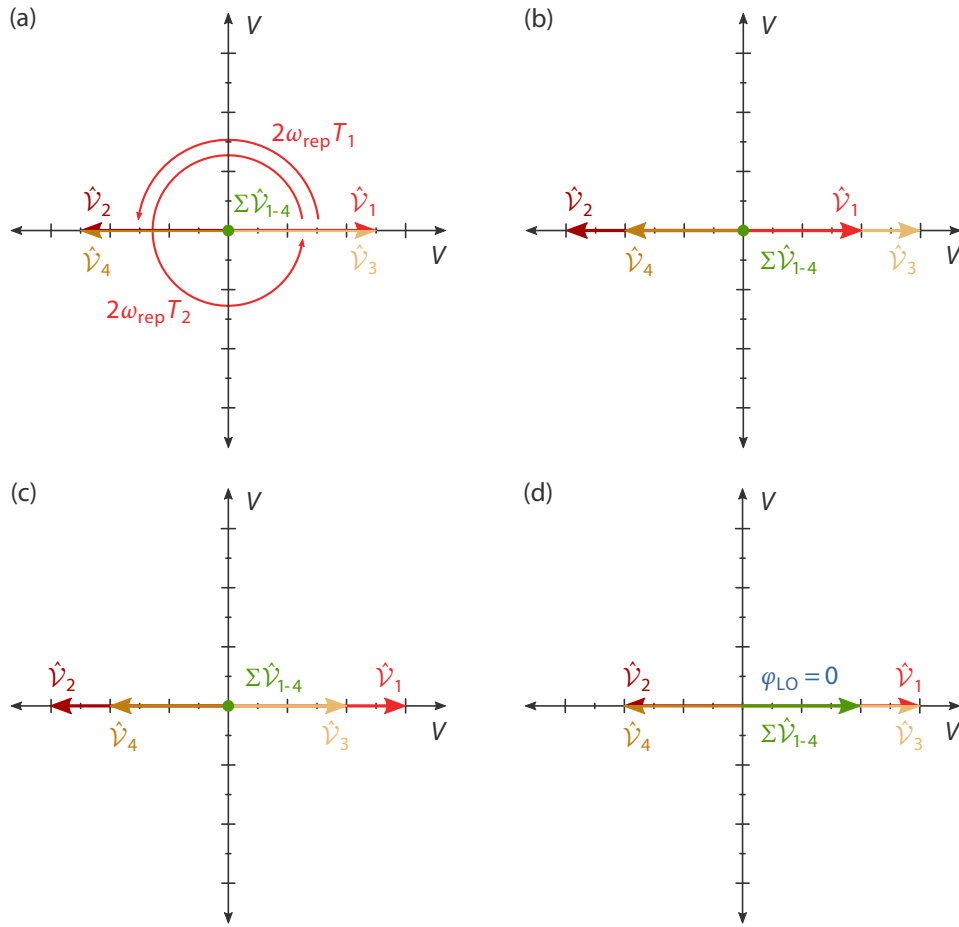


**Figure 3.5: Phasor Representation of the Signal Superposition at the Second Harmonic** | The four pulse trains created in the L2RF setup are plotted at their correct phase angle while the dimensions are scaled according to the depicted error condition such that the phase of the created error signal becomes obvious.

(a) nominal working point

(b) phase error  $\Delta\varphi_{RF}$

(c) bias voltage error  $\Delta V_b$

(d) splitting ratio error  $\Delta r_s$

The three measurement channels for phase errors  $\Delta\varphi_{\text{RF}}$ , bias voltage errors  $\Delta V_{\text{b}}$  and splitting ratio errors  $\Delta r_{\text{s}}$  are separated by either the harmonic they are detected at or by the LO phase, as specified in equations (3.69) to (3.71).

The combined output signal in equation (3.68) contains several terms and cannot be further simplified because the arguments of the contained trigonometric functions cannot be combined. For a first analytic examination one can however omit most of the error terms, which allows to obtain a rather compact result for the different output channels. For the analysis of the output characteristics of the L2RF phase detector in the next section, mainly the general response of the measurement channels and the crosstalk between them will be examined.

### 3.11 Analysis of the General Laser-to-RF Output Equations

As already mentioned, the complexity of the full output equation prevents an immediate analysis. Instead, some assumptions have to be made in order to investigate all three output signals of the L2RF setup and the most interesting error conditions.

Especially the numerous trigonometric functions in the equations are impossible to be simplified because their arguments are mostly unique. These functions will therefore be linearized in selected cases. This procedure is also known as *small angle approximation* [ZHS03]. The trigonometric functions are replaced with the first terms of their TAYLOR series which is a valid assumption for small angles. The sine and cosine functions present in the output equations can be approximated with

$$\sin(x) \approx x \quad \text{and} \quad \cos(x) \approx 1 \quad \{|x| \ll 1\}. \quad (3.72)$$

Some of the values which will be defined in the next paragraphs are familiar, because they have already been used in the previous chapters. However, in order to have a complete set of parameters for the investigation of the output equation presented here those parameters are briefly explained together with the newly introduced ones.

In the special case of the L2RF output equation all  $\Delta$  terms are assumed to be close to zero because they represent small deviations from otherwise already specified values. There are currently six  $\Delta$  terms in the equation where three of them are associated to measurement terms and three of them to error terms. Actual measurement values are represented by the phase error  $\Delta\varphi_{\text{RF}}$ , the bias voltage error  $\Delta V_{\text{b}}$  and the splitting ratio error  $\Delta r_{\text{s}}$ . The nominal values of these quantities are specified with

$$\varphi_{\text{RF}} = 0, \quad V_{\text{b}} = V_{\text{b},0} \quad \text{and} \quad r_{\text{s}} = 1/2. \quad (3.73)$$



Additionally, the output equation contains the LO phase error  $\Delta\varphi_{\text{LO}}$ . The LO phase is adjusted according to the measurement channel investigated. All three measurement signals, defined in equation (3.73) need to be detected at their specific LO phase angle of

$$\varphi_{\text{LO},\varphi_{\text{RF}}} = -\pi/4, \quad \varphi_{\text{LO},V_{\text{b}}} = \pi/4 \quad \text{and} \quad \varphi_{\text{LO},r_{\text{s}}} = 0. \quad (3.74)$$

Finally the two delay errors  $\Delta T_1$  and  $\Delta T_2$  are associated with the following nominal delays, which were determined for the use of a dual output MZM.

$$T_1 = \frac{1}{4} \frac{1}{f_{\text{rep}}} + \Delta T_1 \quad T_2 = \frac{1}{2} \frac{1}{f_{\text{rep}}} + \Delta T_2 \quad (3.75)$$

The RF frequency  $f_{\text{RF}}$  is assumed to amount to six times the laser repetition rate  $f_{\text{RF}}$ , which is the FLASH and European XFEL case. The modulation frequency at which the measurement signals are read out is the first harmonic  $h_1$  of the laser repetition rate  $f_{\text{rep}}$  for the detection of the phase and bias voltage errors  $\Delta\varphi_{\text{RF}}$  and  $\Delta V_{\text{b}}$ , while the splitting ratio error  $\Delta r_{\text{s}}$  is detected at the second harmonic  $h_2$ .

$$f_{\text{RF}} = 6f_{\text{rep}} = 1.3 \text{ GHz} \quad h_n = \{1, 2\} \quad (3.76)$$

Whenever during the following analysis the term *working point* is used, it refers to the case that all six  $\Delta$  values are zero, except for the one representing the currently investigated measurement channel, named by the appropriate subscript.

In order to get an impression of the structure of the equations and the relations between the parameters, the first evaluation will always be simplified by assuming the delay errors vanished. The corresponding output equation will be called  $\mathcal{V}^\dagger$ , where the superscripted dagger is tied to the condition

$$\Delta T_1 = \Delta T_2 = 0. \quad (3.77)$$

The full output equation which is the basis for all following evaluations can be found in equations (3.65) to (3.68).

### 3.11.1 Examination of the Phase Error Channel

The output signal from the phase error channel is detected at  $\varphi_{\text{LO},\varphi_{\text{RF}}}$  and  $h_1$ . The following result is obtained, evaluating the general output equation but omitting the delay errors. The

result in equation (3.78) is much more complicated if delay errors are present, which are therefore omitted for a first analysis. The equation consists otherwise of the  $\Delta$  terms which were explained in the previous section and the peak output voltage  $\hat{\mathcal{V}}$  which is a common factor in all output equations derived for measurements at the first harmonic  $h_1$ .

$$\mathcal{V}_{\varphi_{\text{RF}}}^{\dagger} = \frac{\hat{\mathcal{V}}}{\sqrt{2}} \left[ (2\Delta r_s \cos(\Delta\varphi_{\text{LO}}) + \sin(\Delta\varphi_{\text{LO}})) \sin(\Delta V_b \Theta_{\pi}) \cos(\Theta_{\pi} \hat{V}_{\text{RF}} \sin(\Delta\varphi_{\text{RF}})) \right. \\ \left. - (2\Delta r_s \sin(\Delta\varphi_{\text{LO}}) + \cos(\Delta\varphi_{\text{LO}})) \cos(\Delta V_b \Theta_{\pi}) \sin(\Theta_{\pi} \hat{V}_{\text{RF}} \sin(\Delta\varphi_{\text{RF}})) \right] \quad (3.78)$$

The *small angle approximation* can now be used to simplify equation (3.78). Equations approximated in this way will be in general denoted with  $\tilde{\mathcal{V}}$ . The result can be found in equation (3.79).

$$\tilde{\mathcal{V}}_{\varphi_{\text{RF}}}^{\dagger} = \frac{\hat{\mathcal{V}}}{\sqrt{2}} \left[ (2\Delta r_s + \Delta\varphi_{\text{LO}}) \Theta_{\pi} \Delta V_b - (1 + 2\Delta r_s \Delta\varphi_{\text{LO}}) \Theta_{\pi} \hat{V}_{\text{RF}} \Delta\varphi_{\text{RF}} \right] \quad (3.79)$$

The output approximation from equation (3.79) has the general form of a linear equation. The error terms multiplied with the phase error  $\Delta\varphi_{\text{RF}}$  represent errors of the sensitivity of the phase detector or – in other words – linear errors. These terms are of minor interest as long as the phase detector is used in a [phase-locked loop \(PLL\)](#). In this case the phase error is eliminated in a feedback loop, such that the sensitivity has no influence on the performance.

The constant term in the output equation represents offset errors and it always influences the output although it is very unlikely that this term can make a major contribution to the output signal. First of all it consists exclusively of second order errors, which means that the product of two error terms can be found here, where both are meant to be not present or at least very small. Furthermore the bias voltage error is controlled in its own feedback loop, which should prevent this term from appearing at all.

Removing all error terms and thus regarding equation (3.78) under the *working point* condition reveals the ideal output equation of the [L2RF](#) phase detector in equation (3.80). The nested sine functions represent the response of the [MZM](#).

$$\mathcal{V}_{\varphi_{\text{RF}}}^{\dagger} \Big|_{\text{working point}} = - \frac{\hat{\mathcal{V}}}{\sqrt{2}} \sin(\Theta_{\pi} \hat{V}_{\text{RF}} \sin(\Delta\varphi_{\text{RF}})) \quad (3.80)$$

Figure 3.6 depicts the output voltage of the phase error channel according to equation (3.80) and normalized to  $\hat{v}/\sqrt{2}$  which reads

$$\mathcal{V}_{\varphi_{\text{RF}}, \text{norm}} = -\sin\left(\pi\left(\frac{\hat{V}_{\text{RF}}}{V_{\pi}}\right)\sin(\Delta\varphi_{\text{RF}})\right). \quad (3.81)$$

The steepness of the signal in the zero crossing and thus the sensitivity of the phase detector grows with the ratio between RF voltage and  $\pi$  modulation voltage. The additional zero crossings created for high ratios between these voltages have to be carefully observed because they appear as potential locking points for a PLL although the sensitivity in these points is significantly reduced, compared to the regular zero crossings.

The *small angle approximation* of equation (3.80) exposes the ideal output signal in equation (3.82) which is linearized around the *working point*.

$$\left.\tilde{\mathcal{V}}_{\varphi_{\text{RF}}}\right|_{\text{working point}} = -\frac{\hat{v}}{\sqrt{2}} \Theta_{\pi} \hat{V}_{\text{RF}} \Delta\varphi_{\text{RF}} \quad (3.82)$$

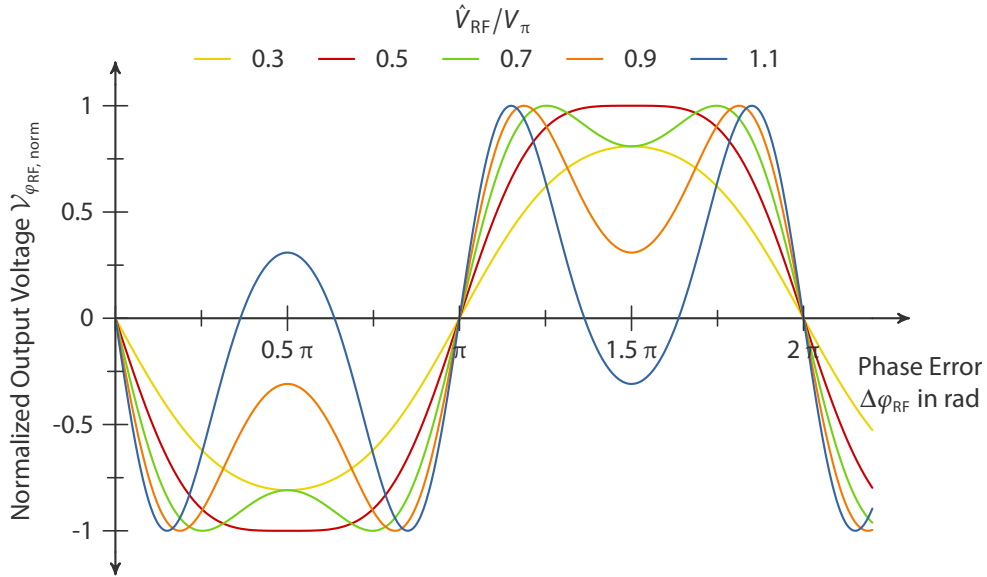


**Figure 3.6: Normalized Output Voltage of the L2RF Phase Error Measurement Channel** | Increasing the RF voltage at the MZM increases the sensitivity but might also create additional zero crossings. The picture depicts the characteristic MZM response for different RF voltage to  $\pi$  modulation voltage ratios.

### 3.11.2 Sensitivity and Noise of the L2RF Phase Detector

The sensitivity  $K_{\phi,rad}$  of the setup in V/rad can be extracted from equation (3.82) to be

$$K_{\phi,rad} = -\frac{\hat{V}}{\sqrt{2}} \Theta_{\pi} \hat{V}_{RF}. \quad (3.83)$$

By inserting the peak output voltage  $\hat{V}$  from equation (3.67) and the normalized  $\pi$  modulation factor  $\Theta_{\pi}$  from equation (3.19) one obtains the full form of equation (3.83):

$$K_{\phi,rad} = -\sqrt{2} \pi \frac{\hat{V}_{RF}}{V_{\pi}} Z_{50} R_{PD} P_{in}^* a_{MZM} a_{mix} a_{RF} a_{bp} a_{LNA} \eta_m \eta_d. \quad (3.84)$$

Equation (3.84) can be simplified by collecting all electrical gains in the new factor  $a_{el}$  and by combining the optical input power  $P_{in}^*$  and all optical losses to the power  $P_{PD}$  at the photodiode. The conversion from V/rad to V/s is performed by the multiplication with  $2\pi$  and the RF frequency  $f_{RF}$ .

$$K_{\phi} = -2\sqrt{2} \pi^2 \frac{\hat{V}_{RF}}{V_{\pi}} Z_{50} R_{PD} P_{PD} a_{el} f_{RF} \quad (3.85)$$

$$P_{PD} = P_{in}^* a_{MZM} \eta_m \eta_d \quad (3.86)$$

$$a_{el} = a_{mix} a_{RF} a_{bp} a_{LNA} \quad (3.87)$$

The noise floor of the detector is caused by shot noise from the photodiode and thermal noise from the load resistor behind the photodiode. The shot noise  $I_{n,shot}$  of the photodiode is defined as

$$I_{n,shot} = \sqrt{2eR_{PD} \Delta f P_{PD}}, \quad (3.88)$$

where  $e$  is the elementary charge and  $\Delta f$  the bandwidth. The dark current of the photodiode is much smaller than the photocurrent<sup>1</sup> and therefore does not significantly contribute to the shot noise. The load resistor  $Z_{50}$  can be used to convert the shot noise to its voltage equivalent and the multiplication by  $a_{el}$  reveals the amount of noise at the output of the L2RF phase detector caused by the photodiode:

$$V_{n,shot} = a_{el} Z_{50} I_{n,shot}. \quad (3.89)$$

<sup>1</sup>for example  $< 3 \text{ nA}$  dark current compared to a photocurrent of  $0.95 \text{ A W}^{-1} * 1 \text{ mW} = 0.94 \text{ mA}$  for an ET-3500F photodiode [ET3.5k]

The thermal noise  $V_{n,\text{thermal}}$  from the load resistor  $Z_{50}$  amounts at the output of the L2RF phase detector to

$$V_{n,\text{thermal}} = a_{\text{el}} \sqrt{4KT_{\text{abs}} \Delta f Z_{50}}, \quad (3.90)$$

where  $K$  is BOLTZMANN's constant,  $T_{\text{abs}}$  the absolute temperature and  $\Delta f$  the bandwidth. Both noise sources are uncorrelated and therefore summed up by quadratic addition.

The use of a voltage amplifier with a load resistor  $Z_{50}$  is only advisable as long as the noise floor is dominated by shot noise instead of thermal noise. It is beneficial to use a transimpedance amplifier for the photodiode readout if the thermal noise is the dominant contribution [Hob01]. The optical power  $P_{\text{PD},\text{eq}}$  at which both noise sources are equal is calculated as a figure of merit for this decision by solving equations (3.89) and (3.90) for  $P_{\text{PD},\text{eq}}$ .

$$V_{n,\text{thermal}} \stackrel{!}{=} V_{n,\text{shot}} \quad (3.91)$$

$$P_{\text{PD},\text{eq}} = 4KT_{\text{abs}} (2eR_{\text{PD}}Z_{50})^{-1} \quad (3.92)$$

One should consider using a transimpedance amplifier for the photodiode readout if the available optical power is less than  $P_{\text{PD},\text{eq}} \approx 1.1 \text{ mW}$ . This value has been calculated from equation (3.92) for a temperature  $T_{\text{abs}} = 293 \text{ K}$  and a responsivity  $R_{\text{PD}} \approx 0.95 \text{ A W}^{-1}$ .

The signal-to-noise ratio (SNR) of the detector can only be improved if parameters of equation (3.85) are increased, which do not contribute to the noise floor. The shot noise increases with the square root of the optical power at the photodiode  $P_{\text{PD}}$  while the sensitivity  $K_{\phi}$  grows proportionally to the optical power. An increase of the optical power improves the SNR by square. The optical power should be as high as possible without saturating the photodiode. The application of a dual output MZM doubles the optical power at the photodiode compared to the application of a single output MZM. This is of tremendous benefit for the optical power budget. To increase the optical power, one can also optimize the incoupling efficiencies in order to reduce optical losses.

Equation (3.85) reveals that the detection scheme is actually balanced. The optical input power  $P_{\text{in}}^*$ , which is according to equation (3.67) proportional to the optical power at the photodiode  $P_{\text{PD}}$  has an influence on the sensitivity of the setup, while the actual working point is in the zero crossing of the output equation. This point is a fixed point of the equation and therefore not affected by changes of the input power. The setup actually detects the balance of certain pulse trains – or their unbalance in case they are modulated, which is a relative measurement independent of the optical power level.

The RF voltage  $\hat{V}_{\text{RF}}$  and the  $\pi$  modulation voltage  $V_{\pi}$  are contained in the sensitivity but not in the noise terms. They can be used to increase the modulation depth at the MZM. Their influence in increasing the sensitivity has been presented in figure 3.6.

Finally, an increase of the RF frequency also increases the absolute sensitivity<sup>1</sup> of the phase detector, but this is a common property of phase detectors (see section 5.3). The frequency is often predetermined in applications at free-electron lasers (FELs), and can thereby not be freely used to increase the sensitivity independent of the SNR. The laser repetition rate however has no contribution to the sensitivity of the phase detector.

The RF chain also facilitates various opportunities to increase the sensitivity of the setup. In the *working point* the detected error signals are vanished from the spectrum and around the *working point* they are very small. This circumstance permits to use high gain amplifiers which can still be operated in their linear regime because the error signals in the working point are small. The SNR however is not affected by the electrical gain  $a_{el}$  because it is included in the noise and sensitivity terms.

One additional error source are DC offset errors of the RF mixer or the LNA, which might directly influence the output signals of the L2RF phase detector by creating an additional offset term in the output equation. These errors have to be considered during device selection. They are not covered by the above equations. They can however be avoided by implementing a more sophisticated readout scheme in which the photodiode signals are not mixed down to baseband. This option will be briefly addressed in chapter 6.

### 3.11.3 Evaluation of the Bias Voltage Error Channel

Moving on to the analysis of the bias voltage error channel, a procedure similar to the analysis of the phase output channel can be used. The parameters for the analysis are  $\varphi_{LO, V_b}$  and  $h_1$ . The obtained equation is presented in equation (3.93). The result is familiar, yet not identical to the previous output equation of the phase error channel.

$$\mathcal{V}_{V_b}^\dagger = \frac{\hat{V}}{\sqrt{2}} \left[ (\cos(\Delta\varphi_{LO}) - 2\Delta r_s \sin(\Delta\varphi_{LO})) \sin(\Delta V_b \Theta_\pi) \cos(\Theta_\pi \hat{V}_{RF} \sin(\Delta\varphi_{RF})) \right. \\ \left. + (\sin(\Delta\varphi_{LO}) - 2\Delta r_s \cos(\Delta\varphi_{LO})) \cos(\Delta V_b \Theta_\pi) \sin(\Theta_\pi \hat{V}_{RF} \sin(\Delta\varphi_{RF})) \right] \quad (3.93)$$

The *small angle approximation* of the output equation already has been proven to be useful during the analysis of the phase error equation. The linearized bias voltage error output equation, found in equation (3.94) also turns out to have a linear form. Like in the previous case, only the constant term is of real interest, because the bias voltage is kept in a feedback loop where changes in the sensitivity can be tolerated. The constant term consists only of second order terms, where one element is always the phase error – which is not supposed

<sup>1</sup> The relative sensitivity  $K_{\varphi, rad}$  in V/rad is of course not affected, but the absolute sensitivity  $K_\varphi$  in V/s where the higher frequency indeed plays a role is often specified.

to have a major contribution because the active phase feedback should always keep the phase error at zero.

$$\tilde{\mathcal{V}}_{V_b}^\dagger = \frac{\dot{\mathcal{V}}}{\sqrt{2}} \left[ (\Delta\varphi_{LO} - 2\Delta r_s) \Theta_\pi \hat{V}_{RF} \Delta\varphi_{RF} + (1 - 2\Delta r_s \Delta\varphi_{LO}) \Theta_\pi \Delta V_b \right] \quad (3.94)$$

Most of the terms vanish in the *working point* and reveal the ideal output equation of the bias voltage error channel which can be found in equation (3.95). The sine function originates again from the MZM response.

$$\mathcal{V}_{V_b} \Big|_{\text{working point}} = \frac{\dot{\mathcal{V}}}{\sqrt{2}} \sin(\Theta_\pi \Delta V_b) \quad (3.95)$$

In equation (3.96), the approximated output equation in the *working point* represents the ideal response of the bias voltage error channel for small errors.

$$\tilde{\mathcal{V}}_{V_b} \Big|_{\text{working point}} = \frac{\dot{\mathcal{V}}}{\sqrt{2}} \Theta_\pi \Delta V_b \quad (3.96)$$

Comparing the output equations from the phase and the bias channel reveals the possibility of crosstalk between these channels. The constant term in each equation refers to the respective opposite channel. This crosstalk can be caused by either a wrongly adjusted splitting ratio or an error of the LO phase. At least the latter condition can be easily imagined. Both channels are detected at the same frequency and just separated by the  $\pi/2$  phase shift between the LO signals of the two involved mixers. It is obvious that each channel can receive crosstalk from the other channel if its LO signal is not perfectly in phase to the error signal of this channel. In this case the LO is no longer orthogonal to the second error signal which then leaks into the currently regarded measurement channel. Nevertheless, both channels are usually operated in feedback loops, such that both the bias and phase error signals are supposed to be strongly suppressed in a real setup and therefore can also not cause significant crosstalk.

One should finally keep in mind that the above analyses have been performed under the condition that no delay errors are present. The delay errors have to be separately investigated and one can already presume that additional error terms will be found in the output equations then. This question will be further pursued after the next section, where the analysis of the third measurement channel which detects the splitting ratio will be performed.

### 3.11.4 Analysis of the Splitting Ratio Error Channel

The splitting ratio error is detected at the second harmonic of the laser repetition rate with the parameters  $\varphi_{\text{LO},r_s}$  and  $h_2$ . The general output equation of the splitting ratio error channel is presented in equation (3.97). Interestingly, neither phase nor bias voltage errors can possibly contribute to this signal. There is also no constant error term in the equation, but the sensitivity scales with the cosine of the LO phase. This is very advantageous because in this case small drifts of the LO phase have almost no influence on the actual channel response.

$$\mathcal{V}_{r_s}^\dagger = 2\hat{\mathcal{V}} \cos(\Delta\varphi_{\text{LO}}) \Delta r_s \quad (3.97)$$

The *small angle approximation* of equation (3.97) is obtained straight forward. The splitting ratio error channel shows a linear response to the splitting ratio error around the *working point* as expected.

$$\left. \tilde{\mathcal{V}}_{r_s} \right|_{\text{working point}} = 2\hat{\mathcal{V}} \Delta r_s \quad (3.98)$$

### 3.11.5 First Order Error Contributions to the Output Signals

Although it has already been mentioned that the general output equations are very complex, it turns out that their *small angle approximation* reveals some interesting details. Equation (3.99) shows the approximated full output equation of the phase error channel. The equation presents a linear equation for the phase error output, comparable to equation (3.79), just that this time the delay errors have not been neglected.

$$\begin{aligned} \tilde{\mathcal{V}}_{\varphi_{\text{RF}}} = \frac{\hat{\mathcal{V}}}{2\sqrt{2}} & \left[ \Theta_\pi \hat{V}_{\text{RF}} \Delta\varphi_{\text{RF}} \left[ -2(1 + 2\Delta r_s \Delta\varphi_{\text{LO}}) + \Delta T_2 \omega_{\text{rep}} (2\Delta r_s - \Delta\varphi_{\text{LO}}) \right. \right. \\ & \left. \left. + \Delta T_1 \omega_{\text{rep}} (\Delta r_s - 1/2) [(\Delta\varphi_{\text{LO}} - 1)(\Delta T_2 \omega_{\text{rep}} + 2) + 4] \right] \right. \\ & + \Theta_\pi \Delta V_b \left[ 2(2\Delta r_s + \Delta\varphi_{\text{LO}}) + \Delta T_2 \omega_{\text{rep}} (2\Delta r_s \Delta\varphi_{\text{LO}} - 1) \right. \\ & \left. + \Delta T_1 \omega_{\text{rep}} (\Delta r_s - 1/2) [(\Delta\varphi_{\text{LO}} - 1)(\Delta T_2 \omega_{\text{rep}} + 2) + 4] \right] \\ & + \Theta_\pi \hat{V}_{\text{RF}} \omega_{\text{RF}} \Delta T_1 \left[ (\Delta r_s - 1/2) [(\Delta\varphi_{\text{LO}} + 1)(\Delta T_2 \omega_{\text{rep}} - 2) + 4] \right] \\ & + \Theta_\pi \hat{V}_{\text{RF}} \omega_{\text{rep}} \omega_{\text{RF}} \Delta T_1^2 \left[ (\Delta r_s - 1/2) [(\Delta\varphi_{\text{LO}} - 1)(\Delta T_2 \omega_{\text{rep}} + 2) + 4] \right. \\ & \left. \left. + \Delta T_2 \omega_{\text{rep}} (1 - 2\Delta r_s \Delta\varphi_{\text{LO}}) + \Delta T_1 \Delta T_2 \omega_{\text{rep}}^2 (\Delta r_s - 1/2) (1 - \Delta\varphi_{\text{LO}}) \right] \right] \quad (3.99) \end{aligned}$$



The linear term with respect to the phase error can be found in the first two lines of equation (3.99). Its dependency on several  $\Delta$  terms can be regarded as potential gain error. Practically, the gain error is however of minor importance if the L2RF phase detector is used in a feedback loop which forces the phase error to vanish. The remaining part of the equation however represents the constant term of the equation or the offset error. Most of its components are of higher order. Two of them however are of the first order and they should get some special attention – especially because the phase error channel is the most important channel of the setup. Each of these first order terms can cause an offset in the measurement channel, which would be falsely interpreted as phase error, although this false phase error would have been caused by a different error condition. In order to evaluate the significance of this error, one can equate the output voltage that would be potentially created by the error signal with the nominal output equation of the phase channel, which can be found in equation (3.82). The voltage signal created by the error can thus be related to an equivalent phase drift.

One of the first order offset errors is caused by an error of the first delay  $T_1$ . The corresponding term can be found in equation (3.99) in the fifth line. The corresponding phase error  $\Delta\phi_{\text{RF}}$  in the nominal output equation can be converted to a timing error by replacing it with  $\omega_{\text{RF}} \Delta t_{\text{RF}, T_1}$  which leads to the following relationship.

$$-\frac{\hat{V}}{\sqrt{2}} \Theta_{\pi} \hat{V}_{\text{RF}} \omega_{\text{RF}} \Delta t_{\text{RF}, T_1} = -\frac{\hat{V}}{2\sqrt{2}} \Theta_{\pi} \hat{V}_{\text{RF}} \omega_{\text{RF}} \Delta T_1 \quad (3.100)$$

$$\Delta t_{\text{RF}, T_1} = \frac{\Delta T_1}{2} \quad (3.101)$$

In conclusion, errors of the first delay  $\Delta T_1$  translate to a measurement error of half the delay error. This significant influence has to be considered during the design process of the L2RF phase detector. The other first order offset error originates from errors of the second delay  $\Delta T_2$ . The term can be found at the beginning of the last line of equation (3.99). The analysis of the effect of this offset error is performed in the same way as before, while the relation between the angular RF frequency  $\omega_{\text{RF}}$  and the angular repetition rate  $\omega_{\text{rep}}$  is substituted with  $n$  and the normalization factor  $\Theta_{\pi}$  from the MZM is expanded according to equation (3.19).

$$\frac{\hat{V}}{\sqrt{2}} \Theta_{\pi} \hat{V}_{\text{RF}} \omega_{\text{RF}} \Delta t_{\text{RF}, T_2} = \frac{\hat{V}}{2\sqrt{2}} \omega_{\text{rep}} \Delta T_2 \quad (3.102)$$

$$\Delta t_{\text{RF}, T_2} = \frac{1}{2} \frac{\omega_{\text{rep}}}{\omega_{\text{RF}}} \frac{1}{\Theta_{\pi} \hat{V}_{\text{RF}}} \Delta T_2 \quad (3.103)$$

$$= \frac{1}{2\pi n} \frac{V_{\pi}}{\hat{V}_{\text{RF}}} \Delta T_2 \quad (3.104)$$

The order of magnitude of the influence of this error term can only be evaluated by making presumptions and entering a few practical parameters into equation (3.104). The estimated value, calculated in equation (3.105), is generated by using a typical  $\pi$  modulation voltage  $V_\pi$  of 5 V, a laser repetition rate at the sixth sub-harmonic  $n$  of the RF frequency and an RF voltage  $\hat{V}_{\text{RF}}$  applied to the MZM which corresponds to an RF power of 27 dBm in a 50  $\Omega$  system. These values are typical values – the frequency ratio even exactly – from the actual implementations for FLASH and the European XFEL .

$$\Delta t_{\text{RF}, T_2}^{\text{est}} \approx \frac{1}{53} \Delta T_2 \quad (3.105)$$

Concerning the phase error channel, two first order offset errors are present in the final output equation. Both have been evaluated. Errors of the first delay  $\Delta T_1$  cause, according to equation (3.101), phase measurement errors of half the delay error. The construction of the first delay therefore has to be done with special care concerning potential drifts. Measurement errors originating from the second delay error  $\Delta T_2$  however are suppressed to a larger extend which depends on further properties of the setup. The implementation of the second delay is thus less critical compared to the first one, although its stability should not be neglected. The remaining error terms, namely the LO phase error  $\Delta \varphi_{\text{LO}}$  and the splitting ratio error  $\Delta r_s$  have only higher order contributions to the previously presented phase error measurement channel.

A similar analysis of the bias voltage error channel can be performed. The approximated full output equation for small angles is given in equation (3.106). The structure is already familiar from equation (3.99) while small details of the equation are different. Only one first order offset error term is for example present in this equation. All remaining errors are of higher order.

$$\begin{aligned} \tilde{V}_{V_b} = \frac{\dot{V}}{2\sqrt{2}} & \left[ \Theta_\pi \Delta V_b \left[ 2 (1 - 2 \Delta r_s \Delta \varphi_{\text{LO}}) + \Delta T_2 \omega_{\text{rep}} (2 \Delta r_s + \Delta \varphi_{\text{LO}}) \right. \right. \\ & \left. \left. + \Delta T_1 \omega_{\text{rep}} (\Delta r_s - 1/2) [(\Delta \varphi_{\text{LO}} + 1) (\Delta T_2 \omega_{\text{rep}} - 2) + 4] \right] \right. \\ & + \Theta_\pi \hat{V}_{\text{RF}} \Delta \varphi_{\text{RF}} \left[ 2 (\Delta \varphi_{\text{LO}} - 2 \Delta r_s) - \Delta T_2 \omega_{\text{rep}} (1 + 2 \Delta r_s \Delta \varphi_{\text{LO}}) \right. \\ & \left. \left. + \Delta T_1 \omega_{\text{rep}} (\Delta r_s - 1/2) [(\Delta \varphi_{\text{LO}} + 1) (\Delta T_2 \omega_{\text{rep}} - 2) + 4] \right] \right. \\ & + \Theta_\pi \hat{V}_{\text{RF}} \omega_{\text{RF}} \Delta T_1 \left[ (\Delta r_s - 1/2) [(1 - \Delta \varphi_{\text{LO}}) (\Delta T_2 \omega_{\text{rep}} + 2) - 4] \right] \\ & + \Theta_\pi \hat{V}_{\text{RF}} \omega_{\text{rep}} \omega_{\text{RF}} \Delta T_1^2 \left[ (\Delta r_s - 1/2) [(\Delta \varphi_{\text{LO}} + 1) (\Delta T_2 \omega_{\text{rep}} - 2) + 4] \right. \\ & \left. \left. - \Delta T_2 \omega_{\text{rep}} (\Delta \varphi_{\text{LO}} + 2 \Delta r_s) + \Delta T_1 \Delta T_2 \omega_{\text{rep}}^2 (1/2 - \Delta r_s) (1 + \Delta \varphi_{\text{LO}}) \right] \right] \quad (3.106) \end{aligned}$$

The first order error term can again be found in the fifth line of equation (3.106) and it is again the first delay  $\Delta T_1$  which has a significant influence on the offset of the bias voltage error output signal. With regard to the operation of the L2RF setup this error is less critical because the bias voltage error measurement is dedicated to an internal feedback – in contrast to the phase measurement which is the dedicated output signal of the L2RF phase detector. If special care of  $T_1$  has already been taken during the optimization of the phase measurement channel, such that this delay error is limited or very small, the bias voltage error measurement is also not substantially affected by it any more. The remaining error terms are again of higher order and therefore of minor importance.

The last remaining channel is the splitting ratio error measurement channel. The full equation for the splitting ratio error channel is very complicated without providing much information. Even approximated for small angles it contains many error terms of both constant and linear nature, while all of the offset terms are at least of the second order. The small angle approximation of the splitting ratio error measurement channel in the *working point* can be found in equation (3.98). A deeper analysis of this channel is not necessary at this point.

Additionally this output is in the present setup only used for monitoring purposes. A splitting ratio feedback loop might be implemented in future for setups which have to operate with single output MZMs. See chapter 6 for an outlook on future options to extend the L2RF phase detector.

### 3.12 Summary of the Theoretical Analysis

A full mathematical representation of the L2RF phase detector has been developed in this chapter. Starting from the first delay line the path of the laser pulse trains through the whole setup has been described. The spectra of the electrical signals from the photodiode have been derived. They were used for a first, brief analysis of the modulation and a graphical display of different spectra together with the spectral envelope. Furthermore, the remaining part of the detection process up to the output of the RF mixer was covered.

The *small angle approximations* of the full output equations have been shown and the important first order offset error terms discussed. Special care has to be taken of the delays  $T_1$  and  $T_2$  because their drift significantly influences the performance of the setup, while LO phase drifts  $\Delta\phi_{LO}$  and variations of the splitting ratio error  $\Delta r_s$  turned out to be less critical as they appear only in higher order error terms.

The photodetection process involved in the pulse train detection in the L2RF setup is only meant to accurately measure the amplitude of the pulse trains but not their phase. This is an important finding, because phase measurements with photodiodes are extremely delicate

(see section 5.3). Actually phase drifts at the photodiode would have the same effect to the setup like drifts of the LO phase  $\Delta\varphi_{\text{LO}}$ . Nevertheless the analysis of the output equations has already proven that the LO phase – and therefore also the phase of the signals from the photodiode – has only negligible influence on the output signals.

Additionally, options to improve the sensitivity of the setup have been briefly evaluated. All theoretical background needed for an actual implementation of a L2RF phase detector has been laid out and the following chapter will move on to the realization of the L2RF phase detector, starting with the first prototype.

## Prototypes and Implementation

The last two chapters focused on the working principle of the [laser-to-RF \(L2RF\)](#) phase detector while the following chapter will cover the actual hardware implementation. The [L2RF](#) phase detector in general consists of two parts. The laser pulse trains are processed in the optical setup. This part includes the [MACH-ZEHNDER modulator \(MZM\)](#) in which the laser pulse trains interact with the [radio frequency \(RF\)](#) signal and the actual phase measurement takes place. The second part is the readout electronics. It starts from the photodiode and leads to the final [direct current \(DC\) low-noise amplifier \(LNA\)](#) which amplifies the baseband signal from the [RF](#) mixer.

Two laboratory prototypes of the [L2RF](#) phase detector have been constructed for performance verification and in order to gain experience with the [L2RF](#) setup. The first prototype has been used to conduct proof-of-principle measurements and to investigate the [L2RF](#) detection scheme in general. This prototype was mainly built from bulk components. For the second prototype, the optical setup and the readout electronics of the [L2RF](#) phase detector have been replaced by integrated and engineered versions. The second prototype has been used to verify the performance of these custom build components which have been designed for the construction of an integrated [L2RF](#) phase detector which is suited to be operated in an accelerator environment.

The laboratory experiments were conducted with a commercial [erbium-doped fiber laser \(EDFL\)](#)<sup>1</sup> as timing reference. Like the [master laser oscillator \(MLO\)](#) in the optical synchronization system, this laser operates at a repetition rate of 216.6 MHz and at a comparable central wavelength of about 1560 nm. The laser features a fiber-coupled and a free-space output. Both, the optical output power and the central wavelength depend on the mode-locking state of the laser which itself is influenced by changes of environmental conditions. The free-space output delivers up to 100 mW of optical output power which is sufficient for the conducted experiments. The repetition rate of this laser is phase-locked to a low frequency drift 1.3 GHz reference signal in order to allow long-term stable operation of the whole test bench and to prevent slow phase and frequency drifts.

---

<sup>1</sup>Menlo Systems GmbH: M-Comb Femtosecond Erbium Laser, see [[MComb](#)]

In order to investigate the performance of the [L2RF](#) phase detector, each prototype consists of two identical [L2RF](#) phase detectors. One [L2RF](#) phase detector has been used as in-loop phase detector while the second one has been used as out-of-loop phase detector. The out-of-loop phase detector is needed to independently monitor the performance of the in-loop phase detector during regular operation.

A low phase noise [dielectric resonator oscillator \(DRO\)](#) is used as [RF](#) source for each of the laboratory prototypes. The phase of this initially free running oscillator is measured with respect to the phase of the reference laser pulse train in the in-loop [L2RF](#) phase detector and the [DRO](#) is finally phase-locked to this reference. This part of the prototype represents the actual [phase-locked loop \(PLL\)](#). The second [L2RF](#) phase detector, used as so-called out-of-loop phase detector is operated with the exactly same laser pulse train and the same [RF](#) signal. This setup allows to independently measure the actual phase drift and jitter between the laser pulse train and the [RF](#) signals and therefore allows to validate the performance of the in-loop [L2RF](#) phase detector and the associated [PLL](#).

The measurement results from both prototypes are analyzed and discussed at the end of this chapter in section 4.7. A third prototype has been constructed after the two laboratory prototypes have been characterized. For this integrated prototype the engineered optics and readout electronics have been employed together with additional parts to assemble a prototype which is suited for an accelerator environment. It is integrated into a 19" rack mount housing and sensitive parts are decoupled carefully from environmental influences like temperature, humidity and vibrations. Further requirements like the required number of outputs, power levels and interfaces to available external infrastructure have already been considered during the development of the prototype.

## 4.1 The First Laboratory Prototype

The pulse patterns needed for proper operation of the [L2RF](#) phase detector are created in the optical setup. Two delay lines are involved in this pulse pattern generation. The length, splitting ratio and general specification for these delays under the consideration of the requirements for the operation at the [Free-Electron Laser in Hamburg \(FLASH\)](#) and the European [X-ray Free-Electron Laser \(XFEL\)](#) have been worked out in chapter 3 while specific parameters can be found in sections 3.1 and 3.11. The modulated pulse train from the optical setup is finally analyzed using custom built readout electronics. The optical setup of the [L2RF](#) phase detector is divided into two separate parts. The first part of the optical setup is shared between the in-loop and the out-of-loop phase detector in the special case of the first laboratory prototype. The modulated pulse train from the optical setup is finally analyzed using custom built readout electronics.

### 4.1.1 Construction of the First Delay Line

The first part of the optical setup is schematically presented in figure 4.1. The figure depicts the so-called first delay line which includes the splitting, delay and recombination of the laser pulse train that needs to be performed before it enters the MZM.

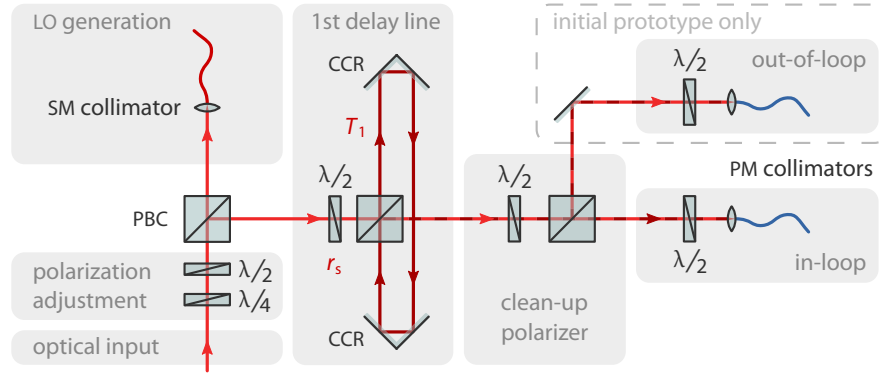


**Figure 4.1: Block Diagram of the First Part of the Optical Setup** | The first part includes the fundamental polarization adjustment, the local oscillator (LO) tap, the first delay line and the incoupling for the fiber-coupled MZM.

A part of the laser pulse train is tapped off before entering the delay line. This signal is used for the generation of the local oscillator (LO) signal, which is needed to operate the RF mixers in the readout electronics. A quarter-wave ( $\lambda/4$ ) plate is used to linearize the polarization of the incident light. The second waveplate is a half-wave ( $\lambda/2$ ) plate which is used to adjust the amount of light tapped off in the first polarizing beam cube (PBC) for the LO generation.

The delay line is constructed around a PBC which performs both the splitting and recombination, while two hollow metal corner-cube retroreflectors (CCRs) guide the tapped off part of the laser pulse train around the PBC and thereby delay it with respect to the immediately transmitted part. The splitting ratio is adjusted by rotating the upstream  $\lambda/2$  waveplate which changes the plane of polarization of the pulse train before entering the PBC. The alignment and the precise adjustment of the delay length is realized by mounting at least one CCRs on a manual translation stage. Angular adjustment of the CCRs is not needed, because their reflected beams are intrinsically parallel to the incident beams – regardless of the angle of incidence. The optical phase relation between the pulse trains during the recombination behind the delay line does not matter because the delay separates the pulses temporally. The delay line therefore does not need to be optically phase-matched in order to enable the successful recombination of both pulse trains. The delay length is defined only by the accuracy and delay requirements of the L2RF setup.

The recombined pulse trains from the first delay line now need to be coupled into an optical fiber in order to be transmitted to the integrated and fiber-coupled MZM. The MZM is equipped with polarization maintaining (PM) fibers because it most efficiently modulates light in one plane of polarization (see appendix A for more details). The two pulse trains from the first delay line however are orthogonally polarized after their recombination. An additional PBC is therefore used as polarizer in front of the PM fiber collimator leading to the MZM. The polarization of the two pulse trains from the delay line is therefore adjusted by a  $\lambda/2$  waveplate before entering this third PBC such that ideally half of each pulse train is transmitted through the PBC and half of each pulse train is reflected by it. The transmitted and reflected parts of both pulse trains behind the polarizer are always linearly polarized and they always share the same plane of polarization, while with respect to each other the transmitted and reflected parts are orthogonally polarized.

Another  $\lambda/2$  waveplate between this PBC and the MZM fiber collimator is used to adjust the common plane of polarization of the combined pulse trains to the slow axis of the PM fiber behind the fiber collimator and thus also to the modulating axis of the MZM. The MZM itself is considered to already belong to the second part of the optical setup because the splitting for the second delay line is performed inside the utilized dual output MZM.

A photograph of the first delay line from the first prototype can be found in figure D.1 in appendix D where in general photographs of different prototypes and setups can be found. In comparison to figure 4.1, the actual setup included additional lenses which were used to condition the laser beam for better incoupling into the PM fiber collimators leading to the MZMs and thereby improve the incoupling efficiency. The setup also included additional kinematically mounted mirrors which are needed to align the setup. Both have been omitted during the previous schematic presentation.

The residual laser pulse trains at the reflected output of the polarizer after the first delay line have no application in the L2RF phase detector and they are therefore usually dumped. These pulse trains were used in the first L2RF prototype to actually operate the out-of-loop measurement setup instead of building a dedicated first delay line for this purpose (see also the photograph in figure D.1). This modification allowed to increase the power efficiency of the first prototype and reduced its complexity. In the second laboratory prototype however independent optical setups are used for the in-loop and the out-of-loop measurement in order to compare two fully independent L2RF phase detectors.

### Polarization Dependent Beam Combination

The part of the pulse trains which is transmitted by the clean-up polarizer is used to operate the L2RF setup while the reflected light remains unused. This circumstance originates from the fact, that two laser beams can never be combined with the same state of polarization using PBCs without losing at least half of the optical power in the required polarizer. The



overall procedure has already been discussed in section 3.2 where the intrinsic insertion loss associated to the delay line has been introduced in equation (3.10) as the delay efficiency  $\eta_d$ .

Alternative methods of laser beam combining like dichroic elements are unsuited here, because the wavelength of both pulse trains is obviously identical. Reflective beam splitters can combine beams with the same polarization and wavelength but nevertheless suffer during recombination from the same intrinsic insertion loss like PBCs because they are only partly transparent. Additionally their splitting or recombination ratio is not even adjustable. The same applies to fiber couplers which also have intrinsic losses of the same degree. Because the recombination is supposed to happen with a delay between both pulse trains, one could implement an interleaving combination scheme with a fast optical switch which allows to combine the full optical power in the same plane of polarization. This idea was however dismissed in favor of the passive and thus technically robust solution presented above and the necessary optical losses are accepted at this point.

#### 4.1.2 Construction of the Second Delay Line

The second part of the optical setup is depicted in figure 4.2. This part was built twice, once for the in-loop and once for the out-of-loop phase detector of the first prototype. It contains the dual output MZM [EOMz] and the second delay line. The length of the delay line can be fine tuned by a short free-space segment which also contains a  $\lambda/2$  waveplate. The  $\lambda/2$  waveplate is needed to compensate a possible rotation offset between the two involved PM fiber collimators. Both the delayed and the non-delayed outputs of the MZM are recombined in a PM combiner. The PM combiner couples each input signal to one principle axis of its output fiber and thereby transmits both input signals fully to the photodiode. The photodiode is not polarization sensitive<sup>1</sup> and in contrast to the MZM does not require both signals to be identically polarized.

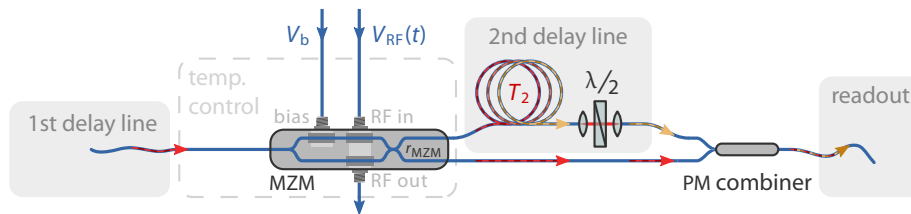


**Figure 4.2: Block Diagram of the Second Part of the Optical Setup** | The second part consist of the MZM and the second delay line. It is mostly constructed from fiber components.

<sup>1</sup> Actually, photodiodes can suffer from polarization-dependent loss (PDL). This circumstance is discussed in section 3.3 and it is uncritical for the L2RF phase detector.

A photograph of the fiber setup which comprises the second delay line and the MZMs is depicted in figure D.2. An active temperature control of the MZM has been implemented after the photograph has been taken. After detection by the photodiode, the generated electrical pulse train is analyzed by the readout electronics.

#### Active Temperature Control of the MZM

The MZM within the second part of the in-loop and out-of-loop optical prototypes is mounted to a temperature controlled aluminum plate and isolated from external temperature fluctuations with a flexible elastomeric foam<sup>1</sup>. This arrangement prevents temperature induced phase drifts in the MZM. It is furthermore possible to characterize the temperature coefficient of the MZM beforehand in order to choose an operating temperature where the temperature coefficient of the MZM is zero, which eliminates the sensitivity to temperature variations.

#### 4.1.3 Readout Setup of the First Laboratory Prototype

The readout setup for the first prototype has been implemented based on RF mixers, as described in section 3.9. Four detector channels were built in order to detect bias and phase errors measured at both the in-loop and the out-of-loop L2RF phase detector. All four channels were able to share the same LO signal because they were all operated at the same frequency. Figure 4.3 presents one of these four channels including the common LO generation. Figure D.3 shows a photograph of the complete readout electronics of the first prototype.

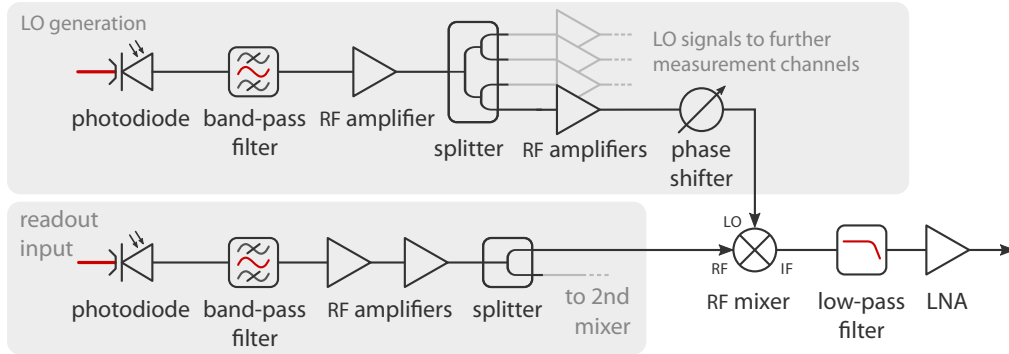


**Figure 4.3: Block Diagram of a Single Channel Detector for the L2RF Phase Detector** | This setup was built from bulk components for the first prototype of the L2RF phase detector. The LO generation is simultaneously used for all four identical measurement channels operated at the first prototype.

<sup>1</sup>NH/Armaflex, an elastomeric foam with a thermal conductivity of less than 0.04 W/(m K), see [Arflx]

The LO signal is band-pass filtered from the output of the LO photodiode (ET-3500F, see [ET3.5k]), amplified in an RF amplifier (ZX60-33LN+, see [ZX60]) and split up into the four required LO signals (ZMSC-4-3, see [ZMSC]). The LO signals are further amplified in an additional RF amplifier (ZFL-500LN, see [ZFL]) to the required 7 dBm of RF power. Each signal is fed through a manually adjustable phase shifter such that the working point of the respective RF mixer can be adjusted. This working point includes the phase shift of  $\pi/2$  needed to separate the bias voltage and phase error signals during detection. Attenuators to adapt power levels, to reduce reflections and to improve the matching between components have been used, although they are not specifically mentioned because they are not relevant to the general working principle but are rather specific to the prototype setup.

The processing of the error signals is performed similarly. The desired frequency component is band-pass filtered from the frequency comb available after the readout photodiode (ET-3500F, see [ET3.5k]). This signal is then fed through two RF amplifiers (ZX60-33LN+, see [ZX60] and ZFL-500LN, see [ZFL]) where it is amplified by about 40 dB (already taking losses and utilized attenuators into account). This is easily possible without saturating RF components because the error signal vanishes in the ideal working point. The amplified error signal from each L2RF phase detector is split (ZX10-2-20, see [ZX10]) between two mixers in order to measure the bias voltage and phase error signals which are encoded at the same frequency (see section 3.10).

Each signal is applied to an RF mixer (ZFM-2000+, see [ZFM]) and mixed down to baseband. The mixer output is low-pass filtered at 1.9 MHz (SLP-1.9+, see [SLP]) in order to remove the sum frequency and higher order mixing products from the output signal. Attenuators are used again to improve the matching between components.

The signal which is obtained from the RF mixer is amplified in a DC LNA based on the analog devices AD797 operational amplifier [AD797]. Integrated into a small connectorized housing, the LNA supports the manual selection of four different gains which allow to adjust the readout setup to the bit resolution and to the voltage range of a following analog-to-digital converter (ADC). As a side effect one limits the bandwidth of the output signal due to the fixed gain bandwidth product of the amplifier. Additionally, the LNA decouples the mixer from potential influences from external components due to its reverse isolation and thus increases the reliability of the setup.

### LO Generation Details

The LO generation is mandatory for the operation of the RF mixers in the individual readout channels. The LO frequency needs to be identical to the modulation frequency of the observed channel and the LO power has to be sufficient to drive the RF mixer. The parameters for the four implemented readout setups have been laid out in section 3.10. The implementation of the LO generation is performed by tapping off a small portion of

light from the reference pulse train before it enters the first delay line in the first part of the optical prototype. This pulse train is guided to the LO photodiode.

The L2RF setup is supposed to be always built in a way that the modulation frequency is identical to one of the harmonics of the reference pulse train. The LO frequency has to be identical to the modulation frequency and is therefore always available in the frequency comb of the reference laser pulse train. Thus one can always extract the desired LO frequency from the spectrum of the pulse train.

The power levels obtained directly from the photodiode are usually not sufficient to drive a passive level 7 or level 10 RF mixer<sup>1</sup>. About –18 dBm of RF power are delivered by a typical reverse biased indium gallium arsenide (InGaAs) PIN photodiode at the fundamental frequency component of a 1 mW optical pulse train from the FLASH MLO as long as the RF bandwidth of the photodiode is higher than the repetition rate of the pulse train. An RF power of 7 dBm or even 10 dBm could not be reached in laboratory tests because the photodiode saturates much earlier. The extracted signal is therefore amplified with conventional RF amplifiers to the required level. Minor power fluctuations are of no concern for the detection principle as long as the RF mixer is saturated (see appendix B).

It is a huge benefit of the readout electronics, that the LO signal is created directly from the reference pulse train because this ensures intrinsic phase stability between the LO signal and the detected error signal. The prototype readout setup included a manual phase shifter in each LO line, which was used to adjust the correct working point for each RF mixer. Additional LO phase drifts can be caused by phase drifts of components like amplifiers and filters or by temperature induced length changes of optical fibers and RF cables. They have only second order influence on the measurement accuracy of the L2RF phase detector as shown in equations (3.78) and (3.99).

After the setup procedure is briefly discussed, the overall controller structure of the first prototype will be described in the following section together with the layout of the actual RF part of the prototype.

#### 4.1.4 Assembly of the First Laboratory Prototype

Figure 4.4 presents the complete first prototype. The block diagram is composed from components which have been introduced in figures 4.1 to 4.3. Newly added are the bias voltage control loops, the components around the in-loop PLL and the additional RF components which belong to the 1.3 GHz RF signal.

<sup>1</sup>These numbers refer to the LO power required to saturate the LO port of a passive RF mixer and thereby achieve the lowest possible conversion loss. This number is a device parameter and it can be found in the datasheet of the RF mixer.

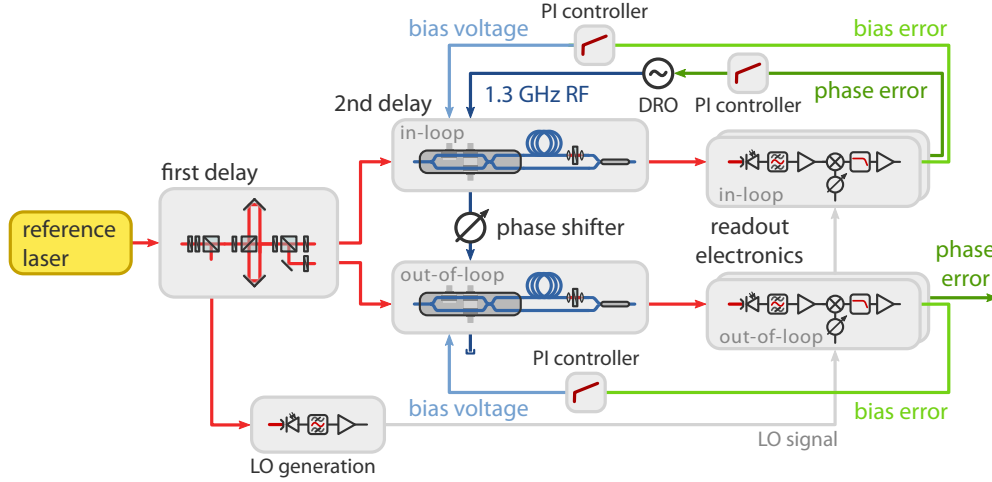


**Figure 4.4: Complete Block Diagram of the First Laboratory Prototype** | The previously presented blocks are assembled to the first laboratory prototype. The control loops are used to operate it. The out-of-loop phase error characterizes the performance of the **L2RF** phase detector.

A commercial **DRO** [Sto<sup>+</sup>06], manufactured by Poseidon Scientific Instruments (PSI)<sup>1</sup> has been utilized in the presented laboratory prototype. The **DRO** has been integrated as local, voltage controllable **RF** source operating at the desired accelerator frequency of 1.3 GHz. The **PLL** driving this **DRO** is locked by controlling its frequency and so obviously also its phase.

The **DRO** delivers around 13 dBm of **RF** power, which are for the operation of the prototype boosted by an **RF** amplifier (ZRL-1150LN+, see [ZRL]) such that 21 dBm are finally delivered to the first **MZM**. The **RF** power has a direct influence on the sensitivity of the **L2RF** phase detector as discussed in section 3.11.2. Two splitters (ZAPD-2+, see [ZAPD]) are installed before and behind the amplifier, which allow to monitor transparently the quality of the 1.3 GHz **RF** signal. Figure 4.4 only shows the **DRO**, the remaining components are omitted.

The **RF** signal in the test setup is terminated in a 50  $\Omega$  termination after being fed through both **MZMs**. The **L2RF** phase detector can only be operated if the **RF** signal is properly aligned to the laser pulses. The out-of-loop detector requires a phase shifter to adjust its working point while the phase relation of the so-called in-loop detector is controlled by the **PLL**. Therefore an additional manual phase shifter is inserted into the **RF** connection between the two **MZMs**.

<sup>1</sup>Originally being an independent Australian company, PSI has recently been acquired by the US American corporation Raytheon which seems to continue most of the original portfolio.

The feed-through option is a special feature of **MZMs** which is very useful in providing an **RF** signal to applications. Instead of internally terminating the **RF** signal behind the electrodes within the **MZM**, the **RF** signal is coupled out and available at an output port. This kind of **MZM** has two main advantages. The achievable sensitivity of the detector scales with the applied **RF** power (see section 3.11.2). The damage threshold concerning **RF** power is usually lower for internally terminated types due to thermal constraints which limits the achievable sensitivity. The second advantage is, that the **RF** signal available at the output port of the **MZM** is precisely synchronized to the laser pulse train in case a **PLL** is active.

If no **MZM** with an **RF** output is available the situation immediately becomes more complicated. In this case an output signal has to be split off before the **RF** signal enters the **MZM**. The required splitter can easily degrade the phase stability of the **RF** output signal which no longer originates directly from the **MZM**. Usually, both the **MZM** (to achieve high sensitivity) and the application require high **RF** power. The required **RF** power needed to achieve the same sensitivity of the **L2RF** setup and to maintain the previous output power needs to be doubled due to the signal splitting. The feed-through option however allows to use the same **RF** signal for the measurement and later as output signal for applications. In the case of the used EOSpace **MZM** [EOMz], this signal is only attenuated by the **RF** insertion loss of about 1.5 dB.

## 4.2 Operation and Adjustment of the L2RF Phase Detector

After installing all components, the setup needs to be adjusted for operation. Concerning the optical setup this adjustment covers not only the alignment of the free-space components – which is the first step to be performed – but also the setting of appropriate splitting ratios and delay lengths. A convenient measure for both parameters is the **RF** spectrum of the pulse train at the output of the optical setup. As explained in chapter 2, each parameter causes a specific modulation of the **RF** spectrum at a particular modulation frequency (see section 2.7.1 to recall the specific attribution). The spectrum can be measured using a photodiode and an **RF** spectrum analyzer.

The first delay line can be isolated from the setup and adjusted by blocking the second delay line, applying a fixed bias voltage to the **MZM** and by disconnecting the **RF** signal. The observed spectrum is only influenced by the delay length and splitting ratio of the first delay line. Both have to be iteratively optimized until the frequency component at the associated modulation frequency has vanished completely. The same iterative optimization procedure has to be applied to the second delay line. The splitting ratio at the second delay line is controlled by the bias voltage of the **MZM**. The adjustment procedure also needs to be performed while no **RF** signal is connected and one has to keep in mind, that this

delay line is associated to another modulation frequency. In a laboratory environment, it is convenient to use an RF spectrum analyzer to see the whole RF spectrum of the pulse train but it is also possible to observe only the isolated signal at the modulation frequency by using the readout electronics.

The adjustment procedure of the splitting ratio at the first delay line is more complicated for the first laboratory prototype because this delay line needs to serve two detector setups at once. The splitting ratio changes for both connected L2RF phase detectors inversely. The pulse balancing at the input of each MZM depends on the combined settings of the  $\lambda/2$  waveplates in front of the delay line and in front of the following polarizer.

After the adjustment of each delay line, the incoupling into the respective PM fiber collimators should be checked and optimized by the  $\lambda/2$  waveplates mounted in front of them. Each fiber collimator is followed by a polarization selective device (MZM, PM combiner) and the optimization is as simple as finding the waveplate setting with the highest transmission through that device.

The electrical components for the readout need to be set up next. The LO signal needs to be checked and the correct power levels have to be supplied to each mixer. The adjustment of the measurement channels is performed by the mechanical phase shifters inserted into each LO channel. The error signals are separated by a phase shift of  $\pi/2$  and each readout setup is supposed to only receive one of them. The goal of the adjustment is thus to minimize cross talk between the readout channels and to maximize their sensitivity.

The phase error channels of both L2RF phase detectors are set up while the RF signal still needs to be switched off. The bias voltage of each MZM is being modulated and the phase shifter of the associated phase error channel is adjusted such, that this bias voltage modulation is fully suppressed in each phase error measurement channel. The RF mixers in both L2RF phase detectors follow a cosine characteristic (see appendix B). By suppressing the modulated bias error signal, the working point of this error channel is aligned to a zero crossing of the cosine mixer characteristic. The phase error signal which is phase shifted by  $\pi/2$  with respect to the bias error signal will thus be measured at either a maximum or a minimum of the cosine mixer characteristic. Both operating points guarantee the highest possible output signal from the mixer. The steepness of the cosine mixer characteristic in the zero crossing allows the precise suppression of cross talk from the bias error signal into the phase error channel at the adjusted working point.

The bias error measurement channels of both the in-loop and out-of-loop L2RF phase detectors should receive now a coarse adjustment by maximizing the detected modulation of the bias voltage. The fine adjustment will later improve the sensitivity of the bias voltage error channel and eliminate possible cross talk from the phase error channel. At this point, a fine adjustment is not possible because the working point of the RF mixer is now



in the maximum or minimum part of the cosine function and insensitive to LO phase adjustments.

The bias voltage modulation is now switched off and one can finally switch on the RF signal. A beat-note is visible in the output signal of the phase error channels of both L2RF phase detectors as long as the DRO is not phase-locked to the reference laser. The beat-note might also be visible in the bias error channel. The phase of the bias error channels should now be fine adjusted until the beat-note is no longer visible in their output signal.

After the adjustment of the last error channel one can close the PLL and phase-lock the DRO to the reference laser pulse train by feeding back the phase error signal of the in-loop phase detector to the control voltage input of the DRO via a proportional-integral (PI) controller. The bias feedbacks of both measurement channels can now also be operated. Each error signal is fed back to the bias input of the corresponding MZM via further PI controllers.

The in-loop L2RF phase detector is permanently operated in its working point due to the active PLL. The phase at the out-of-loop phase detector is arbitrary and needs to be manually adjusted by the phase shifter in the RF path between the two MZMs in order to reach the working point. The output signal of the phase measurement channel of the out-of-loop phase detector has to be tuned to zero. The phase detector can also reliably measure non-zero phase errors. The measurement range depends on the sensitivity of the L2RF phase detector and the output range of the involved DC LNA which saturates at a certain voltage. The intrinsic error suppression of the setup however only applies at the working point at zero phase difference.

A calibration of the setup needs to be performed in order to be able to interpret the measurement results. The PLL is opened and the phase to voltage conversion coefficient is calculated from the steepness of the beat-note in its zero crossing. The slope in the zero crossing  $s_{\text{beat}}$  and the period of the beat-note  $T_{\text{beat}}$  need to be determined. One period of the beat-note corresponds to a phase shift of  $2\pi$  between the laser pulse train and the RF signal. The calibration constant  $K_\phi$  which allows to convert the voltage signals from the L2RF output to a delay is calculated by following equation (4.1).

$$K_\phi = s_{\text{beat}} T_{\text{beat}} f_{\text{RF}} \quad [K_\phi] = \text{V/s} \quad (4.1)$$

Typical calibration constants which have been achieved with the specified components are in the range of 0.5 mV/fs to 2 mV/fs (each for the lowest available LNA gain of 10). While the calibration constant can be improved by implementing higher amplification factors in the readout chain, the signal-to-noise ratio (SNR) of the setup can only be improved by increasing the optical power on the photodiode or by increasing the modulation depth at the MZM. An improved alignment of the optical setup or an increase of the RF power at the MZM should therefore always be considered first.



### 4.3 Practical Considerations on Possible Error Sources

Many of the previously described adjustments are performed by the minimization of output signals because they rely on null measurements. A precise offset compensation of the involved **DC LNAs** is therefore highly advised. Any offset of these amplifiers leads to imprecise adjustments. Offset drifts in the phase error channel are even interpreted as phase drifts. A possible solution to this problem is offered in chapter 6.

The utilized **RF** filters need a very high stop-band attenuation. Before filtering, the same frequencies are present in the spectrum of the **LO** and the error signal. If any other than the desired frequency component is transmitted to both inputs of the **RF** mixer, this frequency component is also mixed to the baseband and superposed with the output signal of the detector. This effect is worse if the disturbing frequency component still has the original amplitude while the detected frequency component is extinct in the working point. Despite from selecting high quality **RF** band-pass filters, an additional low-pass filter can support the suppression of unwanted harmonics.

Phase drifts detected by the out-of-loop **L2RF** phase detector do not have to indicate measurement errors of the **L2RF** phase detector. Instead, the **L2RF** phase detector might be measuring an actual phase drift which is caused by a real phase shift of one of the involved signals. This situation is caused by the measurement setup instead of the phase detector.

In order to characterize the detector and not the measurement setup, one has to ensure by all means that the phase of the measured signals is constant over time. Potential sources of an unwanted external phase drift are the beam transport from where the laser beams are split up until they arrive at each **MZM** and the transport of the **RF** signal between the **MZMs**. In figure 4.5, the affected paths are highlighted in the already known block diagram of the first prototype.

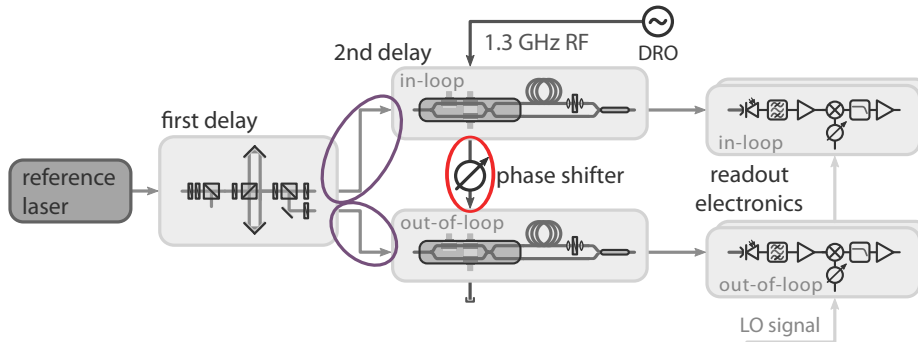


**Figure 4.5: Typical Sources for Phase Drifts of the Measurement Setup** | In order to characterize the **L2RF** phase detector instead of the measurement setup, the above highlighted connections need to be phase stable.

The beam transport is highlighted in purple. It involves free-space and fiber transport. Both types suffer from temperature changes which cause thermal expansion of breadboards, fibers and even the optical bench itself. Fibers are furthermore susceptible to humidity changes, which has been confirmed in an in-house measurement at [DESY](#). Typical values for standard [PM](#) and [single mode fiber \(SMF\)](#) are in the order of 2.5 fs/(m %RH). A uniform drift of both arms does not affect the presented prototype. The effect can therefore be mitigated if the free-space and in-fiber transport to both [MZMs](#) are of equal length.

The transport of the [RF](#) signal between the [MZMs](#) (highlighted in red) however is far more critical because each length change of this cable or the phase shifter mounted there is directly detected by the out-of-loop phase detector. Temperature induced length variations of [RF](#) cables are a well known circumstance and it was initially assumed that the used cables could be length stabilized by accurate temperature control. However it turned out during later measurements with the second laboratory prototype, that [RF](#) cables also show a significant humidity dependence. Three different cables have been characterized in order to investigate this matter.

#### 4.4 RF Cable Characterization

As a reference, a standard coaxial cable (Pasternack, PE-SR402FL, see [\[SR402\]](#)) has been tested. This cable type has been used in the initial [L2RF](#) prototype for all [RF](#) connections. Furthermore two cables which are advertised by their manufacturer as being phase stable have also been tested (Sucoflex 404, see [\[HS404\]](#) and Phasemaster 190E, see [\[PM190\]](#)). All three cables are flexible and can be easily handled in a laboratory environment. While the temperature coefficients of these cables are specified by the manufacturer, humidity effects are usually not addressed in the data sheets. The characterization has been carried out in a climate chamber where humidity and temperature can both be controlled independently and in a wide range. In addition to the humidity coefficients, the temperature coefficients have also been determined.

The specimens have been mounted into the climate chamber and connected to a 1.3 GHz [RF](#) source. The phase difference between output and input has been recorded with [AD8302](#) (see [\[AD8302\]](#)) based phase detectors. The humidity characterization has been performed at three different temperatures. The humidity coefficients have been measured by applying a humidity step of 30 %RH to the specimens after they have been acclimatized in the chamber. The  $1/e$  time constants of the cables humidity susceptibility has been determined to be 8 h for the Pasternack cable and 20 h for each of the phase stable cables. The humidity coefficients have been calculated from the measurement data and they are presented in table [4.1](#).

The temperature coefficient shows larger variations over the operating temperature and has therefore been determined at sixteen temperatures distributed over a temperature range

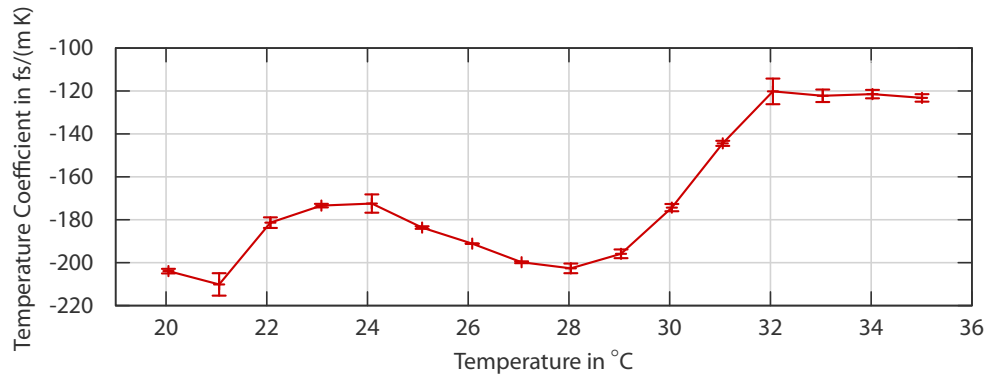
**Table 4.1: Experimentally Determined Humidity Coefficients of RF Cables |**

The coefficients have been measured at three different temperatures which are specified in the table. So-called phase stable cables show a factor two to four improved humidity performance over the standard cable.

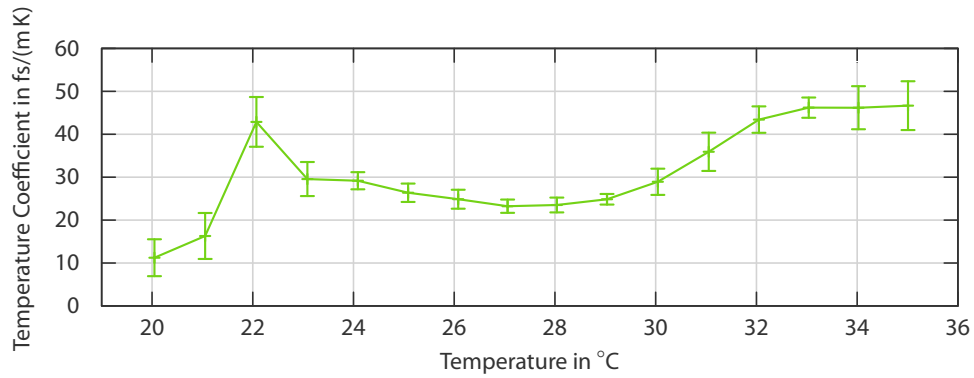
cable type	humidity coefficients in fs/(m %RH) at 1.3 GHz			
	temperature:	21 °C	25 °C	29 °C
Pasternack Enterprises Inc.				
PE-SR402FL [SR402]		8.9	9.6	10.3
Huber + Suhner AG				
Sucoflex 404 [HS404]		2.6	3.5	5.0
Teledyne Storm Microwave				
Phasemaster 190E 874 [PM190]		2.1	3.4	4.6

from 20 °C to 35 °C and a relative humidity of 39 %RH. The measurements of the phase stable cables have been repeated four times and the measurement of the standard coaxial cable has been performed twice. The results are presented in figure 4.6. Depicted are the mean values and the standard deviations of the measurements. Especially at the measurements of the phase stable cables the measurement uncertainty is caused by environmental influence on the measurement setup in conjunction with the comparably small overall drift of the tested cables. The samples had a length of 6 m (Phasemaster 190E) and 10 m (Sucoflex 404). Longer samples which could have mitigated the effect were not available at the time the measurement was performed due to very long lead times. The sample of the standard cable (Pasternack, PE-SR402FL) also had a length of 10 m but due to its higher temperature coefficient, environmental influences on the measurement setup did play a less important role compared to the measured phase drift.

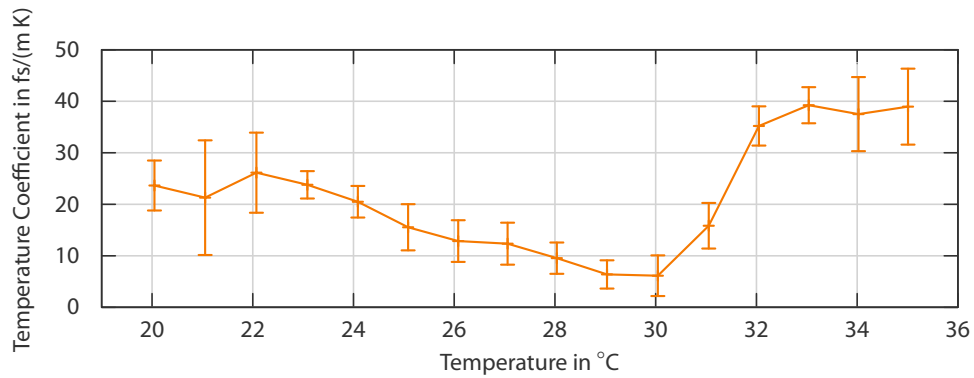
The temperature performance relative to the reference sample of the standard cable can be improved depending on the operating temperature by a factor between three and twenty in case of the Phasemaster 190E cable while the humidity performance can be improved at the same time by a factor between two and four. One can easily conclude, that phase critical connections should be made – even in a well controlled environment – by special phase stable cables. Nevertheless, critical cable connections have to be kept as short as possible if femtosecond performance is demanded. Additionally the cable performance can be significantly influenced by choosing an operating temperature with low temperature and humidity coefficients.



(a) Temperature Coefficients of the Pasternack PE-SR402FL Cable



(b) Temperature Coefficients of the Huber + Suhner Sucoflex 404 Cable



(c) Temperature Coefficients of the Teledyne Phasemaster 190E Cable

**Figure 4.6: Experimentally Determined RF Cable Temperature Coefficients** | The measurement has been carried out at a relative humidity of 39 %RH and an RF frequency of 1.3 GHz. The phase stable cables show a significant improvement over the tested standard coaxial cable.

## 4.5 The Second Laboratory Prototype

After the proof-of-principle experiments with the first laboratory prototype had delivered successful measurement results (see section 4.7.1), the construction of a second prototype has been pursued. This prototype included two major integration steps. First of all, the complete optical setup was combined and miniaturized in a compact, fully engineered optical unit and second, the detector electronics have been advanced from a huge assembly of bulk components to a compact and integrated device, based on a single [printed circuit board \(PCB\)](#). Almost all bulk components from the first laboratory prototype are replaced with specifically engineered devices.

Only the components around the 1.3 GHz setup have not yet been integrated at this time. The [DRO](#) still serves as [RF](#) source and its signal is amplified by the same amplifier as before. The phase critical components between the [MZMs](#) however have been exchanged. In order to minimize the influence on the measurement result by the [RF](#) transport from the in-loop to the out-of-loop [MZM](#), a smaller phase shifter (Aeroflex Weinschel 980-4, see [\[PS980\]](#)) was used together with the shortest available piece of Phasemaster 190E cable (250 mm).

### 4.5.1 Integrated Optics for the L2RF Phase Detector

The optical components have been integrated on a single, solid aluminum baseplate. The design of the baseplate was supported by a rapid prototyped (3D-printed) preproduction mock-up where the feasibility of the design and options for the alignment could be tested before the production of the real baseplate started. A photograph of the prototype of the baseplate is depicted in figure D.4.

A housing has been constructed for environmental decoupling. The baseplate and the housing have been designed in a way that they can fit into a three [rack unit \(U\)](#), 19" standard housing with a depth of 450 mm and fill only half of its width such that sufficient free space remains for electronics. All free-space components on the baseplate are mounted in an angle of 1° to 3° to the beam such that possible reflections are separated from the laser pulse train and not transmitted back to the optical reference. The risk of double reflections which would follow the pulse train to the readout electronics is also minimized this way.

The baseplate is designed to be operated as end station of a length stabilized optical fiberlink and therefore equipped with a fiber instead of a free-space input for the reference laser pulse train. The fiberlink itself is terminated with – and stabilized up to – a fiber-coupled [FARADAY rotating mirror \(FRM\)](#) [\[Zum<sup>+</sup>13\]](#). All components between this [FRM](#) and the [MZM](#) of the L2RF phase detector are not drift compensated and require therefore the best achievable passive stabilization. This includes the fibers from the [FRM](#) to the free-space optics, the complete free-space path through the first delay line and the optical fibers up to

the **MZM**. The complete baseplate is for this reason actively temperature controlled and humidity sealed by a fully closed housing. Additionally, all unstabilized fibers are supposed to be kept as short as possible.

The baseplate has been constructed for different operation scenarios. This is addressed by the option to mount an alternative **MZMs** and by a huge adjustment range of the length of the first delay line. The overall layout of components did not change significantly from the first prototype but some small improvements have been made.

Behind the input fiber collimator, the optical setup is equipped with a pair of one  $\lambda/2$  and one  $\lambda/4$  waveplate followed by a **PBC** acting as polarizer. In the second prototype, the **L2RF** phase detectors are fed by a simple **single mode (SM)** fiber where these components are used to linearly polarize the input laser pulse train. The polarizer and the waveplates can also be used for power adjustments. The setup provides the option to couple the light which is not transmitted by the polarizer into a fiber collimator and use it for future applications (for example measurements for an active polarization control). The option to motorize the two discussed waveplates and thereby gain remote control over their setting and the input polarization is also foreseen. An active polarization control is required in case the **L2RF** setup is operated behind a **SM** fiberlink although from practical considerations this polarization control is easier to implement at the start of the fiber link in its **link stabilization unit (LSU)**. The advantage is, that continuous maintenance access is possible in the synchronization room where the **LSUs** are located whereas the accelerator tunnel is closed during operation. For **FLASH** and the European **XFEL** it is planned to operate **PM** fiberlinks [Syd<sup>+</sup>14] where these components are not needed as long as no significant cross-coupling into the fast axis of the **PM** fiber occurs during the transport.

The hollow metal **CCRs** from the first prototype have been replaced with solid glass ones in order to minimize optical losses in the setup. It nevertheless needs to be mentioned, that the polarization of the incident and reflected beams of a **CCR** are not necessarily identical. The polarization of the reflected beam is altered by the **CCR** depending on the angle and point of incidence. This phenomenon can be particularly observed for solid glass **CCRs** which rely on total internal reflection. Metal coated or hollow metal **CCRs** also show this behavior – although to a far lesser extent [He<sup>+</sup>13]. Therefore it is highly advised to insert a clean-up polarizer into the actual delay line. An additional **PBC** is perfectly suited for this task. Practically this **PBC** is mounted face-down between the second **CCR** and the **PBC** used for splitting and recombination of the pulse train. This clean-up polarizer blocks all unwanted states of polarization which would not properly exit the delay line but instead start over to run a second time through it. One **CCR** is mounted on a manual three axis translation stage while the second one has a fixed mount which can be placed at different positions in a 88 mm range. The overall delay of the first delay line can be adjusted from 0.99 ns to 1.58 ns.

The remaining components after the delay line have not been altered from the first prototype. The first delay line is followed by the clean-up polarizer which transmits half of each pulse train from the delay line into the MZM. There is an option foreseen to couple the reflected light from the clean-up polarizer into an additional fiber collimator and use it for future monitoring tasks.

The MZM itself is mounted thermally conductive on the temperature controlled aluminum baseplate. The baseplate has been designed in a way, that not only the EOspace MZM [EOMz] foreseen for the operation at a wavelength of 1550 nm can be mounted, but also MZMs for 800 nm from the German company Jenoptik<sup>1</sup> fit on the baseplate.

The baseplate finally provides two additional fiber collimators, one of them mounted on a manual translation stage and an adjustable  $\lambda/2$  waveplate between them. These collimators are needed for the fine adjustment of the otherwise fiber-coupled second delay line. Further mounting options are foreseen for multiple temperature sensors, a humidity sensor and a mounting angle where the two involved FC/APC connectors (practically the two connectors at the output fibers of the MZM) can be fixed. The fiber components are guided through the free-space optics directly on the temperature stabilized aluminum baseplate and fixed to it by tape.

Different from the situation in the laboratory, environmental conditions in an accelerator environment are less stable. Humidity for example is not controlled at all in the tunnels of FLASH and the European XFEL. The temperature is also not precisely controlled in the tunnels although the so-called low-level radio frequency (LLRF) racks in which the L2RF phase detectors are going to be installed are equipped with air conditioning units. The temperature in the racks is however only specified with an accuracy of  $\pm 1$  K because high-end digital electronics and other power consuming devices are housed there. This accuracy is by far not sufficient to achieve the desired femtosecond performance from the L2RF setup. It is additionally not known which level of vibrations has to be anticipated from a fully equipped rack. It was therefore decided to take countermeasures against all three potential error sources which are temperature, humidity and vibrations.

### Active Temperature Control

The baseplate is manufactured from aluminum. Aluminum has a very good thermal conductivity of about 204 W/(m K) [Dah<sup>+</sup>13] which is supposed to minimize thermal gradients over the baseplate. The size of the baseplate was minimized as much as possible but the miniaturization was limited by the number of components needed to cover all mandatory and optional requirements. Two high power PELTIER elements which can each transport a thermal load of 30 W are mounted below the baseplate and driven by an analog

<sup>1</sup>Further information about the MZM portfolio of Jenoptik is available at <http://www.jenoptik.de/produkte/optoelektronische-systeme/lichtmodulation/integriert-optische-modulatoren-iom/amplitudenmodulator>

temperature controller (PTC10k-CH, see [PTC10k]). One of them is mounted directly below the MZM which is known to be sensitive to temperature variations [Jan12]. The reference sensor for the controller (a 10 kΩ negative temperature coefficient of resistance (NTC) thermistor) is mounted right next to the MZM because the highest thermal stability is required at this point. The complete baseplate including the housing and the bottom side of the baseplate is isolated with 9 mm of elastomeric foam (see [Arflx]). The final position of the mounted PELTIER elements and the thermal isolation are presented in figure D.5. The photograph shows an improved isolation on two sides of the optical setup which have been introduced during the assembly of the accelerator prototype but which were not present during the laboratory measurements. Polypropylene screws are used to mount the baseplate to the heat sink in order to limit the thermal coupling. The heat sink has continuous longitudinal cooling fins on its bottom side and the same footprint as the baseplate. Ventilation openings in the front and rear panel of the 19" housing allow air to flow through the cooling fins from the front to the rear side which is the air flow direction forced by the air conditioning unit in the rack. The heat sink is sealed to the housing by tape which prevents air from the ventilation openings in the front and rear panels of the housing to reach other components than the heat sink.

### Passive Vibration Damping

The complete assembly of heat sink and optics is mounted on 4 rubber dampers and floating within the 19" housing to compensate external vibrations. The rubber dampers are shown in figure D.14 where the first heat sink is mounted to the bottom plate of the 19" housing.

### Passive Humidity Sealing

The humidity sealing as the third protective measure is mainly performed by the housing which surrounds the optical setup. The aluminum baseplate is already diffusion resistant but one has to close all open threads with screws in order to leave no openings. The initial cover has been constructed from high density polyethylene (HD-PE) which can only absorb less than 0.01 % of water relative to its own weight and thus is also a very good water vapor barrier. The housing is held together by polypropylene screws for thermal reasons and all connections between the different parts have been either glued or equipped with gaskets.

All in- and outgoing fibers and small cables are simply guided through the front gasket of the cover which still seals sufficiently well. The RF cables at the MZM however are too thick for this procedure. The MZM is therefore mounted in a pocket of the baseplate. Special drill holes allow to guide all RF connections directly out through the baseplate via SubMiniature version A (SMA) adapters. The holes are sealed with rubber o-ring gaskets as shown in the photographs in figures D.7 and D.8.

The housing can slow down effects of outside humidity changes but not avoid them completely because it is not vacuum tight. As an additional measure against humidity variations,



a dust-proof sachet with 250 g of a special silica gel called PROSorb (see [ProS]) is therefore mounted below the cover inside the compartment. PROSorb can hold up to 30 % of water relative to its own weight at 50 %RH which is more than ordinary silica gel can hold. A photograph of the arrangement of components inside the housing where also the PROSorb sachet is visible can be found in figure D.6. The silica gel acts as humidity buffer because it can store and release humidity from and to the air.

### Climate Chamber Measurements

Both the active temperature control and the passive humidity stabilization have been tested in a climate chamber. The measurement setup is presented in the photograph in figure D.9. The development of the humidity inside the housing after a jump of the environmental humidity by 15 %RH is plotted in figure 4.7. The measurement took two weeks. The offsets between the curves have to be attributed to the interchangeability of the used sensors, which is given in the data sheet [HIH4] to be only  $\pm 5$  %RH. The first investigated housing has only been sealed but the humidity inside still slowly adopted the outside parameters during the measurement. The second housing however showed only a change of 2.3 %RH peak-to-peak in these two weeks because it was equipped with PROSorb.

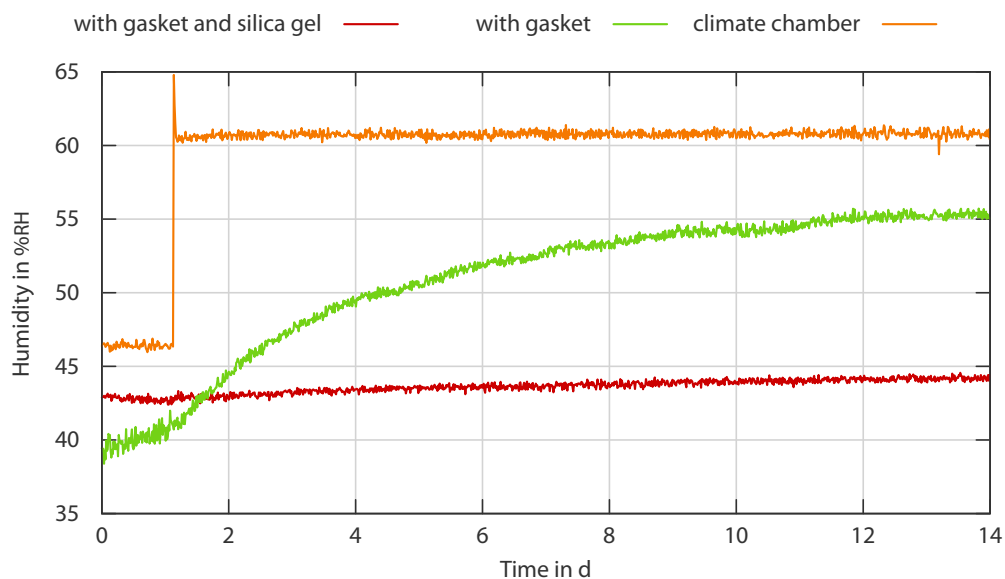


**Figure 4.7: Humidity Stability in Housings for the L2RF Phase Detector** | Both housings are sealed but only one housing is equipped with PROSorb as humidity buffer.

The temperature stability of the baseplate has also been measured in the climate chamber. The temperature controller can only fix the temperature at the point where its reference

sensor is mounted. A temperature gradient will emerge over the baseplate as soon as the outer temperature is different from the internal temperature and the gradient will also change with the external temperature. The figure of merit is the suppression factor by which the temperature controller can suppress outside temperature changes at the point where its sensor is mounted. Additionally, the question arises, by how much the temperature is influenced by outside temperature changes at the corner of the baseplate. The complete optical assembly has been tested by a step of the outside temperature of 30 K. After the settling time a variation of 0.3 K has been detected at the [MZM](#), 1.4 K have been detected in the corner of the baseplate next to the sensor and 3.1 K in the corner with the largest distance from the sensor (worst case). The suppression factors for outside temperature variations are therefore found to be between 10 and 100. The temperature stability of the baseplate when the [L2RF](#) phase detector is operated in the [LLRF](#) racks can therefore be expected to be around  $\pm 0.01$  K close to the [MZM](#) and  $\pm 0.1$  K worst case at the outer border of the baseplate. The only option to improve this performance is by increasing the isolation around the housing.

The [L2RF](#) setup consists of about 250 mm of unstabilized fiber<sup>1</sup> which will – if guided at the outer corner of the housing – drift by 2.5 fs taking the expected temperature stability at this point of  $\pm 0.1$  K and the thermal coefficient of standard [SMF](#) of 50 fs/(m K) (worst case assumption from [[Bou<sup>+</sup>12](#)]) into account. Additionally, there are about 530 mm of free-space beam transport over the aluminum baseplate. Assuming a mean temperature variation of about  $\pm 0.025$  K and taking the thermal expansion coefficient of aluminum of 23.8  $\mu\text{m}/(\text{m K})$  [[Dah<sup>+</sup>13](#)] into account this temperature change will lead to another 2 fs of drift. The combined estimated drift therefore amounts to 4.5 fs which is well within the budget of 10 fs – especially because the estimation is conservative. Humidity influences are not regarded here, because the construction of the housing together with the PROSorb humidity buffer practically prevents them.

### Latest Modifications

The latest modification of the optical setup concerned the material of its housing. Initially, the walls were made from [HD-PE](#) in order to shield its content from humidity changes while providing reasonably low thermal conductivity. During the adaption for a different wavelength/repetition rate combination by [[Tit<sup>+</sup>14](#)] who uses the same baseplate, it turned out, that the resistance to bending of the baseplate was not strong enough for the implementation of a single output [MZM](#) based [L2RF](#) setup. This setup crucially relies on the splitting ratio stability of the first delay line which is not the case for dual output [MZM](#) based setups as explained in section 2.6. The plate can practically be slightly bent by tightening the mounting screws or mounting the top cover. Thereby the alignment and so the

<sup>1</sup>This includes already the unstabilized fiber between the [FRM](#) forming the end of the length stabilized fiberlink and the input fiber collimator of the [L2RF](#) setup.

splitting ratio of the first delay line is changed. The fact was confirmed in an in-house [finite element \(FE\)](#) analysis. Three options and the original configuration have been evaluated in a standard test case in order to improve the situation. The [FE](#) calculations were performed for the case when the baseplate is fixed in a support at one side and loaded by a constant force on the opposite side while the elastic deflection was computed. The evaluated options are:

**Increase the thickness of the baseplate by 15 mm** and thereby increase its stiffness.

Due to the limited space in the 19" housing this option is only suitable for laboratory operation. It had to be discarded although the simulation promised about 83 % less bending in the test case and one can expect a better heat distribution in the baseplate due to its thicker body.

**Change the material of the housing to aluminum** (except the top cover) and provide thereby additional stabilization to the baseplate through the solid housing. This option decreases the thermal performance because an aluminum housing conducts heat better than a housing made from [HD-PE](#). This option has been implemented because it nevertheless promised a good result of 79 % reduction in bending in the simulation.

**Change the material of the baseplate to steel** and thereby increase its stiffness by increasing [YOUNG's](#) modulus. This modification significantly decreases the thermal performance because the temperature gradient on the baseplate increases due to the by a factor of four to fourteen lower thermal conductivity of steel compared to aluminum (the factor depends on the actual alloy [[Dah<sup>+</sup>13](#)]). The temperature stability is considered so important that this option was not further pursued. Additionally, the bending decreased in the simulation only by 48 % which is less than in the previous cases.

While the long-term measurements in the laboratory have been still performed with the initial [HD-PE](#) housing, the accelerator prototype is as a precaution against mechanical stress already equipped with the new aluminum housing. Additionally, the thermal isolation at the long sides of the housing was increased together with the change of material in order to compensate for the increased thermal conductivity of aluminum. Only the long sides of the housing allowed to use 25 mm of isolation because the optical assembly already fills the 19" housing in height and depth. The heat sink and the vibration damping rubber buffers also have not been used in the laboratory. There was no vibration damping needed on the optical bench which also served as heat sink for the [PELTIER](#) elements for the thermal control. A final look on the integrated optics is provided by the photograph in figure [D.10](#).

### 4.5.2 Integrated Readout Electronics

The readout electronics of the first laboratory prototype consist of bulk components which occupy too much space to be installed into the foreseen 19" housing. Additionally, they are not remote controllable. For this reason a project for the miniaturization by integration of the electronics on a PCB in the frame of a master thesis has been started and successfully completed [Jan12]. The technical realization is laid out in detail in the final thesis and will not be repeated here. Instead basic information on important changes of the implementation of the readout device is provided together with relevant design parameters for its operation.

The laboratory setup included two RF mixers per L2RF phase detector, each equipped with a dedicated phase shifter used to adjust the working point. In the integrated readout electronics however these RF mixers have been replaced by one single in-phase and quadrature phase (I/Q) demodulator. Such a device can be used to decompose an RF signal into its in-phase and quadrature (I and Q) components and it is therefore perfectly suited to detect the  $\pi$  phase shifted signals from the L2RF setup. Internally an I/Q demodulator is usually composed of a 90° hybrid which is used to generate two,  $\pi/2$  phase shifted LO signals which drive the two internal mixers. The input signal is mixed in the internal RF mixers with both internal LO signals and thereby the I/Q components of the input signal relative to the LO signal are detected. Only one LO phase shifter is needed to operate the demodulator.

The signal chains of the integrated readout electronics each start with a photodiode – one for the detection of the three error signals from the L2RF phase detector and the second one for the generation of the required LO signals. The photodiodes are mounted on the PCB and can be accessed via FC/APC connectors from outside the housing. In addition to the two error signals which are detected by the I/Q demodulator, the integrated electronics include a third readout channel which is suited to detect the splitting ratio error at the first delay line. This third channel will allow in the future to set up a feedback loop and actively control the splitting ratio which is otherwise only passively monitored.

Behind the photodiode which detects the modulated error signal a directional coupler is integrated which is directly guided outside the housing. The coupler allows to monitor the complete modulated frequency comb before any processing is performed and thereby to precisely analyze the current state of the setup without interfering with the actual readout electronics.

The internal voltage controlled phase shifters are driven via digitally controlled on-board digital-to-analog converters (DACs). Three digitally controlled RF attenuators in the RF paths and shift registers used to control the gain of the three output LNAs can be controlled via a serial parallel interface (SPI) bus. For monitoring purposes, two PT-1000 temperature sensors are additionally mounted on the PCB. They are connected using the 4-wire method

to the outside of the housing. The device needs to be powered by positive supply voltages of 7 V and 15 V from which internally all required voltages are created.

Figure 4.8 provides a schematic overview on the main RF components in the readout electronics. The monitoring coupler behind the photodiode has been omitted. The utilized I/Q demodulator needs a LO signal at twice the frequency of its RF signal. Therefore the LO chain can also be used to drive the RF mixer, which is operated at this higher frequency.

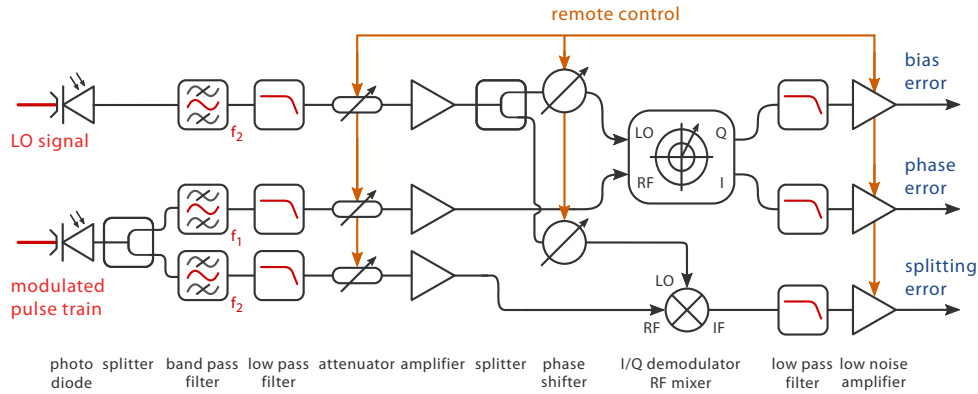


**Figure 4.8: Schematic Block Diagram of the Integrated Readout Electronics** | The principle signal generation of all three channels is depicted. Figure adapted from [Jan12].

The complete circuit is designed on a single PCB which is mounted in a compact housing. The integrated detector electronics have been used in the second laboratory prototype and the accelerator prototype. The photograph in figure D.13 shows the readout PCB operated in an open housing.

## 4.6 The Accelerator Prototype of the REFM-OPT

After further long-term measurements with the second laboratory prototype, which are presented in section 4.7.2, the next step has been the integration of the L2RF phase detector into a 19" device suited for operation at FLASH and the European XFEL. The L2RF phase detector has a dedicated name at these facilities. Fully integrated and providing the features described below, it is called the optical reference module (REFM-OPT).

It is not planned to include a DRO like it was used during the laboratory measurements into each REFM-OPT. Instead the REFM-OPT is supposed to use 1.3 GHz signals which are centrally distributed in the accelerator to the locations where the REFM-OPT is supposed to be operated. The reason for this decision is the requirement, that all LLRF devices

throughout the accelerator should be provided with the same correlated phase noise. This is not possible if a dedicated DRO is installed in each REFM-OPT. Additionally, the reliability of the overall LLRF system is increased by relying on central and redundant components like a central radio frequency master oscillator (RF-MO) for the 1.3 GHz supply because the probability of failure of one of several individual DROs throughout the accelerator is comparably high.

The 1.3 GHz RF signals are transported from the RF-MO to specific locations in the accelerator tunnel by long RF cables which experience phase drifts due to environmental changes along them. At the European XFEL, these RF cables are planned to be additionally stabilized by an RF based interferometer [Czu<sup>+</sup>13] following the concept from [Cul11]. In DESY internal tests, a phase drift suppression factor of 300 has been achieved<sup>1</sup> for the RF interferometer. In the case of the European XFEL, temperature variations in the accelerator tunnel will lead to residual phase drifts which depend on the length and the type of the used RF cable and the suppression factor. Especially for long transmission lines the achievable stability of this technique does not fulfill the femtosecond requirements of the LLRF system although other subsystems with relaxed stability requirements can be directly supplied. Additionally, this system provides a very high reliability. For femtosecond accuracy at the LLRF system however a laser-based synchronization solution like the REFM-OPT, which in return is more complex and expensive, needs to be implemented on top of the RF interferometer.

One custom part is still missing for the construction of the prototype of the REFM-OPT. In all laboratory measurements up to now, the RF signal has been provided by a local DRO dedicated to the L2RF setup. This is not the case for the REFM-OPT where the 1.3 GHz signal is externally provided. The removal of the DRO from the setup does also remove the tuning point for the 1.3 GHz phase. Therefore the need for a phase actuator arose and it was decided that this problem should be solved by another piece of custom hardware. This project has been handled by [Jan<sup>+</sup>14] and it is called the REFM-OPT actuator (REACT) electronics. Details can be found in the cited paper, such that here only the general requirements and thoughts concerning the integration of the REFM-OPT will be laid out.

#### 4.6.1 The REFM-OPT 1.3 GHz Actuator Electronics

In the LLRF system, the REFM-OPT needs to supply a varying number of customers with phase stable RF signals. The number of customers and their power requirements dictate the output characteristics of the REFM-OPT. At FLASH, up to four external devices from the LLRF system with the need for femtosecond precision synchronization will be connected to one REFM-OPT, which are usually one drift calibration module (DCM), one or two

<sup>1</sup>personal communication, Dominik Sikora, February 2015

LO generation modules (LOGMs) and a possible connection to a slave LLRF station. These devices need to be provided with a maximum of 21 dBm of RF power each. Even short interconnection cables to these external devices can easily lead to the loss of the femtosecond synchronization accuracy. The installation of an RF splitter behind the MZM is not an option due to the additional phase drifts added to the output signal by it. Both, the splitter and the integrated REACT electronics have to be installed in front of the MZM where they are within the L2RF PLL and phase drifts induced by these components are compensated. It was decided that the RF splitter is not included in the integrated REACT electronics which allows to exchange it later for a splitter with less or more outputs as needed.

In order to determine the phase stability between different outputs of an RF splitter, the envisioned custom made splitter selected for the REFM-OPT has been tested by [Jan<sup>+</sup>14] and the phase stability between two outputs has been found to be below 20 fs/K at a temperature of 28 °C. By providing an active temperature control of the splitter, the desired femtosecond accuracy therefore is easily achievable. This should not be confused with the input to output phase stability of the splitter which is much worse but does not matter in the presented setup because the splitter is operated inside the L2RF PLL.

The REACT electronics in summary needs to provide the following minimal features:

- A remote controllable RF switch is required behind the RF input, to disable the RF signal in the complete REFM-OPT in order to adjust the L2RF phase detector.
- RF power monitors are needed at the input and output of the board for supervision and to implement a feedback for the output RF power. They should be connected via directional couplers to the main line.
- Direct access to the 1.3 GHz RF signal at the output of the REFM-OPT for phase noise measurements should be provided by a directional coupler.
- A remote controllable RF attenuator which can compensate fluctuations of the RF input power should be foreseen.
- A vector modulator to adjust the phase and the amplitude of the 1.3 GHz RF signal is required. Alternatively, a phase shifter can be implemented if it covers at least one period of the 1.3 GHz RF signal.
- The board must provide at least 29 dBm of 1.3 GHz RF power such that four connected devices can be supplied with 21 dBm of RF power via a four-way RF splitter.

The demanded features have already been implemented in the vector modulator based prototype of the integrated REACT electronics by [Jan<sup>+</sup>14]. Because lower additional 1.3 GHz phase noise is expected from it, a second alternative prototype which is based on a phase shifter instead of a vector modulator will be fabricated soon.



#### 4.6.2 Integration and Assembly of the REFM-OPT Prototype

Not all devices were available in their final revision when the REFM-OPT prototype has been assembled. The RF splitter is still a bulk device from the company Mini-Circuits and supposed to be replaced by the tested custom made splitter in the final REFM-OPT. The analog temperature controller is designated to be replaced with a digital controller which can be remotely parametrized and promises to create less waste heat. A two channel optical power monitor is included as dedicated device which supervises the optical power in the fiberlink and the L2RF optics.

The temperature monitoring and control board (TMCB) is responsible for all control tasks like the PLL and the bias feedback of the L2RF phase detector but also for all monitoring tasks. This board also provides the connectivity to the accelerator control system via Ethernet. It was developed at DESY and will be used in various LLRF devices at the European XFEL.

The complete REFM-OPT is powered by a central and redundant 19" DC power supply called power supply module (PSM). The PSM supplies all LLRF 19" components in a rack. A power entry board called fuse and relay board (FRED) has been designed which is foreseen to be placed in all 19" units and therefore also in the REFM-OPT. The FRED implements management functionality for the 19" crate. It is also remote controllable via Ethernet and designed specifically to support the TMCB.

Photographs of the final REFM-OPT prototype are shown in figures D.15 to D.17 where the internals and the front and rear panel of the REFM-OPT prototype are presented.

As a first mounting step, the heat sinks are fixed at the bottom of the housing. One heat sink is dedicated to the optical setup, the second one to the electrical setup. Both heat sinks can be mounted on rubber dampers for vibration isolation which is currently only done for the optical setup. The heat sinks are isolated from each other by 9 mm of elastomeric foam in order to minimize thermal crosstalk between both thermal zones. The optical setup has been pre-aligned and adjusted externally and it is simply mounted on its dedicated heat sink without further modifications. All electrical components are mounted in the left half (seen from the front) of the 19" housing. The REACT electronics and the L2RF readout electronics can be stacked because they have the same footprint. The REACT electronics need to be mounted at the bottom, because the integrated high power RF amplifier needs direct contact to the heat sink. The temperature controller is also mounted directly to the heat sink, while the FRED is positioned in the rear left corner and like the optical power monitor mounted to the side wall of the housing. As the last device the TMCB is mounted on top of the other components.

The individual hardware components of the REFM-OPT prototype have all been separately tested before they were mounted. The REFM-OPT prototype will be installed at FLASH when the software for the internal digital controller is finalized and thoroughly tested.



## 4.7 Measurement Results from the L2RF Prototypes

Both presented laboratory prototypes have been investigated in terms of their performance. The long-term stability has been analyzed during drift measurements and evaluated by an out-of-loop phase detector. Environmental parameters like temperature and humidity have been recorded together with internal parameters like the bias voltage or the splitting ratio error in order to reveal possible correlations. The noise floor of both prototypes has furthermore been measured and the achievable accuracy has been determined.

### 4.7.1 Measurement Results from the First Prototype

The out-of-loop phase detector has first been calibrated. Its sensitivity was found to be  $K_{\phi,1}^{\text{ool}} = 1.27 \text{ mV/fs}$ . The long-term measurement lasted 40 h and the results are presented in figure 4.9. The data has been taken at a data rate of 0.1 Hz. The achieved out-of-loop performance printed in subfigure (a) was a huge success because 14.9 fs peak-to-peak and 3.8 fs [root mean square \(rms\)](#) drift have not been achieved before for a L2RF phase detector at 1.3 GHz (see chapter 5 for an overview on alternative techniques and competing results).

One should keep in mind, that for this kind of in-loop/out-of-loop measurements the phase error of the in-loop detector is actively suppressed by the PLL and always zero. This means that every measurement error of the in-loop detector is not detected as such and falsely compensated by the PLL. The phase drift measured at the out-of-loop phase detector therefore represents the combined phase drifts of the measurement setup plus the measurement errors of both the in-loop and out-of-loop L2RF phase detectors. The errors can never be separated from each other but the performance of a single detector can still be expected to be better than or equal to the actual measurement result.

One detail about the measurement has however been particularly conspicuous. The time domain shape of the drift curve in subfigure (a) shows a significant similarity to the development of the humidity in the laboratory over the measurement time presented in subfigure (b). A further indication for the humidity influence is the time shift between the humidity change and the caused phase drift. Humidity changes usually have a much slower influence on components compared to temperature changes.

The measured drift seems to be additionally superposed by another, not humidity related drift because the humidity at the start and at the end of the measurement is almost identical for several hours, while the measured phase drift seems to have another, linearly decreasing component which might for example relate to the measured temperature variations of the optical bench of about 0.28 K peak-to-peak from subfigure (c), the 1.3 % change of the optical input power from subfigure (d) or another unaccounted source.

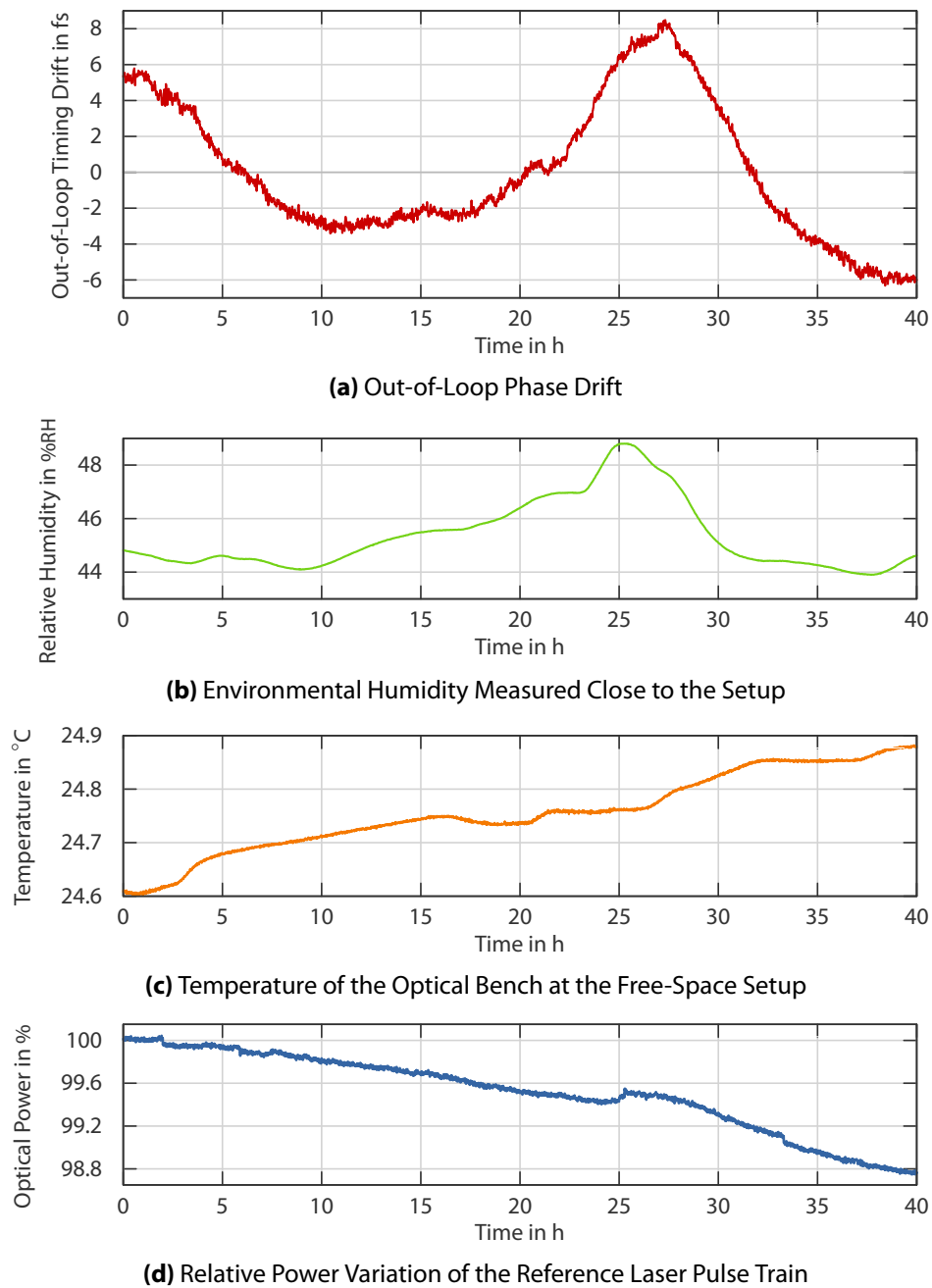


**Figure 4.9: Long-term Drift Measurement of the First Laboratory Prototype |** The acquired measurement data and selected environmental parameters during the measurement are presented. The out-of-loop drift is correlated to the humidity development.

It was believed at the time the measurement has been made that the unequal length of the input fibers of the two involved MZMs in the first prototype led to the humidity induced phase change at the out-of-loop detector. The length mismatch amounted to 0.4 m. Multiplied with the humidity coefficient of standard SMF of 2.5 fs/(m %RH) and the peak-to-peak humidity variation during the measurement of about 4.9 %RH, a peak-to-peak drift of 4.9 fs is covered. This is about one third of the measured drift. Another 4 fs seem to be caused by the linear component of the measured phase drift which leaves about another 6 fs of unaccounted humidity influence.

A possible explanation was discovered later, after the humidity dependence of RF cables had been proven. At the time the measurement was taken, the connection between the two MZMs has been established by 0.6 m of coaxial Pasternack PE-SR402FL cable and a phase shifter. The humidity coefficient of 9.6 fs/(m %RH) and the peak-to-peak humidity change of about 4.9 %RH would explain another 28 fs of drift from the RF cables which is more than actually has been measured. However if one takes the experimentally determined  $1/e$  time constant of about 8 h for humidity induced phase drifts of the Pasternack cable into account and considers, that the humidity peak in the laboratory lasted about 6 h FWHM, the overall drift can be explained by these effects.

It can be difficult to find, correctly identify and remove sources of unwanted drift. At least the attribution to humidity changes was obvious in the presented case due to the clear resemblance in shape. The linear component however cannot be clearly identified because multiple possible error sources cannot be excluded.

Another figure of merit of the L2RF phase detector is the achievable measurement accuracy. The detector is fundamentally limited by its noise floor, below which no phase measurements can be performed. The noise floor is defined by shot noise from the photodiode and thermal noise from the 50  $\Omega$  resistor behind it, which both propagate through the readout electronics. The noise floor can be observed when no RF signal is connected to the L2RF phase detector. A baseband measurement of the voltage spectral density (VSD) of the corresponding signal from the first prototype is presented in the upper plot of figure 4.10. The cut-off at 2 MHz originates from the low-pass filter which is installed behind the RF mixer in order to remove the higher order mixing products. The noise floor is found to be at a level of  $-117$  dBV/Hz. The spikes in the lower frequency range originate from electro-magnetic interference (EMI). The integral of the baseband noise is presented in the lower plot of figure 4.10. The plot is already converted to its equivalent in femtoseconds by applying  $K_{\phi,1}^{\text{ool}}$ . Additionally the integral over each decade is specified in the upper part of the plot. The combined noise<sup>1</sup> up to 1 MHz amounts to 1.12 fs. The last decade is not taken into account because the measured data is already partly outside the frequency range of the detector.

<sup>1</sup>The integrals from the individual decades need to be summed up by quadratic addition.

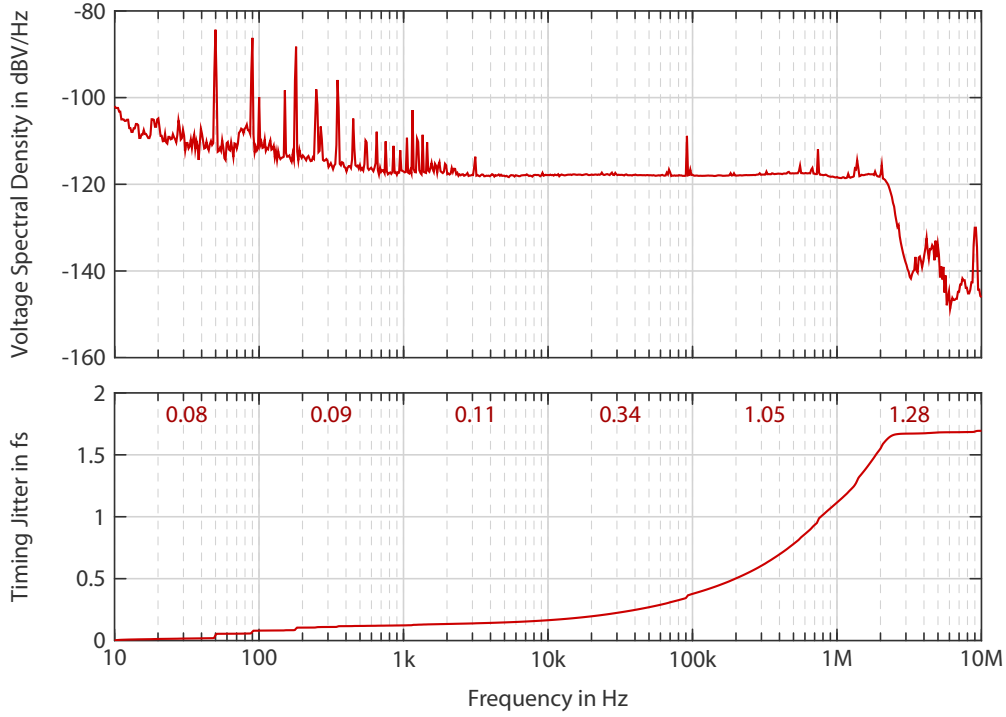


**Figure 4.10: Detector Noise Measurement of the First Laboratory Prototype |** The measurement was performed without an RF signal connected to the setup. The presented detector noise limits the phase detector resolution. The conversion of the integrated voltage noise by  $K_\phi$  shows the impact of the detector noise in femtoseconds.

The accuracy can be improved by increasing the sensitivity  $K_\phi$  of the setup without deteriorating the SNR. The improvement therefore needs to be made in the optical part of the setup and not at the detector electronics. A higher RF voltage at the MZM or an MZM with a lower  $\pi$  modulation voltage  $V_\pi$  are for example such options. At the same time the optical power can be increased as long as the photodiode is not saturated.

#### 4.7.2 Measurement Results from the Second Prototype

After the assembly and commissioning of the second prototype including the engineered readout electronics and the integrated optics, its performance has been evaluated in long- and short-term measurements. In contrast to the measurements of the first laboratory prototype, an active humidity control has been installed in the laboratory. The connection between the MZMs is performed with a phase stable cable (see section 4.4) and a smaller

RF phase shifter (see section 4.5). Because the engineered optical setup is now used which has a fiber-coupled input, the reference laser is directly coupled into a SM fiber and split by a 50/50 SM in-fiber directional coupler. Each output signal is provided to one of the two L2RF phase detectors. It was ensured that the fibers from the splitter to the input fiber collimators of both phase detectors have exactly the same length, that these fibers are kept short and that as much as possible of them is installed within the temperature and humidity stabilized optical compartment.

Using the integrated optics, a single L2RF phase detector can operate from an optical input power of 12 mW and supply the desired power level of 1 mW to each the LO and the readout photodiode. The photodiode has to be operated below saturation such that even the smallest amplitude fluctuations on top of the pulse train caused by small phase errors between the optical reference pulse train and the RF signal can be detected.

The highest optical losses occur at the first delay line (3 dB) and the integrated MZM (4.3 dB). The incoupling efficiency for a well aligned setup is typically found to be above 90 %. The delayed pulse train can be coupled in slightly less efficient compared to the directly transmitted pulse train due to its longer path. The remaining losses are attributed to the clean-up polarizer in the delay line and to losses at the remaining optical components.

A first long-term measurement has been interrupted by a power cut after only a few hours. Figure 4.11 shows the data recorded after the setup was brought back to operation. The optical compartments had to be opened after the power outage to check the optical alignment. The sensitivity  $K_{\phi,2}^{\text{ool}} = 1.41 \text{ mV/fs}$  of the out-of-loop phase detector of the second prototype has been determined before the long-term measurements started. The internal DC LNA has been set to a gain of twenty. Because the air conditioning and the humidity control in the laboratory had been switched off, the setup needed about one day to stabilize again. The optical bench for example took about ten hours to reach its equilibrium temperature and it took twenty hours for the humidity control to lower the relative humidity in the room to the setpoint of 46 %RH.

The measurement data has been taken with a sample rate of 0.1 Hz. The peak-to-peak out-of-loop error finally amounts to 12 fs for the last 48 h. The last 12 h however show an unrivaled peak-to-peak stability of 3.6 fs. A performance of an L2RF phase detector at an RF frequency of 1.3 GHz at this level has not been reported before.

The feature around 66.5 h after the start of the measurement has been caused by an accidental restart of a server in the control system which caused one bias feedback to malfunction. After the feedback has been set in operation again, the L2RF setup returned to the identical operating point. The whole glitch is therefore disregarded during the performance evaluation.

It is difficult to adjust the working point of the out-of-loop phase detector with the desired accuracy by adjusting the phase of a 1.3 GHz signal on a femtosecond level by a manual

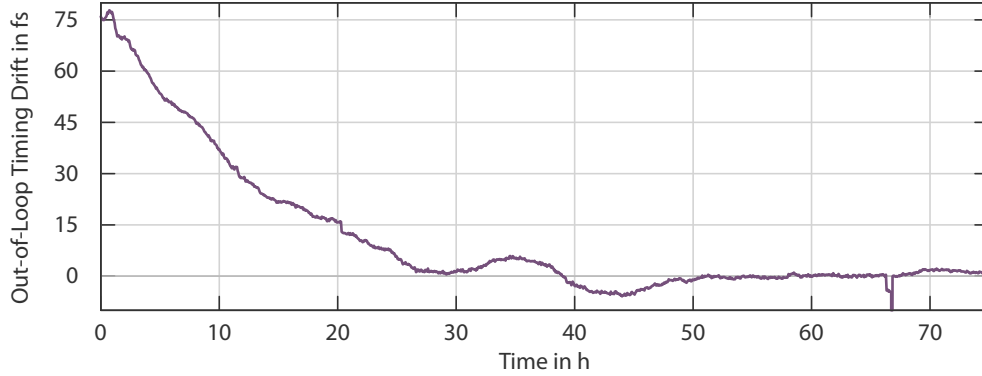


**Figure 4.11: Long-term Drift Measurement of the Second Laboratory Prototype** | A previous measurement has been interrupted by a power cut. The initial burn-in phase is related to the humidity and temperature in the laboratory which need to stabilize first. The glitch at the end of the measurement is caused by an accidentally restarted server in the control system. The system returns immediately to the old state after the server is restarted.

phase shifter. An offset of 90 fs has been subtracted from the plot because only relative phase errors between the two signals are relevant. However, the operation of a [L2RF](#) phase detector at an offset phase influences the error suppression of the setup. Variations of the optical input power for example can in such a case directly influence the measured value because they change the sensitivity of the [L2RF](#) phase detector.

Especially by considering that the presented measurement reveals the combined errors from two independent [L2RF](#) phase detectors, it becomes clear that the desired performance of sub 10 femtoseconds has been reached by the setup.

The detector noise floor has been evaluated in the top plot of figure 4.12 by measuring the [VSD](#) at the out-of-loop phase detector while the [RF](#) signal was disconnected. The topology of the integrated readout electronics is slightly different from the dedicated readout electronics of the first laboratory prototype. The cut-off frequency of the readout electronics depends on the remote adjustable gain of the [DC LNA](#) which can in this way be used to control the bandwidth of the [L2RF](#) phase detector. The lowest gain factor of ten has been used for the presented measurement in order to achieve the highest possible bandwidth. The sensitivity  $K_\phi$  has been reevaluated between the long-term and the noise floor measurements because of the new gain. A value of  $K_{\phi,3}^{\text{ool}} = 0.72 \text{ mV/fs}$  has been determined for the noise floor evaluation.

Concerning [EMI](#) the [VSD](#) looks much better compared to the previous measurement. The improved shielding of the compact housing did reduce most spikes in the spectrum except for the 50 Hz line. The noise floor is raised with respect to the previous setup by about 4 dB

to a level of  $-113$  dBV/Hz while the sensitivity is cut by half compared to the first prototype. The SNR is therefore about a factor of two smaller compared to the first prototype due to the lower LNA gain. The level of the noise floor depends on the modulation at the MZM (available parameters are the RF peak voltage  $\hat{V}_{\text{RF}}$  and the  $\pi$  modulation voltage  $V_{\pi}$ ) and the optical power. These parameters have been identical to the operation of the first prototype. The reason for the elevated noise floor is therefore not clear and the first prototype did not exist anymore at the time the measurements have been made, such that no cross-checks could be performed.

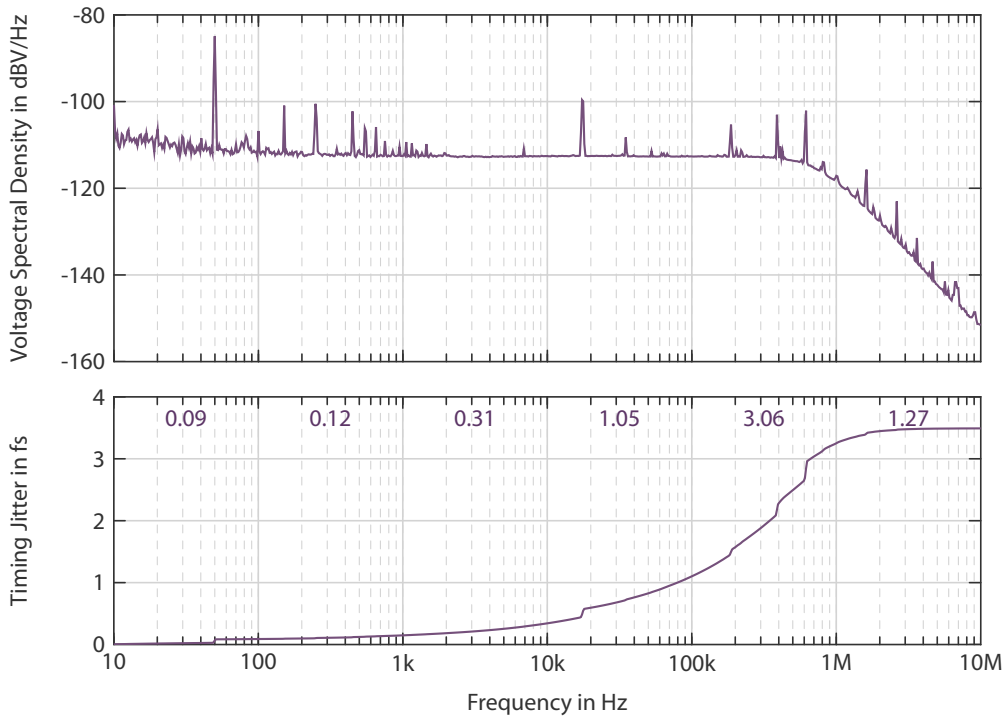


**Figure 4.12: Detector Noise Floor Measured at the Second Laboratory Prototype** | The measurement was performed without an RF signal connected to the setup. The presented detector noise limits the phase detector resolution. The conversion of the integrated voltage noise by  $K_{\phi}$  shows the impact of the detector noise in femtoseconds.

The integral and the noise contributions per decade are depicted in the bottom plot of figure 4.12. Integrated over the usable bandwidth, the noise floor up to 750 kHz amounts to 3.08 fs. By limiting the bandwidth to 50 kHz one obtains an equivalent of 0.83 fs for the noise floor.

The laboratory in which the long term measurements are carried out is normally closed

during measurements. For test purposes and because the laboratory was needed for other work, another long-term measurement has been conducted with the second prototype while the laboratory was regularly used. The acquired data is presented in figure 4.13. The measurement was running for one week.

The peak-to-peak drift amounts to 21.7 fs. The measured drift still represents the combined drifts from the measurement setup, the in-loop and the out-of-loop L2RF phase detector. There is no direct relation to the optical power of the laser pulse train visible although the out-of-loop detector was not operated in its ideal working point. However, there still seems to exist a relation to the temperature because all temperature spikes are repeated in the phase measurement. The Phasemaster cable which connects the in-loop and the out-of-loop setup is too short to be responsible for an effect of this magnitude, therefore only the phase shifter remains as potential source for the presented drifts. The humidity dependence seems to be mostly eliminated. the highest peak after three days for example is almost not visible in the drift plot.

For accelerator operation one has to keep in mind, that user shifts usually last 8 h. Even under the presented environmental conditions, the sub 10 femtosecond requirement is met for most eight hour periods during the measurement. Only the temperature step of 0.5 K during the third day causes slightly higher drifts in the prototype setup.

The measurement emphasizes the robustness of the L2RF detection scheme, which is long-term stable even under the presented demanding environmental conditions. At 1.3 GHz, even the presented peak-to-peak drift of 21.7 fs has not been achieved before in a one week measurement.



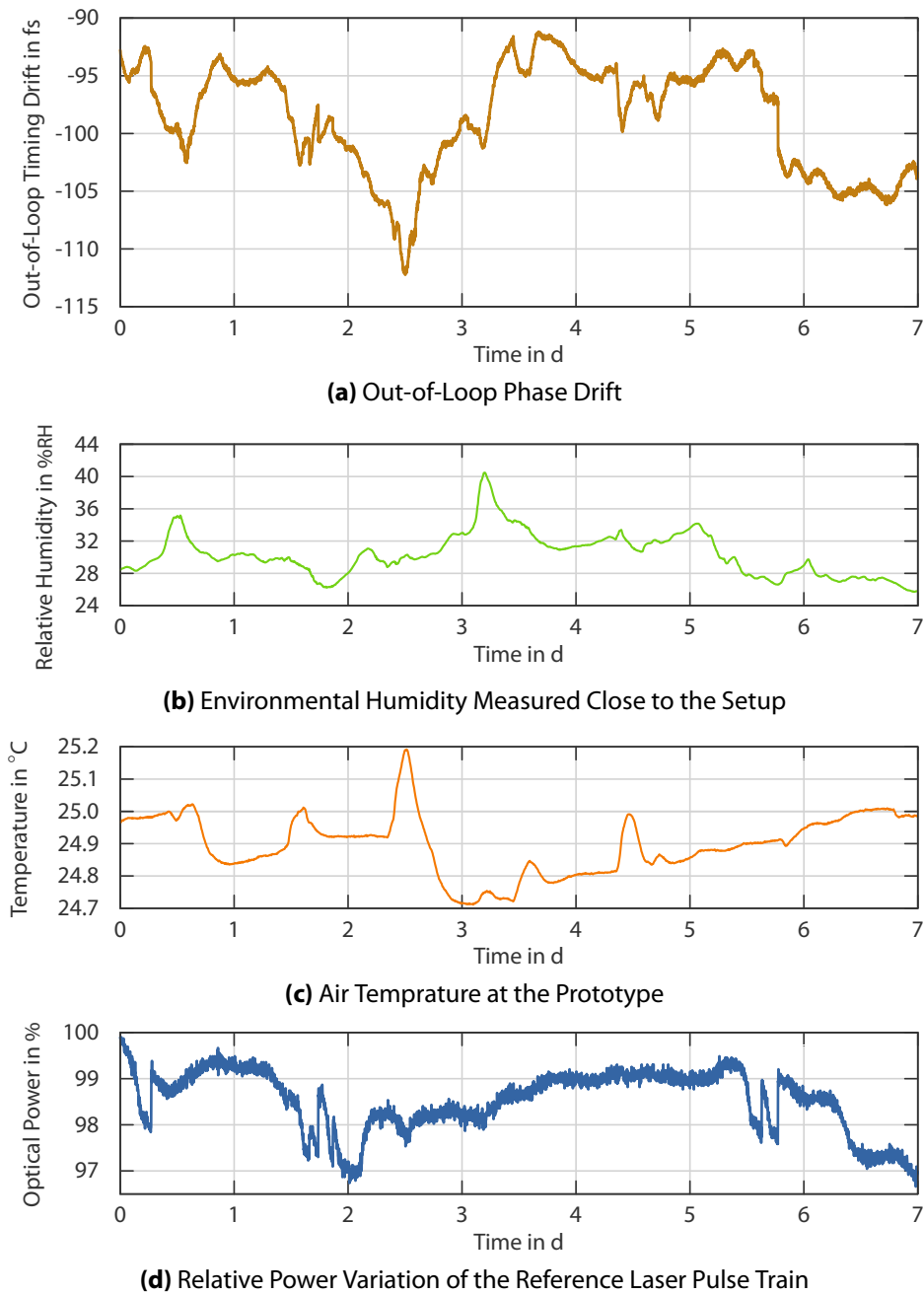


**Figure 4.13: Long-term Drift Measurement of the Second Laboratory Prototype** | The acquired measurement data and selected environmental parameters during the measurement are presented. The laboratory has been regularly used during this measurement.



## RF Distribution Techniques

The presented [laser-to-RF \(L2RF\)](#) phase detector is only one of a few available solutions to the problem of phase stable [radio frequency \(RF\)](#) reference signal distribution. In literature, this problem is frequently discussed under the term [phase reference distribution system \(PRDS\)](#). The oldest alternatives to the presented scheme are unstabilized and stabilized [RF](#) signal distribution via coaxial cables. More sophisticated schemes use [continuous wave \(CW\)](#) lasers and optical fibers to distribute reference signals. When using a pulsed optical synchronization system, further techniques besides the [L2RF](#) phase detector are available to either extract [RF](#) reference signals from the optical pulse train or to stabilize [RF](#) signals with respect to the optical phase reference.

In the following sections, several measurement results from different setups are quoted. These results can only be compared with caution, because some schemes directly include the transport of [RF](#) signals to remote locations, while especially for the pulsed optical synchronization system usually the performance of the conversion setup without the transport is given.

### 5.1 Conventional RF Transport

[RF](#) transport by coaxial cables in accelerators is limited by the phase drift of the utilized cable and by its insertion loss<sup>1</sup>. For the [Free-Electron Laser in Hamburg \(FLASH\)](#) different [PRDS](#) have been evaluated in [[Czu07](#)].

CZUBA suggests temperature stabilized [RF](#) cables for the transport of 1.3 GHz reference signals. A phase drift of 220 fs is anticipated for the longest distance at [FLASH](#) of 300 m with a temperature stabilization of the cable to  $\pm 0.5$  K. A reference distribution scheme based on [CW](#) laser signals is furthermore proposed to meet future synchronization requirements. Such schemes are briefly illustrated in the next section. Pulsed optical synchronization systems still were in the prototype stage at this time and they have therefore not been taken into account.

<sup>1</sup>Cellflex 15/8" cable for example has a comparably low insertion loss of  $26 \text{ dB km}^{-1}$  at 1.3 GHz [[Czu<sup>+</sup>13](#)].

The RF based interferometer [FBC00; Cul11] which is now being implemented at the European X-ray Free-Electron Laser (XFEL) as baseline RF synchronization technique [Czu<sup>+</sup>13] is already mentioned in the above thesis as potential future stabilization technique. The technique provides multiple stabilized outputs along its transmission line which is a unique feature. Alternative optical and electrical techniques require point-to-point connections for each end station. The transmission distance of the RF based interferometer is limited due to the cable insertion loss. The accuracy is given by the phase drift suppression factor<sup>1</sup>, the temperature coefficient of the utilized cable and the temperature stability in the accelerator tunnel. A single interferometer link is supposed to deliver sub 100 femtosecond stability at each of its outputs [Czu<sup>+</sup>13].

In the implementation for the European XFEL, several interferometers will be daisy-chained in order to cover the full accelerator length. The overall phase drifts are minimized by resynchronizing the RF signal between two interferometers using the optical reference module (REFM-OPT). The REFM-OPTs are foreseen in the most timing critical locations, such that there even femtosecond synchronization can be directly provided.

## 5.2 RF Transport Based on Continuous Wave Lasers

To overcome the limiting insertion loss of RF cables, lasers and optical fibers<sup>2</sup> have been considered since a long time for signal transport (see for example [Lut87]). In CW laser-based synchronization systems, the laser amplitude is usually modulated by the RF signal using electro-optic (EO) amplitude modulators. The extraction is performed with photodiodes. The extracted RF signals frequently need to be further amplified because the RF power delivered by photodiodes is for many applications not sufficient.

The drift of the fiberlink can be detected either by RF phase detection or by interferometric techniques. For both methods, at least a part of the optical signal is transmitted back to the start of the fiberlink – in either the same or a second optical fiber.

There are different approaches to deal with the phase drifts of the involved optical fibers. The fiber drifts can be simply measured and transmitted to the system at the end station which has to take them into account. The reference signal is not immediately stabilized at the extraction point in such a scheme. Alternatively, the drifts can be actively and directly compensated by either adjusting the wavelength of the used laser or by introducing optical components of variable length like optical delay lines or piezo-actuated fiber stretchers to the fiberlink.

<sup>1</sup>In DESY internal tests, a phase drift suppression factor of 300 has been achieved.  
personal communication, Dominik Sikora, February 2015

<sup>2</sup>The insertion loss of SMF-28e+ at 1550 nm amounts for example to only 0.2 dB km<sup>-1</sup> [SMF28e].

One such system has been implemented at the [Lawrence Berkeley National Laboratory \(LBNL\)](#). An interferometric detection scheme involving optical frequency shifting at the end station has been implemented. The phase of the extracted RF signal is corrected after the photodetection. Details on the implementation can be found at [\[Wil<sup>+</sup>10\]](#). After the transport over 2.2 km of fiber, a [root mean square \(rms\)](#) drift of 19.4 fs has been achieved during a 60 h measurement period. The peak-to-peak drift is not presented but can be estimated from plots to be notably higher.

Another system is commercially distributed by the Slovenian company Instrumentation Technologies<sup>1</sup>. Here the laser wavelength is adjusted in order to compensate the drift of the fiberlink. The detection is performed with RF phase detectors. Details on the implementation have been published in [\[Tra<sup>+</sup>10\]](#). A performance of 128 fs has been reached for a 180 m fiberlink over a period of 65 h. Meanwhile, the setup has been improved and a performance of less than 40 fs drift over 24 h is promised by the manufacturer.

The system proposed by CZUBA for [FLASH](#) was also based on RF phase detection of the photodetected optical signal. The phase has been corrected with an optical delay line. In prototype measurements in 2007, a performance of 250 fs has been achieved over 2 h for a 5 km fiberlink [\[Czu07\]](#). The system was never implemented at [DESY](#). Instead, the pulsed optical synchronization system has been investigated and realized. The advantages of pulsed optical synchronization systems for [free-electron lasers \(FELs\)](#) have been discussed in section 1.2.

## 5.3 RF Transport Based on Pulsed Lasers

Soon after the invention of the pulsed optical synchronization system the first attempts to extract RF signals from optical pulse trains were performed. The most simple way to do this is to select the desired harmonic with a band-pass filter from the photodetected signal and to amplify it if required. This scheme is called the direct conversion scheme. The laser repetition rate has to be chosen beforehand such that the required frequency exists in the frequency comb.

All systems which rely on photodiodes to extract phase stable RF signals from optical pulse trains suffer from the so-called [amplitude modulation/phase modulation \(AM/PM\)](#) conversion. Amplitude variations of the optical signal cause phase variations of the extracted RF signal [\[CV06; Zha<sup>+</sup>12\]](#). Additionally, photodiodes and other RF components like filters and amplifiers are highly phase sensitive to changes of the environmental temperature. The additional temperature and humidity sensitivity of the involved cables has been discussed

---

<sup>1</sup>The system is called Libera Sync 3, see [http://www.i-tech.si/accelerators-instrumentation/libera-sync-3/how-does-it-work\\_5](http://www.i-tech.si/accelerators-instrumentation/libera-sync-3/how-does-it-work_5)

in section 4.4. In [Lor<sup>+</sup>07], temperature coefficients of a complete direct conversion setup of more than 300 fs K<sup>-1</sup> have been determined.

There are efforts to circumvent the AM/PM conversion by characterizing individual hand-picked photodiodes in order to operate them with an optical power, where the AM/PM coefficient is low or zero. Usually the optical power at the photodiode and the temperature of the photodiode is in this case actively stabilized.

Another scheme, used to obtain RF signals from pulsed optical fiberlinks is the so-called **balanced optical-microwave phase detector (BOM-PD)** [KKL06]. The BOM-PD represents a phase detector between an optical pulse train and an RF signal like the L2RF phase detector. It is based on a fiber-coupled SAGNAC loop interferometer. An EO phase modulator is inserted into the fiber loop and operated by the RF signal. The voltage induced phase shift between the co- and counter-propagating pulses causes an amplitude modulation of the optical pulse train at the output of the fiber loop. The phase modulator needs to be precisely biased in order to tune the SAGNAC loop into its working point. In [KK10] a performance of 6.1 fs over 8 h has been measured in an out-of-loop measurement at an RF frequency of 10 GHz.

The feasibility of this scheme for a lower RF frequency of 1.3 GHz has been evaluated in 2009 at DESY [Fel<sup>+</sup>09]. An rms performance of 9.6 fs has been achieved over a period of 7 h. The peak-to-peak drift can be estimated from plots to be notably higher. Two main disadvantages of lowering the RF frequency are presented in [Fel<sup>+</sup>09]: The sensitivity of the detector depends on the steepness of the RF signal in its zero crossing – which is reduced by the frequency reduction about a factor of eight compared to the 10 GHz measurements presented above. The internal phase modulator modulates both, the co- and counter-propagating pulses in the SAGNAC loop at this lower operating frequency, where one pulse can always pass the modulator transparently at 10 GHz. Therefore the modulation depth is reduced and the biasing also becomes more complicated.

With the L2RF phase detector, a new scheme for the femtosecond synchronization of RF signals to optical pulse trains has been developed in this thesis. As presented, this new scheme performs well even for RF frequencies as low as 1.3 GHz.

Meanwhile also the BOM-PD has been improved to a new setup called **fiber-loop optical-microwave phase detector (FLOM-PD)**. This setup was proposed as a free-space setup in [KKP04] and implemented as a fiber-coupled setup in [JK12]. The biasing of the fiber loop is performed passively by a combination of two FARADY rotators and a  $\lambda/4$  waveplate. A new readout scheme using a balanced detector has also been introduced. In [KJS14] an out-of-loop rms phase drift of 5 fs has been measured in 48 h for the FLOM-PD. The peak-to-peak value is again not given but the presented plot suggest a peak-to-peak drift of about 25 fs. The measurements have again been performed at 10 GHz.

## Outlook

The final prototype of the [laser-to-RF \(L2RF\)](#) phase detector for accelerator usage is integrated into a three [rack unit \(U\)](#), 19" housing. Half of the available space is occupied by the optical setup, the other half by the detector and actuator electronics. Space requirements in accelerators are tight and smaller setups can be easier isolated from environmental influences. Therefore, further iterations of the [L2RF](#) phase detector will benefit from a further integration and miniaturization.

The current optical setup is already partly fiber-coupled but the first delay line is constructed by free-space optics. An all-fiber optical setup will save a tremendous amount of space on the optical side and help to downsize the complete [L2RF](#) phase detector. An active polarization control is not required if the fiber setup is constructed from [polarization maintaining \(PM\)](#) fibers. The splitting ratio and the length of the first delay line however need to be kept precisely adjustable in such a setup.

The splitting can be performed in a directional coupler. The splitting ratio is not adjustable, but the optical power of its output signals can be balanced by an in-fiber, voltage controlled attenuator which is inserted into one output. Fiber-coupled attenuators are for example off the shelf available as [micro-electro-mechanical system \(MEMS\)](#) devices. The splitting ratio adjustment becomes easier by choosing a coupler with an unbalanced splitting ratio like for example 55/45. The arm with the higher optical power can be precisely attenuated down to the level of the arm with the lower optical power. The splitting ratio is in this way not only one-time adjustable – it is continuously remote controllable.

The length of the first delay line needs to be adjustable as well. Most of the delay can be created in fiber. Only the fine-tuning has to happen in a small, adjustable free-space delay. Such delays are commercially available as sealed and maintenance free, fiber-coupled devices. For the recombination of the pulses, a [PM](#) combiner should be used. The fibers and fiber components can be installed together with the [MACH-ZEHNDER modulator \(MZM\)](#) on a small temperature controlled plate and in a humidity stabilized housing.

Besides from the miniaturization, it is intended to modify the [L2RF](#) phase detector such, that the same design can be operated at many different frequencies. The current integrated optics accomplish this by providing a highly adjustable first delay line. An all-fiber setup

can accordingly be tailored to any required frequency because the delay length can be freely chosen during the splicing process.

The readout of the L2RF phase detector is however currently performed by analog in-phase and quadrature phase (I/Q) demodulation. The integrated detector electronics are designed and suited for only one specific frequency and can therefore not be employed for different frequencies. Digital I/Q demodulation can be performed at different error frequencies without expensive hardware modifications.

The desired readout frequency needs to be extracted from the photodiode signal by band-pass filtering and – if required – amplification before the signal is sampled. Direct sampling without down-mixing is possible for the current modulation frequencies using ultra-fast analog-to-digital converters (ADCs) available nowadays. The error signal only needs to be mixed down to an intermediate frequency (IF) if the modulation frequency is too high for direct sampling. Even the influence of direct current (DC) offsets can be removed if the error signal is not mixed down to the baseband for detection. In each case, the integrated detector electronics would not be required any more. This modification would make the L2RF phase detector more versatile in terms of frequency coverage because the remaining radio frequency (RF) components can be easily adopted to different frequencies.

It has been discussed in section 3.11.2 to improve the signal to noise ratio of the detector by using a transimpedance instead of a voltage amplifier to amplify the photodiode signal. This option should be taken into account whenever only low optical power levels are available such that the photodiode readout is dominated by thermal noise instead of shot noise.

Another proposal for further developments is relevant for applications where only single output MZMs are available. One difficulty of these setups is, that splitting ratio errors and phase drifts cannot be separated in the final error signal because they have the same modulation frequency. The all-fiber setup proposed above already provides the option to actively control the splitting ratio which is highly advised in this case. The control signal for such an active feedback can only be extracted from the pulse train before it is modulated in the MZM. Amplitude modulations before the MZM originate from a non ideal splitting ratio. The detection can be performed by integrated analog electronics or direct sampling and digital I/Q demodulation – the regular detector electronics just need to be duplicated for this task. If the required signal is extracted from the part of the pulse train, which is removed during the polarization clean-up in front of the MZM, no additional optical power needs to be provided for the splitting ratio control.



# Chapter

## Summary



Modern [free-electron lasers \(FELs\)](#) require the precise synchronization of many different subsystems in order to deliver the required femtosecond precision. At [DESY](#), a pulsed optical synchronization system has become an integral part of the [Free-Electron Laser in Hamburg \(FLASH\)](#). An improved version of the same system is currently implemented for the upcoming European [X-ray Free-Electron Laser \(XFEL\)](#). The [bunch arrival-time monitors \(BAMs\)](#) and the [laser-to-laser \(L2L\)](#) synchronization are the established applications of the optical synchronization system and they are permanently used during regular [FEL](#) operation. A technique to directly provide phase stable [radio frequency \(RF\)](#) signals to dedicated devices in the accelerator tunnel has been missing in the past. Especially the [low-level radio frequency \(LLRF\)](#) system, in which the acceleration modules are controlled, requires an [RF](#) reference signal with sub 10 femtosecond stability in order to reach the envisioned [FEL](#) performance. The [laser-to-RF \(L2RF\)](#) phase detector invented in this thesis provides a method to measure with femtosecond precision the phase of [RF](#) signals with respect to a phase stable optical reference pulse train. This measurement allows to actively stabilize the phase of the [RF](#) signal.

The central component of the [L2RF](#) phase detector in which the optical pulse train interacts with the [RF](#) signal is an integrated [MACH-ZEHNDER modulator \(MZM\)](#). Different configurations of [L2RF](#) phase detectors based on single output and dual output integrated [MZMs](#) have been presented and evaluated. The most sophisticated configuration has been chosen for implementation. It allows to measure the phase relation between the reference laser pulse train and an [RF](#) signal independently of other internal parameters. The detection scheme is balanced and in the first order insensitive to changes of the power of the [RF](#) signal as well as it is in the first order insensitive to changes of the optical power of the reference pulse train. This scheme does not rely on the phase stability of the photodiode which is used to detect the error signals or on the phase stability of other [RF](#) components in the detection chain because the phase error signal is encoded in an amplitude modulation of the reference pulse train.

The chosen configuration has subsequently been analyzed mathematically. The spectral representation of the amplitude modulated pulse train has been investigated and the full output equations have been derived. Possible error sources were taken into account. It

was proven that most error sources only have second or even higher order influence on the phase measurement. Only length changes of the first and second internal delay have a direct influence on the measurement result.

Three prototypes of the L2RF phase detector have been built. The first prototype has been constructed from bulk components and used to study the detection scheme and to practically prove the performance. In order to isolate sensitive components from environmental humidity and temperature changes, a sealed and temperature stabilized optical setup has been engineered. It was tested together with the integrated version of the detector electronics in a second prototype. A peak-to-peak performance of 3.6 fs over 12 h has been proven in measurements. The L2RF phase detector therefore not only fulfills the requirement to provide sub 10 femtosecond stability but it also delivers the currently best known performance for L2RF phase detection at an RF frequency of 1.3 GHz.

Based on these results, the engineered components have been used to build a third prototype. This prototype is fully integrated in a 19" housing and suited to be operated in an accelerator environment. The L2RF phase detector is extended in this device by actuator electronics and a digital controller board, which allow to control the phase of the RF signal in a phase-locked loop (PLL). This optical reference module completes the pulsed optical synchronization system by providing phase stable RF reference signals to the LLRF systems at FLASH and the European XFEL. It will improve the stability and timing accuracy of these FELs.

# Appendix



## Integrated MZI Based Optical Amplitude Modulators

The **MACH-ZEHNDER interferometer (MZI)** can be distinguished from the well known **MICHELSON** interferometer by the fact that both interferometer branches of the **MZI** are passed only once by the involved light. In an **MZI**, the incoming beam is split and both output signals are recombined again. The output intensity of the device depends on the phase relation between both branches. Figure A.1 shows a schematic sketch of an **MZI**.

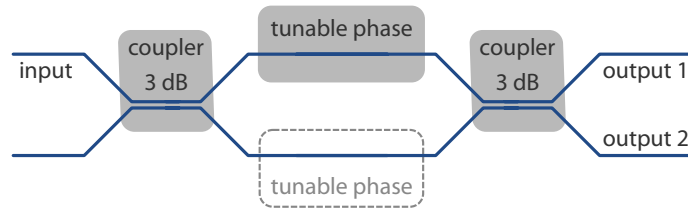


**Figure A.1: Schematic Sketch of an MZM** | The input signal is split and recombined. The intensity at both outputs is controlled by the phase relation between the two interferometer arms.

A common application is to use the **MZI** as optical intensity modulator by inserting an object of tunable optical path length in one of the interferometer arms. This can be for example an object with tunable index of refraction which then allows to control the output intensity of the **MZI**. The index of refraction of special crystals can be voltage controlled by exploiting the **electro-optic (EO)** **POCKELS** effect. A device making use of this effect is generally called an **electro-optic modulator (EOM)**. Following [Sal<sup>+</sup>11] the linear index change  $\Delta n_r$  caused by the **POCKELS** effect is given by

$$\Delta n_r = \frac{n_{r,\text{eff}}^3}{2} r_{\text{eff}} E_{\text{eff}}. \quad (\text{A.1})$$

In this equation  $n_{r,\text{eff}}$  refers to the index of refraction before any electrical field  $E_{\text{eff}}$  is applied to the crystal and  $r_{\text{eff}}$  is the **EO** coefficient. Both parameters depend on the material and

geometry of the crystal and the actual crystal axis used for propagation. Such an EO material can for example be used directly to build a phase modulator. One can use it to build an amplitude modulator based on an MZI – which is then called **MACH-ZEHNDER modulator (MZM)**. A large variety of MZMs is nowadays commercially available as integrated devices. They are popular because of their small size and easy handling. These devices are usually maintenance free because they are fiber-coupled and based on optical waveguides.

Integrated MZMs have the same structure as presented in figure A.1. The optical input signal is first split and then either only one branch or both branches are phase modulated. The uniform modulation of both branches permits to use the MZM additionally as phase modulator. The voltage required for full modulation is reduced, if both branches are inversely phase modulated in a so-called push-pull configuration. Finally, both signals are recombined. For splitting and recombination either Y-junctions or conventional 3 dB directional couplers can be foreseen directly in the optical waveguide [ST91]. The actual phase change  $\Delta\phi$  caused by the EO Pockels effect is defined in [Sal<sup>+</sup>11] to be

$$\Delta\phi = \gamma \Delta n_r \frac{2\pi}{\lambda} L. \quad (\text{A.2})$$

In this equation,  $L$  is the modulation length,  $\lambda$  the wavelength of the laser light and  $\gamma$  is the optical confinement factor. It specifies the portion of the optical mode which is confined in the active layer of the modulator.

The integrated MZM used in the **laser-to-RF (L2RF)** setup is a traveling wave modulator made from **Lithium-Niobate (LiNbO<sub>3</sub>)** and suited for the optical C-band [EOMz]. The fabrication process of integrated LiNbO<sub>3</sub> MZMs is comprehensively summarized in [Woo<sup>+</sup>00], where also information on typical applications and the reliability of integrated MZMs is provided. The microwave signal driving the modulator propagates internally along the waveguide in which the optical signal is confined. The optical and the microwave signal need to be velocity matched in a traveling wave modulator for its most efficient operation. The procedure of velocity matching has huge influence on the geometrical and technical design process. [Bet02] provides an historical overview of the development of velocity matched modulators during the last 40 years and outlines important steps towards today's well matched devices.

The actual modulation efficiency in the waveguide depends on the polarization of the involved light due to the anisotropy of the used LiNbO<sub>3</sub> crystal. Integrated MZMs are frequently equipped with polarizers such that only the most efficient polarization can pass the device. The transmission  $\Gamma$  of an MZM can be expressed as the relation of output intensity  $I_{\text{out}}$  to the input intensity  $I_{\text{in}}$ , which reads

$$\Gamma = \frac{I_{\text{out}}}{I_{\text{in}}} = \frac{1}{2} (1 + \cos(\Delta\phi - \phi_0)) \quad (\text{A.3})$$

in case the input splitter equally divides the input signal to both branches [Sal<sup>+</sup>11]. Equation (A.3) does not consider optical losses as they occur in any real MZM and it additionally assumes an extinction ratio of the device of zero. The externally controlled phase mismatch  $\Delta\phi$  is biased by the phase shift of  $\phi_0$  which accounts for a possible intrinsic length mismatch of the interferometer arms. Equation (A.3) now needs to be extended by the so-called  $\pi$  modulation voltage  $V_\pi$  at which exactly a  $\pi$  phase shift between both MZM branches is induced. The phase mismatch  $\Delta\phi$  is in this model controlled by the bias voltage  $V_b$  while the intrinsic phase shift  $\phi_0$ , which is actually device specific, is expressed by its voltage equivalent  $V_{b,0}$ . The phase mismatch  $\Delta\phi$  and therefore also  $V_{b,0}$  can drift – for example due to temperature changes.

$$\Gamma = \frac{1}{2} \left( 1 + \cos \left( \frac{\pi}{V_\pi} (V_b - V_{b,0}) \right) \right) \quad (\text{A.4})$$

The  $\pi$  modulation voltage can be calculated by taking equations (A.1) to (A.4) into account [Sal<sup>+</sup>11]. This representation is however not complete, because the effective electrical field  $E_{\text{eff}}$  is for example only replaced by the applied voltage over the distance between the electrodes  $V/d$  where the geometry of the electrodes and the optical waveguide is not accounted. The velocity matching is also not taken into account although it has a huge influence on the  $\pi$  modulation voltage. Equation (A.5) should therefore be understood as approximation.

$$V_\pi = \frac{\lambda}{n_{\text{r,eff}}^3 r_{\text{eff}}} \frac{d}{\gamma L} \quad (\text{A.5})$$

The preliminary output formula in equation (A.4) does not yet include all important device parameters. Integrated MZMs are usually equipped with two electrodes, one for radio frequency (RF) signals  $V_{\text{RF}}(t)$  and one direct current (DC) electrode for the bias voltage  $V_b$ . Due to the slightly different design, usually two independent  $\pi$  modulation voltages are associated with these electrodes. It is furthermore common to specify the characteristic of the MZM using a sine instead of a cosine function. The phase shift needed for this mathematical transition is covered by the device parameter  $V_{b,0}$ . The transmission in terms of intensity and power is identical because intensity and power are proportional to each other. Equation (A.4) can therefore be also applied to the optical power. The optical output power  $p_{\text{MZM}}(t)$  relative to the optical input power  $p_{\text{opt}}(t)$  finally reads

$$p_{\text{MZM}}(t) = \frac{p_{\text{opt}}(t)}{2} \left( 1 + \sin \left( \frac{\pi}{V_{\pi,\text{DC}}} (V_b - V_{b,0}) + \frac{\pi}{V_{\pi,\text{RF}}} V_{\text{RF}}(t) \right) \right) \quad (\text{A.6})$$

Equation (A.6) is now extended for a dual output MZM. If the internal combiner of the MZM is fabricated as 3 dB directional coupler where the coupling depends on the phase

relation between the two signals and both coupler outputs are guided out of the device, they are inversely modulated by the applied voltage. The regular optical output power  $p_{\text{MZM}}(t)$  and the inverted optical output power  $p'_{\text{MZM}}(t)$  are defined according to equations (A.7) and (A.8). The factors  $a_{\text{MZM}}$  and  $a'_{\text{MZM}}$  account for optical losses in the device. The modulation factor  $r_{\text{MZM}}(t)$  in equation (A.9) is derived directly from equation (A.6).

$$p_{\text{MZM}}(t) = a_{\text{MZM}} (1/2 + r_{\text{MZM}}(t)) p_{\text{opt}}(t) \quad (\text{A.7})$$

$$p'_{\text{MZM}}(t) = a'_{\text{MZM}} (1/2 - r_{\text{MZM}}(t)) p_{\text{opt}}(t) \quad (\text{A.8})$$

$$r_{\text{MZM}}(t) = \frac{1}{2} \sin \left( \frac{\pi}{V_{\pi, \text{DC}}} (V_{\text{b}} - V_{\text{b},0}) + \frac{\pi}{V_{\pi, \text{RF}}} V_{\text{RF}}(t) \right) \quad (\text{A.9})$$

For many applications of **MZMs** it is crucial that the device is constantly and accurately biased in its optimum working point at half transmission. The modulator has the steepest response at this point and the outputs – in case of a dual output modulator – are balanced. The bias voltage  $V_{\text{b}}$  needs to be equal to the device parameter  $V_{\text{b},0}$ . Bias drifts however are a widely known phenomenon. The bias voltage is required to constantly compensate the changing device parameter  $V_{\text{b},0}$  in order to keep the **MZM** in its working point.

There are in fact multiple reasons for this drift and the most prominent one is usually the electrically induced drift, which is an intrinsic effect of the modulator [Sal<sup>+</sup>11]. The applied bias voltage causes the electrical charges in the modulator to be redistributed and thereby creates a depolarizing electrical field. Another source for bias voltage drifts are for example thermally induced imbalances between the two arms of the interferometer. The known effects are summarized in [Sal<sup>+</sup>11] and a substantial list of references is provided for the mentioned effects. The **L2RF** phase detector works most efficiently with a correctly biased internal **MZM**. Therefore a bias control scheme has been implemented and it is presented in section 2.2.



## Synchronous Detection Using Double-Balanced RF Mixers

The **radio frequency (RF)** mixer is a three port device which is frequently used for frequency conversion and phase or amplitude detection. There is a huge variety of **RF** mixers commercially available and most of these mixers are optimized for specific tasks. An extensive overview of different types of mixers and their application is for example given in [SB10]. The following section will deal with general properties of **RF** mixers and focus on the double-balanced diode ring based mixer.

The mixer ports are typically labeled **RF** input and **local oscillator (LO)** input while the output is mostly called **intermediate frequency (IF)** output<sup>1</sup>. The names are dedicated to the classical usage in a superheterodyne receiver, which is what is used in most analog radios. In this case, the **RF** signal is picked up by an antenna. The **LO** signal originates from a tunable oscillator which ensures by its tunability that a certain frequency range can be covered by the receiver. The **IF** output represents the input signal which is mixed down to a fixed intermediate frequency. The key property of the superheterodyne receiver is that the actual detection circuit for the **IF** signal can be built at a fixed frequency, while the **LO** signal is tunable in order to provide a certain reception range. This classical and widespread naming convention will be obeyed throughout this thesis, with the exception of the **RF** input. In order to not confuse this signal with the **RF** signal present within the **laser-to-RF (L2RF)** phase detector at the **MACH-ZEHNDER modulator (MZM)**, the **RF** input of the mixer is just called input.

The **LO** and input signals are assumed to be single frequency harmonic oscillations as shown in equations (B.1) and (B.2). The description of the mixer and the conversion properties is very convenient with signals with such narrow bandwidth, although real signals might be more complex to calculate.

$$v_{\text{LO}}(t) = \hat{V}_{\text{LO}} \cos(\omega_{\text{LO}} t - \varphi_{\text{LO}}) \quad (\text{B.1})$$

$$v_{\text{in}}(t) = \hat{V}_{\text{in}} \cos(\omega_{\text{in}} t - \varphi_{\text{in}}) \quad (\text{B.2})$$

<sup>1</sup> Actually this is true for frequency down-conversion while for up-conversion the roles of the **RF** and **IF** ports are swapped.

Mathematically, the RF mixer performs a multiplication between its input signals. This is a widely used representation. In the case of two harmonic RF signals, this multiplication is equivalent to the multiplication of two cosine functions, as performed in equation (B.3) [Rub06]. One problem of this approach is immediately visible because the resulting term has to be corrected by a factor of  $1 \text{ V}^{-1}$  in order to obtain the correct physical unit. On the other hand, this simple multiplication shows immediately the most important property of the RF mixer – the frequency conversion.

$$v_{\text{IF}}^{\text{gen}}(t) = \frac{1}{1 \text{ V}} \frac{\hat{V}_{\text{in}} \hat{V}_{\text{LO}}}{2} \left[ \cos((\omega_{\text{LO}} - \omega_{\text{in}}) t - (\varphi_{\text{LO}} - \varphi_{\text{in}})) + \cos((\omega_{\text{LO}} + \omega_{\text{in}}) t - (\varphi_{\text{LO}} + \varphi_{\text{in}})) \right] \quad (\text{B.3})$$

The general IF signal  $v_{\text{IF}}^{\text{gen}}(t)$  consists of two cosine terms, representing oscillations at the sum and at the difference of the input frequencies. This process is called up- or down-conversion. In usual applications one of these frequency shifted components is selected with a band-pass filter. If the phase and the amplitude of the LO signal are constant, phase and amplitude of the input signal are transferred to the IF signal and can be detected there.

Figure B.1 shows the basic circuit of a double-balanced diode ring based RF mixer. The input and the LO input are usually not exchangeable at the double-balanced mixer because the baluns balancing the inputs are coupled differently on each port. In most operating conditions, the diodes in the ring are operated as switches, which is true if the diodes are saturated and the LO signal is significantly larger compared to the input signal. The harmonic LO signal practically acts as a square signal if its level is well above the saturation threshold. For simplification, one can perform calculations with the first element of the FOURIER expansion of a square wave [Rub06].

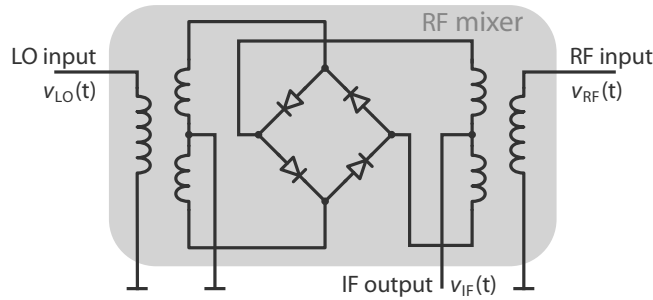


**Figure B.1: Schematic Circuit of a Double-Balanced Diode Ring Mixer** | The input and output signals use ground as reference. Figure adapted from [Rub06].

The diodes are operated as switches and connect the input signal with alternating polarity to the IF output. The transmission polarity is periodically inverted whenever the LO polarity

changes and the opposite diode pair is switched on. This operating mode is independent of the actual LO power as long as the LO input is saturated and the diodes are operated like switches. In the ideal case without internal losses, the input signal is fully transmitted to the IF output. The polarity however is periodically alternated by the LO signal.

This behavior can be modeled mathematically by approximating the LO switched diodes with a unity square wave which is multiplied with the input signal in order to simulate the mixing process [Rub06]. The unity square wave has an amplitude of one which corresponds to the loss free transmission by the fully switched diodes, while the alternating sign represents the alternating polarity of the mixer transmission. The FOURIER series of a unity square wave is given by

$$v_{LO}^{sq}(t) = \frac{4}{\pi} \left[ \cos(\omega_{LO}t - \varphi_{LO}) - \frac{1}{3} \cos(3(\omega_{LO}t - \varphi_{LO})) + \frac{1}{5} \cos(5(\omega_{LO}t - \varphi_{LO})) - \dots + \dots \right]. \quad (B.4)$$

Only the first order term is taken into account for the output signal, because the mixing products of the harmonic terms are anyway filtered out after the mixer. The multiplication of the first term of the square LO signal  $v_{LO}^{sq}(t)$  with the general harmonic input signal  $v_{in}$  from equation (B.2) yields the IF voltage

$$v_{IF}^{sq}(t) = \frac{4}{\pi} \frac{\hat{V}_{in}}{2} \left[ \cos((\omega_{LO} - \omega_{in})t - (\varphi_{LO} - \varphi_{in})) + \cos((\omega_{LO} + \omega_{in})t - (\varphi_{LO} + \varphi_{in})) \right]. \quad (B.5)$$

The sum and difference frequency terms are again present while the IF signal no longer depends on the LO signal power which is entirely used to switch the diodes. By applying a low-pass or band-pass filter to the result, one obtains the single sideband (SSB) output signal which reads for the lower sideband

$$v_{IF}^{SSB}(t) = \frac{4}{\pi} \frac{\hat{V}_{in}}{2} \left[ \cos((\omega_{LO} - \omega_{in})t - (\varphi_{LO} - \varphi_{in})) \right]. \quad (B.6)$$

The SSB conversion gain  $g_c$ , which actually is a conversion loss in case of a passive mixer is in general obtained by relating the SSB IF output power to the input power and therefore defined as

$$g_c = 10 \log_{10} \left( \frac{P_{IF}}{P_{in}} \right), \quad [g_c] = \text{dB}. \quad (B.7)$$

The input power  $P_{in}$  can be obtained from equation (B.2) and the output power  $P_{IF}^{SSB}$  from

equation (B.6). Assuming in both cases harmonic signals and an RF impedance  $Z_{50}$  of  $50\ \Omega$ , they amount to

$$P_{\text{in}} = \frac{\hat{V}_{\text{in}}^2}{2Z_{50}} \quad \text{and} \quad P_{\text{IF}}^{\text{SSB}} = \frac{\hat{V}_{\text{in}}^2}{2Z_{50}} \frac{4}{\pi^2}. \quad (\text{B.8})$$

The calculated conversion gain  $g_c^{\text{min}}$  of  $-3.92\ \text{dB}$  is the minimal intrinsic conversion loss one can expect from an RF mixer under the previously described operating conditions. Because no electrical losses have been accounted so far, the conversion gain of real components is actually even lower [Rub06].

If the input and LO frequencies are chosen to be identical, the lower sideband returns a direct current (DC) signal. The lower sideband can be extracted from the IF signal by low-pass filtering. In order to obtain the correct level of the output signal one can use the SSB conversion gain  $g_c$  which is usually given in the mixer data sheet and already accounts for the specific losses of the device. The conversion gain needs to be converted to a voltage gain following equation (B.9). By combining these statements with equation (B.6), one obtains the simplified mixer output equation presented in equation (B.10).

$$a_{\text{mix}} = 10^{\frac{g_c}{20}} \quad [g_c] = \text{dB} \quad (\text{B.9})$$

$$V_{\text{mix}} = a_{\text{mix}} \hat{V}_{\text{in}} \cos(\varphi_{\text{in}} - \varphi_{\text{LO}}) \quad (\text{B.10})$$

The argument of the cosine in equation (B.10) defines the working point and thereby also the operation mode of the mixer. The mixer can be used as a pure phase detector around the point where the cosine evaluates to zero but it can also be used for amplitude detection. In this case the cosine is supposed to evaluate to one.

## Pulse Trains and Their FOURIER Transform

Using the FOURIER transform allows to transform time domain signals into the frequency domain. This method is used during this thesis to explore the spectral and time domain properties of pulse trains composed of DIRAC delta pulses. This section will briefly introduce the theoretical background and mathematical tools, needed to perform FOURIER transforms of such signals.

The FOURIER transform  $\mathcal{F}$  of a time domain function  $x(t)$  into the angular frequency domain function  $\hat{x}(\omega)$  is defined as

$$\hat{x}(\omega) = \mathcal{F}\{x(t)\}(\omega) = \frac{1}{\sqrt{2\pi}} \int_{-\infty}^{\infty} x(t) e^{-j\omega t} dt. \quad (\text{C.1})$$

This is the most commonly used definition throughout literature found for example in [ZHS03]. The coefficient  $\sqrt{2\pi}^{-1}$  is needed when the FOURIER transform is performed to the angular frequency domain and the transformation is supposed to be symmetric with the inverse transformation. It can be omitted when the FOURIER transform is performed to the regular frequency domain or if symmetry is of no concern. Accordingly, the time domain function  $x(t)$  has a regular frequency domain representation  $\hat{x}(f)$  of

$$\hat{x}(f) = \mathcal{F}\{x(t)\}(f) = \int_{-\infty}^{\infty} x(t) e^{-j2\pi f t} dt. \quad (\text{C.2})$$

The inverse FOURIER transform from the regular frequency domain back to time domain has to be performed according to equation (C.3).

$$x(t) = \mathcal{F}\{\hat{x}(f)\}(t) = \int_{-\infty}^{\infty} \hat{x}(f) e^{j2\pi f t} df \quad (\text{C.3})$$

## C.1 Important Properties of FOURIER Transforms

Some additional properties of the FOURIER transform will be needed and they are therefore named here explicitly. These properties can be found in [ZHS03].

The *time shifting property* of the FOURIER transform states that a time shift in the time domain converts to a complex phase term in the frequency domain. Equation (C.4) demonstrates this circumstance for a function  $x(t)$  which is time (or phase) shifted by  $T_0$  in the time domain.

$$\mathcal{F}\{x(t - T_0)\}(f) = e^{-j2\pi f T_0} \mathcal{F}\{x(t)\}(f) \quad (\text{C.4})$$

Furthermore the FOURIER transform obeys the *principle of linearity*, which also means one can solve certain problems by superposition. Specifically, the FOURIER transform of the sum of two time domain functions  $x(t)$  and  $y(t)$  scaled by the factors  $a$  and  $b$  equals the scaled sum of their transforms as presented in equation (C.5).

$$\mathcal{F}\{ax(t) + by(t)\}(f) = a \mathcal{F}\{x(t)\}(f) + b \mathcal{F}\{y(t)\}(f) \quad (\text{C.5})$$

The *scaling property* relates scaling of the time scale to inverse scaling of the frequency scale and vice versa. Equation (C.6) demonstrates this by introducing the scaling factor  $a$  to the argument of the time domain function  $x(t)$ .

$$\mathcal{F}\{x(at)\}(f) = \frac{1}{|a|} \mathcal{F}\{x(t)\}(f/a) \quad (\text{C.6})$$

## C.2 The DIRAC Delta Pulse and the DIRAC Pulse Train

The DIRAC delta function  $\delta(t)$  represents an idealized pulse at the origin and is described by

$$\delta(t) = \begin{cases} +\infty, & t = 0 \\ 0, & t \neq 0 \end{cases} \quad (\text{C.7})$$

while the integral over this pulse evaluates per definition to unity [Jam11] as presented in equation (C.8).

$$\int_{-\infty}^{\infty} \delta(t) dt = 1 \quad (\text{C.8})$$

Strictly speaking, the DIRAC delta is not a genuine function but it can be understood as a SCHWARTZ distribution [ZHS03]. The classical calculations performed here are nevertheless well defined and established [ZHS03]. It is furthermore an interesting side note that the physical unit of the DIRAC delta is equal to the inverse unit of its argument. One example is given in equation (C.9).

$$[\delta(t)] = \frac{1}{[t]} = s^{-1} \quad (C.9)$$

An important attribute of the DIRAC delta function is the so-called *sifting property* shown in equation (C.10). The multiplication with the DIRAC delta function under the integral picks – or sifts out – the value of  $x(t)$  at the time  $T_0$  where the DIRAC pulse occurs [Jam11].

$$\int_{-\infty}^{\infty} \delta(t - T_0) x(t) dt = x(T_0) \quad (C.10)$$

The FOURIER transform of a single DIRAC delta pulse follows directly from the *sifting property*. The DIRAC pulse is not shifted and therefore the natural exponential function has to be evaluated only at the time of zero, where its value – and therefore the value of the whole integral – is one [Jam11].

$$\begin{aligned} \mathcal{F}\{\delta(t)\}(f) &= \int_{-\infty}^{\infty} \delta(t) e^{-j2\pi f t} dt \\ &= 1 \end{aligned} \quad (C.11)$$

A regular spaced pulse train can be idealized as a train of time shifted DIRAC delta pulses. In general, the function describing such a train of shifted DIRAC delta pulses is called the Sha function (III) [Jam11]. The basic Sha function with unity pulse spacing is shown in equation (C.12). The DIRAC delta pulses within the Sha function are according to their definition infinitesimally short.

$$\text{III}(x) = \sum_{b=-\infty}^{\infty} \delta(x - b) \quad (C.12)$$

The pulse spacing of the Sha function can be scaled by  $T$  as follows, while the relation to the unity Sha function can be derived using the *scaling property* of the DIRAC delta function (see equation (C.6)).

$$\text{III}_T(t) = \sum_{b=-\infty}^{\infty} \delta(t - bT) \quad (\text{C.13})$$

$$= \sum_{b=-\infty}^{\infty} \delta(T(t/T - b)) = \frac{1}{T} \text{III}(t/T) \quad (\text{C.14})$$

### C.3 FOURIER Series and FOURIER Transform of DIRAC Pulse Trains

Complex FOURIER series have to be introduced, because they will be needed to derive the *power spectral density (PSD)* and the FOURIER transform of the Sha function. The general ansatz function for the complex FOURIER series of a time domain function  $x(t)$  is according to [ZHS03]

$$x(t) = \sum_{b=-\infty}^{\infty} c_b e^{jb \frac{2\pi}{T} t}, \quad (\text{C.15})$$

where the complex FOURIER coefficients  $c_b$  have to be calculated by

$$c_b = \frac{1}{T} \int_{-T/2}^{T/2} x(t) e^{-jb \frac{2\pi}{T} t} dt. \quad (\text{C.16})$$

In order to obtain the FOURIER series corresponding to the scaled Sha function, the FOURIER coefficients  $c_{\text{III},b}$  have to be determined. Equation (C.17) has been defined using the general formula for the FOURIER coefficients given in equation (C.16). The Sha function can be replaced with a single DIRAC delta pulse because only one pulse can be found within the integration limits, which leads to equation (C.18). The integral can be easily solved by applying the *sifting property* of the DIRAC delta function (see equation (C.10)) in the same way it was used to derive the FOURIER transform of a single DIRAC delta pulse. The integration limits are not infinite but the DIRAC delta pulse is zero for any argument outside of these limits. The value of the integral is therefore one according to the definition of the DIRAC delta. The result in equation (C.19) states that all FOURIER coefficients of the scaled Sha function are finally identical [SiSa08].



$$c_{\text{III},b} = \frac{1}{T} \int_{-T/2}^{T/2} \text{III}_T(t) e^{-jb \frac{2\pi}{T} t} dt \quad (\text{C.17})$$

$$= \frac{1}{T} \int_{-T/2}^{T/2} \delta(t) e^{-jb \frac{2\pi}{T} t} dt \quad (\text{C.18})$$

$$c_{\text{III}} = \frac{1}{T} \quad (\text{C.19})$$

The FOURIER coefficients can be entered now into the equation of the general FOURIER series (see equation (C.15)) in order to obtain the FOURIER series equal to a scaled Sha function:

$$\text{III}_T(t) = \frac{1}{T} \sum_{b=-\infty}^{\infty} e^{jb \frac{2\pi}{T} t}. \quad (\text{C.20})$$

Equation (C.20) states the general equivalence between a series of regular spaced DIRAC pulses and its complex FOURIER series representation with the calculated FOURIER coefficients. The same relation can be used in the frequency domain by a simple substitution of variables in order to formulate an alternative representation of a DIRAC comb. If the time  $t$  is replaced by the frequency  $f$  and the period  $T$  by the repetition rate  $T^{-1}$  one obtains equation (C.21), which will be needed during the calculation of the FOURIER transform of the scaled Sha function.

$$\sum_{b=-\infty}^{\infty} \delta(f - b/T) = T \sum_{b=-\infty}^{\infty} e^{jb2\pi T f} \quad (\text{C.21})$$

The scaled Sha function can finally be transferred to the regular frequency domain using the FOURIER transform which reveals its spectral representation. The summation in equation (C.22) can be moved out of the integral due to the *principle of linearity* (see equation (C.5)). The *time shifting property* of the FOURIER transform (see equation (C.4)) allows to do the same with the time shift of the DIRAC pulses. The integral in equation (C.23) evaluates by definition to one as it represents the FOURIER transform of a single DIRAC delta function. The remaining sum of natural exponential functions from the time shift can be expanded to the FOURIER series of a DIRAC comb (see equation (C.21)), exposing an additional factor of  $1/T$  as presented in equation (C.25). The frequency domain representation of a time domain pulse train is thus a regular spaced frequency comb. The FOURIER transform of the Sha function is again a Sha function in the frequency domain. The line

spacing is inverted relative to the time domain representation because it is scaled by  $1/T$ . The result is confirmed by [Jam11].

$$\mathcal{F}\{\text{III}_T(t)\}(f) = \int_{-\infty}^{\infty} \sum_{b=-\infty}^{\infty} \delta(t - bT) e^{-j2\pi f t} dt \quad (\text{C.22})$$

$$= \sum_{b=-\infty}^{\infty} e^{-jb\omega T} \int_{-\infty}^{\infty} \delta(t) e^{-j2\pi f t} dt \quad (\text{C.23})$$

$$= \frac{1}{T} \sum_{b=-\infty}^{\infty} \delta(f - b/T) \quad (\text{C.24})$$

$$= \frac{1}{T} \text{III}_{1/T}(f) \quad (\text{C.25})$$

The obtained frequency comb is defined as infinite sum of DIRAC delta pulses which are distributed from negative to positive infinity just as their time domain counterpart is defined. In summary, the FOURIER transform of a Sha function is another Sha function.

## C.4 Spectral Representations of Signals

The FOURIER transform which represents the complex spectral representation of a signal contains its amplitude and phase information in the frequency domain. Especially the existence of the phase term can be depicted by simply exploiting the *time shifting property* of the FOURIER transform (see equation (C.4)). FOURIER transforming a DIRAC pulse train which is time shifted by  $T_0$  leads to the following result which contains a complex phase term in the frequency domain:

$$\mathcal{F}\{\text{III}_T(t - T_0)\}(f) = e^{-j2\pi f T_0} \frac{1}{T} \text{III}_{1/T}(f) \quad (\text{C.26})$$

$$= e^{-j2\pi f T_0} \frac{1}{T} \sum_{b=-\infty}^{\infty} \delta(f - b/T). \quad (\text{C.27})$$

The phase term evolves with the frequency, while the amplitude of the frequency comb is independent and constant for all frequencies. This finding about the constant amplitude was also present in the result for the FOURIER coefficients of the Sha function, which were all equal (see equation (C.19)). This circumstance originates from the fact that the time domain pulse train consists of infinitesimal short DIRAC delta pulses which by definition have unlimited bandwidth.

An alternative frequency domain representation called **energy spectral density (ESD)** can only be obtained for so-called energy signals [Pap62]. These are signals with a finite energy like transient signals, pulses or other time limited wave forms. Mathematically, these signals are called *square integrable* – which means the integral of the signal squared may not be infinite.

*PARSEVAL's theorem* states that the overall energy of a signal  $x(t)$  does not change when this signal is transferred to its frequency domain representation. The right hand side integrand in equation (C.28) is actually called the **ESD** of the signal  $x(t)$  while the left hand side integrand is referred to as the instantaneous power of the signal  $x(t)$ . The overall energy of the signal can be either calculated by integrating its power over all times or its spectral density over all frequencies – which is precisely the meaning of *PARSEVAL's theorem* [ZHS03].

$$\int_{-\infty}^{\infty} |x(t)|^2 dt = \int_{-\infty}^{\infty} |\mathcal{F}\{x(t)\}(f)|^2 df \quad (\text{C.28})$$

Strictly speaking one also has to additionally scale the **ESD** with the system impedance  $Z$ , such that it is not only proportional to the energy of the signal but actually represents the energy in a physical sense. This scaling with a constant factor on both sides of the equation does neither violate *PARSEVAL's theorem* nor change the shape of the spectrum. It is for this reason that the scaling is often omitted in the field of signal theory where the qualitative analysis of a signal is mostly of concern.

Harmonic signals usually have unlimited energy because they are unlimited in time. Therefore, the **ESD** is not defined for them. If however such a signal has for all times a finite power it can be called a power signal and the **power spectral density (PSD)** can be calculated in order to investigate the spectral properties of this signal [Pap62].

In order to calculate the **PSD**, at first the average power  $P_x$  of the signal  $x(t)$  has to be regarded. This is done by integrating the squared signal over a fixed period of time  $2T$  called the observation period which returns the signal energy in this time span. The average power in this time span is obtained by averaging the energy over the observation period [Pap62]. Subsequently, this period of time is expanded to infinity. If the average power is not zero or does not grow to infinity it is possible to obtain the **PSD** of  $x(t)$ , while the mean power of the signal is calculated following equation (C.29).

$$P_x = \lim_{T \rightarrow \infty} \frac{1}{2T} \int_{-T}^T |x(t)|^2 dt \quad (\text{C.29})$$

A similar procedure can be used to calculate the autocorrelation function  $R_{xx}(t)$  of the

signal  $x(t)$  [Pap62]. The autocorrelation of a complex signal is defined in equation (C.30), where  $x^*(t)$  denotes the complex conjugate of  $x(t)$ . This function is again first calculated for a fixed observation period  $2\mathcal{T}$  which is subsequently extended to infinity.

$$R_{xx}(t) = \lim_{\mathcal{T} \rightarrow \infty} \frac{1}{2\mathcal{T}} \int_{-\mathcal{T}}^{\mathcal{T}} x^*(\tau) x(\tau + t) d\tau \quad (\text{C.30})$$

The autocorrelation for a time shift of zero returns the average power, which reads

$$R_{xx}(0) = P_x. \quad (\text{C.31})$$

The spectrum of the autocorrelation is finally revealed by FOURIER transforming the autocorrelation function. The result is per definition called the **power spectral density (PSD)**, denoted with  $S_{xx}(f)$  [Pap62]. This statement is well known as the *WIENER-KHINCHINE theorem* from the field of statistical signal analysis and distributions [Jam11].

$$S_{xx}(f) = \mathcal{F}\{R_{xx}(t)\}(f) \quad (\text{C.32})$$

The above statement can be proven by applying an ideal band-pass filter to the signal  $x(t)$ . It is possible to show then that the power of the output signal of the band-pass filter is equal to the integral over the FOURIER transform of the autocorrelation of the input function within the limits of the pass band frequency range of the filter. Therefore it is perfectly justified to call  $S_{xx}(f)$  the **PSD** of the signal  $x(t)$ . The derived equations are valid for continuous, deterministic signals. They do not cover stochastic processes or non-deterministic noise. Further reading on stochastic signals is provided in [Pap62], while [Qui<sup>+</sup>13] deals specifically with the non-deterministic photodetection of optical pulse trains.

## C.5 The Power Spectral Density of General FOURIER Series

To calculate the **PSD** of a scaled DIRAC pulse train one needs to derive its autocorrelation and find the FOURIER transform of the result. As a first step the autocorrelation  $R_{\mathcal{FF}}(t)$  of the general equation for a complex FOURIER series (see equations (C.15) and (C.16)) are now calculated. The result is tailored later to a DIRAC pulse train by replacing the FOURIER coefficients  $c_d$  and their complex conjugate  $c_b^*$  with the unique coefficient of the DIRAC comb  $c_{\text{III}}$ , which is actually simpler to calculate because this parameter is real and identical for all frequencies (see equation (C.19)). The derivation also takes the scaling

factor  $a$  and the time shift  $T_0$  into account. The following equations make furthermore use of the observation period  $\mathcal{T}$  and the angular frequency  $\omega = 2\pi f$ .

$$R_{\mathcal{F}\mathcal{F}}(t) = \lim_{\mathcal{T} \rightarrow \infty} \frac{1}{2\mathcal{T}} \int_{-\mathcal{T}}^{\mathcal{T}} \sum_{b=-\infty}^{\infty} a^* c_b^* e^{-jb\omega(\tau-T_0)} \sum_{d=-\infty}^{\infty} a c_d e^{jd\omega(\tau-T_0+t)} d\tau \quad (\text{C.33})$$

One can first pull the summations and all variables not depending on  $\tau$  out of the limes and the integral because they are constant for these operations, leading to equation (C.34). The difference of two natural exponentials with inverted exponent in equation (C.36) resulting from the evaluation of the integral can be replaced by a sine in equation (C.37) which can again be simplified to a sinc function in equation (C.38).

$$R_{\mathcal{F}\mathcal{F}}(t) = |a|^2 \sum_{b,d=-\infty}^{\infty} c_b^* c_d e^{j\omega[d(t-T_0)+bT_0]} \lim_{\mathcal{T} \rightarrow \infty} \frac{1}{2\mathcal{T}} \int_{-\mathcal{T}}^{\mathcal{T}} e^{j(d-b)\omega\tau} d\tau \quad (\text{C.34})$$

$$= |a|^2 \sum_{b,d=-\infty}^{\infty} c_b^* c_d e^{j\omega[d(t-T_0)+bT_0]} \lim_{\mathcal{T} \rightarrow \infty} \frac{1}{2\mathcal{T}} \left[ \frac{1}{j(d-b)\omega} e^{j(d-b)\omega\tau} \right]_{-\mathcal{T}}^{\mathcal{T}} \quad (\text{C.35})$$

$$= |a|^2 \sum_{b,d=-\infty}^{\infty} c_b^* c_d e^{j\omega[d(t-T_0)+bT_0]} \lim_{\mathcal{T} \rightarrow \infty} \frac{e^{j(d-b)\omega\mathcal{T}} - e^{-j(d-b)\omega\mathcal{T}}}{2j(d-b)\omega\mathcal{T}} \quad (\text{C.36})$$

$$= |a|^2 \sum_{b,d=-\infty}^{\infty} c_b^* c_d e^{j\omega[d(t-T_0)+bT_0]} \lim_{\mathcal{T} \rightarrow \infty} \frac{2j \sin((d-b)\omega\mathcal{T})}{2j(d-b)\omega\mathcal{T}} \quad (\text{C.37})$$

$$= |a|^2 \sum_{b,d=-\infty}^{\infty} c_b^* c_d e^{j\omega[d(t-T_0)+bT_0]} \lim_{\mathcal{T} \rightarrow \infty} \text{sinc}((d-b)\omega\mathcal{T}) \quad (\text{C.38})$$

It is obvious after integrating that the limit of the sinc function in equation (C.38) is zero – except in the case where the argument of the sinc function becomes zero itself, which happens when  $b$  is equal to  $d$ . In this case the limit of the sinc function is one. The two dimensional summation is therefore simplified to a one dimensional summation containing only the non-zero summands by setting  $b$  equal to  $d$  which reveals the following result for the autocorrelation of a general FOURIER series:

$$R_{\mathcal{F}\mathcal{F}}(t) = |a|^2 \sum_{b=-\infty}^{\infty} |c_b|^2 e^{jb\omega t}. \quad (\text{C.39})$$

The autocorrelation function of a general complex FOURIER series in equation (C.39) is another FOURIER series, just that the FOURIER coefficients have to be taken by their

squared norm. In case the FOURIER parameters are not complex, this condition reduces to a simple square. The same applies to the constant scaling factor  $a$  of the FOURIER series which also appears by its squared norm in the autocorrelation result.

Phase shifts of the initial FOURIER series however cancel out during the autocorrelation due to the multiplication with the complex conjugate of the FOURIER series itself. Regarded from a physical instead of a signal theory point of view, the PSD needs to be scaled by the system impedance  $Z$  like the ESD which is missing in the previous presentation – a common circumstance in the field of signal analysis.

The derivation of the autocorrelation of a sum of two individually time shifted and scaled but otherwise identical FOURIER series  $R_{\mathcal{F}\mathcal{F}_+}(t)$  looks slightly different, although the actual derivation can be performed in almost the same way as presented before. The parameters are named like in the previous equation, which are the individual scaling factors  $a_0$  and  $a_1$  with their complex conjugates  $a_0^*$  and  $a_1^*$ , the individual time shifts  $T_0$  and  $T_1$  and the common FOURIER coefficients  $c_d$  with their complex conjugate  $c_b^*$ . The different elements of the equation are first sorted in equation (C.41). Basically, everything not depending on  $\tau$  is factored out of the integral which is then identical to the one in equation (C.34). Therefore it is also here possible to reduce the two dimensional sum to a one dimensional sum by evaluating the integral. Furthermore the brackets are expanded such that the structure of the equation is visible in equation (C.42).

$$R_{\mathcal{F}\mathcal{F}_+}(t) = \lim_{\mathcal{T} \rightarrow \infty} \frac{1}{2\mathcal{T}} \int_{-\mathcal{T}}^{\mathcal{T}} \sum_{b=-\infty}^{\infty} \left[ a_0^* c_b^* e^{-jb\omega(\tau-T_0)} + a_1^* c_b^* e^{-jb\omega(\tau-T_1)} \right] \cdot \sum_{d=-\infty}^{\infty} \left[ a_0 c_d e^{jd\omega(\tau-T_0+t)} + a_1 c_d e^{jd\omega(\tau-T_1+t)} \right] d\tau \quad (\text{C.40})$$

$$= \lim_{\mathcal{T} \rightarrow \infty} \frac{1}{2\mathcal{T}} \int_{-\mathcal{T}}^{\mathcal{T}} e^{j(d-b)\omega\tau} d\tau \sum_{b,d=-\infty}^{\infty} \left[ a_0^* c_b^* e^{jb\omega T_0} + a_1^* c_b^* e^{jb\omega T_1} \right] \cdot \left[ a_0 c_d e^{-jd\omega T_0} + a_1 c_d e^{-jd\omega T_1} \right] e^{jd\omega t} \quad (\text{C.41})$$

$$= |a_0|^2 \sum_{b=-\infty}^{\infty} |c_b|^2 e^{jb\omega t} + a_0^* a_1 \sum_{b=-\infty}^{\infty} |c_b|^2 e^{jb\omega(t+(T_0-T_1))} + a_0 a_1^* \sum_{b=-\infty}^{\infty} |c_b|^2 e^{jb\omega(t+(T_1-T_0))} + |a_1|^2 \sum_{b=-\infty}^{\infty} |c_b|^2 e^{jb\omega t} \quad (\text{C.42})$$

To further simplify equation (C.42), two assumptions have to be made, which foreshadow already the purpose of this derivation because they narrow down the scope of the final result. The equation is later used to calculate the PSD of the sum of two or more FOURIER pulse

trains. Therefore all FOURIER coefficients are assumed to be equal and real. Additionally the general scaling factors  $a_0$  and  $a_1$  are also assumed to be real, which reads

$$c_d = c_b^* = c \quad \text{and} \quad \{c, a_0, a_1 \in \mathbb{R}\}. \quad (\text{C.43})$$

Using the above assumptions equation (C.42) turns into

$$\begin{aligned} R_{\mathcal{FF}_+}^\dagger(t) = & a_0^2 c \sum_{b=-\infty}^{\infty} c e^{jb\omega t} + a_0 a_1 c \sum_{b=-\infty}^{\infty} c e^{jb\omega(t+(T_0-T_1))} \\ & + a_0 a_1 c \sum_{b=-\infty}^{\infty} c e^{jb\omega(t+(T_1-T_0))} + a_1^2 c \sum_{b=-\infty}^{\infty} c e^{jb\omega t}. \end{aligned} \quad (\text{C.44})$$

Now the FOURIER transform  $S_{\mathcal{FF}_+}^\dagger(f)$  of equation (C.44) has to be found in order to calculate the PSD. All four summands can be FOURIER transformed individually and the constant factors can be factored out of the FOURIER transform by using the *principle of linearity* (see equation (C.5)). The time shifts are covered by applying the *time shifting property* (see equation (C.4)) of the FOURIER transform.

$$S_{\mathcal{FF}_+}^\dagger(f) = c \left[ a_0^2 + a_0 a_1 e^{j\omega(T_0-T_1)} + a_0 a_1 e^{j\omega(T_1-T_0)} + a_1^2 \right] \mathcal{F} \left\{ \sum_{b=-\infty}^{\infty} c e^{jb\omega t} \right\}(f) \quad (\text{C.45})$$

$$= c \left[ a_0^2 + a_1^2 + 2a_0 a_1 \cos(\omega(T_1 - T_0)) \right] \mathcal{F} \left\{ \sum_{b=-\infty}^{\infty} c e^{jb\omega t} \right\}(f) \quad (\text{C.46})$$

$$= c \left| a_0 e^{-j\omega T_0} + a_1 e^{-j\omega T_1} \right|^2 \mathcal{F} \left\{ \sum_{b=-\infty}^{\infty} c e^{jb\omega t} \right\}(f) \quad (\text{C.47})$$

Equation (C.47) shows that the PSD of the sum of two identical FOURIER series with one unique FOURIER coefficient  $c$  equals the squared norm of the sum of the phasors associated with the two signals, multiplied by the FOURIER coefficient  $c$  and the FOURIER transform of the series itself. This principle can be extended to more than two signals. If the calculations from above are performed for four signals, one obtains accordingly

$$S_{\mathcal{FF}_\Sigma}^\dagger(f) = c \left| a_0 e^{-j\omega T_0} + a_1 e^{-j\omega T_1} + a_2 e^{-j\omega T_2} + a_3 e^{-j\omega T_3} \right|^2 \mathcal{F} \left\{ \sum_{b=-\infty}^{\infty} c e^{jb\omega t} \right\}(f). \quad (\text{C.48})$$

## C.6 The Power Spectral Density of DIRAC Pulse Trains

The preceding results can now be used to calculate the PSD of a scaled (by a real factor of  $a$ ) and time shifted (by  $T_0$ ) FOURIER pulse train with a repetition period of  $T_{\text{rep}}$ . The

pulse train is first replaced by its FOURIER series representation in equation (C.49). The autocorrelation  $R_{\text{III}}(t)$  of this pulse train can be calculated following equations (C.33) to (C.38) and the result is to be found in equation (C.51).

$$a\text{III}_{T_{\text{rep}}}(t - T_0) = \frac{a}{T_{\text{rep}}} \sum_{b=-\infty}^{\infty} e^{jb \frac{2\pi}{T_{\text{rep}}}(t-T_0)} \quad (\text{C.49})$$

$$R_{\text{III}}(t) = \left( \frac{a}{T_{\text{rep}}} \right)^2 \sum_{b=-\infty}^{\infty} e^{jb \frac{2\pi}{T_{\text{rep}}} t} \quad (\text{C.50})$$

$$= \frac{a^2}{T_{\text{rep}}} \text{III}_{T_{\text{rep}}}(t) \quad (\text{C.51})$$

Considering equation (C.32) the PSD of the FOURIER pulse train  $S_{\text{III}}(f)$  can be calculated by FOURIER transforming the previous result – which by the use of equation (C.25) turns out as follows in equation (C.53). The equation makes use of the repetition rate  $f_{\text{rep}}$  which is the reciprocal of the repetition period  $T_{\text{rep}}$ .

$$S_{\text{III}}(f) = \mathcal{F}\{R_{\text{III}}(t)\}(f) \quad (\text{C.52})$$

$$= \left( \frac{a}{T_{\text{rep}}} \right)^2 \text{III}_{f_{\text{rep}}}(f) \quad (\text{C.53})$$

One finally has to combine the results from equations (C.48) and (C.53) in order to calculate the PSD of a signal, composed by the sum of four individually shifted and scaled DIRAC pulse trains.

$$S_{\text{III}\Sigma}(f) = \left| \frac{1}{T_{\text{rep}}} (a_0 e^{-j\omega T_0} + a_1 e^{-j\omega T_1} + a_2 e^{-j\omega T_2} + a_3 e^{-j\omega T_3}) \right|^2 \text{III}_{f_{\text{rep}}}(f) \quad (\text{C.54})$$

This rather specific equation has been derived in anticipation of the study of the **laser-to-RF (L2RF)** principle, during which the analysis of the PSD of exactly such a signal will be required.

Most notably, the DIRAC pulse train is not only invariant to the FOURIER transform, but also to the autocorrelation and the calculation of the PSD. The part of equation (C.54) in front of the DIRAC comb can be regarded as the continuous envelope of the PSD.

This general representation of the PSD is used to investigate the spectral properties of modulated laser pulse trains generated by the **L2RF** setup. The mathematical analysis of the **L2RF** setup and its signals are presented in chapter 3 where also the definitions from this chapter are recalled.



## Photographs

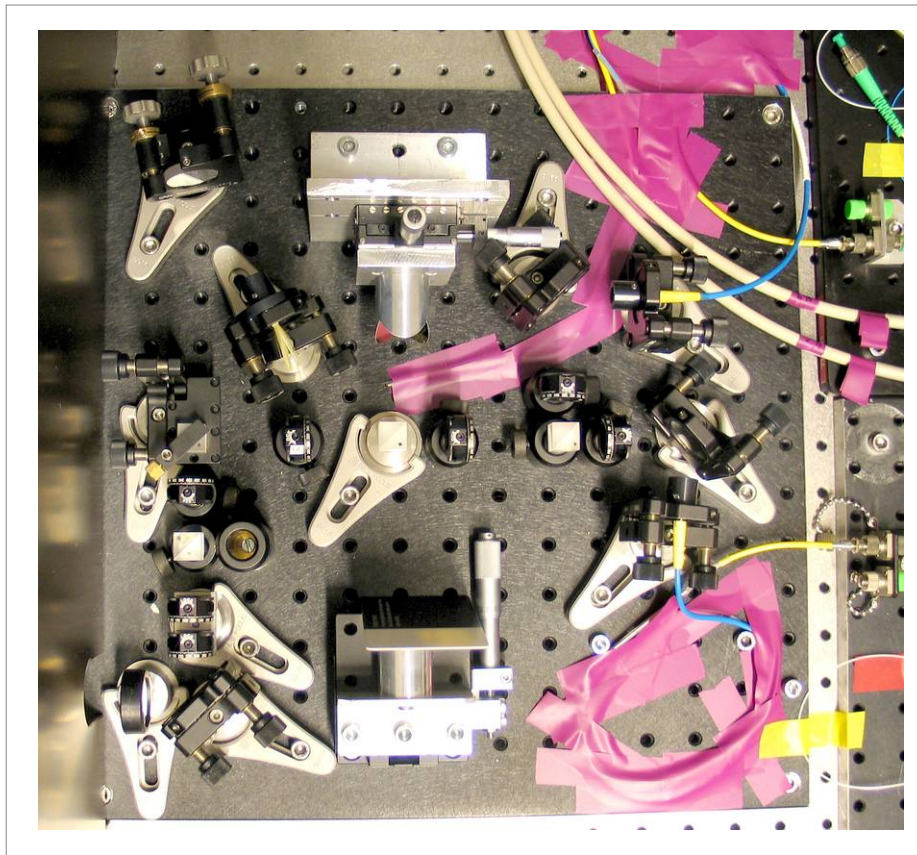


**Figure D.1: The First Delay Line of the First Laboratory Prototype** | The laser input is in the lower left corner. The lower CCR is covered by a detector card during alignment. The length of the first delay line is adjusted by the translation stage at the lower CCR, the alignment is performed by the two dimensional translation stage at the upper CCR. The PM collimators with blue fibers on the right hand side lead to one L2RF setup each. The LO generation is located in the upper left corner. The fiber from this collimator has no tubing and it is therefore hardly visible.

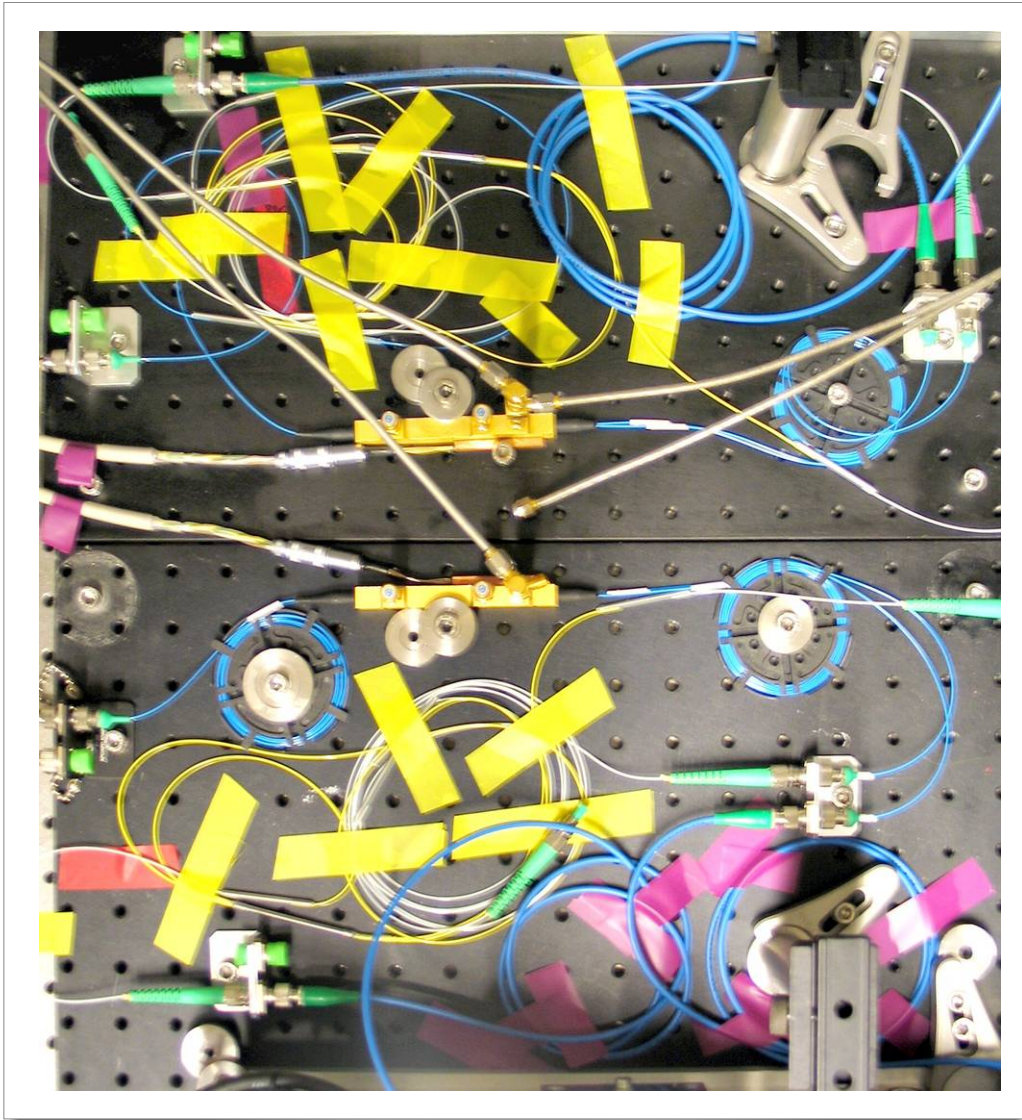


**Figure D.2: The Second Delay Line of the First Laboratory Prototype** | The two fiber inputs from the first delay line on the left hand side are directly connected to the integrated MZMs in the center. The MZMs have not yet been thermally isolated and actively temperature controlled in this early stage of the prototype. The second delay line is realized in fiber. The free-space delay lines needed to fine tune the length of each are not shown. The recombination of both signals in the second delay line is performed in a PM combiner.



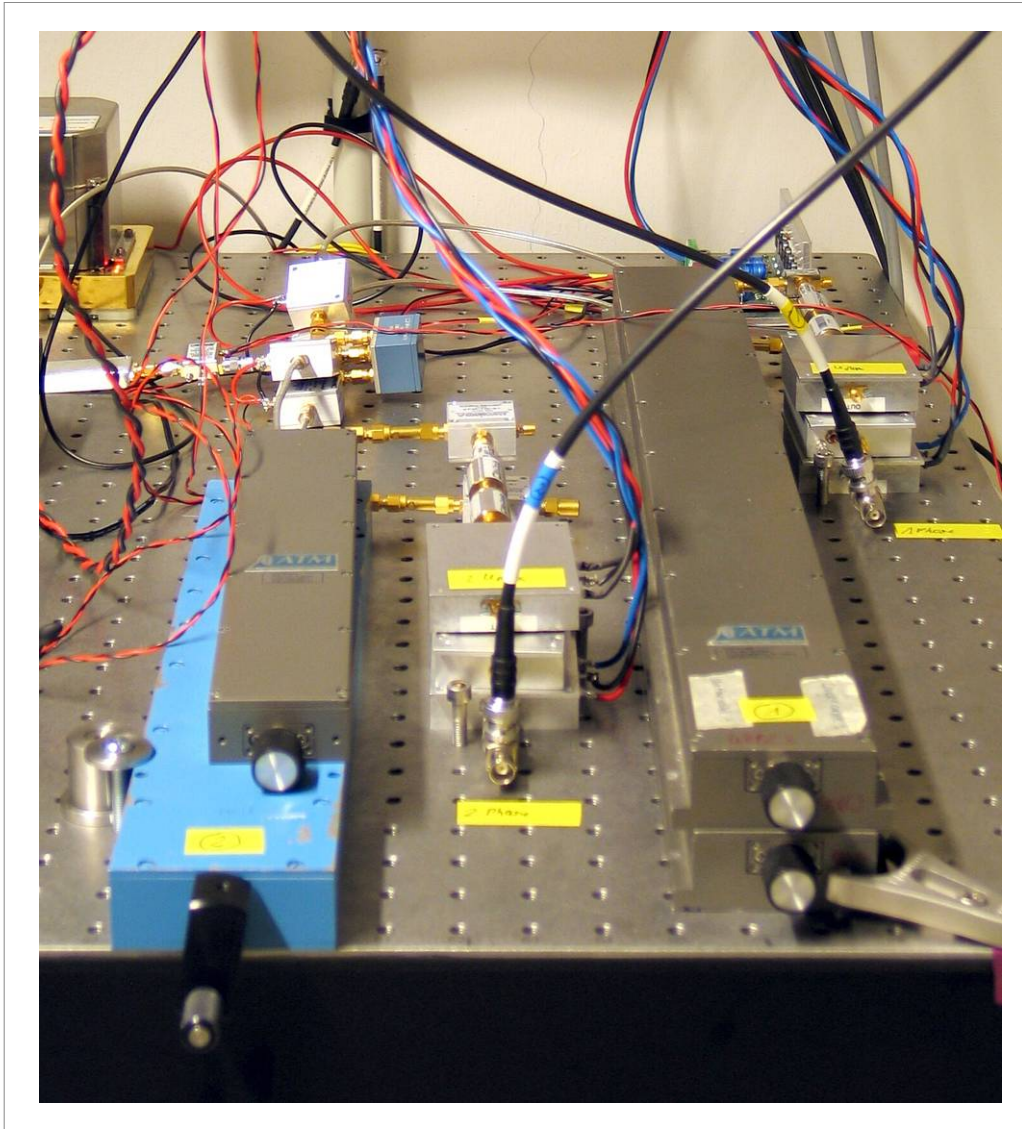


**Figure D.3: The Readout Electronics of the First Laboratory Prototype** | The readout electronics of the first prototype contain in this stage two channels per **L2RF** phase detector used to detect the phase and bias error signals at each setup. The **LO** phase which defines the working point is adjusted by the depicted manual phase shifters. The actual **LO** generation with the four-way splitter is located in the rear of the optical bench. Additionally in the upper left corner a part of the 1.3 GHz **DRO** used as **RF** source is visible.

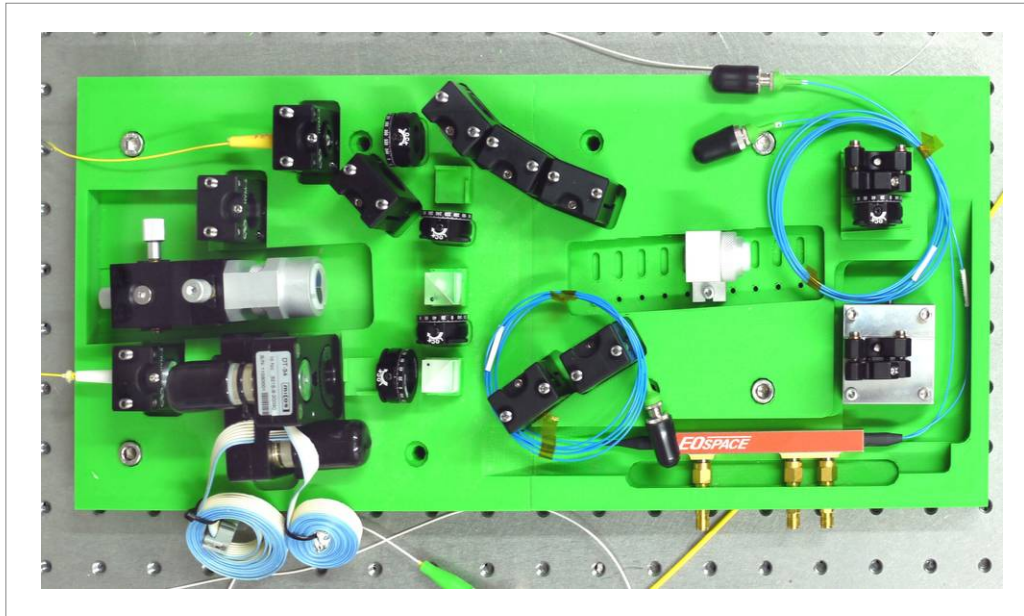


**Figure D.4: Rapid Prototyping of the Integrated L2RF Optics** | The polarization adjustment behind the input fiber collimator in the lower left corner can be optionally motorized (shown here). The first delay line is composed by CCRs in the center of the plate. The left CCR is adjustable in terms of alignment and delay length. A coarse delay length setting can be performed at the right CCR which allows to cover frequency ratios for different scenarios. The fiber leading to the MZM is shown in the upper right corner. The MZM is mounted in the lower part of the plate in a special pocket. The free-space components on the right hand side are dedicated to the fine-tuning of the length of the second delay line. Critical optical elements are tilted with respect to the beam path in order to mitigate reflections.

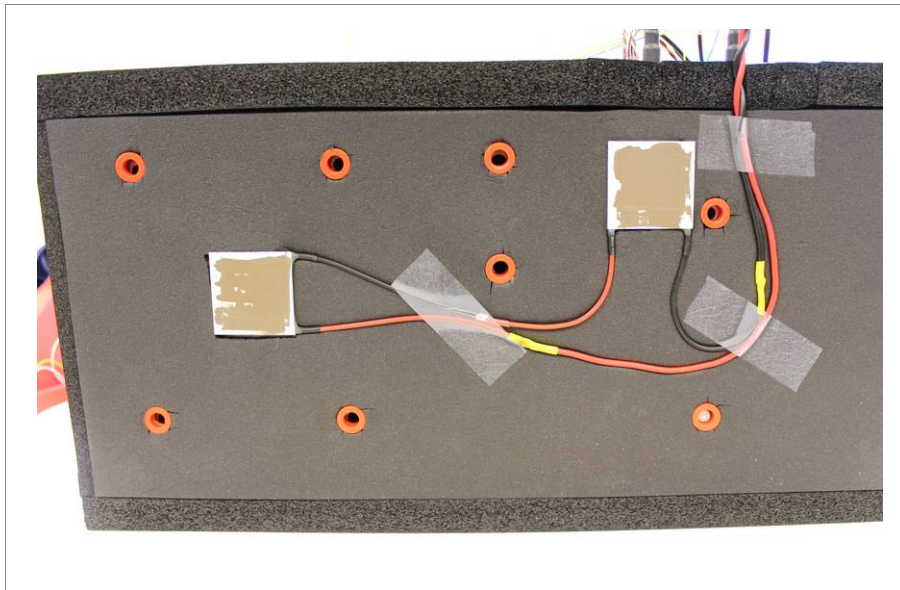


**Figure D.5: Thermal Control of the Integrated L2RF Optics Using Peltier Elements** | The Peltier elements are glued to the baseplate with thermally conductive glue and thermally conductive paste has already been applied to their bottom side. The complete optical assembly is isolated with elastomeric foam according to the available space in the 19" housing. The mounting screws for the heat sink are distributed such that they fit between components on the top side while still allowing to hold both Peltier elements.



**Figure D.6: Side View on the Integrated L2RF Optics Showing the Humidity Buffer** | A two-chamber sachet with 250 g of PROSorb silica gel is mounted to the top cover for humidity stabilization of the setup. One chamber is shown.

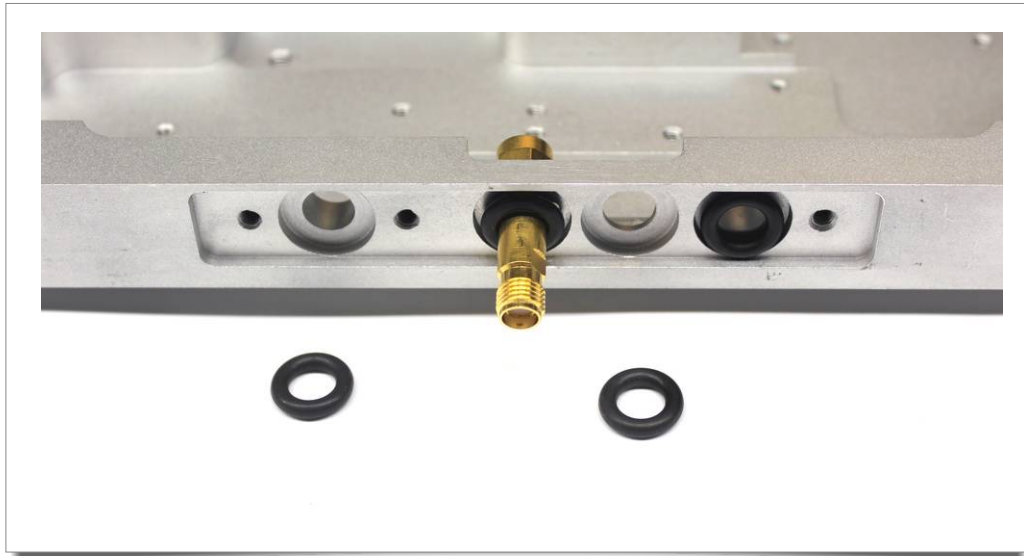


**Figure D.7: RF Feed-Through Sealing with Rubber O-Ring Gaskets** | Standard SMA adapters are used as feed-throughs. The available drill holes allow to mount MZMs from the companies EOSpace and Jenoptik.



**Figure D.8: RF Feed-Through Sealing Assembled** | The cover seals the gaskets by applying pressure to them. Unused drill holes are sealed by additional o-ring gaskets while the cover is closed at these positions. Different covers allow to mount different types of MZMs.



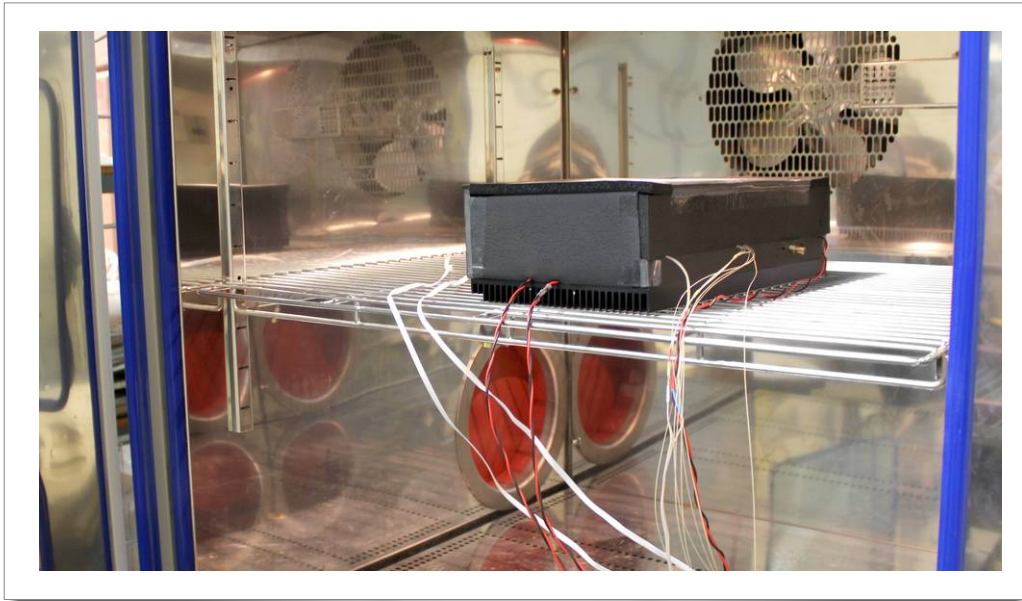


**Figure D.9: Temperature and Humidity Characterization in a Climate Chamber |**

The integrated optics of the [L2RF](#) phase detector are tested in a climate chamber which allows to independently control temperature and humidity in a wide range. The integrated optics are mounted on the foreseen heatsink and actively temperature controlled by two [Peltier](#) elements. The thermal isolation is assembled according to the space available in the 19" housing foreseen for the [REFM-OPT](#). The temperatures of the heatsink and at various positions on the baseplate are monitored by sensors. Additionally the assembly is sealed. In order to stabilize the inside relative humidity, a humidity buffer of 250 g of [PROSorb](#) silica gel is mounted inside. The relative humidity is monitored inside and outside of the integrated optics by humidity sensors in order to test the assembly.

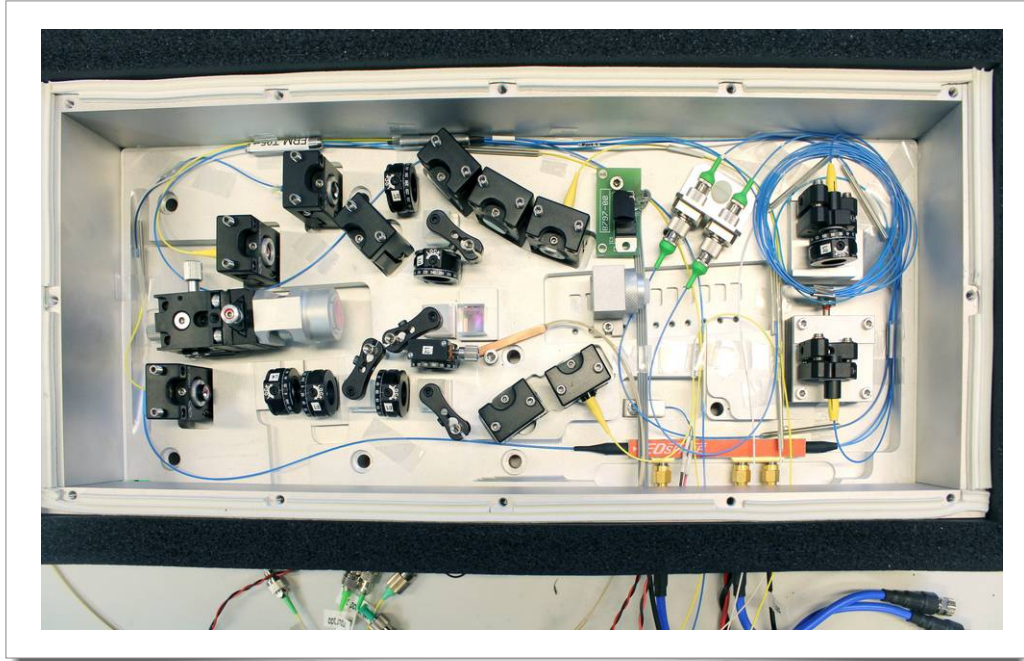


**Figure D.10: Final Integrated Optics for the L2RF Phase Detector** | The presented setup is fully equipped and ready for integration into the [REFM-OPT](#). In addition to the optical components, which have already been explained in figure [D.4](#), a humidity sensor (small [PCB](#) in the upper part of the picture) and a temperature sensor (copper block in the center of the picture) are mounted on the baseplate for monitoring purpose. The sensor for thermal control is mounted next to the [MZM](#) below a small metal plate. The output fibers of the [MZM](#) are still connectorized and not cut and spliced like the other fiber components. This allows to easily exchange the [MZM](#) in case of damage. The phase information is at this point of the setup already encoded in the amplitude of the laser pulse train. The setup is therefore tolerant to length changes of these fibers. The delay lengths are adjusted for the [FLASH](#) and European [XFEL](#) frequency ratio. The [FRM](#) which terminates the fiberlink which supplies the setup with its reference signal is an in-fiber component and located in the upper left corner of the box. Considering the fiber length required for splicing and the required bending radii this is the closest possible position to the input fiber collimator in the lower left corner.



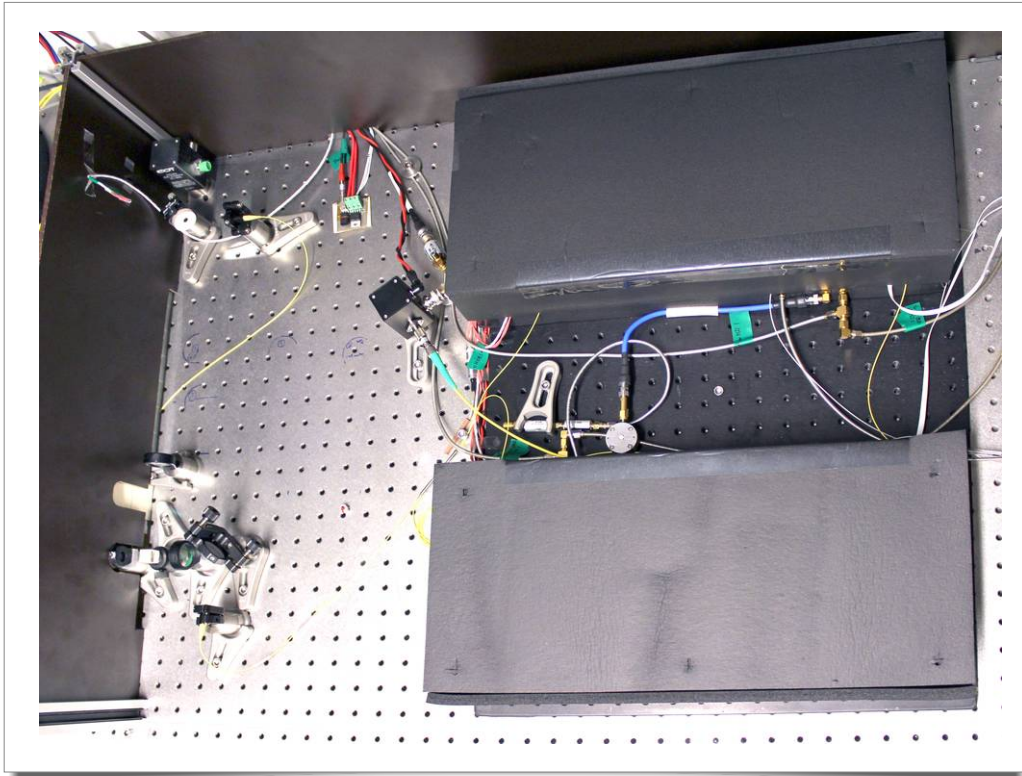


**Figure D.11: Out-of-Loop Measurement of the Second L2RF Prototype (Optics) |**

The integrated optical setups of two **L2RF** phase detectors are mounted on an optical bench. The assemblies are closed, actively temperature controlled and humidity stabilized. The optical reference laser is located outside of the lower left corner of the picture. A 3 dB fiber splitter is used to distribute the optical reference signal to both setups. The fibers behind the splitter are kept as short as possible and the length to both phase detectors is precisely equal. The **RF** signal between both setups is transported by 250 mm of phase stable Phase-master 190 cable (blue). The phase between **RF** signal and laser pulse train at the out-of-loop phase detector and therefore its working point is adjusted by the round phase shifter connected to this cable.

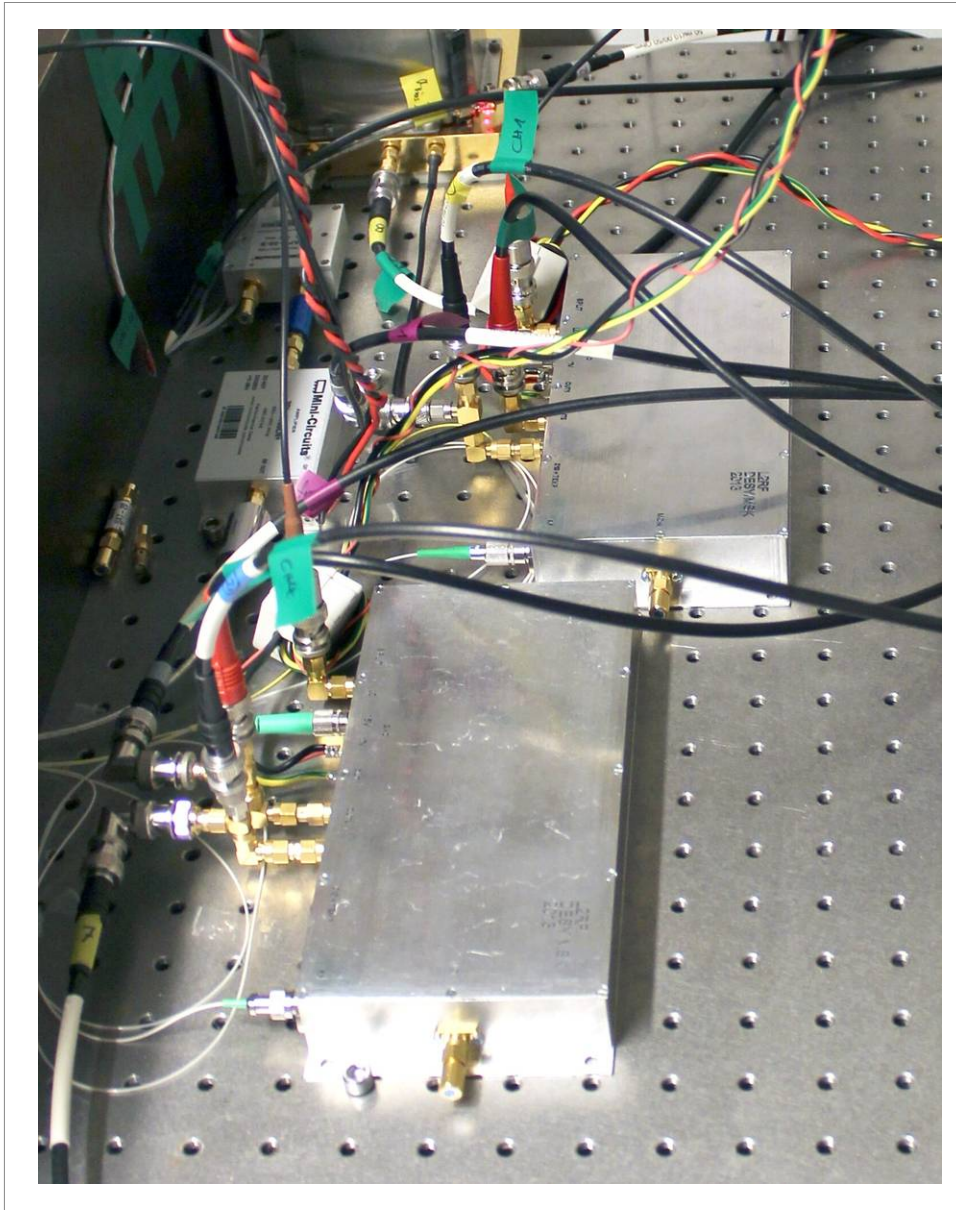


**Figure D.12: Out-of-Loop Measurement of the Second L2RF Prototype (Read-out)** | The optical signals from the in-loop and out-of-loop setups are analyzed using two independent prototypes of the integrated readout electronics. The different error signals are either fed to feedback loops or to a data acquisition unit in order to perform long-term measurements. In the upper left corner of the picture, the RF generation chain is visible in the background. The signal from the DRO is amplified before being transferred to the MZM.

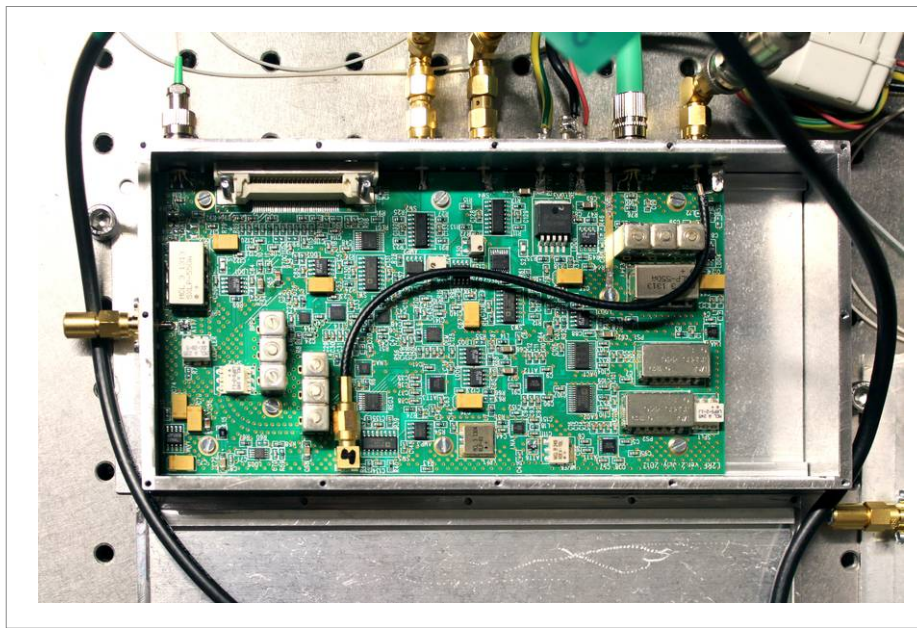


**Figure D.13: Internals of the Integrated Readout Electronics** | The device covers the three measurement channels for phase, bias voltage and splitting ratio errors. Internal parameters like the LO phase or attenuator settings are digitally controllable. Internal photodiodes detect the signals and a diagnostics port allows direct access to the modulated pulse train after detection.

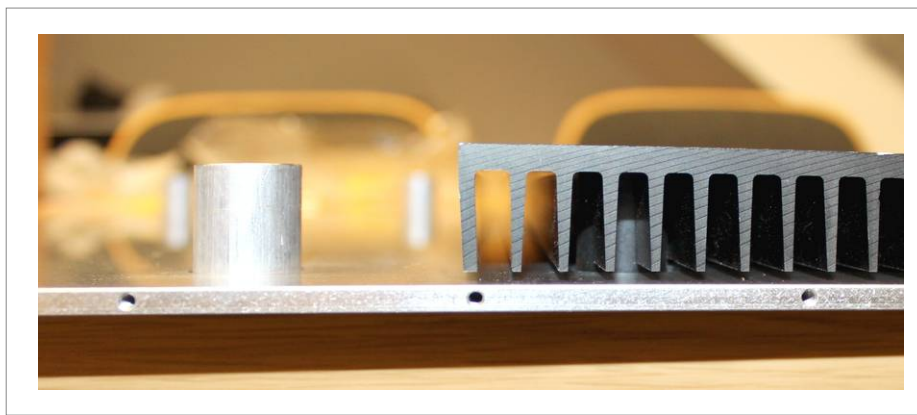


**Figure D.14: Vibration Damping for the Integrated Optics inside the REFM-OPT** | The heatsink for the integrated optics is mounted on four rubber bumpers for vibration damping (right hand side). The heat sink for the electrical part is mounted on aluminum cylinders (left hand side).





**Figure D.15: REFM-OPT Prototype Internals** | The integrated [L2RF](#) optics occupy about half of the 19" housing. The isolated cover of the optical assembly is removed from the setup and visible in the upper left corner of the picture. The humidity buffer is mounted to this top cover. The [REACT](#) electronics are mounted directly to the heatsink and below the integrated [L2RF](#) readout electronics. Both components have the same footprint, therefore the [REACT](#) electronics are not visible in the picture. The [FRED](#) board is mounted to the lower left side wall as well as an integrated two channel optical power monitor. The [PCB](#) in the lower right corner is the so-called [TMCB](#), which is used as digitizer for all monitoring signals and as main controller of the [REFM-OPT](#). The [RF](#) output splitter and the temperature controller are mounted below the [TMCB](#).



**Figure D.16: REFM-OPT Prototype Front View** | The two Ethernet sockets are connected to the [TCMB](#) and the [FRED](#) and used respectively for control and management of the [REFM-OPT](#). The high-density D-sub connector is connected to the programming interfaces of the internal microcontrollers and [FPGAs](#). Monitoring ports from both the [L2RF](#) readout and the [REACT](#) electronics are provided on the front panel as well as two phase stabilized 1.3 GHz outputs. The main power switch controls the [DC](#) supply voltages via the [FRED](#) and the status of the connected [DC](#) supply voltages is displayed by individual [LEDs](#).

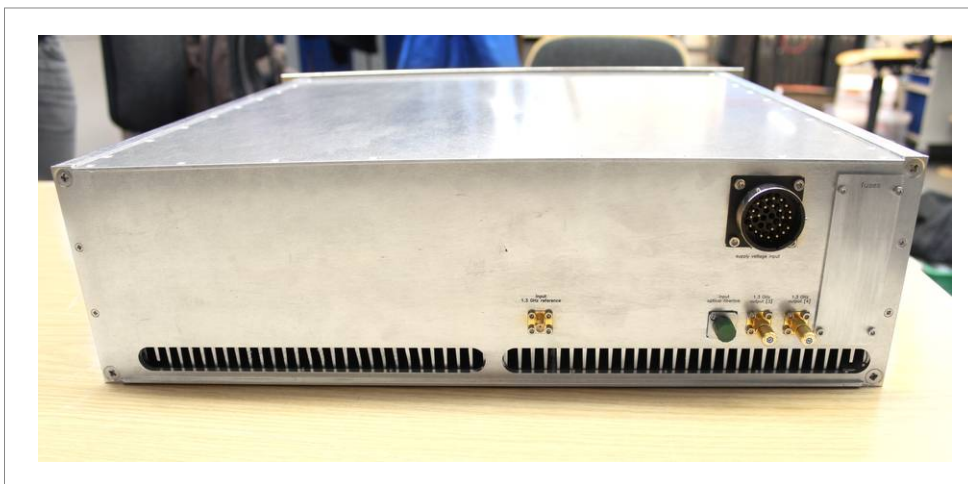


**Figure D.17: REFM-OPT Prototype Rear View** | The input of the 1.3 GHz [RF](#) and the optical reference signals are located at the rear face of the [REFM-OPT](#) prototype. Additionally, two phase stabilized 1.3 GHz [RF](#) outputs are available there. The [DC](#) supply voltage input is connected to the [FRED](#). Individual fuses for all supply voltages are accessible from the rear face and thereby externally exchangeable.



---

## Bibliography

- [And<sup>+</sup>00] ANDRUSZKOW, J. et al.: First Observation of Self-Amplified Spontaneous Emission in a Free-Electron Laser at 109 nm Wavelength. In: *Physical Review Letters* 85 (Oct. 30, 2000) Nr. 18, pages 3825–3829. doi: 10.1103/PhysRevLett.85.3825
- [Bet02] BETTS, Gary E.: LiNbO<sub>3</sub> external modulators and their use in high performance analog links. In: CHANG, William S. (editor): *RF Photonic Technology in Optical Fiber Links*. 1st edition. Cambridge, UK: Cambridge University Press, 2002, pages 81–132
- [Boc12] BOCK, Marie Kristin: *Measuring the Electron Bunch Timing with Femtosecond Resolution at FLASH*. PhD thesis. Hamburg, Germany: Universität Hamburg, 2012. URL: <http://www-library.desy.de/preparch/desy/thesis/desy-thesis-13-008.pdf>
- [Bou<sup>+</sup>12] BOUSONVILLE, Michael et al.: New Phase Stable Optical Fiber. In: *Proceedings of BIW 2012*. Newport News, VA, USA, Apr. 2012, pages 102–103. URL: <http://accelconf.web.cern.ch/AccelConf/BIW2012/papers/mopg033.pdf>
- [Bra<sup>+</sup>12] BRANLARD, Julien et al.: The European XFEL LLRF System. In: *Proceedings of IPAC 2012*. New Orleans, LA, USA, May 2012, pages 55–57. URL: <http://accelconf.web.cern.ch/AccelConf/IPAC2012/papers/M00AC01.pdf>
- [Cul11] CULLERTON, Edward: 1.3 GHz Phase Averaging Reference Line for Fermilab's NML. Conference Talk. Proceedings of LLRF2011. Hamburg, Germany, Oct. 2011. URL: <https://indico.desy.de/getFile.py/access?contribId=27&sessionId=6&resId=0&materialId=slides&confId=3391>
- [CV06] CURRIE, Marc ; VURGAFTMAN, Igor: Microwave phase retardation in saturated InGaAs photodetectors. In: *IEEE Photonics Technology Letters* 18 (July 2006) Nr. 13, pages 1433–1435. doi: 10.1109/LPT.2006.877552

## Bibliography

- [Czu07] CZUBA, Krzysztof: *RF Phase Reference Distribution System for the TESLA Technology Based Projects*. PhD thesis. Warsaw, Poland: Warsaw University of Technology, 2007. URL: <http://cds.cern.ch/record/1523225/files/EuCARD-B00-2013-002.pdf>
- [Czu<sup>+</sup>13] CZUBA, Krzysztof et al.: Overview of the RF Synchronization System for the European XFEL. In: *Proceedings of IPAC2013*. Shanghai, China, May 2013, pages 3001–3003. URL: <http://accelconf.web.cern.ch/AccelConf/IPAC2013/papers/WEPME035.pdf>
- [Czw<sup>+</sup>14] CZWALINNA, Marie Kristin et al.: Performance Study of High Bandwidth Pickups Installed at FLASH and ELBE for Femtosecond-Precision Arrival Time Monitors. In: *Proceedings of FEL2014*. Basel, Switzerland, Aug. 2014, pages 893–897. URL: <http://accelconf.web.cern.ch/AccelConf/FEL2014/papers/THP069.pdf>
- [Dah<sup>+</sup>13] DAHLHOFF, Heinrich et al.: *Tabellenbuch Mechatronik*. 7th edition. Haan-Gruiten, Germany: Verlag Europa-Lehrmittel, Jan. 24, 2013
- [Fel<sup>+</sup>09] FELBER, Matthias et al.: Long-Term Femtosecond Stable RF Signal Generation from Optical Pulse Trains. In: *Proceedings of PAC2009*. Vancouver, BC, Canada, May 2009, pages 4165–4167. URL: <http://accelconf.web.cern.ch/AccelConf/PAC2009/papers/TH6REP088.pdf>
- [Fel<sup>+</sup>14] FELBER, Matthias et al.: New MTCA.4-based Hardware Developments for the Control of the Optical Synchronization Systems at DESY. In: *Proceedings of IBIC2014*. Monterey, CA, USA, Sept. 2014, pages 152–156. URL: <http://accelconf.web.cern.ch/AccelConf/IBIC2014/papers/MOPD07.pdf>
- [Fle11] FLEGEL, Ilka: *Blitzlicht. DESY erzeugt brillante Lichtblitze für eine tiefergehende Sicht der Dinge*. Edited by DEUTSCHES ELEKTRONEN SYNCHROTRON DESY. Hamburg, Germany, Sept. 2011. URL: [http://pr.desy.de/sites2009/site\\_pr/content/e113/e143399/e143411/2011\\_ForschungmitPhotonen\\_BLITZLICHT\\_ger.pdf](http://pr.desy.de/sites2009/site_pr/content/e113/e143399/e143411/2011_ForschungmitPhotonen_BLITZLICHT_ger.pdf)
- [FBC00] FRISCH, Josef C. ; BROWN, David G. ; CISNEROS, Eugene L.: Performance of the Prototype NLC RF Phase and Timing Distribution System. In: *Proceedings of BIW2000*. Cambridge, MA, USA, May 2000, pages 365–373. URL: <http://www.slac.stanford.edu/cgi-wrap/getdoc/slac-pub-8458.pdf>
- [He<sup>+</sup>13] HE, Wenjun et al.: Polarization properties of a corner-cube retroreflector with three-dimensional polarization ray-tracing calculus. In: *Applied Optics* 52 (July 1, 2013) Nr. 19, pages 4527–4535. doi: 10.1364/AO.52.004527



- [Hob01] HOBBS, Philip C. D.: Photodiode Front Ends: The Real Story. In: *Optics and Photonics News* 12 (Apr. 1, 2001) Nr. 4, pages 44–47. doi: 10.1364/OPN.12.4.000044
- [Hon<sup>+</sup>14] HONKAVAARA, Katja et al.: FLASH: First Soft X-Ray FEL Operating Two Undulator Beamlines Simultaneously. In: *Proceedings of FEL 2014*. Basel, Switzerland, Aug. 2014, pages 635–639. URL: <http://accelconf.web.cern.ch/AccelConf/FEL2014/papers/WEB05.pdf>
- [Jam11] JAMES, John. F.: *A Student's Guide to Fourier Transforms: With Applications in Physics and Engineering*. 3rd edition. Cambridge, UK: Cambridge University Press, May 2011. 161 pages
- [Jan12] JANAS, Ewa: *Precise optical-electrical synchronization system for accelerators FLASH and XFEL*. MSc thesis. Warsaw, Poland: Warsaw University of Technology, 2012. URL: [http://wof-cluster.desy.de/sites2009/site\\_msk/content/localfsExplorer\\_read?currentPath=/afs/desy.de/group/msk/www/html/Publikationen/Diplomarbeiten/diploma\\_janas.pdf](http://wof-cluster.desy.de/sites2009/site_msk/content/localfsExplorer_read?currentPath=/afs/desy.de/group/msk/www/html/Publikationen/Diplomarbeiten/diploma_janas.pdf)
- [Jan<sup>+</sup>14] JANAS, Ewa et al.: Design and Integration of the Optical Reference Module at 1.3 GHz for FLASH and the European XFEL. In: *Proceedings of IPAC 2014*. Dresden, Germany, July 2014, pages 2768–2770. URL: <http://accelconf.web.cern.ch/AccelConf/IPAC2014/papers/WEPRI115.pdf>
- [JK12] JUNG, Kwangyun ; KIM, Jungwon: Microwave signal synchronized with a mode-locked Er-fiber laser with ultralow residual phase noise and drift. In: *2012 Conference on Lasers and Electro-Optics (CLEO)*. San Jose, CA, USA, May 2012, pages 1124–1125. doi: 10.1364/CLEO\_SI.2012.CTh4A.5
- [Kim07] KIM, Jungwon: *High-precision optical and microwave signal synthesis and distribution*. PhD thesis. Cambridge, MA, USA: Massachusetts Institute of Technology, 2007. doi: 1721.1/42230
- [KJS14] KIM, Jungwon ; JUNG, Kwangyun ; SHIN, Junho: Microwave synthesis and remote transfer using attosecond-jitter mode-locked fiber lasers. In: *2014 International Topical Meeting on Microwave Photonics (MWP) and the 2014 9th Asia-Pacific Microwave Photonics Conference (APMP)*. Sapporo, Japan, Oct. 2014, pages 48–50. doi: 10.1109/MWP.2014.6994486
- [KK10] KIM, Jungwon ; KÄRTNER, Franz X.: Subfemtosecond-drift microwave signal synthesis from femtosecond mode-locked lasers. In: *2010 Conference on Lasers and Electro-Optics (CLEO) and Quantum Electronics and Laser Science Conference (QELS)*. San Jose, CA, USA, May 2010. doi: 10.1364/CLEO.2010.CTuDD4

## Bibliography

- [KKL06] KIM, Jungwon ; KÄRTNER, Franz X. ; LUDWIG, Frank: Balanced optical-microwave phase detectors for optoelectronic phase-locked loops. In: *Optics Letters* 31 (Dec. 2006) Nr. 24, pages 3659–3661. doi: [10.1364/OL.31.003659](https://doi.org/10.1364/OL.31.003659)
- [KKP04] KIM, Jungwon ; KÄRTNER, Franz X. ; PERROTT, Michael H.: Femtosecond synchronization of radio frequency signals with optical pulse trains. In: *Optics Letters* 29 (Sept. 2004) Nr. 17, pages 2076–2078. doi: [10.1364/OL.29.002076](https://doi.org/10.1364/OL.29.002076)
- [Kim<sup>+</sup>04] KIM, Jungwon et al.: Large-Scale Timing Distribution and RF-Synchronization for FEL Facilities. In: *Proceedings of FEL 2004*. Trieste, Italy, Sept. 2004, pages 339–342. URL: <http://accelconf.web.cern.ch/AccelConf/F04/papers/TUAOS03/TUAOS03.PDF>
- [Löhl09] LÖHL, Florian: *Optical Synchronization of a Free-Electron Laser with Femtosecond Precision*. PhD thesis. Hamburg, Germany: Universität Hamburg, 2009. URL: <http://www-library.desy.de/preparch/desy/thesis/desy-thesis-09-031.pdf>
- [Lor<sup>+</sup>07] LORBEER, Bastian et al.: Noise and Drift Characterization of Direct Laser to RF Conversion Scheme for the Laser Based Synchronization System for FLASH at DESY. In: *Proceedings of PAC 2007*. Albuquerque, NM, USA, June 2007, pages 182–184. URL: <http://accelconf.web.cern.ch/AccelConf/p07/papers/MOPAN017.pdf>
- [Lut87] LUTES, G.: Reference Frequency Distribution Over Optical Fibers: a Progress Report. In: *41st Annual Symposium on Frequency Control*. Philadelphia, PA, USA, May 1987, pages 161–166. doi: [10.1109/FREQ.1987.201018](https://doi.org/10.1109/FREQ.1987.201018)
- [Mad71] MADEY, John M. J.: Stimulated Emission of Bremsstrahlung in a Periodic Magnetic Field. In: *Journal of Applied Physics* 42 (Apr. 1, 1971) Nr. 5, pages 1906–1913. doi: [10.1063/1.1660466](https://doi.org/10.1063/1.1660466)
- [MM09] MAEDA, Yoichi ; MONTALTI, Francesco: *Optical Fibres, Cables and Systems*. Edited by GASTONE BONAVENTURA. ITU Recommendation 415-10. Geneva, Switzerland: International Telecommunication Union, 2009. 299 pages. URL: [http://www.itu.int/dms\\_pub/itu-t/opb/hdb/T-HDB-OUT.10-2009-1-PDF-E.pdf](http://www.itu.int/dms_pub/itu-t/opb/hdb/T-HDB-OUT.10-2009-1-PDF-E.pdf)
- [Mai13] MAINI, Anil K.: *Lasers and Optoelectronics: Fundamentals, Devices and Applications*. 1st edition. Chichester, UK: John Wiley & Sons, Sept. 2013. 637 pages
- [Pap62] PAPOULIS, Athanasios: *The Fourier Integral and Its Applications*. 1st edition. New York, NY, USA: McGraw-Hill Book Company Inc., 1962. 320 pages

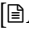



- [Pfe14] PFEIFFER, Sven: *Symmetric Grey Box Identification and Distributed Beam-Based Controller Design for Free-Electron Lasers*. PhD thesis. Hamburg, Germany: Technische Universität Hamburg-Harburg, 2014. URL: <http://www-library.desy.de/preparch/desy/thesis/desy-thesis-14-030.pdf>
- [Qui<sup>+</sup>13] QUINLAN, Franklyn et al.: Exploiting shot noise correlations in the photodetection of ultrashort optical pulse trains. In: *Nature Photonics* 7 (Apr. 2013) Nr. 4, pages 290–293. doi: [10.1038/nphoton.2013.33](https://doi.org/10.1038/nphoton.2013.33)
- [Rön<sup>+</sup>14] RÖNSCH-SCHULENBURG, Juliane et al.: Operation of FLASH with Short SASE-FEL Radiation Pulses. In: *Proceedings of FEL 2014*. Basel, Switzerland, Aug. 2014. URL: <http://accelconf.web.cern.ch/AccelConf/FEL2014/papers/tub04.pdf>
- [Rub06] RUBIOLA, Enrico: Tutorial on the double balanced mixer. In: *ArXiv Physics e-prints - Instrumentation and Detectors* (Aug. 2006). arXiv:physics/0608211
- [ST91] SALEH, Bahaa E. A. ; TEICH, Malvin Carl: *Fundamentals of Photonics*. 1st edition. New York: John Wiley & Sons Inc., Sept. 20, 1991. 992 pages
- [Sal<sup>+</sup>11] SALVESTRINI, Jean Paul et al.: Analysis and Control of the DC Drift in LiNbO<sub>3</sub>-Based Mach-Zehnder Modulators. In: *Journal of Lightwave Technology* 29 (May 2011) Nr. 10, pages 1522–1534. doi: [10.1109/JLT.2011.2136322](https://doi.org/10.1109/JLT.2011.2136322)
- [Sch<sup>+</sup>05] SCHLARB, Holger et al.: Next Generation Synchronization System for the VUV-FEL at DESY. In: *Proceedings of FEL 2005*. Stanford, CA, USA, Aug. 2005, pages 118–121. URL: <http://accelconf.web.cern.ch/AccelConf/F05/papers/mopp036.pdf>
- [Sch<sup>+</sup>14] SCHMIDT, Christian et al.: Performance of the MTCA.4 based LLRF System at FLASH. In: *Proceedings of IPAC2014*. Dresden, Germany, July 2014, pages 2433–2435. URL: <http://accelconf.web.cern.ch/AccelConf/IPAC2014/papers/WEPME067.pdf>
- [SDR08] SCHMÜSER, Peter ; DOHLUS, Martin ; ROSSBACH, Jörg: *Ultraviolet and Soft X-Ray Free-Electron Lasers: Introduction to Physical Principles, Experimental Results, Technological Challenges*. Berlin / Heidelberg, Germany: Springer-Verlag, 2008. doi: [10.1007/978-3-540-79572-8](https://doi.org/10.1007/978-3-540-79572-8)
- [Sch10] SCHNEIDER, Jochen R.: FLASH – from accelerator test facility to the first single-pass soft x-ray free-electron laser. In: *Journal of Physics B: Atomic, Molecular and Optical Physics* 43 (Sept. 6, 2010) Nr. 19, page 194001. doi: [10.1088/0953-4075/43/19/194001](https://doi.org/10.1088/0953-4075/43/19/194001)

## Bibliography

- [Sch11a] SCHREIBER, Siegfried: First Lasing in the Water Window With 4.1 nm at FLASH. In: *Proceedings of FEL 2011*. Shanghai, China, Aug. 2011, pages 164–165. URL: <http://accelconf.web.cern.ch/AccelConf/FEL2011/papers/tuobi2.pdf>
- [Sch11b] SCHULZ, Sebastian: *Implementation of the Laser-Based Femtosecond Precision Synchronization System at FLASH*. PhD thesis. Hamburg, Germany: Universität Hamburg, 2011. URL: <http://www-library.desy.de/preparch/desy/thesis/desy-thesis-14-012.pdf>
- [Sch<sup>+</sup>15] SCHULZ, Sebastian et al.: Femtosecond all-optical synchronization of an X-ray free-electron laser. In: *Nature Communications* 6 (Jan. 20, 2015), page 5938. doi: 10.1038/ncomms6938
- [Sch<sup>+</sup>13] SCHULZ, Sebastian et al.: Femtosecond-precision synchronization of the pump-probe optical laser for user experiments at FLASH. In: *Proceedings of SPIE – Advances in X-ray Free-Electron Lasers II: Instrumentation*. Volume 8778. Prague, Czech Republic, Apr. 2013. doi: 10.1117/12.2021572
- [SiSa08] SINGH, R. P. ; SAPRE, S. D.: *Communication Systems: Analog & Digital*. 2nd edition. New Delhi, India: Tata McGraw-Hill Education, 2008. 608 pages
- [SB10] SORRENTINO, R. ; BIANCHI, Giovanni: *Microwave and RF Engineering*. 1st edition. Chichester, UK: John Wiley & Sons, 2010. 912 pages
- [Sto<sup>+</sup>06] STOCKWELL, P. et al.: A Low Phase Noise 1.3 GHz Dielectric Resonator Oscillator. In: *2006 IEEE International Frequency Control Symposium Proceedings (FCS 2006)*. Miami, FL, USA, June 2006, pages 882–885. doi: 10.1109/FREQ.2006.275506
- [Syd<sup>+</sup>14] SYDLO, Cezary et al.: Femtosecond Timing Distribution for the European XFEL. In: *Proceedings of FEL 2014*. Basel, Switzerland, Aug. 2014, pages 669–671. URL: <http://accelconf.web.cern.ch/AccelConf/FEL2014/papers/THP090.pdf>
- [Tit<sup>+</sup>14] TITBERIDZE, Mikheil et al.: Novel Femtosecond Level Synchronization of Titanium Sapphire Laser and Relativistic Electron Beams. In: *Proceedings of IBIC 2014*. Monterey, CA, USA, Sept. 2014, pages 174–178. URL: <http://accelconf.web.cern.ch/AccelConf/IBIC2014/papers/MOPD12.pdf>
- [Tra<sup>+</sup>10] TRATNIK, Jurij et al.: Femtosecond Electro-Optical Synchronization System with Long-Term Phase Stability Results. In: *Proceedings of IPAC 2010*. Kyoto, Japan, May 2010, pages 2881–2883. URL: <http://accelconf.web.cern.ch/AccelConf/IPAC10/papers/WEPEB080.pdf>

- [Wil<sup>+</sup>10] WILCOX, Russel et al.: Stable Transmission of RF Signals on Optical Fiber Links. In: *Proceedings of IPAC 2010*. Kyoto, Japan, May 2010, pages 1399–1401. URL: <http://accelconf.web.cern.ch/AccelConf/IPAC10/papers/tupea033.pdf>
- [Woo<sup>+</sup>00] WOOTEN, Ed L. et al.: A Review of Lithium Niobate Modulators for Fiber-Optic Communications Systems. In: *IEEE Journal of Selected Topics in Quantum Electronics* 6 (Jan. 2000) Nr. 1, pages 69–82. doi: 10.1109/2944.826874
- [ZHS03] ZEIDLER, Eberhard ; HACKBUSCH, Wolfgang ; SCHWARZ, Hans Rudolf: *Teubner-Taschenbuch der Mathematik*. 2nd edition. Stuttgart, Germany: Vieweg + Teubner Verlag, Nov. 2003. 1300 pages
- [Zha<sup>+</sup>12] ZHANG, Wei et al.: Amplitude to phase conversion of InGaAs PIN photodiodes for femtosecond lasers microwave signal generation. In: *Applied Physics B: Lasers and Optics* 106 (Feb. 2012) Nr. 2, pages 301–308. doi: 10.1007/s00340-011-4710-1
- [Zum<sup>+</sup>13] ZUMMACK, Falco et al.: Status of the Fiber Link Stabilization Units at FLASH. In: *Proceedings of IBIC 2013*. Oxford, UK, Sept. 2013, pages 139–142. URL: <http://accelconf.web.cern.ch/AccelConf/IBIC2013/papers/mopc33.pdf>

## Data Sheets

- [AD797] ANALOG DEVICES INC.: AD797 – *Ultralow Distortion, Ultralow Noise Operational Amplifier*. Data Sheet. Revision J. URL: [http://www.analog.com/static/imported-files/data\\_sheets/AD797.pdf](http://www.analog.com/static/imported-files/data_sheets/AD797.pdf)
- [AD8302] ANALOG DEVICES INC.: AD8302 – *RF/IF Gain and Phase Detector*. Data Sheet. Revision A. URL: [http://www.analog.com/static/imported-files/data\\_sheets/AD8302.pdf](http://www.analog.com/static/imported-files/data_sheets/AD8302.pdf)
- [Arflx] ARMACELL SWITZERLAND AG: NH/Armaflex – *Flexible Elastomeric Foam*. Data Sheet. URL: [http://www.armacell.com/WWW/armacell/ACwwwAttach.nsf/ansFiles/NHArmaflexPDSUKROIDigital.pdf/\\$File/NHArmaflexPDSUKROIDigital.pdf](http://www.armacell.com/WWW/armacell/ACwwwAttach.nsf/ansFiles/NHArmaflexPDSUKROIDigital.pdf/$File/NHArmaflexPDSUKROIDigital.pdf)
- [EOMz] EOSPACE INC.: AX-1X2-0K3-12-PFA-PFAP – *Lithium Niobate Modulator*. Serial Number: 67129. Data Sheet. Shipped with the modulator, internal documentation, Oct. 28, 2008

## Data Sheets

- [ET3.5k] ELECTRO-OPTICS TECHNOLOGY INC.: *ET-3500F – PIN Photodiode*. Data Sheet. URL: <http://www.eotech.com/content/userfiles/12.5GHz%20Photodetectors.pdf>
- [HIH4] HONEYWELL: *HIH-4000 – Humidity Sensor*. Data Sheet. URL: <https://sensing.honeywell.com/honeywell-sensing-hih4000-series-product-sheet-009017-5-en.pdf>
- [HS404] HUBER+SUHNER AG: *Sucoflex 404 – Low Loss, Phase Stable RF Cable*. Data Sheet. URL: <http://www.hubersuhner.com/de/Recent-Products/Sucoflex-400>
- [MComb] MENLOSYSTEMS GMBH: *M-Comb – Femtosecond Erbium Laser*. Data Sheet. URL: [http://www.menlosystems.com/assets/datasheets/MENLO\\_M-Comb-D-EN\\_2016-05\\_3w.pdf](http://www.menlosystems.com/assets/datasheets/MENLO_M-Comb-D-EN_2016-05_3w.pdf)
- [Orig15] ONEFIVE GMBH: *Origami-15 – Ultra-Low-Noise Soliton Femtosecond Laser Module*. Data Sheet. URL: [http://www.onefive.com/img/products/origami\\_datasheet.pdf](http://www.onefive.com/img/products/origami_datasheet.pdf)
- [PM190] TELEDYNE STORM MICROWAVE: *Phasemaster 190E – Highly Shielded Phase Stable Cables*. Data Sheet. URL: [http://www.teledynestorm.com/pdf/Phase\\_Master\\_190E.pdf](http://www.teledynestorm.com/pdf/Phase_Master_190E.pdf)
- [ProS] LONG LIFE FOR ART: *PROSorb – Humidity Stabilizer*. Data Sheet. URL: <http://www.cwaller.de/english.htm?eprosorb.htm~information>
- [PS980] WEINSCHEL (API TECHNOLOGIES CORP.): *980-4 – Coaxial Phase Shifter*. Data Sheet. Sept. 30, 2012. URL: <http://weinschel.apitech.com/weinschel/pdfiles/wmod980.pdf>
- [PTC10k] WAVELENGTH ELECTRONICS INC.: *PTC10k-CH – Chassis Mount Temperature Controller*. Data Sheet. Revision H. URL: <http://www.teamwavelength.com/downloads/datasheets/ptcck-ch.pdf>
- [SLP] MINI-CIRCUITS: *SLP-1.9+ – Low Pass Filter*. Data Sheet. Revision B. URL: <http://www.minicircuits.com/pdfs/SLP-1.9+.pdf>
- [SMF28e] CORNING INCORPORATED: *SMF-28e+ – optical fiber*. Data Sheet. URL: [https://www.corning.com/media/worldwide/coc/documents/PI1463\\_07-14\\_English.pdf](https://www.corning.com/media/worldwide/coc/documents/PI1463_07-14_English.pdf)
- [SR402] PASTERNAK ENTERPRISES INC.: *PE-SR402FL – Formable 141 Semi-Rigid Coax Cable*. Data Sheet. URL: <http://www.pasternack.com/images/ProductPDF/PE-SR402FL.pdf>
- [ZAPD] MINI-CIRCUITS: *ZAPD-2+ – 2-Way Power Splitter/Combiner*. Data Sheet. Revision A. URL: <http://www.minicircuits.com/pdfs/ZAPD-2.pdf>

- [ZFL] MINI-CIRCUITS: *ZFL-500LN – Low Noise Amplifier*. Data Sheet. Revision D. URL: <http://www.minicircuits.com/pdfs/ZFL-500LN.pdf>
- [ZFM] MINI-CIRCUITS: *ZFM-2000+ – Level 7 Frequency Mixer*. Data Sheet. Revision B. URL: <http://www.minicircuits.com/pdfs/ZFM-2000+.pdf>
- [ZMSC] MINI-CIRCUITS: *ZMSC-4-3 – 4-Way Power Splitter/Combiner*. Data Sheet. Revision B. URL: <http://www.minicircuits.com/pdfs/ZMSC-4-3.pdf>
- [ZRL] MINI-CIRCUITS: *ZRL-1150LN+ – Low Noise Amplifier*. Data Sheet. Revision J. URL: <http://www.minicircuits.com/pdfs/ZRL-1150LN+.pdf>
- [ZX10] MINI-CIRCUITS: *ZX10-2-20 – 2-Way Power Splitter/Combiner*. Data Sheet. Revision E. URL: <http://www.minicircuits.com/pdfs/ZX10-2-20.pdf>
- [ZX60] MINI-CIRCUITS: *ZX60-33LN+ – Low Noise Amplifier*. Data Sheet. Revision B. URL: <http://www.minicircuits.com/pdfs/ZX60-33LN+.pdf>





---

## Publications

### Patents

SCHLARB, H. ; **LAMB, T.**: *System and Method for Generating a Synchronisation Control Signal*. Assignee: Deutsches Elektronen-Synchrotron (DESY). EP 2560250. Aug. 10, 2012. Patent Application, also filed under DE 102011 111 114 and US 201 300 449 75, granted under US 9 106 044

### Conference Proceedings

BOCK, M. K. ; BOUSONVILLE, M. ; FELBER, M. ; GESSLER, P. ; **LAMB, T.** ; RUZIN, S. ; SCHLARB, H. ; SCHMIDT, B. ; SCHULZ, S.: Benchmarking the Performance of the Present Bunch Arrival Time Monitors at FLASH. In: *Proceedings of DIPAC 2011*. Hamburg, Germany, May 2011, pages 365–367. URL: <http://accelconf.web.cern.ch/AccelConf/DIPAC2011/papers/tupd28.pdf>

BOCK, M. K. ; **LAMB, T.** ; BOUSONVILLE, M. ; FELBER, M. ; GESSLER, P. ; SCHLARB, H. ; SCHMIDT, B. ; SCHULZ, S.: Report on the Redesign of the Fibre Link Stabilisation Units at FLASH. In: *Proceedings of FEL 2011*. Shanghai, China, Aug. 2011, pages 370–373. URL: <http://accelconf.web.cern.ch/AccelConf/FEL2011/papers/wepa19.pdf>

BOUSONVILLE, M. ; BOCK, M. K. ; FELBER, M. ; HUNZIKER, S. ; JABŁONSKI, S. ; KOWNACKI, P. ; LADWIG, T. ; **LAMB, T.** ; SCHLARB, H. ; SCHULZ, S. ; SYDLO, C.: New Phase Stable Optical Fiber. In: *Proceedings of BIW 2012*. Newport News, VA, USA, Apr. 2012, pages 102–103. URL: <http://accelconf.web.cern.ch/AccelConf/BIW2012/papers/mopg033.pdf>

BRANLARD, J. ; AYVAZYAN, G. ; AYVAZYAN, V. ; BARMUTA, P. ; BUTKOWSKI, Ł. ; BOU HABIB, S. ; CICHALEWSKI, W. ; CZUBA, K. ; GNIDZIŃSKA, K. ; GRECKI, M. ; GRZEGRZÓŁKA, M. ; HOFFMANN, M. ; JAŁMUŻNA, W. ; JANAS, E. ; JEŻYŃSKI, T. ; KOROLCZUK, S. ; KUDŁA, I. M. ; **LAMB, T.** ; LUDWIG, F. ; MAKOWSKI, D. ; MAVRIČ, U. ; MIELCZAREK, A. ; NAPIER-ALSKI, A. ; OLIWA, K. ; PEREK, P. ; PFEIFFER, S. ; PIEKARSKI, J. ; PIOTROWSKI, A. ; POŻ-  
 NIAK, T. ; PRZYGODA, K. ; RUTKOWSKI, I. ; SCHLARB, H. ; SCHMIDT, C. ; SIKORA, D. ;  
 SZEWIŃSKI, J. ; WEDDIG, H.-C. ; WIERBA, W. ; YANG, B. ; ZEMBALA, Ł. ; ŻUCKOCIŃSKI,  
 M.: The European XFEL LLRF System. In: *Proceedings of IPAC2012*. New Orleans, LA,  
 USA, May 2012, pages 55–57. URL: [http://accelconf.web.cern.ch/AccelConf/  
 IPAC2012/papers/M00AC01.pdf](http://accelconf.web.cern.ch/AccelConf/IPAC2012/papers/M00AC01.pdf)

FELBER, M. ; CZWALINNA, M. K. ; FENNER, M. ; GERTH, C. ; HEUER, M. ; JANAS, E. ;  
 KOZAK, T. ; **LAMB, T.** ; MAVRIČ, U. ; MÜLLER, J. ; PEIER, P. ; PRĘDKI, P. ; PRZYGODA, K. ;  
 SCHLARB, H. ; SYDŁO, C. ; TITBERIDZE, M. ; ZUMMACK, F. ; BUTKOWSKI, Ł. ; KILLEN-  
 BERG, M. ; RUZIN, S.: Implementation of MTCA.4-based Controls for the Pulsed Optical  
 Synchronization Systems at DESY. In: *Proceedings of FEL 2015*. Daejeon, Korea, Aug. 2015,  
 pages 115–117. doi: [10.18429/JACoW-FEL2015-MOP040](https://doi.org/10.18429/JACoW-FEL2015-MOP040)

FELBER, M. ; CZWALINNA, M. K. ; DUHME, H. T. ; FENNER, M. ; GERTH, C. ; HEUER,  
 M. ; JANAS, E. ; KOZAK, T. ; **LAMB, T.** ; MAVRIČ, U. ; MÜLLER, J. ; PEIER, P. ; PRĘDKI,  
 P. ; PRZYGODA, K. ; SCHLARB, H. ; SCHULZ, S. ; STEFFEN, B. ; SYDŁO, C. ; SZEWIŃSKI,  
 J. ; TITBERIDZE, M. ; WALTER, T. ; WEDEL, R. ; ZUMMACK, F.: New MTCA.4-based  
 Hardware Developments for the Control of the Optical Synchronization Systems at DESY.  
 In: *Proceedings of IBIC2014*. Monterey, CA, USA, Sept. 2014, pages 152–156. URL:  
<http://accelconf.web.cern.ch/AccelConf/IBIC2014/papers/MOPD07.pdf>

FELBER, M. ; BOCK, M. K. ; BREUNLIN, J. ; GESSLER, P. ; HACKER, K. E. ; **LAMB, T.** ;  
 LUDWIG, F. ; SCHLARB, H. ; SCHMIDT, B. ; SCHULZ, S. ; WISSMANN, L. G.: RF-based  
 Synchronization of the Seed and Pump-Probe Lasers to the Optical Synchronization System  
 at FLASH. In: *Proceedings of FEL 2010*. Malmö, Sweden, Aug. 2010, pages 544–547. URL:  
<http://accelconf.web.cern.ch/AccelConf/FEL2010/papers/thoa3.pdf>

FELBER, M. ; BOCK, M. K. ; BOUSONVILLE, M. ; GESSLER, P. ; **LAMB, T.** ; RUZIN, S. ;  
 SCHLARB, H. ; SCHMIDT, B. ; SCHULZ, S.: Upgrade of the Optical Synchronization System  
 for FLASH II. In: *Proceedings of FEL 2011*. Shanghai, China, Aug. 2011, pages 496–498. URL:  
<http://accelconf.web.cern.ch/AccelConf/FEL2011/papers/thpa14.pdf>

GESSLER, P. ; BOCK, M. K. ; BOHM, C. ; BOUSONVILLE, M. ; CZUBA, K. ; FELBER, M. ; HIDVÉGI, A. ; HOFFMANN, M. ; JEŻYŃSKI, T. ; **LAMB, T.** ; LUDWIG, F. ; MAKOWSKI, D. ; PETROSYAN, G. ; PETROSYAN, L. ; REHLICH, K. ; SCHULZ, S. ; VETROV, P. ; ZIMMER, M.: Next Generation Electronics Based on  $\mu$ TCA for Beam-Diagnostics at FLASH and XFEL. In: *Proceedings of DIPAC2011*. Hamburg, Germany, May 2011, pages 294–296. URL: <http://accelconf.web.cern.ch/AccelConf/DIPAC2011/papers/tuob03.pdf>

JANAS, E. ; CZUBA, K. ; CZWALINNA, M. K. ; FELBER, M. ; KOWNACKI, P. ; **LAMB, T.** ; SCHLARB, H. ; SCHULZ, S. ; SIKORA, D. ; SYDLO, C. ; SZEWIŃSKI, J. ; TITBERIDZE, M. ; ZUMMACK, F.: Design and Integration of the Optical Reference Module at 1.3 GHz for FLASH and the European XFEL. In: *Proceedings of IPAC2014*. Dresden, Germany, July 2014, pages 2768–2770. URL: <http://accelconf.web.cern.ch/AccelConf/IPAC2014/papers/WEPRI115.pdf>

KUNTZSCH, M. ; BOCK, M. K. ; BOUSONVILLE, M. ; BÜCHNER, A. ; FELBER, M. ; GENSCHE, M. ; JOCHMANN, A. ; KIRSCHKE, T. ; **LAMB, T.** ; LEHNERT, U. ; RÖSER, F. ; SCHLARB, H. ; SCHULZ, S.: Concept of Femtosecond Timing and Synchronization Scheme at ELBE. In: *Proceedings of IPAC2011*. San Sebastián, Spain, Sept. 2011, pages 565–567. URL: <http://accelconf.web.cern.ch/AccelConf/IPAC2011/papers/mopo037.pdf>

KUNTZSCH, M. ; BOCK, M. K. ; BOUSONVILLE, M. ; BÜCHNER, A. ; FELBER, M. ; GENSCHE, M. ; **LAMB, T.** ; LEHNERT, U. ; RÖSER, F. ; SCHLARB, H. ; SCHULZ, S. ; SYDLO, C.: Status of the Femtosecond Synchronization System at ELBE. In: *Proceedings of BIW2012*. Newport News, VA, USA, Apr. 2012, pages 12–14. URL: <http://accelconf.web.cern.ch/AccelConf/BIW2012/papers/mobp03.pdf>

**LAMB, T.** ; BOCK, M. K. ; FELBER, M. ; JABLONSKI, S. ; LUDWIG, F. ; SCHLARB, H. ; SCHULZ, S.: Characterization of the Engineered Photodiode-based Fiber Link Stabilization Scheme for Optical Synchronization Systems. In: *Proceedings of IPAC2012*. New Orleans, LA, USA, May 2012, pages 2627–2629. URL: <http://accelconf.web.cern.ch/AccelConf/IPAC2012/papers/weppd049.pdf>

**LAMB, T.** ; BOCK, M. K. ; BOUSONVILLE, M. ; FELBER, M. ; GESSLER, P. ; LUDWIG, F. ; RUZIN, S. ; SCHLARB, H. ; SCHMIDT, B. ; SCHULZ, S.: Development of an Alternative, Photodiode-based, Femtosecond Stable Detection Principle for the Link Stabilization in the Optical Synchronization Systems at FLASH and XFEL. In: *Proceedings of DIPAC2011*. Hamburg, Germany, May 2011, pages 380–382. URL: <http://accelconf.web.cern.ch/AccelConf/DIPAC2011/papers/tupd35.pdf>

**LAMB, T.** ; CZWALINNA, M. K. ; FELBER, M. ; GERTH, C. ; JANAS, E. ; SCHLAR, H. ; SCHULZ, S. ; SYDLO, C. ; SZEWIŃSKI, J. ; TITBERIDZE, M. ; ZUMMACK, F.: Femtosecond Stable Laser-to-RF Phase Detection for Optical Synchronization Systems. In: *Proceedings of IBIC2013*. Oxford, UK, Sept. 2013, pages 447–450. URL: <http://accelconf.web.cern.ch/AccelConf/IBIC2013/papers/TUPC33.pdf>

**LAMB, T.** ; BOCK, M. K. ; BOUSONVILLE, M. ; FELBER, M. ; GESSLER, P. ; JANAS, E. ; LUDWIG, F. ; RUZIN, S. ; SCHLAR, H. ; SCHMIDT, B. ; SCHULZ, S.: Femtosecond Stable Laser-to-RF Phase Detection Using Optical Modulators. In: *Proceedings of FEL2011*. Shanghai, China, Aug. 2011, pages 551–554. URL: <http://accelconf.web.cern.ch/AccelConf/FEL2011/papers/thpa32.pdf>

SCHULZ, S. ; BOUSONVILLE, M. ; CZWALINNA, M. K. ; FELBER, M. ; HEUER, M. ; KOZAK, T. ; KUH, A. ; **LAMB, T.** ; MÜLLER, J. ; PEIER, P. ; PRĘDKI, P. ; RUZIN, S. ; SCHLAR, H. ; STEFFEN, B. ; SYDLO, C. ; ZUMMACK, F.: Past, Present and Future Aspects of Laser Based Synchronization at FLASH. In: *Proceedings of IBIC2013*. Oxford, UK, Sept. 2013, pages 753–756. URL: <http://accelconf.web.cern.ch/AccelConf/IBIC2013/papers/wepc32.pdf>

SCHULZ, S. ; BOCK, M. K. ; FELBER, M. ; GESSLER, P. ; HACKER, K. E. ; **LAMB, T.** ; LUDWIG, F. ; SCHLAR, H. ; SCHMIDT, B. ; WISSMANN, L. G.: Performance of the FLASH Optical Synchronization System with a Commercial Sesam-Based Erbium Laser. In: *Proceedings of FEL2010*. Malmö, Sweden, Aug. 2010, pages 581–584. URL: <http://accelconf.web.cern.ch/AccelConf/FEL2010/papers/thpa05.pdf>

SCHULZ, S. ; BOCK, M. K. ; BOUSONVILLE, M. ; FELBER, M. ; GESSLER, P. ; **LAMB, T.** ; LUDWIG, F. ; RUZIN, S. ; SCHLAR, H. ; SCHMIDT, B.: Progress and Status of the Laser-Based Synchronization System at FLASH. In: *Proceedings of DIPAC2011*. Hamburg, Germany, May 2011, pages 383–385. URL: <http://accelconf.web.cern.ch/AccelConf/DIPAC2011/papers/tupd36.pdf>

SYDLO, C. ; CZWALINNA, M. K. ; FELBER, M. ; GERTH, C. ; JABŁONSKI, S. ; **LAMB, T.** ; SCHLAR, H. ; SCHULZ, S. ; ZUMMACK, F.: Development Status of Optical Synchronization for the European XFEL. In: *Proceedings of IBIC2013*. Oxford, UK, Sept. 2013, pages 135–138. URL: <http://accelconf.web.cern.ch/AccelConf/IBIC2013/papers/mopc32.pdf>

SYDLO, C. ; CZWALINNA, M. K. ; FELBER, M. ; GERTH, C. ; JABŁONSKI, S. ; **LAMB, T.** ; SCHLAR, H. ; SCHULZ, S. ; ZUMMACK, F.: Femtosecond Timing Distribution for the European XFEL. In: *Proceedings of FEL2014*. Basel, Switzerland, Aug. 2014, pages 669–671. URL: <http://accelconf.web.cern.ch/AccelConf/FEL2014/papers/THP090.pdf>

TITBERIDZE, M. ; FELBER, M. ; FLÖTTMANN, K. ; GRÜNER, F. J. ; JANAS, E. ; **LAMB, T.** ; MAIER, A. R. ; SCHLARB, H. ; SYDLO, C. ; ZEITLER, B.: Novel Femtosecond Level Synchronization of Titanium Sapphire Laser and Relativistic Electron Beams. In: *Proceedings of IBIC2014*. Monterey, CA, USA, Sept. 2014, pages 174–178. URL: <http://accelconf.web.cern.ch/AccelConf/IBIC2014/papers/MOPD12.pdf>

TITBERIDZE, M. ; EPP, S. ; FELBER, M. ; FLÖTTMANN, K. ; GRÜNER, F. J. ; JANAS, E. ; **LAMB, T.** ; MAIER, A. R. ; MAVRIČ, U. ; MÜLLER, J. ; SCHLARB, H. ; SYDLO, C. ; ZEITLER, B.: Present and Future Optical-to-Microwave Synchronization Systems at REGAE Facility for Electron Diffraction and Plasma Acceleration Experiments. In: *Proceedings of IPAC 2015*. Richmond, VA, USA, May 2015, pages 833–836. URL: <http://accelconf.web.cern.ch/AccelConf/IPAC2015/papers/MOPHA026.pdf>

ZUMMACK, F. ; CZWALINNA, M. K. ; FELBER, M. ; JABŁONSKI, S. ; **LAMB, T.** ; SCHLARB, H. ; SCHULZ, S. ; SYDLO, C.: Status of the Fiber Link Stabilization Units at FLASH. In: *Proceedings of IBIC2013*. Oxford, UK, Sept. 2013, pages 139–142. URL: <http://accelconf.web.cern.ch/AccelConf/IBIC2013/papers/mopc33.pdf>

